UNIVERSIDADE
BEIRA INTERIOR

Insights into Droplet-Surface Collisions for Aeronautical Applications

Daniela Filipa Santo Ribeiro

Tese para obtenção do Grau de Doutor em
Engenharia Aeronáutica
(3º ciclo de estudos)

Orientador: Prof. Doutor André Resende Rodrigues da Silva

junho de 2024

UNIVERSIDADE
BEIRA INTERIOR

Insights into Droplet-Surface Collisions for Aeronautical Applications

Daniela Filipa Santo Ribeiro

Tese para obtenção do Grau de Doutor em
Engenharia Aeronáutica
(3º ciclo de estudos)

Orientador: Prof. Doutor André Resende Rodrigues da Silva

Júri:
Prof. Doutor Joaquim Mateus Paulo Serra
Prof. Doutor Jorge Manuel Martins Barata
Doutora Flávia Vieira Barbosa
Prof. Doutor Daniel Cardoso Vaz
Prof. Doutor Miguel Rosa Oliveira Panão
Prof. Doutora Ana Sofia Oliveira Henriques Moita

26 de abril de 2024

Declaração de Integridade

Eu, Daniela Filipa Santo Ribeiro, que abaixo assino, estudante com o número de inscrição $d2332$ do Curso 3° Ciclo em Engenharia Aeronáutica da Faculdade de Engenharias, declaro ter desenvolvido o presente trabalho e elaborado o presente texto em total consonância com o **Código de Integridades da Universidade da Beira Interior**.

Mais concretamente afirmo não ter incorrido em qualquer das variedades de Fraude Académica, e que aqui declaro conhecer, que em particular atendi à exigida referenciação de frases, extratos, imagens e outras formas de trabalho intelectual, e assumindo assim na íntegra as responsabilidades da autoria.

Universidade da Beira Interior, Covilhã 06 / 06 / 2024

Assinado por: **Daniela Filipa Santo Ribeiro**
Num. de Identificação: 14520972
Data: 2024.06.06 12:17:03+01'00'

Dedication

This thesis is dedicated to my family, who taught me the great lesson that you can be whoever you want and that everything you will need in life is already around you.

“Hoping to share with them some of the delight that I have myself felt, in contemplating the exquisite forms that the camera has revealed, and in watching the progress of a multitude of events, compressed indeed within the limits of a few hundredths of a second, but none the less orderly and inevitable, and of which the sequence is in part easy to anticipate and understand, while in part it taxes the highest mathematical powers to elucidate.”

A. M. Worthington

Acknowledgements

First, I would like to acknowledge my supervisor, Professor André Resende Rodrigues da Silva, who also guided me through my Master's thesis and supported me to continue this journey and to board in this adventure that significantly enriched my academic path. I would like to thank him for believing in my capabilities and for the knowledge he shared with me.

I would also like to acknowledge the Institute of Aerospace Thermodynamics - ITLR of the University of Stuttgart where I developed part of this study. I would like to show gratitude to my colleague Dr. Patrick Foltyn for all the research work developed together. Also, I am grateful to Dr. Grazia Lamanna and to Professor Bernhard Weigand for all the guidance.

I would like to thank the Aeronautics and Astronautics Research Center (AEROG) of the Laboratório Associado em Energia, Transportes e Aeronáutica (LAETA) who provided me with all the tools to perform my research. My gratitude to Professor Jorge Barata, who always advised me and supported the research studies. I would also like to acknowledge Professor Miguel Panão for the insightful scientific discussions. I will never forget to acknowledge our technician Mr. Rui Paulo. To all Master students who crossed my way during these last years, I hope that sharing my knowledge with you has enriched your research.

To my Ph.D. colleagues Inês Ferrão and Daniel Rodrigues, who faced this journey with me and supported me every step of the way, I would like to say that without them it would never be this pleasant. I would also like to thank all my friends for their unconditional friendship and for all the encouragement along this journey.

Last but not least, a special acknowledgment to my family for everything they always have done for me. They were never the louder applause in the room but they were always there to encourage me.

This study was developed under the scope of Fundação para a Ciência e a Tecnologia (FCT) through the project UID/EMS/50022/2020, and the Ph.D. scholarship with the reference SFRH/BD/140009/2018. Finally, thanks to Fundação Luso-Americana para o Desenvolvimento (FLAD) which supported my travel to the United States of America to present my conference papers through the projects 05/2020 and 2022/0095.

Abstract

The droplet impact can seem a simple subject but the originated mechanisms are really complex and still not completely understood by the scientific community. These studies are important for a large variety of areas, however, this thesis is focused on aeronautical applications, such as fuel injection in aero-engines and coatings. In this way and in order to reduce fossil fuel consumption, it is proposed to introduce biofuels in the civil aviation sector. This thesis is divided into three main sections: single droplet impact upon smooth and micro-structured surfaces with variable wettability, single droplet impact upon thin liquid films, and single droplet impact upon heated smooth surfaces.

For single droplet impact upon dry smooth and micro-structured surfaces with variable wettability, three perspectives of the phenomenon were acquired: top, lateral, and bottom perspective. The surface wettability was varied by applying plasma treatments, which do not alter the roughness of the surface. The structured surfaces were composed of four different arrangements of regular micro-structures. Deposition, splashing, and rebound were observed both on the impact with smooth and structured surfaces, and the results were compared with spreading/splashing thresholds proposed in the literature. The impact morphologies were identified and analyzed and the spreading phase was studied.

For single droplet impact on thin liquid films, first, the universality of deposition/splashing boundaries available in the literature was evaluated. Secondly, the study focused on a seldom-known phenomenon called bubble encapsulation. In this phenomenon, after prompt and crown splash, the crown sheet walls start to bend inwards and eventually close forming an empty bubble above the liquid film. The occurrence and repeatability of this phenomenon were observed as well as their characteristics, formation mechanisms, and phenomenologies. Finally, an empirical correlation was proposed to predict the onset of bubble encapsulation.

Finally, for the study of droplet impact upon heated smooth surfaces, a heating device was used to heat a thin stainless steel plate. All four heat transfer regimes were observed and it was possible to identify differences in the outcomes depending on the amount of biofuel presented in the mixture. The evaporation time was also evaluated.

Keywords

Droplet collisions, aeronautical applications, SAF, heat transfer, micro-structured surfaces, wettability, bubble encapsulation, Jet fuel, liquid films, atomization

Resumo

O impacto de gotas pode parecer um tema simples, mas os mecanismos que o originam são muito complexos e ainda não são completamente compreendidos pela comunidade cientifica. Estes estudos são importantes para uma grande variedade de áreas, porém esta tese foca-se nas aplicações aeronáuticas, como a injeção de combustível em motores aeronáuticos e em revestimentos. Desta forma e para reduzir o consumo de combustíveis fósseis é proposta a introdução de biocombustíveis no sector de aviação civil. Esta tese é dividida em três principais partes: impacto de uma gota em superfícies lisas ou micro-estruturadas com molhabilidade variável, impacto de uma gota em filmes de líquido finos, e impacto de uma gota em superfícies lisas aquecidas.

No impacto de uma gota em superfícies lisas e micro-estruturadas com molhabilidade variável, três perspetivas do fenómeno foram capturadas: perspetiva de topo, lateral e de baixo. Variou-se a molhabilidade da superfície aplicando tratamentos de plasma, que não alteram a rugosidade da superfície. As superfícies estruturadas eram compostas por quatro disposições diferentes de micro-estruturas regulares. Deposição, splashing e rebound foram observados tanto nos impactos com superfícies lisas como estruturadas e os resultados foram comparados com critérios spreading/splashing presentes na literatura. As morfologias do impacto foram identificadas e analisadas e a fase de spreading foi estudada.

Para o impacto de gotas em filmes de líquido finos, primeiro, a universalidade dos critérios de deposição/splashing disponíveis na literatura foi avaliada. Em segundo lugar, o estudo focou-se num evento pouco conhecido chamado bubble encapsulation. Neste fenómeno, após prompt e crown splash, as paredes da coroa começam a curvar para dentro e eventualmente fecham formando uma bolha vazia em cima do filme de líquido. A ocorrência e repetibilidade deste fenómeno foi observada tal como as suas características, mecanismos de formação e fenomenologias. Por fim, foi proposta uma correlação empírica que prevê a ocorrência de bubble encapsulation.

Finalmente, para o estudo do impacto de uma gota numa superfície lisa aquecida, foi utilizado um sistema de aquecimento para aumentar a temperatura da superfície de uma placa fina de aço inoxidável. Todos os quatro regimes de transferência de calor foram observados e foi possível identificar diferenças nos resultados dependendo da quantidade de biocombustível presente na mistura. O tempo de evaporação também foi medido.

Palavras-chave

Colisão de gotas, aplicações aeronáuticas, SAF, transferência de calor, superfícies micro-estruturadas, molhabilidade, bubble encapsulation, Jet Fuel, filmes de liquido, atomização

Resumo alargado

O estudo do impacto de gotas em superfícies é de extrema importância para uma grande variedade de áreas de investigação e tem várias aplicações. Algumas das possíveis aplicações são a injeção direta de combustível em motores de combustão interna ou turbinas de gás, revestimentos, arrefecimento de sistemas, extinção de fogo, erosão dos solos, entre muitas outras. Nesta tese o impacto de gotas únicas em superfícies foi estudado considerando aplicações aeronáuticas. Como é de conhecimento geral, a indústria dos transportes é essencial para a humanidade, mas também é responsável por uma quantidade significativa de emissões poluentes. Isso acontece, pois o sector dos transportes é dependente de combustíveis fósseis. A disponibilidade deste tipo de combustíveis não só é limitada como prejudica o meio ambiente. Desta forma, combustíveis alternativos sustentáveis tem sido introduzidos no setor dos transportes. No entanto, o setor da aviação depende quase exclusivamente de combustíveis fósseis. A humanidade apercebeu-se que isso precisa de mudar e vários estudos tem sido desenvolvidos para incluir combustíveis alternativos sustentáveis neste setor que está em expansão exponencial. Soluções incluindo energia solar ou hidrogénio como fontes de combustível tem sido exploradas ao longo dos últimos anos e apesar da primeira não parecer poder ser aplicada na aviação civil num futuro próximo, o hidrogénio parece prometedor. Porém, só se espera a sua implementação na aviação civil daqui a várias décadas.

A aviação civil necessita de uma solução a curto prazo que ajude a cumprir as metas estabelecidas para 2050. Uma solução possível e de fácil aplicação é a introdução de biocombustíveis nas misturas de combustível que entram em combustão nas motores de combustão interna que já se encontram em circulação. Assim, sem alterar as aeronaves ou fazendo apenas pequenas alterações nos motores em circulação é possível reduzir o consumo de combustíveis fósseis e também as emissões poluentes por eles produzidas. Na verdade, esta medida já está a ser implementado por várias companhias aéreas em voos experimentais, descritos nesta tese.

O processo de combustão é complexo e é de extrema relevância entender como funciona ao adicionar uma percentagem de biocombustível a um combustível convencional. Deste modo misturas de combustíveis sustentáveis alternativos e combustíveis convencionais são considerados neste estudo de forma a compreende os processos físicos que podem ocorrer dentro da câmara de combustão interna.

Esta tese está dividida em três grandes partes: impacto de uma gota em superfícies lisas e micro-estruturadas com molhabilidade variável, impacto de uma gota em filmes de líquido finos e impacto de uma gota em superfícies lisas aquecidas. Misturas com combustíveis sustentáveis alternativos e combustíveis convencionais foram usadas nas duas últimas partes deste estudo.

A primeira parte deste estudo inclui o impacto de gotas em superfícies lisas e micro-estruturadas.

Os fluidos utilizados neste foram água destilada e isopropanol. A molhabilidade das superfícies foi alterada utilizando tratamento de plasma. Assim, foi possível variar a molhabilidade sem ter de alterar o material ou a rugosidade das superfícies, que constitui uma das novidades deste estudo. Quanto às superfícies micro-estruturadas, quatro padrões compostos por micro-estruturas regulares foram considerados com diferentes dimensões e espaçamentos entre eles. Variou-se a molhabilidade da superfície aplicando tratamentos de plasma, que não alteram a rugosidade da superfície. As superfícies estruturadas eram compostas por quatro disposições diferentes de micro-estruturas regulares. Deposição, splashing e rebound foram observados tanto nos impactos com superfícies lisas como estruturadas e os resultados foram comparados com critérios spreading/splashing presentes na literatura. As morfologias do impacto foram identificadas e analisadas e a fase de spreading foi estudada.

Para o impacto de gotas em filmes de líquido finos, primeiro, a universalidade dos critérios de deposição/splashing disponíveis na literatura foi avaliada. Em segundo lugar, o estudo focou-se num evento pouco conhecido chamado bubble encapsulation. Neste fenómeno após prompt e crown splash, as paredes da coroa começam a curvar para dentro e eventualmente fecham formando uma bolha vazia em cima do filme de líquido. A ocorrência e repetibilidade deste fenómeno foi observada tal como as suas características, mecanismos de formação e fenomenologias. Por fim, foi proposta uma correlação empírica que prevê a ocorrência de bubble encapsulation.

Finalmente, para o estudo do impacto de uma gota numa superfície lisa aquecida, foi utilizado um sistema de aquecimento para aquecer uma placa fina de aço inoxidável. Todos os quatro regimes de transferência de calor foram observados e foi possível identificar diferenças nos resultados dependendo da quantidade de biocombustível presente na mistura. O tempo de evaporação também foi medido.

Contents

1 Introduction **1**

1.1 Context and Motivation . . . 1
1.2 Objectives . . . 3
1.3 Contribution . . . 3
1.4 Organization . . . 6

2 Literature Review **9**

2.1 Introduction . . . 9
2.2 Droplet-surface Interactions . . . 9
2.2.1 Applications . . . 9
2.2.2 Impingement governing parameters . . . 10
2.3 Droplet Impact onto Dry Surfaces . . . 11
2.3.1 Spread/splash transition criteria . . . 13
2.4 Droplet Impact onto Liquid Surfaces . . . 14
2.4.1 Bubble encapsulation . . . 16
2.4.2 Spread/splash transition criteria . . . 20
2.5 Droplet Impact onto Heated Surfaces . . . 23

3 Experimental Methodology **25**

3.1 Introduction . . . 25
3.2 Droplet Impact onto Dry Cold Surfaces . . . 25
3.2.1 Experimental Setup . . . 25
3.2.2 Surface Samples . . . 29
3.2.3 Definition and measurement of surface wettability . . . 33
3.2.4 Plasma treatments . . . 35
3.2.5 Parameter Space . . . 37
3.2.6 Experimental Procedure . . . 38
3.2.7 Image Processing and Evaluation . . . 39
3.3 Droplet Impact onto Liquid Surfaces . . . 40
3.3.1 Experimental Setup . . . 41
3.3.2 Fluids . . . 43
3.3.3 Parameter Space . . . 43
3.3.4 Experimental Procedure . . . 46
3.3.5 Image Processing and Evaluation . . . 47
3.4 Droplet Impact onto Heated Dry Surfaces . . . 49
3.4.1 Experimental setup . . . 49
3.4.2 Fluids . . . 52
3.4.3 Parameter Space . . . 53
3.4.4 Experimental Procedure . . . 53

3.4.5 Image Processing and Evaluation 54

4 Results and Discussion **55**
4.1 Introduction 55
4.2 Droplet Impact onto Dry Surfaces 55
4.2.1 Droplet impact onto smooth Surfaces 55
4.2.1.1 Deposition/splashing boundary 56
4.2.1.2 Spreading evaluation 57
4.2.1.3 Impact morphologies 61
4.2.2 Droplet impact onto micro-structured Surfaces 69
4.2.2.1 Deposition/splashing boundary 70
4.2.2.2 Spreading evaluation 74
4.2.2.3 Impact morphologies 76
4.3 Droplet Impact onto Liquid Surfaces 94
4.3.1 How accurate are transition criteria? 95
4.3.2 Bubble encapsulation 102
4.3.2.1 Occurrence and Repeatability of Bubble Encapsulation 102
4.3.2.2 Phenomenologies of Bubble Encapsulation 108
4.3.2.3 Propagation of the First Perturbation Imposed on the Liquid Film 113
4.3.2.4 Bubble Geometry 115
4.3.2.5 Onset of bubble encapsulation 117
4.3.2.6 Evolution of the Crown sheet Angle 124
4.4 Droplet Impact onto Heated Surfaces 127
4.4.1 Heat Transfer Regimes 127
4.4.2 Evaporation Time 130

5 Conclusions **133**
5.1 Conclusions 133
5.2 Future Work 138

Bibliography **141**

List of Figures

2.1 Bubble Encapsulation Visualization Over the Years. 18
2.2 Drop Impact Mechanisms. 21
2.3 Heat transfer regimes for single droplet impact upon heated dry surfaces from Liang and Mudawar 24

3.1 Schematic of the image acquisition unit - front view on the left side, and top view on the right side. The different colors indicate the different light paths, yellow for the bottom perspective, green for the top perspective, and red for the lateral perspective. Dashed light paths emerge from the sketch plane. The droplet impact point is marked by the given coordinate system. 26
3.2 Principle of the total internal reflection configuration: (a) dry surface on which all light rays are reflected; (b) wetted surface with curved profile leads to partial diffraction of light exiting to the top-side of the prism; (c) perspective-corrected image showing the dry and wetted areas on a smooth surface. The middle of the droplet is also wetted, however, due to the horizontal droplet lamella the total internal reflection condition is met again; (d) perspective-corrected image showing the dry and wetted areas on a micro-structured surface. 27
3.3 Dimensions of the structured surfaces: a) grooves ($S1$), b) pillars with a square cross section ($S2 - S4$). The respective dimensions are summarized in Tab. 3.1. 30
3.4 Micro-structured Lexan®-surfaces of different dimensions acquired with Scanning Electron Microscopy (SEM). The magnification of each image is given at the respective image. The specimen stage was tilted by $30°$: a) grooves ($S1$), b) $60\ \mu m\ \times 60\ \mu m$ pillars ($S2$), c) $30\ \mu m\ \times 30\ \mu m$ pillars ($S3$). and d) $15\ \mu m\ \times 15\ \mu m$ pillars ($S4$). 31
3.5 Definition of the droplet impact conditions and the apparent contact angle θ_{app}. 33
3.6 Plasma machines of the type FEMTO, manufactured by *Diener electronic GmbH & Co KG*: (a) plasma activation to promote the wetting behavior, and (b) plasma polymerization to decrease the wetting behavior. 36
3.7 The raw images versus the corrected images for each perspective. 40
3.8 Experimental setup for single droplet impact upon thin liquid films: 1) high-speed digital camera; 2) macro lens; 3) syringe pump; 4) stainless steel dispensing needle; 5) liquid film container; 6) computer; 7) diffusion glass; 8 and 9) set of LED's. 42
3.9 Image processing to determine the pixel size: (a) raw image; (b) binarized image; (c) measurement of the outer diameter of the needle ($2x$ magnification). 48
3.10 Experimental facility: 1) high-speed digital camera; 2) macro lens; 3) syringe pump; 4) straight tip needle; 5) heating device; 6) stainless-steel impact surface; 7) type-K thermocouple; 8) controller of the heating device; 9) data logger; 10) computer; 11) difussion glass; 12) set of LEDs. 50

3.11 Heating device with four embedded cartridge heaters of $250\ W$ equally spaced and a type-K thermocouple in the middle. The black and blue crosses represent the position of the type-K thermocouples used to measure the surface temperature at the stainless-steel plate. 51

4.1 Regime map including all experiments onto dry smooth surfaces and the morphology of their outcomes, deposition, splashing, and rebound, depending on the Weber number We, the Reynolds number Re, and the apparent contact angle θ_{app}. Additionally, it presents the deposition/splashing limit defined by Vander Wal et al. for droplet impact onto dry smooth surfaces. 56

4.2 Spreading diameter D_{spread} normalized with the maximum spreading diameter D_{max} vs. (a) the dimensionless (inertial) time τ and (b) the dimensionless (capillary) time τ_{cap}. 58

4.3 (a) Dimensionless spreading diameter ($(D_{spread}/D_0)_{max}$) over the dimensionless inertial time at which the maximum spreading is reached $\tau((D_{spread}/D_0)_{max})$ depending on the wetting behavior and impact energy (represented by the falling height); (b) Maximum normalized dimensionless spreading diameter $\tilde{D}_{max}$ versus the corresponding time at which this diameter is reached $\tilde{\tau}_{max}$ for the distilled water events; (c) $\tilde{D}_{max}$ in dependency of the wetting behavior (θ_{app}) and the impact energy for the distilled water events; and (d) $\tilde{D}_{max}$ over the apparent contact angle θ_{app} showing the influence of the impact energy and the wetting behavior for the distilled water events. 60

4.4 Description of the droplet morphology evolution depending on the surface wettability and material for the lowest impact energy. 62

4.5 Sequence of images showing the phenomena obtained by the lateral, top, and bottom views: (a) spreading of a water droplet impinging onto a fully wettable Lexan® surface ($\theta_{app} \approx 0°$) for $We = 80$ and $Re = 4130$; (b) partial rebound of a water droplet impinging onto a non-wettable Plexiglas® surface ($\theta_{app} \approx 120°$) for $We = 80$ and $Re = 4130$; (c) splashing of an isopropanol droplet impinging onto a partially wettable Plexiglas® surface ($\theta_{app} \approx 70°$) for $We = 400$ and $Re = 1745$; (d) complete rebound of a water droplet impinging onto a non-wettable Plexiglas® surface ($\theta_{app} \approx 120°$) for $We = 385$ and $Re = 9360$. . 64

4.6 Morphology evolution depending on surface wettability for the second impact energy tested, $h_2 = 0.35\ m$. 66

4.7 Morphology evolution depending on surface wettability for the third impact energy tested, $h_3 = 0.7\ m$. 67

4.8 Morphology evolution depending on surface wettability for the highest impact energy, $h_4 = 1.0\ m$. 68

4.9 Regime map including all experiments onto micro-structured surfaces considering the modified K-factor based on the original K-factor of Vander Wal *et al.* over the roughness factor r introduced by Wenzel and the apparent contact angle θ_{app}. The modified critical K-factor can be calculated from equation (4.7). A roughness factor of $r = 1$ corresponds to the results for the impact on smooth surfaces. 71
4.10 Regime map including all experiments onto micro-structured surfaces using a modified parameter of Tsai et al. extended by the apparent contact angle θ_{app}. α_{mod} was chosen as the relation of the width of the junctions b and the height of the pillars, which can be both extracted from Tab. 3.1 for the respective surface types. The plane for the splashing limit (We_{crit}) can be described by the eq. (4.9). 72
4.11 Regime map including all experiments onto micro-structured surfaces using the dimensionless parameter $hD_0/(w_1w_2)$ extended by the apparent contact angle θ_{app}. This parameter relates the pillar height h, the droplet Diameter D_0, and the structure top area w_1w_2. h, w_1, and w_2 can be extracted from Tab. 3.1 for the respective surface types. The plane for the splashing limit (We_{crit}) can be described by the equation (4.10). 73
4.12 Normalized droplet spreading diameter over the dimensionless time τ and the Wenzel factor r characterizing the surface topography type. 75
4.13 Description of the outcomes and their morphology depending on surface wettability and surface micro-structure pattern for PC and PMMA on the water droplet impact at the lowest impact energy, $We = 80$. 77
4.14 Air entrapment observed from the bottom perspective on the water droplet impact at $We = 80$ onto a fully wettable $S1$ Lexan® surface. Capillary waves emerging due to a bursting bubble at the liquid surface are indicated by the arrow. 78
4.15 Top and bottom views of non-wetted areas caused by heterogeneous wetting on a water droplet impact on a partially wettable $S4$ Lexan® surface, $\theta_{app} \in [75° - 80°]$, $We = 80$. 78
4.16 Partial rebound of a water droplet onto a hydrophobic $S4$ Lexan® micro-structured surface for $We = 80$ from three different perspectives: lateral, top and bottom. 80
4.17 Description of the outcomes and their morphology depending on surface wettability and surface micro-structured pattern for PC and PMMA on the isopropanol droplet impact at the lowest impact energy, $We = 165$. 81
4.18 Directional prompt splash from an isopropanol droplet impinging at $We = 165$ onto a partially wettable $S1$ Plexiglas® surface, $\theta_{app} \in [66° - 73°]$. 82
4.19 Description of the outcomes and their morphologies depending on surface wettability and surface micro-structured pattern for PC and PMMA on the water droplet impact at the second impact energy tested, $We = 205$. 82
4.20 The "button effect" from the top and bottom perspectives for a water droplet impact onto a fully wettable $S3$ Lexan® surface for $We = 205$. 83

4.21 Finger formation normal to the orientation of the grooves and its consequent breakup for a water droplet impact onto a wettable $S1$ Lexan® surface, $\theta_{app} \in [25° - 40°]$, $We = 205$. 84
4.22 Heterogeneous wetting state seen by the top and bottom perspectives for a water droplet impact onto a hydrophobic $S2$ Lexan® surface, $We = 205$. . . . 85
4.23 Partial rebound for a water droplet impinging onto a hydrophobic $S1$ Plexiglas® surface at $We = 205$ from three different perspectives: lateral, top, and bottom. 86
4.24 Description of the outcomes and their morphology depending on the surface wettability and the surface micro-structured pattern for PC and PMMA for the isopropanol droplet impact, $We = 400$. 87
4.25 Directional prompt splash and crown splash with an incomplete crown for the isopropanol droplet impact onto a fully wettable ($\theta_{\text{app}} \approx 0°$) $S1$ Lexan® surface, $We = 400$. 87
4.26 The "cookie effect" seen from the top and bottom perspectives for the isopropanol droplet impact onto a $S3$ Plexiglas® surfaces with $\theta_{app} \in [66° - 73°]$, $We = 400$. 88
4.27 Description of the outcomes and their morphology depending on the surface wettability and the surface micro-structured pattern for PC and PMMA for the water droplet impact at the third impact energy tested, $We = 385$. 89
4.28 Heterogeneous wetting state with small non-wetted points seen by the bottom perspective for a water droplet impact onto a $S2$ Plexiglas® partially wettable surface, $\theta app \in [75° - 80°]$, $We = 385$. 90
4.29 Description of the outcomes and their morphology depending on the surface wettability and the surface micro-structured pattern for PC and PMMA for the isopropanol droplet impact, $We = 715$. 91
4.30 Prompt and crown splash seen from the lateral and top perspectives of an isopropanol droplet impinging onto a fully wettable $S1$ Lexan® surface at $We = 715$. 92
4.31 Description of the outcomes and their morphology depending on the surface wettability and the surface micro-structured pattern for PC and PMMA for the water droplet impact at the higher impact energy tested, $We = 665$. 93
4.32 Description of the outcomes and their morphology depending on the surface wettability and the surface micro-structured pattern for PC and PMMA on the isopropanol droplet impact, $We = 1,165$. 94
4.33 Transition criteria between spread and splash after drop impact onto a liquid film. 97
4.34 Comparison of the experimental results with the proposed transition criteria established by Bai and Gosman, Cossali et al., Tropea and Roisman , and Vander Wal et al. within their validation ranges. Color scheme: Black - the phenomena obtained experimentally agree with the criteria; White - the phenomena obtained experimentally do not agree with the predicted outcome; Grey - do not belong within the validation range of that criterion. 99

4.35 Comparison of the experimental results with the proposed transition criteria established by Bai and Gosman, Cossali et al., Tropea and Roisman, and Vander Wal et al. Color scheme: Black - the phenomena obtained experimentally agree with the criteria within the validation range; White - the phenomena obtained experimentally do not agree with the predicted outcome within the validation range; Grey - the phenomena obtained experimentally agree with the criteria out of the validation range; Beige - the phenomena obtained experimentally do not agree with the predicted outcome out of the validation range. 101
4.36 Experimental results in the present work and the Vander Wal et al. empirical correlation. In the case of $\delta_f = 1$, we plotted a qualitative curve representing an increase of 15% in the splashing criterion value K_c. 102
4.37 A sequence of images showing bubble encapsulation for the following impact conditions: 75% JF/25% HVO, D_0=3.0 mm, $U_0 = 4.2\ m/s$, and $\delta_f = 0.5$. 104
4.38 Evolution of the crown sheet angle during the formation of bubble encapsulation. 105
4.39 Sequence of images showing bubble encapsulation from below for the following impact conditions: 75%JF/25% HVO, $D_0 = 3.0\ mm$, $U_0 = 4.2\ m/s$, and $\delta_f = 0.5$. 106
4.40 First stages of impact seen from the bottom perspective with schematics of the correspondent images from the lateral perspective. Length scale resolution of $31.5\ \mu m/pixel$. 108
4.41 Different phenomenologies during bubble formation for a $3.0\ mm$ droplet of 75% jet fuel/25% HVO mixture at $U_0 = 4.2\ m/s$ and $We_D = 1650$: (a) Phenomenology 1 - only a downward jet is formed by the crown closure for $\delta_f = 0.5$; (b) Phenomenology 2 - both a downward and an upward jet are formed on the crown closure point for $\delta_f = 0.6$; (c) Phenomenology 3 - both a downward and an upward jet are formed on the crown closure point, combined with the ejection of large droplet due to the breakup of the upward jet $\delta_f = 0.4$. 109
4.42 Bubble hemispherical sheet becomes thicker by increasing the dimensionless film thickness. 111
4.43 Reynolds-Ohnesorge map synthesizing the points analyzed in this work, and by other authors, where bubble encapsulation was observed. 112
4.44 Cavity shape during crown sheet development (top) and during bubble encapsulation (bottom), evidencing its collision with the solid surface. 112
4.45 Sequence of images illustrating the propagation velocity of the first perturbation on the liquid film delimited by the red circle in the first frame. 113
4.46 Evolution of the normalized (a) diameter of first perturbation (D_p^*) and (b) velocity (U_p^*). The curves fitting D_p^*, which depend on the logarithm of time and dimensionless film thickness, are used for modeling U_p^*. 114
4.47 Comparing the experimental results for (a) D_p^* and (b) U_p^* with the predictions based on the logarithm of time growth of the first perturbation diameter. . . . 115
4.48 Measurements of bubble height (h_B) and diameter (D_B). 116

4.49 Bubble height h_B and diameter D_B depending on the dimensionless thickness of the liquid film δ_f. 116

4.50 Ohnesorge *vs.* Reynolds number map based on the initial droplet size as length scale, with the conditions resulting in 100%, 80%, and $50 - 80\%$ occurrence of bubble encapsulation. 118

4.51 Bubble encapsulation events compared with the spreading/splashing transition boundary of Vander Wal *et al.*. 120

4.52 Bubble encapsulation events compared with the spreading/splashing transition boundary of Vander Wal *et al.* using the thickness of the liquid film h_f as the characteristic length scale in the calculation of the Ohnesorge number, Oh_f. 121

4.53 Comparison between the events of bubble encapsulation obtained by other authors and by the present study when $p < 0.5$. 122

4.54 Bubble encapsulation events compared with the threshold proposed. 122

4.55 Bubble encapsulation events compared with the adaptation of the threshold proposed. 123

4.56 Crown sheet angle evolution resulting in bubble encapsulation. 124

4.57 Representation of single droplet impact upon a liquid film of the same fluid. Definition of the crown sheet angle α, droplet characteristics (diameter D_0, impact velocity U_0), fluid characteristics (density ρ, surface tension σ, and viscosity μ) and liquid film characteristics (thickness h and dimensionless thickness $\delta = h/D_0$). 125

4.58 Crown sheet angle evolution on the impact of a 75% JF-25% HVO droplet onto a liquid film of the same fluid with $\delta = 0.2$: (a) depending on the dimensionless time τ; (b) depending on the dimensionless time divided by the crown lifetime $\tau/\tau_{lifetime}$. The blue symbols correspond to cases where no bubble is formed and the red case to the only event where bubble encapsulation was observed. . 125

4.59 Crown sheet angle evolution on the impact of a 75% JF-25% HVO droplet onto a liquid film of the same fluid for different dimensionless film thicknesses depending on the dimensionless time: (a) $\delta_f = 0.4$; (b) $\delta_f = 0.6$; (c) $\delta_f = 0.8$; $\delta_f = 1.0$. 126

4.60 Heat Transfer Regimes: Film evaporation for 100% NExBTL at $We = 244$ and $Re = 1099$ at $T_w = 220^\circ\ C$; Nucleate Boiling for 50% Jet A-1 - 50% NExBTL for $We = 305$ and $Re = 2311$ at $T_w = 300^\circ\ C$; Transition Boiling for 100% Jet A-1 for $We = 299$ and $Re = 3746$ at $T_w = 300^\circ\ C$; and Film Boiling for distilled water for $We = 174$ and $Re = 6930$ at $T_w = 300^\circ\ C$. 128

4.61 Heat transfer regimes map depending on the wall temperature T_w and on the Weber number We for all fluids. The heat transfer regimes are identified by the different symbols, empty and filled, and the fluids are identified by different colors. Black for distilled water, blue for 100% Jet A-1, green for 50%JF-50%HVO, and red for 100% NExBTL. 129

4.62 Heat transfer regimes map depending on the wall temperature T_w and on the Reynolds number Re for all fluids. The heat transfer regimes are identified by the different symbols, empty and filled, and the fluids are identified by different colors. Black for distilled water, blue for 100% Jet A-1, green for 50%JF-50%HVO, and red for 100% NExBTL. 130
4.63 Evaporation time for a distilled water droplet depending on wall temperature for two different impact energies. 131

List of Tables

2.1 Summary of bubble encapsulation events presented in the literature. 17

3.1 Dimensions of the micro-structured surfaces and the respective topography parameters used for the evaluation. $S1$ corresponds to grooves, see Fig. 3.3 a), $S2 - S4$ correspond to pillars with a square cross section, see Fig. 3.3 b). R_a, R_z, and R_{sm} are correspond to calculated roughnesses, r is the roughness factor according to Wenzel, and α is the topography parameter introduced by Tsai et al. for describing regularly structured surfaces. The authors have chosen to modify this parameter as $\alpha_{mod} = b/h$. Herein, the diagonal b of the spacing between the individual structure elements is used. 30

3.2 Summary of the fluid properties used for the experimental parameter study at an ambient temperature of $25° \ C$. 35

3.3 Summary of the evaluated parameters. For each column, the indicated parameter range was investigated. The parameters which require a pre-treatment by plasma activation or polymerization are marked. 37

3.4 Physical properties of the fluids: density ρ, surface tension σ, and dynamic viscosity μ. 43

3.5 Droplet diameters used in the experiments of Ribeiro. 44

3.6 The dimensionless thickness of the thinner liquid films for distilled water. . . 44

3.7 Droplet impact Velocities. 45

3.8 Summary of the evaluated parameters on the investigation of bubble encapsulation. 46

3.9 Thermophysical properties of the fluids. 52

3.10 Summary of the parameters used in this study: wall temperature T_w, droplet initial diameter D_0, impact velocity U_0, Weber number We, and Reynolds number Re. 53

4.1 Transition criteria for single droplet impact upon liquid films. 96

4.2 Phenomenologies observed depending on the dimensionless film thickness δ_f and the correspondent dimensionless bubble formation time τ_{bubble}. The uncertainty values are absolute and obtained with a confidence interval of 95%. . 110

4.3 Bubble height h_B, dimensionless bubble height h_B^*, bubble diameter D_B and dimensionless bubble diameter D_B^* for the different dimensionless film thickness δ_f. The uncertainty values are absolute and obtained with a confidence interval of 95%. 115

4.4 Wider parameter space tested in the study of bubble encapsulation. 118

Nomenclature

a, b	parameters in the D_p^* empirical correlation	[−]
A_{avg}	Droplet average area	[m^2]
Bo	Bond number	[−]
Ca	Capillary number	[−]
D_0	Droplet initial diameter	[m]
D_{0max}	Maximum droplet initial diameter	[m]
D_B	Bubble diameter	[m]
D_B^*	Dimensionless bubble diameter	[−]
D_c	Crown diameter	[m]
D_c^*	Dimensionless crown diameter	[−]
D_{in}	Needle inner diameter	[m]
D_{max}	Maximum spreading diameter	[m]
D_p	Diameter of the first perturbation on the liquid film	[m]
D_p^*	Dimensionless diameter of the first perturbation on the liquid film	[−]
D_{spread}	Spreading diameter	[m]
Fr	Froude number	[−]
g	Gravity acceleration	[m/s^2]
h_B	Bubble diameter	[m]
h_B^*	Dimensionless bubble diameter	[−]
h_f	Thickness of the liquid film	[m]
K_c	Critical Threshold	[−]
La	Laplace number	[−]
m	Number of elements	[−]
m_p	Mass of the empty pycnometer	[kg]
m_s	Mass of the pycnometer filled with the substance	[kg]
Oh	Ohnesorge number	[−]
Oh$_D$	Ohnesorge number using the droplet diameter as length scale	[−]
p	Probability of occurrence	[−]
p_0	Air pressure	[Pa]
p_h	Hydrostatic pressure	[Pa]
r	Roughness factor	[−]
r_s	Surface Roughness	[mm]
R	Rebound	[−]
R_a	Arithmetical mean roughness	[-]
Re	Reynolds number	[−]
Re$_D$	Reynolds number using the droplet diameter as length scale	[−]
t	Time after impact	[s]

t_{bubble}	Bubble formation time	[s]
T_{CHF}	Critical heat flux temperature	[° C]
T_{Leid}	Leidenfrost temperature	[° C]
T_{sat}	Saturation temperature	[° C]
T_w	Surface temperature	[° C]
U_0	Impact velocity	[m/s]
V_p	Volume of the pycnometer	$[mL]$
We	Weber number	$[-]$
We_{crit}	Critical Weber number	$[-]$
We_D	Droplet Weber number	$[-]$
z_1, z_2, z_3	Droplet falling height	[m]

Greek Symbols

α_c	Crown angle	[°]
δ_f	Dimensionless liquid film thickness	[−]
Δt_{avg}	Average time	[s]
θ_{app}	Apparent contact angle	[°]
θ_{OWRK}	OWRK contact angle	[°]
θ_Y	Equilibrium Young contact angle	[°]
μ	Dynamic viscosity	[Pa s]
ξ_{crit}	Critical angle	[°]
ξ_1, ξ_2	Critical angle of media 1 and 2	[°]
ρ	Density	[kg/m^3]
σ	Surface tension	[N/m]
τ	Dimensionless inertial time	[−]
τ_{bubble}	Dimensionless bubble formation time	[−]
τ_{cap}	Dimensionless capillary time	[−]

List of Acronyms

AEROG	Aeronautics and Astronautics Research Center
CMOS	Complementary metal-oxide semiconductor
fps	Frames Per Second
HVO	Hydroprocessed Vegetable Oil
JF	Jet fuel
KNMF	Karlsruhe Nano and Micro Facility
LPSM	Laser Pattern Shift Method
microCT	micro-Computed Tomography
NExBTL	Neste Renewable Diesel
OCA	Optical Contour Analysis
PC	Lexan®
PMMA	Plexiglas® (Poly(methyl methacrylate)
SAF	Sustainable Aviation Fuel
SEM	Scanning Electron Microscopy
TTL	Transistor-transistor-logic

Chapter 1

Introduction

In this first chapter, the subject of this thesis will be presented. First, the context and motivation that originated this study will be explained and justified. Secondly, the objectives and research questions of this thesis will be presented. Several contributions to the literature were developed through this research study. Therefore, they will also be described in this chapter. Finally, the organization of the document will be explained.

1.1 Context and Motivation

The transportation sector is vital to humankind. Every day, people and goods travel around the world. Remote locations would not have access to certain essential items if they cannot be transported there by road, plane, or boat. However, the transportation sector consumes a significant amount of energy. The energy consumption duplicated in the last 40 years and it is only expected to keep increasing throughout the years [1]. As a consequence, the pollutant emissions will also increase. In 2017, the transportation sector was responsible for almost a third of the total energy consumption in the world, equivalent to 2808 million tons of fuel [1]. The aviation sector used to operate only with products derived from fossil fuels. Due to that, the aviation sector was responsible for $2\% - 3\%$ of the total carbon emissions of the planet [2].

After the slight slowdown in 2020 due to the Covid-19 pandemic, the aviation sector is expected to exponentially expand to comply with the increasing number of passengers and goods. The modern society is concerned about the scarcity of fossil fuels as well as is aware of the the greenhouse gas and pollutant emissions produced by them. Several solutions are being discussed to introduce sustainable sources of energy in the transportation sector. The use of solar energy is one of the solutions presented [3]. However, a long path is expected until this technology could be applied in civil aviation. Hydrogen-powered aircraft are other option. They have potential to be implemented in civil aviation and fly existing routes with no carbon emissions [4]. Yet, this will imply changes to the airport infrastructures and the exponential increase of green hydrogen production. This technology seems promising and probably will be available in the near future, it still needs to be further developed to be implemented in civil aviation.

A solution that is already being implemented in civil aviation is the introduction of sustainable aviation fuels (SAF). In the European Union, the first airline that flew a commercial flight using bio-jet blends produced from used cooking oil was KLM, on the route Amsterdam-

Paris in June of 2011, on a B737 [5]. Lufthansa was the first airline worldwide to use a blend of biofuel mix from jatropha, camelina, and animal fats, from Neste oil, in scheduled daily operations during a six-month test (more than 1187 flights) with an A321 on the Frankfurt-Hamburg route [5]. The target of the European Advanced Biofuels Flightpath is to ensure the consumption of 2 million tons of sustainably produced paraffinic biofuels in the aviation sector by 2020 [5].

In comparison with other transport sectors, aviation imposes several restrictions in implementing any fuel contender in aviation turbines, such as interchangeability with the current operating fuels in order to avoid logistic issues, and the combustion characteristics that demand a narrow range of potential liquid fuels [2].

The physical processes involved in fuel combustion include fuel atomization and impact, followed by evaporation. The mixture preparation, including the impact on dry and wet surfaces, is recognized as of major importance. The secondary atomization produced by the splashing optimizes the fuel combustion efficiency.

Several research works have been developed [6], including multiple droplet impacts, impacts upon heated surfaces, and impacts upon inclined walls, among many others. There was something missing in all those studies. The most common fluids used were water, glycerol, ethanol, and solutions with different fluids. However, since one of the applications where drop impacts on liquid films are relevant concerns the fuel injection in internal combustion engines, fuel mixtures should be tested. Therefore, the assessment of empirical models, and the morphological hydrodynamic structures associated with drop impact on dry and wetted surfaces, are worthy of further investigation.

One of the goals of this work is to contribute to the implementation of biofuels in the aviation sector. For this reason, the working fluids considered were 100% Jet A-1 and two mixtures with 75%/25% and 50%/50% of Jet A-1 and NExBTL (Neste Renewable Diesel), respectively. Pure water and isopropanol were also used as reference fluids.

The phenomena of droplet impact can be seen as a simple object but originate complex mechanisms that are not completely understood by the scientific community. These studies are relevant for several research areas. However, in this Ph.D. thesis, the focus is its applications to the aviation sector, including fuel injection in internal combustion engines. The introduction of biofuel in civil aviation is proposed to reduce fossil fuel consumption and pollutant emissions.

In this work, single droplet impact upon dry, wet, and heated surfaces is studied. The main goals include identifying the different regimes and outcomes, analyzing their characteristics, and proposing empirical correlations that fit the results and are capable of improving the existing numerical models.

1.2 Objectives

The main objectives of this study are to make efforts to implement biofuels in civil aviation and identify how surface topography can influence the atomization process. To achieve these objectives three different experimental facilities were built and the fluids used are distilled water, isopropanol, and mixtures with jet fuel and biofuel. Considering this, several objectives were defined.

First, design, build, and validate the experimental facilities. Then, perform the three different experimental studies: single droplet impact onto smooth and micro-structured surfaces with variable wettability using distilled water and isopropanol, single droplet impact onto thin liquid films using jet fuel and biofuel mixtures, and single droplet impact upon dry smooth heated surfaces using also jet fuel and biofuel mixtures. After that, the different regimes and outcomes were identified and the impact conditions that allow their occurrence were cataloged. Study the influence of the fluid thermophysical properties and evaluate the main characteristics of the outcomes, e.g., crown height, diameter, angle, and spreading rate and diameter.

Compare the results with the available data presented in the literature. Also, compare the outcomes with empirical correlations defined in the literature. Furthermore, using the experimental data to find empirical correlations capable of establishing boundaries between impact regimes.

1.3 Contribution

What an incredible journey it was to perform and write this thesis. The best part of this adventure is the possibility of exchanging knowledge with the scientific community. Throughout the development of this thesis, several conference and journal papers were produced. The contribution to internal journal papers is the following:

1. Ferrão, Inês; Vasconcelos, Daniel; Ribeiro, Daniela; Silva, André; Barata, Jorge. ”A study of droplet deformation: The effect of crossflow velocity on jet fuel and biofuel droplets impinging onto a dry smooth surface”. Fuel 279 (2020): 118321. http://dx.doi.org/10.1016/j.fuel.2020.118321 [7]

2. Ribeiro, Daniela; Silva, André; Panão, Miguel. ”Insights into Single Droplet Impact Models upon Liquid Films Using Alternative Fuels for Aero-Engines”. Applied Sciences 10 19 (2020): 6698. http://dx.doi.org/10.3390/app10196698 [8]

3. Foltyn, Patrick; Ribeiro, Daniela; Silva, André; Lamanna, Grazia; Weigand, Bernhard. ”Influence of wetting behavior on the morphology of droplet impacts onto dry smooth surfaces”. Physics of Fluids 33 6 (2021): 063305.

http://dx.doi.org/10.1063/5.0053539 [9]

4. Foltyn, Patrick; Lynn K. Rihm; Ribeiro, Daniela; Silva, André; Weigand, Bernhard. Measurement of the lamella thickness during droplet impact onto differently wettable smooth surfaces using an extension of the LASER Pattern Shift Method with naturally occurring patterns". Review of Scientific Instruments, vol. 92, no. 10, p. 105111 (2021). https://doi.org/10.1063/5.0060407 [10]

5. Foltyn, Patrick; Ribeiro, Daniela; Silva, André; Lamanna, Grazia; Weigand, Bernhard. "Influence of wetting behavior on the morphology of droplet impacts onto dry- patterned micro-structured surfaces". Physics of Fluids 34, 123322 (2022). https://doi.org/10.1063/5.0124692 [11]

6. Ribeiro, Daniela; Silva, André R. R.; Panão, Miguel R. O.; "Criterion for bubble encapsulation on drop impact onto a liquid film". Physics of Fluids 35, 033305 (2023). https://doi.org/10.1063/5.0138901 [12]

7. Ribeiro, Daniela; Panão, Miguel; Barata, Jorge; Silva, André; "Insights on bubble encapsulation after drop impact on thin liquid films," International Journal of Multiphase Flow, vol. 164, p. 104450, 2023. https://www.sciencedirect.com/science/article/pii/S030193222300071X [13]

The contribution to conference papers is the following:

1. Ribeiro, Daniela; Panão, Miguel; Barata, Jorge; Silva, André. "Insights on Bubbling Formation after Drop Impact on Thin Liquid Films". Presented in ILASS 2019: 29th European Conference Liquid Atomization & Spray Systems, Paris, 2019. [14]

2. Ferrão, Inês; Ribeiro, Daniela; Barata, Jorge; Silva, André. "Comparative Study of Droplet Impact onto Sloped Surface versus a Droplet Impact onto a Surface with a Crossflow". Presented in 2019 AIAA SciTech: AIAA Science and Technology Forum and Exposition, California, 2019. 10.2514/6.2019-062914 [15]

3. Carrolo, Gabriel; Ribeiro, Daniela; Barata, Jorge; Silva, André. "Aerodynamic Breakup of a Single Droplet due to a Crossflowed Airstream". Presented in 2019 AIAA SciTech: AIAA Science and Technology Forum and Exposition, California, 2019. 10.2514/6.2019-062815 [16]

4. Ferrão, Inês; Ribeiro, Daniela; Barata, Jorge; Silva, André. "Experimental Study of Droplet Impact on Oblique Dry Surface". Presented in 9th European Combustion Meeting, Lisboa, 2019. [17]

5. Vasconcelos, Daniel; Ribeiro, Daniela; Silva, André; Barata, Jorge. "VOF Method: Nu-

merical Analysis of Single Droplets Impinging upon Liquid Films". Presented in 9th European Combustion Meeting, Lisboa, 2019. [18]

6. Vasconcelos, Daniel; Ribeiro, Daniela; Barata, Jorge; Silva, André. "Experimental and Numerical Study of Single Droplets Impinging upon Liquid Films". Presented at 4th Thermal and Fluid Engineering Conference, Las Vegas, 2019. 10.1615/TFEC2019.mph.028384 [19]

7. Vasconcelos, Daniel; Ribeiro, Daniela; Barata, Jorge; Silva, André. "Modelling of Single Droplets Impinging upon Liquid Films using the VOF Method". Presented in the Congress on Numerical Methods in Engineering, Guimarães, 2019. [20]

8. Ribeiro, Daniela; Panão, Miguel; Barata, Jorge; Silva, André. "Morphology of Bubble Formation on Droplet Impact upon Thin Liquid Layers". Presented in 2020 AIAA SciTech: AIAA Science and Technology Forum and Exposition 2020, 2020. 10.2514/6.2020-1577 [21]

9. Vasconcelos, Daniel; Ribeiro, Daniela; Silva, André; Barata, Jorge. "3D Simulations of Droplets Impacting Liquid Films: Crown Parameters Measurements". Presented in 2020 AIAA SciTech: AIAA Science and Technology Forum and Exposition, 2020. 10.2514/6.2020-1578 [22]

10. Pinto, Pedro; Vasconcelos, Daniel; Ribeiro, Daniela; Barata, Jorge; Silva, André. "Collision Dynamics of a Single Droplet onto a Heated Dry Surface: Jet Fuel and HVO Mixtures". Presented in ICLASS 2021, 15th Triennial International Conference on Liquid Atomization and Spray Systems, Edinburgh, 2021. 10.2218/iclass.2021.5982 [23]

11. Cardoso, João; Moura, Cátia; Ribeiro, Daniela; Vasconcelos, Daniel; Barata, Jorge; Silva, André. "Design and Fabrication of a Low Cost, Push-Mode Piezoelectric Stream Droplet Generator with Interchangeable Nozzle". Presented in ICLASS 2021, 15th Triennial International Conference on Liquid Atomization and Spray Systems, Edinburgh, 2021. 10.2218/iclass.2021.5983 [24]

12. Ribeiro, Daniela; Foltyn, Patrick; Silva, André; Lamanna, Grazia; Weigand, Bernhard. "The Influence of Wettability on the Droplet Impact onto Micro-Structured Surfaces". Presented in ICLASS 2021, 15th Triennial International Conference on Liquid Atomization and Spray Systems, Edinburgh, 2021. 10.2218/iclass.2021.5908 [25]

13. Foltyn, Patrick; Ribeiro, Daniela; Silva, André; Lamanna, Grazia; Weigand, Bernhard. "Effect of Surface Wettability on the Droplet Impact Morphologies on Dry Smooth Polycarbonate Surfaces". Presented in ICLASS 2021, 15th Triennial International Conference on Liquid Atomization and Spray Systems, Edinburgh, 2021. 10.2218/iclass.2021.5907 [26]

14. Ribeiro, Daniela; Barata, Jorge; Silva, André. "The Role of Crown Sheet Angle Evolution on the Single Droplet Impact upon a Thin Liquid Film ". Presented in V LAETA Young Researchers Meeting, Lisbon, 2022. [27]

15. Ribeiro, Daniela; Foltyn, Patrick; Silva, André; Lamanna, Grazia; Weigand, Bernhard. "Comparison Between Droplet Impact onto Dry Smooth and Micro-structured Surfaces with Variable Wettability". Presented in V LAETA Young Researchers Meeting, Lisbon, 2022. [28]

16. Ribeiro, Daniela; Barata, Jorge; Silva, André. "The Influence of Liquid Film Thickness on Crown Development: Crown Sheet Angle". Presented at 7th Thermal and Fluids Engineering Conference (TFEC), Las Vegas, 2022. [29]

17. Ribeiro, Daniela; Panão, Miguel; Barata, Jorge; Silva, André. "Analysis and visualization of the perturbations imposed on the liquid film by crown sheet collapse or closure". Presented in 20th International Symposium on Application of Laser and Imaging Techniques to Fluid Mechanics, Lisbon, Portugal, 2022. [30]

18. Ribeiro, Daniela; Barata, Jorge; Silva, André. "Experimental Study of a Single Droplet Impinging Upon a Heated Dry Surface Using Jet Fuel and Biofuel Mixtures". Presented in 31st Conference on Liquid Atomization and Spray Systems, Virtual, 2022. [31]

19. Mendes, André; Vasconcelos, Daniel; Ribeiro, Daniela; Panão, Miguel; Silva, André. "Does liquid film temperature affect single drop impact dynamics?". Presented in 8th Thermal and Fluids Engineering Conference (TFEC), May, Partially Online Virtual and at University of Maryland, 2023. [32]

1.4 Organization

This thesis is divided into five chapters. Chapter 1 introduces the study developed under the scope of this thesis. First, it explains the context and motivation to develop this research investigation, followed by a state of the art in which the main developments in the fields of study are summarized. After that, the objectives established for this study will be presented and the research questions defined. This first chapter ends with the contribution of this thesis and its organization.

Chapter 2 presents the literature review performed during this study. This review includes important findings reported in the literature for all types of droplet impacts studied as well as the physical and heat transfer mechanisms involved.

The third chapter, chapter 3, describes the experimental methodologies applied to the three different types of droplet impact studied. Therefore, this chapter is divided into three main sections: droplet impact upon dry cold surfaces, droplet impact upon liquid films, and droplet

impact upon heated dry surfaces. In each section, the experimental setup, the fluids, the parameter space, the experimental procedure, and the image processing and evaluation are explained in detail.

Chapter 4 shows the results obtained in this study. Similarly to the chapter describing the experimental methodology (chapter 3), this chapter is also divided into three main sections. One section for each type of droplet impact. Within these sections, the results are presented, analyzed, and discussed.

Finally, chapter 5 summarizes all conclusions acquired from this study. Some future work is also proposed based on the conclusions collected from this thesis.

Chapter 2

Literature Review

2.1 Introduction

To develop scientific research there are many steps to be followed. One of the most important ones, if not the most important is to make a literature review to understand how that subject has been addressed by other authors and what has been concluded in the past. This thesis is dedicated to the study of droplet-surface collisions for aeronautical applications. Therefore, in this chapter, all relevant topics will be addressed and explained.

First, a summary of droplet interactions will be presented, including their applications, governing parameters, and physical mechanisms. Then, this literature review will be divided by the main subjects of this research, focusing on the points that are more relevant to the study developed.

2.2 Droplet-surface Interactions

The study of droplet interactions is important for a variety of areas and applications. In this subsection, the possible applications for the study of droplet impact will be described and the general influencing parameters presented.

2.2.1 Applications

The study of droplet impacts is important to a wide variety of applications in many areas. The aeronautical, electronic, and agricultural sectors are part of these areas. From the natural impingement and splashing of raindrops influencing soil erosion and the dispersion of seeds and microorganisms [33] to the direct injection in internal combustion engines [34, 35].

According to Visser et al. [36], the specific case of high-velocity impact of small-scale droplets is a fundamental phenomenon in applications like diesel engines, thermal spraying, spray cleaning, and novel manufacturing technologies based on ink-jet printing technology or laser-induced forward transfer. Further, Macklin and Metaxas [33] reported that it was shown that electrical charges separated by the disintegration of liquid during splashing were responsible for waterfall electrification. The results obtained from the electric charge separation during splashing can be applied to thunderstorm electrification and to the build-up of space charges during rainfall.

Researchers want to understand the mass, momentum and heat transfer interactions [37]. Applications of drop impact upon heated walls include internal combustion engines with direct fuel injection, saline droplet impact on heat transfer tubes of falling-film evaporators in desalinization and refrigeration, water droplet impingement on steam turbine blades and in quenching metal castings and extrusions, and spray cooling in fire extinguishing and electronics cooling system [37].

The cooling of electronic equipment by a liquid spray or droplet stream is also a very important application of these studies [38]. According to Cossali et al. [39], on internal combustion engines, the increased probability for the fuel to impact on intake ducts (gasoline engines) or on pistol bowl (direct injection diesel engines), due to some new arrangements of the engine parameter as higher injection pressure or smaller cylinder dimensions, promoted many investigations on the spray-wall interaction.

In applications of spray or painting, thin liquid films represent the first transition between a dry surface and a thick liquid film. [40]. On the other hand, the success of several applications depends on how the splashing behavior can be controlled [40].

2.2.2 Impingement governing parameters

A significant number of parameters govern the dynamics of droplet impact. The droplet impact parameters, the thermophysical properties of the fluid, the characteristics of the impact target, and the surrounding gas are some of the several parameters involved that help explain the obtained phenomena. To allow the comparison between different studies and to group some of these parameters, dimensionless numbers are commonly used in the study of droplet impact both onto dry or wetted surfaces [41, 42].

The Reynolds number Re is one of the most commonly used dimensionless number in the study of multi-phase flows. It is defined by the ratio between the inertial and viscous forces, as shown in eq. (2.1).

$$Re = \frac{\rho U_0 D_0}{\mu} \quad (2.1)$$

where ρ and μ are the density and dynamic viscosity of the fluid, respectively, and U_0 and D_0 are the droplet impact velocity and diameter, respectively.

The Weber number We is also a common dimensionless number in the study of droplet interactions. It is the ratio between the inertial and surface tension forces. Thus, the Weber number relates the droplet kinetic energy and surface energy σ and is defined in eq. (2.2).

$$We = \frac{\rho U_0^2 D_0}{\sigma} \quad (2.2)$$

By relating the last two dimensionless numbers, the Ohnesorge number Oh can be obtained:

$$Oh = \frac{\mu}{(\rho\sigma D_0)^{1/2}} = \frac{We^{1/2}}{Re} \quad (2.3)$$

which relates the viscous forces to the inertial and surface tension forces.

The Capillary number Ca is relevant in droplet impact studies when the dynamic contact angle and wettability effects play a significant role in the droplet dynamics on dry surfaces. It is described by eq. (2.4) and is the ratio between the viscous and the surface tension forces. This dimensionless number is also the ratio between the Weber and Reynolds numbers.

$$Ca = \frac{\mu}{\sigma} U_0 = \frac{We}{Re} \quad (2.4)$$

On the other hand, the Laplace number La is the inverse of the squared Ohnesorge number Oh. The Laplace number La measures the surface tension and viscous forces acting on the liquid. Thus, it is the ratio between the surface tension and the momentum-transport (dissipation) inside a fluid, eq. (2.5).

$$La = \frac{\rho\sigma}{\mu^2} D_0 = \frac{Re^2}{We} = \frac{We}{Ca^2} = \frac{Re}{Ca} = Oh^{-2} \quad (2.5)$$

The Froude number Fr is the ratio between the inertial and the gravitational forces, as shown in eq. (2.6), where g is the gravity acceleration.

$$Fr = \frac{U_0}{(gD_0)^{1/2}} = \frac{We}{Bo} \quad (2.6)$$

Finally, the Bond number Bo is the ratio between the body (gravitational) forces and the surface tension forces.

$$Bo = \frac{\rho g D_0^2}{\sigma} = \frac{We}{Fr} \quad (2.7)$$

Many other parameters influence the dynamics of droplet impact, such as the dimensionless thickness of the liquid film, the surface roughness, the surface temperature, the surface wettability, and the conditions of the surrounding air, among many others. These governing parameters will be defined and explained throughout this thesis.

2.3 Droplet Impact onto Dry Surfaces

Single droplet impact upon a dry solid surface is a common and outstanding phenomenon. As explained in Section 2.2.1, droplet impact upon dry surfaces is relevant for diverse applications, such as fuel injection in internal combustion engines, spray cooling, spray painting, coatings, soil erosion, and even fire suppression [41]. Different outcomes can be expected from this event like deposition, prompt and crown splash, and partial or complete rebound

[43]. These phenomena will be described in detail in the following.

As expected, surface topography plays a significant role in the droplet impact dynamics with dry solid surfaces. Changing the surface wettability will not affect the regime classification, but it will influence significantly the dynamics of the spreading of the liquid lamella by inducing breakup, as well as full or partial rebound. Therefore, surface wettability is used as a characterizing parameter, and is defined as the ability of a fluid to spread out on a dry solid substrate and it is quantified by the apparent contact angle θ_{app} [41]. The wettability behavior can be defined by different apparent contact angles, which can vary between fully wettable, partially wettable, or non-wettable systems. Wettability is a key parameter for the outcome of droplet impacts.

On fully wettable surfaces, the heat transfer increases between the droplet and the surface due to the thin liquid film that is formed [44, 45]. Contrarily, non-wetting surfaces, which can be generated, e.g., by roughness, are widely known as "repelling surfaces." Their wide range of applications is often related to the underlying self-cleaning mechanism often called the "Lotus effect." To design efficient functional surfaces and materials is essential to understand the physical mechanisms of wetting transition [46].

Up to now, the role of surface characteristics on the dynamic behavior of droplets impinging on a dry surface is not fully understood. Wettability is an equilibrium thermodynamic variable that depends exclusively on the interfacial free surface energies of the surface, according to Young's law [47]. The equilibrium is reached very fast, but the contact angle is a dynamic parameter and an interdependency between spreading behavior and dynamic contact angle can be found[48]. As an example, experiments have shown that the dynamic contact angle depends on the spreading rate which is, however, influencing the dynamic contact angle again[49].

The formation of complete or full wetting ($\theta_{app} = 0$) possibly happens due to the presence of a precursor film on the surface, providing faster-spreading rates since it leads to a force acting in the direction of spreading promoting the further surface wetting. This phenomenon causes a super spreading behavior and inhibits the characterization of the liquid-surface system using the equilibrium contact angle.

In 1997, Mao *et al.* [50] varied the equilibrium contact angle and did not observe changes in the maximum spreading diameter for impacting droplets. Later in 2002, Rioboo *et al.* [51] studied the role of surface wettability on the droplet spreading and observed differences in the final stages of spreading, for non-wettable surfaces. This is supported by the results of Moita and Moreira [52] who show that a decreasing contact angle increases the spreading rate. It should not be forgotten that in these experiments, very low impact velocities were considered, where the wettability effects may be more noticeable. According to Pasandideh-Fard et al. [53], wettability may be negligible for high Weber numbers but seems to be significant for low-impact velocities. Even if wettability may be negligible in some cases, the

contact angles seem to be important in the spreading and receding mechanisms [54], which must not be forgotten in modeling. The spreading characteristics are the most studied features related to wettability, but a question arises: How exactly does wettability influence the outcome of a single droplet impinging on a dry surface? Additionally, what phenomena could be expected depending on the wettability and how do they evolve?

The variation in wetting behavior was usually achieved by droplet impacts on different surface materials. Thus, surface material, wettability and the characteristic roughness, even if it is in nanometric scale, were always exchanged as a complete set [55, 54, 56]. In opposition to that, a systematic study of droplet impacts onto dry solid surfaces is presented at which the surface wettability has been flexibly controlled by plasma activation and plasma polymerization. With this approach it could be set in a range from full wetting to non-wetting while not exchanging the used polymeric material or surface. Further subject of systematic changes had been the droplet fluid, surface material, and impact energy resulting into the impact condition range of $80 < We < 1,165$ and $1,135 < Re < 12,240$. The experimental facility is introduced in detail and has three synchronized perspectives (lateral, top, and bottom) using high-speed imaging. The bottom perspective is a unique feature of the optical setup, which gives insight into interesting phenomena like bubble entrapment at the impact point [57, 58**?**].

2.3.1 Spread/splash transition criteria

Being able to determine the boundary between spreading and splashing is important for several applications as already mentioned.

Vander Wal et al. [40] developed empirical relations for the spreading/splashing boundary for single droplet impact onto dry surfaces and thin liquid films. They performed experiments and used the data to develop empirical correlations. Focusing on the experiments upon dry surfaces, an aluminum diamond-lathed disc was the impact surface with a mean roughness lower than $10\ nm$. The droplet initial diameter was selected to be $D_0 = 2.0\ mm$ due to keeping the spherical shape throughout the free fall. Therefore, concerns about uneven impact were eliminated. The impact velocity was varied. Different fluids were used in the experiments: alkanes, alcohols, water, and a 30 wt % glycerol-water solution. Regarding wettability, the alkanes show a full wetting behavior, while the alcohols, the solution, and water show a contact angle of $\approx 30^\circ$. Finally, they performed three experiments for each set of experimental conditions. This range of experimental conditions resulted in the following parameter space: $988 < Re < 13900$, $127 < We < 1420$, and $2.91 < Ca < 62.0$.

They observed that the splashing boundary is not uniform considering only the Reynolds or the Weber numbers. The Weber number expresses the kinetic energy, while the Reynolds number expresses the momentum. Therefore, individually they cannot describe the splashing boundary and that is why a combination of Weber and Reynolds numbers has been used to define this boundary since it includes both viscosity and surface tension.

As a starting point, they used combinations of Ohnesorge, Reynolds, Weber, and Froude numbers. However, only the power law between the Ohnesorge and Reynolds numbers provided a defined boundary between spreading and splashing. Noteworthy, the Ohnesorge number depends simultaneously on viscosity and surface tension. Vander Wal et al. [40] empirical correlation for single droplet impact dry surfaces is defined in eq. (2.8).

$$Oh\ Re^{0.609} = 0.85 \quad (2.8)$$

Simplifying this equation considering $Re^{0.609} = Re^{0.5}$, the spread/splash boundary can be approximate as:

$$Oh\ \sqrt{Re} = \sqrt{Ca} = 0.85 \quad (2.9)$$

It can be concluded that the spread/splash boundary weakly depends on the droplet's initial diameter D_0. However, it strongly depends on the impact velocity U_0.

2.4 Droplet Impact onto Liquid Surfaces

In single droplet impact upon thin liquid films, the dimensionless thickness of the liquid film is one if not the most significant impact parameter. According to its dimensionless thickness, the liquid films can be classified as thin, intermediate, and thick, and even as shallow or deep pool [59].

The splashing mechanism is one of (if not) the most relevant and studied factors in the literature related to droplet interactions. On a typical vertical impact of a single droplet on a steady liquid film the droplet is initially spherical, and it does not suffer any deformation during the fall. However, a recent study from Ferrão et al. [7] shows the effect of initial droplet deformation on the splashing dynamics. In this study, the droplet is deformed before impact by interacting with an airflow and assumes different shapes while impacting on a surface. It was reported that spherical droplets promote splashing, while deformed droplets promote spreading.

The morphology of splashing includes the formation of a crown with a rim in its upper bound, and from instabilities in this rim, the cusp can emerge, which disintegrates into droplets, the secondary atomization. Cossali et al. [34] were among the first to characterize the crown diameter, thickness, and maximum height. The authors noticed that high Weber number values led to smaller secondary droplets. A few years later, Cossali et al. [60] focused their work on the time evolution of the crown of water droplets impinging upon thin liquid films. They reached several conclusions related to the crown diameter, the non-dimensional crown height, and the mean size of the secondary droplets. However, since they only used one fluid, it is not possible to identify whether their conclusions could be extended to other fluids or not.

Fedorchenko and Wang [61] studied experimentally and theoretically, the region of the fully developed splashing. They used water but also a 70% glycerol-water solution. They developed a model for the central jet formation at the cavity collapse. Some considerations were made about the viscosity of the fluids related to the cavity, the central jet, and the crown ejection. In fluids with low viscosity, the interaction between the capillary wave and the cavity wall has a major influence on the cavity shape, and as a consequence, on the central jet speed. On the other hand, for fluids with high viscosity, the influence of capillary waves is minor. Understanding the roles of the fluid physical properties is essential to understanding how they influence the impact regimes. For example, Range and Feuillebois [62] reported that splashing is highly sensitive to surface tension values.

A parameter particularly relevant to the impacts of droplets on wetted surfaces is the dimensionless thickness of the liquid film and its influence on the droplet dynamic behavior. Vander Wal et al. [63] studied droplets splashing upon liquid films of different depths. They reported that thinner liquid films decreased the critical Weber number, setting the transition between deposition and splash. They also found that the size and number of the splashed droplets depend upon the presence and thickness of the liquid film, and also on the viscosity and surface tension of the fluids. For $\delta < 1$, both prompt and crown splash were spotted, but for $\delta > 1$, prompt splash was limited and crown splash inhibited. Moreover, the number of ejected droplets decreases while their mean size increases, an outcome attributed to the increase of the surface tension and viscosity. In addition, a higher viscosity leads to an increase in the damping forces involved in the morphological development of splash, delaying both prompt and crown types. Therefore, while viscosity promotes splash after drop impact on dry surfaces, in the presence of thin liquid films, its role reverts. Lastly, high surface tension inhibits splashing both for dry and wetted surfaces.

Over the years, researchers wanted to produce thinner liquid films and study these particular impacts. For example, Wang and Chen [64] did experiments centered on the splashing of a single droplet upon very thin liquid films ($\delta < 0.1$). They confirmed that the critical Weber number and the splashing dynamics remain influenced by the thickness of the liquid film. However, the authors also noticed that the critical Weber number converges to a minimum value as δ decreases, which depends on the fluid viscosity and surface characteristics underneath the liquid film.

In the study of droplet impact on wetted surfaces, it is important to understand whether the surface underneath the liquid film influences the outcome. With that in mind, Vander Wal et al. [65] combined the influence of a rough surface and a thin liquid film upon the splashing limit and dynamics. They recognized that both cases substantially changed the splashing limit and dynamic. A rough surface decreased the critical Weber number drastically for the transition to splash, and the surface topography overtakes the importance of other governing parameters, especially in the splashing regime. For example, considerable differences in the surface tension and viscosity became less significant and made the outcome of impact very similar. The splashing behavior of a rough surface covered by a thin liquid film was a

combination of both cases.

Boundaries between the different impact regimes are common and widely reported in the literature. Moreira et al. [66] synthesized several empirical correlations in the literature which established boundaries between the different impact regimes and classified them as very distinct. The main differences were due to the distinct impact conditions that originated them.

Concerning the effect of fluid properties, Zhang et al. [67] centered their work on the numerical simulation of a droplet impinging upon liquid films. They remarked that while surface tension and viscosity decrease, more momentum is imparted to the crown development, increasing its height and decreasing its thickness. In the same way, the formation of prompt splashing is enhanced by the decrease in surface tension and viscosity of the fluid. They found that the Weber number plays a more important role in droplet impact behavior than the Reynolds number. Increasing the Weber number accelerates the impact process and increases the number of splashing droplets.

Other studies concern droplet impacts upon immiscible liquid films (e.g., water and oil), such as the work performed by Che and Matar [68]. Immiscibility induces completely different hydrodynamic behaviors. A water droplet impinging on an oil film creates a compound crown, followed by the formation of a central jet; contrarily, an oil droplet impinging on a water film causes quick spreading. They also studied the influences of some parameters, such as the Weber and Ohnesorge numbers, the viscosity ratio, and the dimensionless thickness of the liquid film. Namely, concerning the last parameter, thicker films show a behavior similar to miscible liquids, with the timescales delayed relative to thinner liquid films. Recently, Burzynski and Bansmer [69] studied the droplet splashing on a thin moving film only for high Weber numbers ($We > 2281$). They reported that the liquid film velocity affects the crown geometry considerably. The high inertial force of the droplet enlarges the expansion of the crown, which causes a larger diameter. Increasing the liquid film velocity leads to an increase in crown thickness, and consequently, will decrease the dimensionless crown diameter, due to the higher inertial forces of the film that alter the spreading process.

Several splashing modes can occur, from prompt to crown splash or partial rebound and jetting [40]. The success of several applications depends on how the splashing behavior can be controlled [40]. Splashing on a thin liquid film is governed by density and surface tension, but independent of viscosity [40], [63].

2.4.1 Bubble encapsulation

Bubble encapsulation is a phenomenon seldom reported in the literature. In previous studies [70], while studying droplet impact onto thin liquid films, for a specific set of impact conditions, after crown splash, the crown sheet wall bends inwards, the jets at the top of the crown merge and close, forming an empty bubble, bubble encapsulation. This phenomenon was unknown by the authors, therefore, an extensive literature research was performed to assess

the physical significance of this outcome, denominated as bubble encapsulation or floating bubble. Table 2.1 presents a summary of the bubble encapsulation events presented in the literature over the years. It includes the goals of the authors and the impact conditions that originate the bubble encapsulation event. In addition, Fig. 2.1 shows an info-graph where you can also follow the observations of bubble encapsulation over the years.

Table 2.1: Summary of bubble encapsulation events presented in the literature.

Author	Goal	Impact Conditions
Worthington [71] (1908)	Evaluate the influence of impact height upon the crater depth.	Water and Milk D_0 large U_0 high
Engel [72] (1966)	Simulate micrometeorites shocking upon spatial vehicles. Focus on cavities.	Water $D_0 \approx 5.0\ mm$ $U_0 > 10\ m/s$ δ_f large $We_D > 6930$
Pan et al. [73] (2008)	Establish boundaries for the central jet creation by high-speed impact of droplets upon liquid films	Water $We_D > 2570$ for $\delta_f > 1$ $We_D > 4000$ for $\delta_f < 1$
Motzkus et al. [74] (2009)	Study the emission of airborne particles due to the impact of droplets onto a liquid film.	50% Water/Ethanol $D_0 = 3.87\ mm$ $U_0 = 4\ m/s$ $\delta_f = 0.31$ $We_D \approx 2020$
Pan and Hung [75] (2010)	Create transition boundaries to characterize the impact of a droplet on thin liquid films.	70% Glycerine $D_0 = 1.38\ mm$ $U_0 = 11.15\ m/s$ $\delta_f = 0.78$ $We_D = 2987$
Geppert et al. [76] (2016)	Simulate diesel droplets impinging upon the lubricating oil film that covers the combustion chamber walls.	Hexadecane $D_0 = 2.55\ mm$ $\delta_f \geq 0.2$ $We_D \geq 1100$
Ribeiro [70] (2018)	Study the impact of single droplets on liquid films to encourage biofuel introduction in civil aviation.	75% Jet A-1/25% NExBTL $D_0 = 3.0\ mm$ $U_0 = 4.2\ m/s$ $\delta_f = 0.5$ $We_D = 1667$

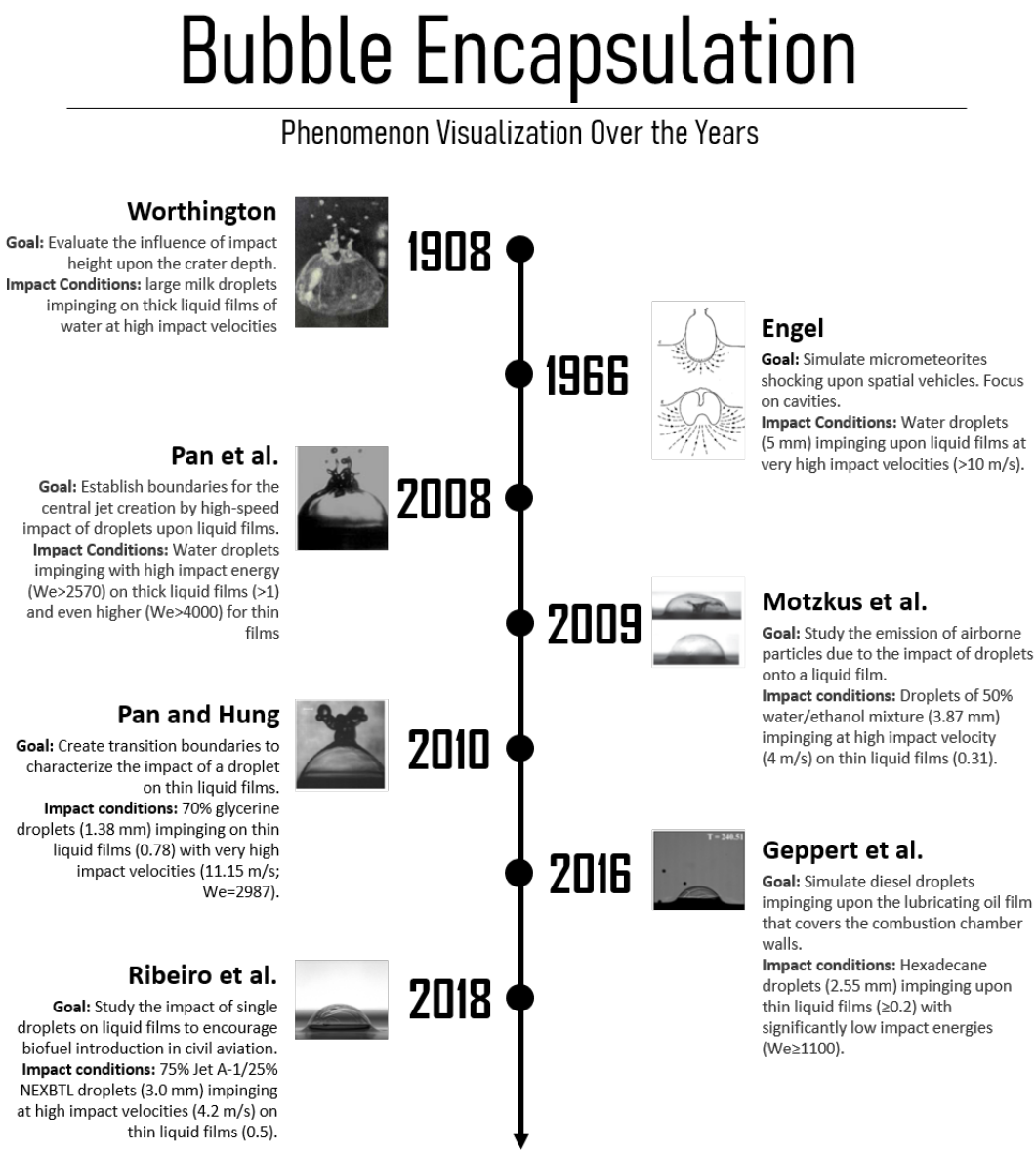

Figure 2.1: Bubble Encapsulation Visualization Over the Years.

More than a century ago, Worthington [71] dedicated a section of his book to the formation of bubbles for high falls. He increased the impact falling height to evaluate its influence on the crater depth and a new phenomenon appeared. Worthington [71] describe it by the closure of the crater "mouth" to form a bubble. He also suggested that both the upward liquid flow towards the crown rim and the action of surface tension promote the formation of the bubble structure. Finally, he reported that if the impact velocity is not high enough, the crown almost closes or it closes but reopens quickly.

A few decades later, Engel [72] studied the impact of single droplets upon liquid targets to simulate micrometeorites shocking on spatial vehicles. Similarly to Worthington [71], the goal of this study was to deeply investigate the cavities originated by these types of impacts.

Once more, it was reported that if the impact energy exceeds a certain threshold, the upper edge of the bubble-thin cylindrical sheet that rises at the top of the cylindrical wave will at last neck in and close to form a spherical bubble above the cavity. This implies that this phenomenon might not be random and a regime threshold can actually be defined. Then, Engel [72] described that a liquid jet develops at the crown closure point moving downwards via the cavity floor. Simultaneously, an upward-moving jet meets and mixes with the downward-moving jet, as can be seen in Fig. 2.1.

Later, Pan et al. [73] focused their work on the impact of high-speed droplets upon liquid layers and reported that at large Weber numbers ($We \geq 2570$) for high dimensionless film thicknesses, the ejected crown close to form a bubble. They found this regime interesting and noticed that more droplets were emitted from the central jet. Additionally, they reported that the transition boundary to bubble encapsulation decreases monotonically while increasing the dimensionless film thickness.

Motzkus et al. [74] studied the mechanisms that could lead to the formation of microdroplets concerning the emission of airborne particles with respect to the safety of nuclear facilities. Some examples of these mechanisms include prompt splash, finger pinching, and bubble bursting. They reported that for low surface tension fluids, the bubble bursting provided a high production of droplets with sizes smaller than $15\ \mu m$. The bubble hemispherical sheet progressively becomes thinner under the effect of the rising bubble and the drainage of the liquid. When the hemispherical thin sheet reaches a critical thickness, the liquid sheet breaks and produces tiny droplets. Many parameters can influence the number and size of the emitted droplets: bubble size, air-liquid surface tension, liquid viscosity, and the thickness of the bubble sheet. However, they only observed one event with the formation and break up of bubbles.

A couple of years later, Pan and Hung [75] extended their research and mentioned that the enclosure of the crown sheet was due to the bending of the upwardly ejected sheet by the gravity force. The bubble trapped inside could cause some underwater perturbations that will eventually affect the transport of fluid or transmission of sound waves. They also identified the two jets, one upwards and the other downwards.

More recently, Geppert et al. [76] experimental and numerically investigated the impact morphology of droplet impingement upon liquid films for two-component systems, in pursuance of simulating the diesel droplets impinging upon the lubricating oil film that covers the combustion chamber walls. Nonetheless, they detected two additional phenomena, jet and bubble formation, and observed that their occurrence was not occasional. Both the central jet and bubble formation have been already observed for one-component droplet-film interactions, but mainly for thicker liquid films ($\delta \geq 0.5$). Thus, it is possible to assume that even for one-component systems, the dynamic of splashing is far more complex than the typical deposition/splashing boundary. In their experiments, the bubble formation occurred for $\delta \geq 0.2$ and $We > 1100$, and they agreed with Worthington [71] about the effects that originate bub-

ble encapsulation. To conclude, they recognize that the lifetime of splashing is longer when the crown sheet closes to form a bubble.

In the same year, Liang and Mudawar [37] recognize that a few authors [74, 77, 78] reported the existence of narrow or closed rims and they believed that this large bubble strongly depends on the dimensionless film thickness and impact velocity.

As mentioned, in previous studies [70], an event of bubble encapsulation was observed. The droplet and liquid film fluid is a mixture of 75% Jet A-1 and 25% NExBTL. Being Jet A-1 a conventional Jet Fuel (JF) and NExBTL (Neste Renewable Diesel) a type of HVO (Hydroprocessed Vegetable Oil), a biofuel. The thickness of the liquid film is considered thin, $\delta = 0.5$, which makes this impact conditions very similar to those of Geppert et al. [76].

As can be seen, this phenomenon lacks more investigation to understand its occurrence, formation mechanisms, main features, and physical significance.

2.4.2 Spread/splash transition criteria

The future of biofuels in the aviation industry depends on how much the induced changes in thermophysical properties affect the combustion process and all its stages, from spray formation to the preparation of the fuel/air mixture. One of the stages that produces a significant impact on the fuel/air mixture preparation is the impact of droplets on interposed surfaces. Additionally, due to the complexity of the several phenomena involved, the adequacy of numerical models to simulate the combustion process relies on accurately describing the outcome of drop impact on dry or wet surfaces. This description includes the morphological behavior of hydrodynamic structures leading to the deposition of fuel or eventual secondary atomization, re-issuing part of the fuel to the combustion chamber, and improving the fuel/air mixture preparation. However, due to the numerous variables that affect the outcome of drop impact, the best approach is to develop empirical correlations based on dimensionless numbers expressing the relation between the inertial, surface tension, and viscous forces involved.

The situation becomes complicated due to the different types of splashing. Thus, empirical correlations and regime maps start to be a function of droplet impact velocity, surface temperature, impact angle, roughness and curvature of the surface, fluid properties, wettability, and impact energy. [40].

The two essential outcomes of drop impact on liquid films are the deposition of a liquid droplet in the film or the generation of secondary droplets through hydrodynamic mechanisms, such as full or partial rebound of the initial droplet, or smaller droplets detaching from the bounding rim of an uprising crown associated with the splashing mechanism. However, the classification of these outcomes is not always unanimous.

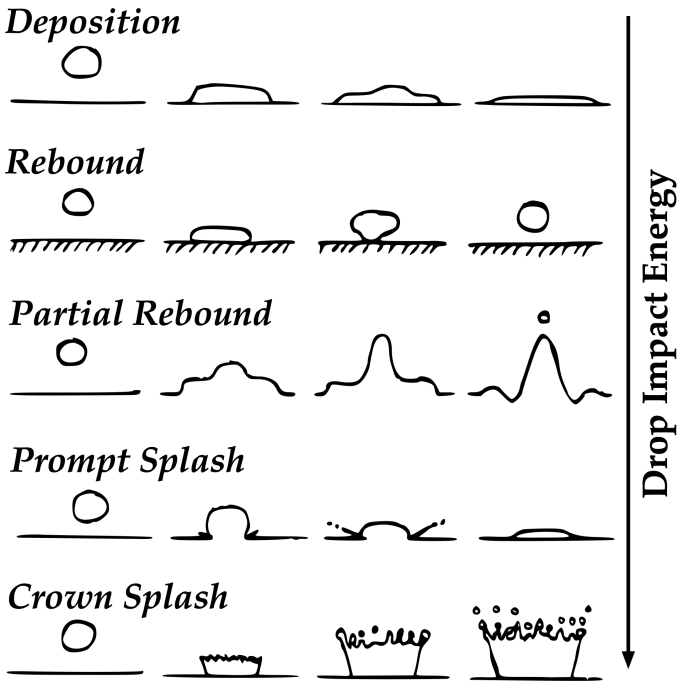

Figure 2.2: Drop Impact Mechanisms.

Rioboo et al. [43] defined a detailed terminology for the several morphological structures emerging from drop impact, being the most relevant for this study droplet deposition, prompt splash, crown splash, complete rebound, and partial rebound. Figure 2.2 presents illustrations of these phenomena organized by the required drop impact energy.

Over the years, finding a correlation that can predict the transition between spreading and splashing has been one of the focus of the droplet impact studies. For droplet impact upon liquid films, several empirical correlations have been proposed. First, it is necessary to identify the differences in the droplet hydrodynamic behavior depending on the liquid film thickness (h_f). Actually, Chandra and Avedisian [38] reported that the spreading of a droplet can significantly change due to the liquid film. Later, focusing their work on distinguishing the spreading behavior between the impact on dry and wetted surfaces, Rioboo et al. [79] showed how maintaining all the impact parameters constant, except the surface conditions, resulted in entirely different drop impact morphological structures. Therefore, it is reasonable to include the effect of the liquid film characteristics in the empirical correlations (in a dimensionless form as $\delta = h_f/D_0$, where D_0 is the droplet diameter before impact) discerning the transition between deposition and the splash which generates secondary atomization.

Usually, the empirical correlations that categorize the outcomes of the impact depend on dimensionless parameters such as the Weber and Reynolds numbers, followed by the Ohnesorge and Laplace numbers, dependent on the former. Most empirical correlations follow a relation between Weber and Reynolds numbers expressed as

$$\mathrm{Re}^{\alpha}\mathrm{We}^{0.8} = K_c \quad (2.10)$$

where K_c is the criterion between a droplet spreading and splashing and the α value varies depending on the criterion.

In the following, several spreading/splashing thresholds available in the literature for single droplet impact upon liquid films will be presented.

Bai and Gosman [80] gathered data from the literature and attempted to catalogue the phenomena and their limits by using dimensionless numbers. In their study, they recognize the lack of data and availability of results about the different impact regimes. However, they proposed a simplified approach for droplet impact onto a wetted wall. They assumed temperatures of the surface below the boiling point of the liquid and that a wetted wall behaves as a very rough dry surface ($r_s > 12\ \mu m$, with r_s the surface roughness). They used the data of Stow and Stainer [81] and proposed the spread/splash boundary proposed in eq. (2.11). Its validation range includes $8000 < Re < 33600$.

$$We_c = 1320\ La^{-0.18} \quad \textbf{(2.11)}$$

Cossali et al. [39]

$$K_L = (Oh^{-0.4}We)_L = 2100 + 5880\ \delta^{1.44} \quad \textbf{(2.12)}$$

Senda et al. (1999)

$$We = (2164 + 7560\ \delta^{1.78})La^{-0.2} \quad \textbf{(2.13)}$$

According to Vander Wal et al. [40] the complex phenomenon of splashing can occur as prompt splash, delayed or crown splashing, partial rebound, and jetting. They believed that even an empirical-based correlation to predict splashing is important since this allows the definition of conditions to have a strong splashing or to inhibit it completely. They investigated both the impact of dry and thin liquid films for isothermal systems. Thin liquid films represent the first transition in applications of sprays and painting onto dry surfaces. Additionally, Vander Wal et al. [40] decided to use thin liquid films since this is the opposite condition to the dry surface case. To avoid the effect of surface roughness, they used a mirrored surface. To guarantee a wide range of impact conditions, 12 different fluids were used, including alkane, alcohols, water, and a $30\ wt\%$ glycerol–water solution. Using the Reynolds and Ohnesorge number they defined a boundary between the non-splash and splash zones. They have considered all splashing modes, except the ones related to rebound.

The impact surface is a diamond-lathed aluminum disk with a mean surface roughness of $< 10\ nm$ and the liquid film has a thickness of $h_f \approx 0.2\ mm$. The droplet and the liquid film are of the same fluid. The droplet initial diameter is $D_0 = 2.0\ mm$ and its shape during

the free fall is spherical. The impact velocity was varied. As mentioned in sec. 2.3.1, these experimental conditions resulted in the following parameter space: $988 < Re < 13900$, $127 < We < 1420$, and $2.91 < Ca < 62.0$.

A liquid film drastically changes the spread/splash limit in comparison with dry surfaces. Following the same methodology as for the dry case, a power law between the Ohnesorge and the Reynolds number was developed and is defined in eq. (2.14).

$$Oh\ Re^{1.17} = 63 \quad (2.14)$$

Moreover, by considering $Re^{1.17} = Re$ and adjusting the value of the constant, the spread/splash threshold can be approximated as:

$$Oh\ Re = \sqrt{We} = 20 \quad (2.15)$$

The critical Weber number We_{crit} is lower for the impact on thin liquid films than on dry surfaces. Vander Wal et al. [40] considered this fact as expected due to the kinematic discontinuity model. Initially, the liquid film is stationary, which creates a large kinematic discontinuity between the liquid film and the impinging droplet. Therefore, the stationary liquid film governs the onset of splashing and viscosity has a smaller role. The lack of fluid viscosity in the definition of the spread/splash boundary reflects the fact that viscosity plays a secondary role, which was also confirmed in Vander Wal et al. [63] observations. The spread/splash threshold on dry surfaces also depends on the impact velocity, but its influence on the impact with thin liquid films is even higher. That is why the splashing starts at lower Weber numbers for thin liquid films.

Huang and Zhang [82]

$$(We\ Re)^{0.25} = 25 + 7\ \delta^{1.44} \quad (2.16)$$

2.5 Droplet Impact onto Heated Surfaces

Studies about droplet impacts are widely reported in the literature [41] and have diverse applications from spray cooling to fuel injection in internal combustion engines.

As known, the civil aviation industry is responsible for a significant portion of atmospheric pollution due to its dependency on fossil fuels [41]. Alternative aviation fuels are required to reduce this problem and fulfill the demand for the decarbonization of the aviation sector by 2050 [83].

Droplet impingement upon heated walls is a complex phenomenon. Heat transfer is strongly affected by the relation between the wall temperature T_w and the saturation temperature T_{sat}. The saturation temperature T_{sat} corresponds to the boiling point since it is the temperature

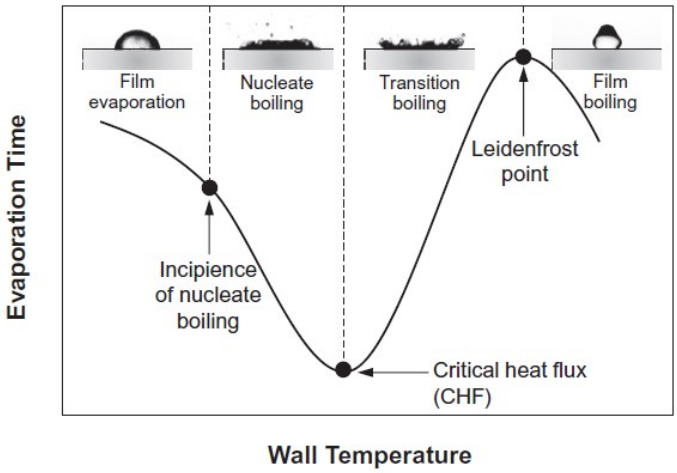

Figure 2.3: Heat transfer regimes for single droplet impact upon heated dry surfaces from Liang and Mudawar [37].

at which the liquid boils for a certain saturation pressure Different heat transfer regimes can be observed: film evaporation, nucleate boiling, transition boiling, and film boiling [6]. Film evaporation occurs when the wall temperature is smaller than the saturation temperature $T_w < T_{sat}$, and nucleate boiling when $T_w = T_{sat}$. On the other hand, transition boiling takes place in the region between the critical heat flux T_{CHF} and the Leidenfrost point T_{Leid}, and film boiling when $T_w > T_{Leid}$. The critical heat flux establishes the shortest droplet lifetime and corresponds to the minimum evaporation time [84]. The Leidenfrost temperature T_{Leid} is the lowest wall temperature of the film boiling regime, first observed by J. G. Leidenfrost. The heat transfer regimes are described in Fig. 2.3.

Several studies have been made about these heat transfer regimes and the parameters that influence them and their characteristics [6].

Chapter 3

Experimental Methodology

3.1 Introduction

This dissertation is divided into three different experimental studies which required three different experimental apparatuses. In this chapter, each experimental setup will be shown and explained in detail. First, the focus is the droplet impact upon dry cold solid surfaces, followed by droplet impact upon liquid cold surfaces, and finally, the study of droplet impacts upon dry heated surfaces. For each case, the different systems that compose the experimental setup will be presented as well as the fluids, the impact targets, and their properties. The meticulous experimental procedure followed is explained and evidently, the major difficulties faced.

3.2 Droplet Impact onto Dry Cold Surfaces

As mentioned in Section 2.2.1 droplet impact onto dry cold surfaces is important in many applications. In this experimental study, a single droplet impinging upon dry cold smooth or micro-structured surfaces with variable wettability was investigated.

Depending on the surface wettability different outcomes can be expected. Thus, in this study, the wettability of the surface samples was changed without altering their material or their topography. This is possible by applying plasma treatments to the surfaces, which will change their wettability without changing other properties. Regular micro-structured surfaces were used under the same experimental conditions to compare with the results from the smooth surfaces.

The hydrodynamic phenomena are captured by using an experimental setup with three different perspectives. In the following sections, the experimental setup will be described and the surface samples presented. The wettability definition as well as the plasma treatments applied will be elucidated. Finally, the parameter space, experimental procedure, and image processing will be explained.

3.2.1 Experimental Setup

The experimental setup for the single droplet impact upon smooth or micro-structured surfaces is composed of three main systems: image acquisition system, droplet dispensing system, and triggering and synchronization system. Figure 3.1 shows the scheme of the exper-

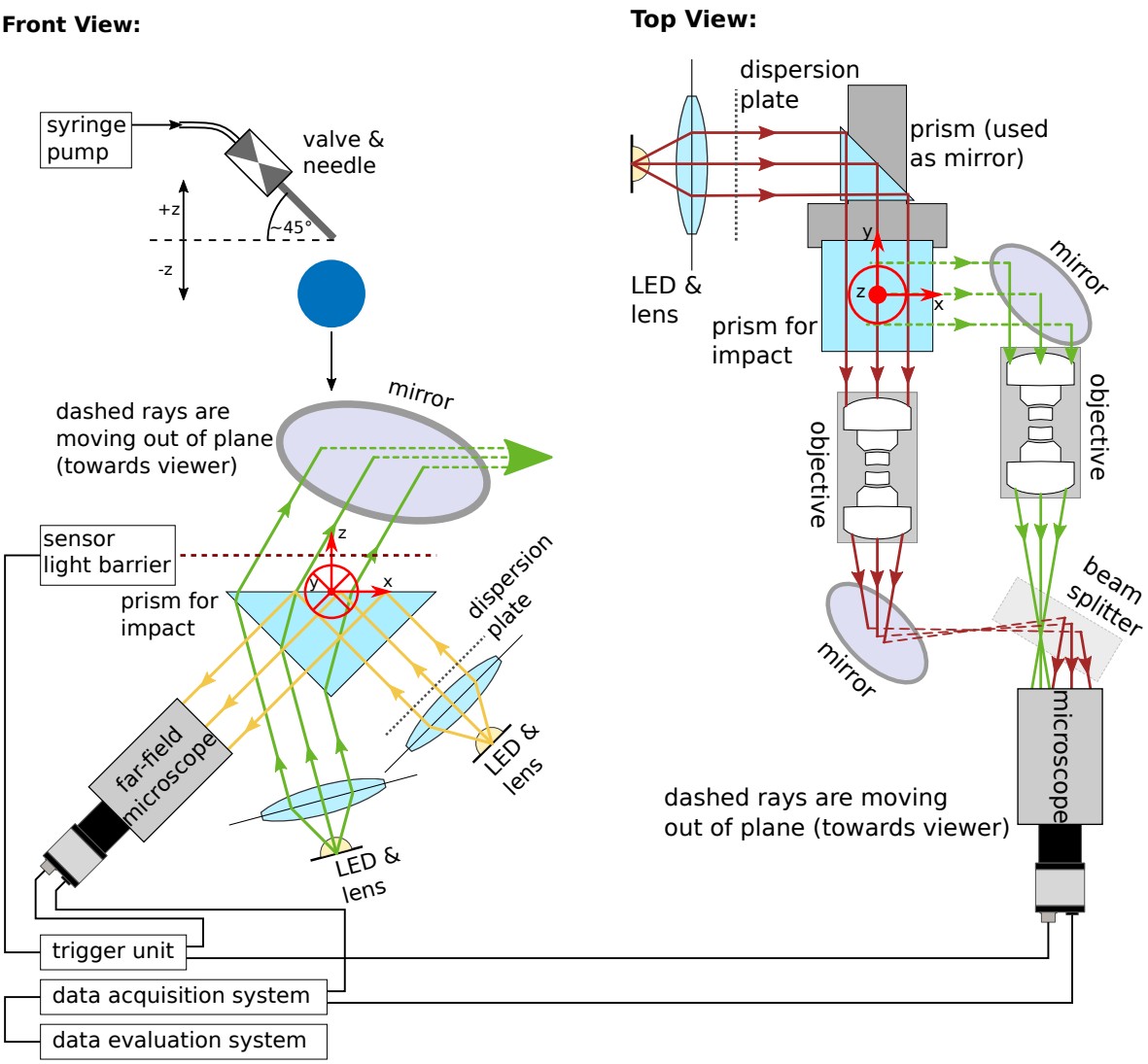

Figure 3.1: Schematic of the image acquisition unit - front view on the left side, and top view on the right side. The different colors indicate the different light paths, yellow for the bottom perspective, green for the top perspective, and red for the lateral perspective. Dashed light paths emerge from the sketch plane. The droplet impact point is marked by the given coordinate system. Modified figure is originally extracted from [9].

imental setup. To record the droplet impact from three different perspectives, lateral, top and bottom perspectives, demands a complex image acquisition system. In Fig. 3.1, each perspective is represented by light paths with a different color. The bottom view is identified by the yellow light rays, the top view by the green rays, and the lateral view by the red light rays.

Two high-speed digital cameras *Photron SA-X2* were synchronized to capture the three different perspectives. This was possible since both the lateral and top views of the phenomena were captured by the same CMOS-Chip (complementary metal-oxide semiconductor) due to the arrangement of the optical equipment. The bottom perspective was acquired in a total internal reflection configuration. However, the top and lateral perspectives were captured as shadowgraphs. The bottom, top, and lateral perspectives have a spatial resolution of $17.0\,\mu m$, $18.1\,\mu m$, and $28.8\,\mu m$, respectively. All images were acquired at a resolution of 1024×672 px^2,

a frame rate of $20000\ fps$, and a shutter time of $1/88888\ s$. Each perspective will be explained in detail to better understand how the image acquisition system works.

The bottom perspective is one of the important novelties of this study. The motivation to use more than the lateral perspective is that partial shadowing of the bottom perspective is essential to understand the complexity of the fine flow patterns created, e.g., by the splashing of a droplet on a steady liquid film [85, 21]. In fact, by using a total internal reflection configuration it is possible to distinguish between wetted and dry areas for droplet impact both on smooth and micro-structured surfaces, as shown in Fig. 3.2. Parallel light to the prism, generated using a *Cree XLamp XHP70 SMD High-Power* LED and an aspheric condenser lens, enters the prism with an angle of $45°$ related to the top surface, see Fig. 3.2 (a). The dispersion plate is used to obtain a more homogeneous light distribution in the image. For a dry surface and due to the occurrence of total internal reflection, the light is reflected, exiting the prism and entering a *Navitar Zoom 6000* far-field microscope mounted to a high-speed camera. The microscope is focused on the region where the droplet is impacting on the surface, indicated by a red cross in Fig. 3.1. For the case shown in Fig. 3.2 (a), the camera is detecting a bright image, without any shadow.

To obtain the total internal reflection configuration several conditions must be taken into account. The critical angle ξ_{crit}, which is the minimum angle of the incident ray, for a total reflection can be calculated by Snell's Law [86]. According to equation (3.1), the critical angle only depends on the ratio of the refractive indices of the adjacent media at the interface n_i/n_j.

$$n_1 \sin \xi_1 = n_2 \sin \xi_2 \quad (3.1)$$

$$\xi_{crit} = \arcsin n_2/n_1 \quad (3.2)$$

For the case with liquid on the top of the surface, Fig. 3.2 (b), the total internal reflection might not occur if the angle of incidence is lower than the critical angle $\xi_{inc} < \xi_{crit}$. The critical angle, according to equation (3.2), for the combination glass prism, made of N-BK7 ($n_1 = 1.514$ @ $680\ nm$) [87], and air ($n_2 \approx 1$ @ $680\ nm$) [88], gives $\xi_{crit} \approx 41.3°$. The wavelength of $680\ nm$ is used as a reference due to the maximum quantum efficiency for the

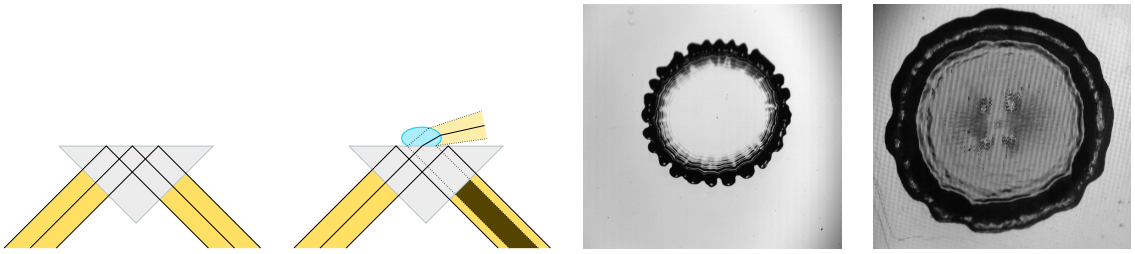

(a) (b) (c) (d)

Figure 3.2: Principle of the total internal reflection configuration: (a) dry surface on which all light rays are reflected; (b) wetted surface with curved profile leads to partial diffraction of light exiting to the top-side of the prism; (c) perspective-corrected image showing the dry and wetted areas on a smooth surface. The middle of the droplet is also wetted, however, due to the horizontal droplet lamella the total internal reflection condition is met again; (d) perspective-corrected image showing the dry and wetted areas on a micro-structured surface.

Photron SA-X2 high-speed cameras [89]. If the top-side of the prism is wetted (compare Fig. 3.2 (a) and (b)) the relation of the refractive indices, specifically n_2, is changing, leading locally to light diffraction and not to total internal reflection. As you can see in Fig. 3.2 (b) and (c), these areas cause dark spots on the camera. However, in Fig. 3.2 (c), the light passes through since the wetted area is again a horizontal surface. Thus, the total internal reflection occurs again. The rim is not horizontal, therefore, it defines the boundary between the wetted and dry areas. Figure 3.2 (d) shows exactly the same situation but for droplet impact onto micro-structured surfaces. Due to the topography of the surface, a clear and doubtless assignment of wetted areas is possible. Thanks to the bottom perspective of the micro-structured surfaces, it is possible to identify heterogeneous wetting states, as will be described ahead.

The lateral perspective is the most common in droplet impact studies. The lateral perspective is identified in Fig. 3.1 by the red light rays. The light is created by a white LED, a lens, and a dispersion plate. Due to the test rig periphery, the light has to be redirected by a small prism used as a mirror into the y-direction. Then, the light traverses the droplet impact area and is used for a diffuse backlight image. To enlarge the optical distance between the impact area and the microscope, a Schneider Kreuznach Symmar $80/5.6$ objective is used for intermediate imaging. As explained before, the lateral and top perspectives share the same CMOS-chip of the camera. To place the lateral view next to the top view on a $50{:}50$ beam splitter plate, it is necessary to shift the lateral view in the x- and y-direction. Thus, a mirror is used to redirect the light rays diagonally upwards. The beam splitter plate works as mirror for this perspective and reflects the rays inside the microscope onto the CMOS-chip of the camera.

The top perspective, represented by the green light rays in Fig. 3.2, is often reported in the literature. The top view is a powerful tool to better understand the dynamics of droplet impact, especially on the impact with micro-structured surfaces. The parallel light for the diffuse backlight images is generated using a white LED and a lens. The light enters the prism and, after being refracted twice at the two interfaces, leaves the prism with a certain angle. To minimize the offset of the light path into the x-direction, the light source is rotated by a small angle. The diffuse backlight image is then projected onto a mirror, which stops the shift in the x-direction. This shift is caused by the prism and it is unavoidable. After that, the rays are reflected by the mirror orthogonally in the y-direction to the microscope. A *WILD Heerbrugg M8 Zoom stereomicroscope* is mounted to the high-speed camera and can provide a magnification range of $1x$ to $40x$. The lateral and top perspectives are combined inside the microscope. However, the working distance is approximately $90\ mm$, which is too small for a simple combination. To make the combination possible, two identical *Schneider Kreuznach Symmar* $80/5.6$ objectives are used for intermediate imaging enlarging the optical paths of both the top and lateral perspectives by $320\ mm$. This enables the shared CMOS-chip, and after passing the objective, the rays are transmitted to a $50{:}50$ beam splitter plate before entering the microscope.

The image acquisition system is controlled by the triggering and synchronization unit. The

falling droplet passes a LASER light barrier and when the droplet cuts the light sheet it provides a TTL-signal (transistor-transistor-logic). This TTL-signal is passed to the high-speed cameras to start the image acquisition system and to an oscilloscope for checking the time synchronization. As mentioned before, the top and lateral perspectives share a CMOS-chip of a *Photron SA-X*2 high-speed camera, consequently, they are automatically synchronized. However, the bottom perspective has to be synchronized with the two other perspectives. To achieve that, one of the high-speed cameras was set as ”primary” and the other as ”replica”. The ”primary” camera receives the TTL-signal and passes this information to the ”replica” camera with a shutter time of $1/88888\ s$ and a frame rate of $20000\ fps$. Due to this procedure, there is no measurable temporal shift between the different perspectives during image acquisition, which is constantly cross-checked by the oscilloscope at a sampling rate of $125\ kHz$ for each channel.

Finally, the description of the droplet dispensing system. A blunt needle with an outer diameter of $0.4\ mm$ is used to generate the impacting droplets. The droplet impact velocity U_0 is varied by changing the droplet falling height. Four different falling heights were chosen, providing four different impact velocities, as will be described in subsection 3.2.5. The impact region of the droplet is strongly influenced by the detachment process at the needle for the two higher heights. To ensure a more deterministic falling trajectory by guaranteeing that the droplet always detaches at the same position of the needle, the needle was tilted $45°$ to one side. The needle is connected to a glass syringe by Teflon® tubes. Glass and Teflon® were chosen as materials to avoid any chemical alterations of the liquid during the dispensing process. There are some parts that are neither glass or Teflon®, but are medical equipment. Although, due to the very short passages of the liquid in the non-glass and non-Teflon® materials, the influence onto the chemical consistency of the liquid droplet is neglected. A medical syringe pump is pumping liquid from the glass syringe at a moderate pumping rate of $0.5\ mL/min$. To avoid back-flow inside the pump, tubes and needle, which may lead to air bubbles, a one-way valve is included. With this adjustment, a homogeneous droplet chain with constant droplet diameter D_0 can be guaranteed at a rate of approximately $1.5\ Hz$. For each experiment, one droplet is randomly selected from the droplet chain to pass a barrier while the rest of the droplets are sorted out.

3.2.2 Surface Samples

The experiments of droplet impact onto dry surfaces were performed both on smooth and structured surfaces. Two different transparent polymeric materials were chosen: Lexan® (PC) and Plexiglas® (Poly(methyl methacrylate), PMMA) for both the smooth and structured surfaces. One of the novelties of this study includes the regular micro-structured surface samples. As mentioned in Section 3.2.1, the total internal reflection configuration of the bottom perspective allowed the observation of heterogeneous wetting states and air entrapment. This was only possible due to the transparency of PC and PMMA both on the smooth and structured surfaces. Four different structured patterns were chosen for the surface specimens. Micrometric grooves and pillars composed these patterns as depicted in Fig. 3.3 and

Table 3.1: Dimensions of the micro-structured surfaces and the respective topography parameters used for the evaluation. $S1$ corresponds to grooves, see Fig. 3.3 a), $S2 - S4$ correspond to pillars with a square cross section, see Fig. 3.3 b). R_a, R_z, and R_{sm} are correspond to calculated roughnesses, r is the roughness factor according to Wenzel [92], and α is the topography parameter introduced by Tsai et al. [93] for describing regularly structured surfaces. The authors have chosen to modify this parameter as $\alpha_{mod} = b/h$. Herein, the diagonal b of the spacing between the individual structure elements is used.

		Dimensions [μm]			Topography parameters						
ID	Type	Edge length	Distance	Height	$R_a\,[\mu m]$	$R_z\,[\mu m]$	$R_{sm}\,[\mu m]$	r	α	α_{mod}	$b\,[\mu m]$
$S1$	grooves	$w_1 = 60$ $w_2 = 500$	$d_1 = 60$ $d_2 = 15$	$h = 20$	10	20	280.5	1.36	1.0	3.1	61.85
$S2$	square pillar	$w = 60$	$d = 60$	$h = 20$	7.5	20	33.9	1.33	1.4	4.2	84.85
$S3$	square pillar	$w = 30$	$d = 30$	$h = 20$	7.5	20	67.6	1.67	1.4	2.1	42.43
$S4$	square pillar	$w = 15$	$d = 15$	$h = 20$	7.5	20	135.4	2.33	1.4	1.1	21.21

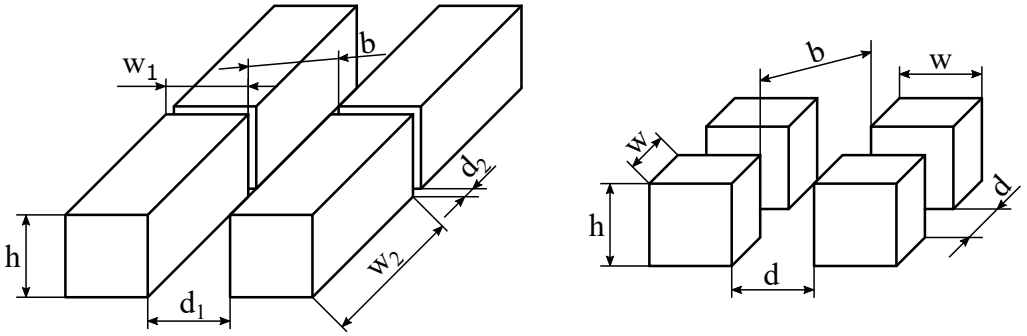

(a) (b)

Figure 3.3: Dimensions of the structured surfaces: a) grooves ($S1$), b) pillars with a square cross section ($S2 - S4$). The respective dimensions are summarized in Tab. 3.1.

their dimensions were described in Tab. 3.1.

The micro-structured surfaces were manufactured in a three-step-procedure, which combines LASER lithography, nickel electroforming and the hot embossing technique [90, 91]. The surface samples were produced at the *Karlsruhe Nano and Micro Facility (KNMF), Germany*. The quality check of the surface samples was performed using Scanning Electron Microscopy (SEM), micro-Computed Tomography (microCT), and classical optical microscopy. An example of the SEM images for the different micro-surface patterns is presented in Fig. 3.4.

For all micro-structured patterns, the height of the structures is kept constant at $h = 20\ \mu m$. The grooves ($S1$), shown in Fig.3.3 (a), are very long pillars with a width of $w_1 = 60\ \mu m$ and a length of $w_2 = 500\ \mu m$. The orthogonal distance between each groove is $d_1 = 60\ \mu m$ while the gap is $d_2 = 15\ \mu m$, into the direction of the grooves, which is due to manufacturing reasons of the hot embossing procedure. Three different patterns of pillars with a square cross-section were also considered ($S2 - S4$), see Fig. 3.3(b). The edge length is equal to the spacing between pillars: $d = w = 60\ \mu m$ for $S2$, $d = w = 30\ \mu m$ for $S3$, and $d = w = 15\ \mu m$ for $S4$. Table 3.1 also includes parameters that describe the topography of the surfaces. There

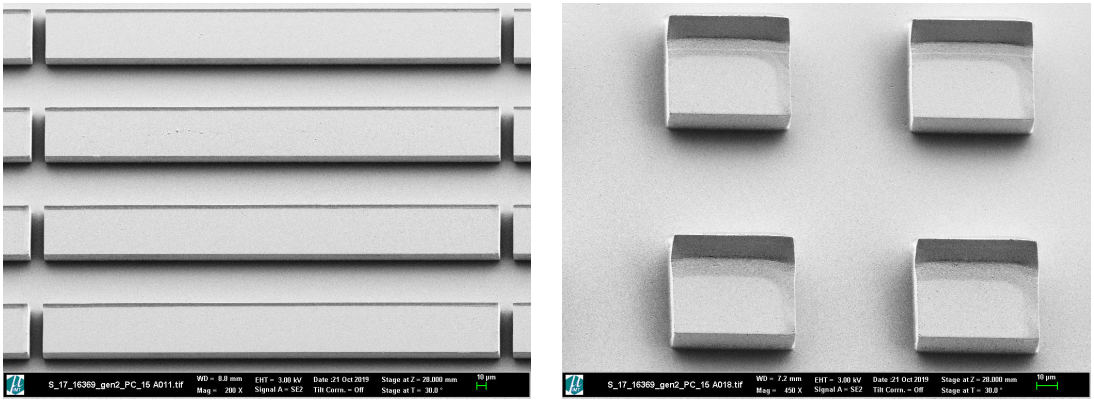

(a) grooves ($S1$, magn.: 99×)

(b) 60 μm × 60 μm ($S2$, magn.: 400×)

(c) 30 μm × 30 μm ($S3$, magn.: 300×)

(d) 15 μm × 15 μm ($S4$, magn.: 500×)

Figure 3.4: Micro-structured Lexan®-surfaces of different dimensions acquired with Scanning Electron Microscopy (SEM). The magnification of each image is given at the respective image. The specimen stage was tilted by 30°: a) grooves ($S1$); b) 60 μm × 60 μm pillars ($S2$); c) 30 μm × 30 μm pillars ($S3$); and d) 15 μm × 15 μm pillars ($S4$). Reprinted from Springer Nature: Droplet Interactions and Spray Processes, Fluid Mechanics and Its Applications 121, Foltyn et al. [90], Fabrication and Evaluation Methods of Micro-structured Surfaces for Droplet Impact Experiments, 2020.

are different length scales to characterize the roughness of a target surface [92, 93, 94]. One of the most common is the arithmetical mean roughness, R_a, also called amplitude average roughness. It is defined in eq. 3.3 as the mean absolute deviation of roughness irregularities from the center line.

$$R_a = \frac{1}{l} \int_0^l |y(x)|\, dx \quad (3.3)$$

Where l is the length of the irregularity and y is the height from the mean line. In this case, a mean plane was considered instead of a mean line since it demands a volumetric approach. As shown in Tab. 3.1, the value of R_a is equal for all square pillar arrangements ($S2 - S4$), $R_a = 7.5\ \mu m$. This happens since the height of the pillars is the same for all cases and the width of the pillars is equal to the spacing between them. The surface composed of grooves ($S1$) presents a higher value, $R_a = 10\ \mu m$. According to Moita and Moreira [95], the mean roughness is not sufficient to describe the surface topography. Also, in their recent studies, Wang et al. [96] confirmed that different definitions of roughness might lead to different results.

Another length scale is R_z, which is defined by the mean of five individual values of distances between the highest peak and the deepest valley for five consecutive sample lengths [94]. For this case, the R_z is the same for all micro-structured patterns, $R_z = 20\ \mu m$, which corresponds to the roughness element height h.

R_{pk} is another significant length scale in characterizing irregular rough surfaces. It is defined as the average height of protruding peaks above the roughness core profile [94]. Since in this study, the surfaces are composed of regular micro-structures, this length scale may not fit properly in this case.

Additionally, the mean width of a profile element, R_{sm}, is also a relevant length scale for the droplet impact on rough surfaces, and it is calculated by equation (3.4), where m is the number of elements and X_{si} is the width of each element.

$$R_{sm} = \frac{1}{m} \sum_{i=1}^{m} X_{si} \quad (3.4)$$

Analogous to the calculation of R_a, a volumetric approach was considered in which volume-equal but cylindrical pillars approximated the rectangular pillars and grooves.

Tsai et al. [93] studied the mechanisms of splashing when a droplet impinges on structured surfaces. They reported that the morphology of splashing is significantly affected by the arrangement of the micropillars. The parameter $\alpha = b/w$ defines the ratio of the largest length scale of the cavity which can be passed by air (b is the diagonal between two elements) related to the roughness element width in one micro-pattern unit (w). For all surfaces composed of pillars with a square cross-section, $S2 - S4$, the value of α is equal, $\alpha = 1.4$. However, it is smaller for $S1$, $\alpha = 1.0$. In their study, Tsai et al. [93] related the critical Weber number We_{crit} to the arrangement of pillars in a two-dimensional plane. However, using the same parameters different critical Weber numbers can be obtained. Additionally, Xu [97] and Courbin et al. [98] concluded that splashing can be inhibited by increasing the pillar's height and by increasing surface roughness, respectively. To account for the three-dimensional shape of the structures, a modified α is introduced, which is the ratio between b and the height of the pillars $\alpha_{mod} = b/h$, similar to the Wenzel factor approach that will be explained next.

In 1936, Wenzel [92] proposed the Wenzel equation for rough surfaces. The roughness factor r defines the ratio between the actual surface area and the projected surface area. This is an important parameter used by several authors to describe the morphology of the outcome. Smooth surfaces have a value of $r = 1$ and rough surfaces have a value of $r > 1$. Although the geometries of $S1$ and $S2$ are different, the roughness factors are almost the same. Regarding the pillars with a square cross-section, $S2 - S4$, r increases while decreasing the pillar width w. All the length scales studied in this work are given in Tab. 3.1 and will help to disclose the role of roughness on the droplet morphology dynamics.

The smooth samples were trashed after each impact, but that is not possible for the structured surfaces. Only a reduced amount of micro-structured specimens are available due to manufacturing constraints. Hence, the specimens have to be reused and the process to allow reusing the samples will be explained in subsection 3.2.6. At the beginning of the experimental campaign, it was not certain if the droplet impacts could damage the tiny micro-structures. Therefore, all structured samples were examined under the microscope and mapped for possible damages after each impact to assess if the pillars were damaged. Yet, no defects or damages were identified. Consequently, it can be assumed that droplet impact does not destroy or damage the surface pillars at least for the number of experiments performed.

3.2.3 Definition and measurement of surface wettability

One of the goals of this study is to investigate droplet impact on surfaces with different wettabilities. The capacity of a liquid to wet a surface can be characterized by the apparent contact angle θ_{app}. In this study, we follow the definition of Marmur et al. [99]. Figure 3.5 shows the definition of the apparent contact angle θ_{app} as the angle on the liquid side between the tangent of the solid surface and the tangent of the liquid-vapor phase. The wettability can be divided into different classes depending on the observable apparent contact angle. Wettable surfaces form apparent contact angles $\theta_{app} < 90°$ and are considered as "hygrophilic". On the other hand, non-wettable surfaces form apparent contact angles $\theta_{app} > 90°$, called "hygrophobic". There are two extreme cases. The surface is considered fully wettable when $\theta_{app} \approx 0°$, also known as "superhygrophilic", and for $\theta_{app} > 150°$ the surface is called "superhygrophobic". The prefix "hygro" stands for liquids in general, while the prefix "hydro" is commonly used for water. According to Marmur et al. [99], the measured apparent contact angle might deviate from the equilibrium Young contact angle θ_Y, described by the following equation [47]:

$$\gamma_S - \gamma_{SL} = \gamma_L \cos\theta_Y \quad (3.5)$$

The Young contact angle θ_Y can be estimated using the free surface energies of the solid γ_S, the solid-liquid γ_{SL}, and the liquid interface γ_L, and it is thermodynamically stable since it has the lowest Gibbs-energy. However, it is difficult to estimate γ_{SL}. Therefore, the prediction with the method of Owens, Wendt, Rabel, and Kaelble (OWRK-model) [100, 101, 102]

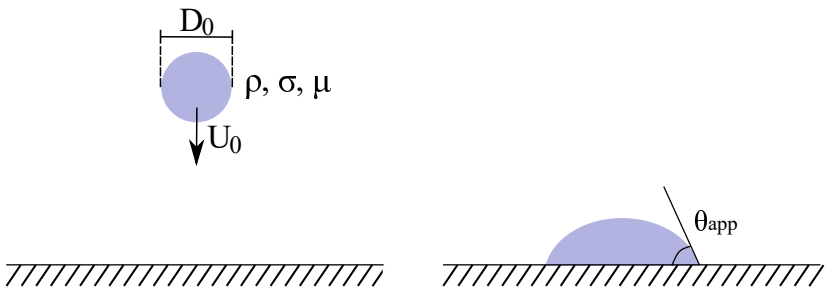

Figure 3.5: Definition of the droplet impact conditions and the apparent contact angle θ_{app}.

is used. Thus, the surface free energies are split into polar and dispersive parts [103]:

$$\gamma_i = \gamma_i^p + \gamma_i^d \quad (3.6)$$

and the solid-liquid interface energy γ_{SL} can be expressed using eq. (3.6):

$$\gamma_{SL} = \gamma_S + \gamma_L - 2\left(\sqrt{\gamma_S^p \gamma_L^p} + \sqrt{\gamma_S^d \gamma_L^d}\right) \quad (3.7)$$

By combining eq. (3.6) and eq. (3.7) into the Young equation, eq. (3.5), the contact angle can be predicted by the following equation:

$$\cos(\theta_{\text{OWRK}}) = 2/\gamma_L \left(\sqrt{\gamma_S^p \gamma_L^p} + \sqrt{\gamma_S^d \gamma_L^d}\right) - 1 \quad (3.8)$$

In this study, experimentally, the sessile drop method was employed to measure the apparent contact angle θ_{app} using an Optical Contour Analysis (OCA) system manufactured by *Data-Physics Instruments GmbH*. The measurement procedure starts by placing the surface sample in which the apparent contact angle will be measured on a height-adjustable platform. Then, a $5\ \mu L$ droplet is produced by a precise pump and remains hanging on the tip of a blunt needle. After that, the height-adjustable platform is moved up very slowly, to guarantee a very low relative velocity between the droplet and the surface and avoid any influence on the apparent contact angle θ_{app}, until reaching the hanging droplet. Finally, diffuse backlight images of the droplet are acquired by a camera mounted to a far-field microscope. The baseline of the droplet is manually defined and an elliptical fit is used for fitting the contour of the droplet shape. The arithmetic average contact angle at the left and right triple points is used as the apparent contact angle. This procedure was repeated several times at different spots randomly distributed to minimize the influence of local inhomogeneities in the free surface energies. The arithmetic mean of these apparent contact angle measurements is considered as the reference value for the surface samples and used in the experiment evaluation.

In this experimental study, the fluids used are distilled water and isopropanol (2-propanol). Their thermophysical properties at ambient temperature are described in Tab. 3.2. Considering the smooth samples, for distilled water on Polycarbonate (Lexan®, PC), the calculated contact angle θ_{OWRK} using eq. (3.8) gives $\theta_{\text{OWRK}} \approx 79.9°$ and the OCA measurement gives $\theta_{app} \approx 79.8°$. To do these calculations $\gamma_{LV}^p = 51.00\ mN\ m^{-1}$ and $\gamma_{LV}^d = 21.80\ mN\ m^{-1}$ were used as the free surface energies of water [104] and $\gamma_{SV}^p = 6.5\ mN\ m^{-1}$ and $\gamma_{SV}^d = 27.7\ mN\ m^{-1}$ for the free surface energies of PC [105]. The contact angle θ_{OWRK} was also calculated for Plexiglas® (PMMA) and compared to the measured θ_{app} and also only shows a small deviation. Thus, the deviation between θ_{OWRK} and θ_{app} is not considered significant for the tested smooth polymeric surface samples. Additionally, the critical remarks presented in the literature [106] about the applicability of these models are not significant for the used cases. In this way, the measured apparent contact angle θ_{app} is used to identify the wetting behavior of the surface samples.

Table 3.2: Summary of the fluid properties used for the experimental parameter study at an ambient temperature of $25° \ C$.

Properties	**Distilled Water**	**Isopropanol (2-propanol)**	**references**
Density ρ $[kg \ m^{-3}]$	997.1	781.5	[107, 108]
Surface tension σ $[N \ m^{-1}]$	0.07198	0.02092	[109, 110]
Dynamic viscosity μ $[mPa \ s]$	0.8897	2.045	[111, 112]

For the micro-structured surfaces, the procedure to define and measure the contact angle is not simple, as explained by Foltyn et al. [90]. The contact angle on regularly structured surfaces ranges with a variance of several degrees up to several tens of degrees. Foltyn et al. [90] reported that the surface samples made of PC show a variance in the contact angle of $\approx 15°$ for the pillars with a square cross-section ($S2 - S4$) to $\approx 43°$ for the grooves ($S1$). Therefore, for each structured sample it was assigned a smooth "partner sample". The apparent contact angle θ_{app} was measured in the smooth "partner sample" and used to define the wettability behavior of the structured sample. As explained in Section 3.2, the wetting behavior of the surface specimens was varied by applying plasma treatments that will be described in the next subsection 3.2.4. In this way, the smooth "partner sample" will receive the same plasma treatments as the structured one. Further, since as reported in subsection 3.2.2 the micro-structured samples have to be reused, they also have to be cleaned using a cleaning procedure that will be explained in the experimental procedure, subsection 3.2.6. In this way, the same cleaning procedure will be applied both on the structured and smooth "partner" samples to keep consistency of the material properties.

3.2.4 Plasma treatments

One of the novelties of this study includes the fact that surface wettability is changed without changing the material or roughness of the target surface. Plasma treatments were applied to the polymeric surfaces to change the wetting behavior of the liquid-solid combination. To promote the wetting behavior of water on the polymeric samples, low-pressure plasma activation was used. On the other hand, to decrease the wetting behavior, by increasing the contact angle, a very thin, nanometric coating was applied to the surface using plasma polymerization. This was performed by two plasma devices of the type FEMTO, manufactured by *Diener electronic GmbH & Co KG*, shown in Fig. 3.6. In these experiments, all surface samples for one specific set of impact conditions were treated together and with some spare samples to measure the apparent contact angle θ_{app}. As explained in subsection 3.2.3, the "partner" samples were treated with the structured samples.

The influence of surface wettability on the droplet morphology has been studied and reported in the literature [54, 56, 113]. To change wettability, the researchers usually varied the surface material or applied coatings that changed the surface topography. By using plasma treatments, the surface wettability is changed without varying the surface material or the surface roughness. In the following, both plasma processes will be explained in detail.

(a) (b)

Figure 3.6: Plasma machines of the type FEMTO, manufactured by *Diener electronic GmbH & Co KG*: (a) plasma activation to promote the wetting behavior, and (b) plasma polymerization to decrease the wetting behavior.

During plasma activation, some groups of the atomic structure of the polymer are replaced by free radicals, like peroxide groups due to the oxygen inside the air. These substitutions enhance the polar part and might even decrease the dispersive part to the surface free energy [114]. If required, the resulting contact angle can even be predicted using eq. (3.8). The activation process is mainly dependent on the activation duration, the discharge current, the used gas, and the gas pressure [114]. In this case, ambient air was used at a pressure of $155 \pm 5\ \mu Pa$. This is the pressure selected since the plasma showed no major changes in distribution and strength inside the chamber in a range between $100\ \mu Pa$ and $200\ \mu Pa$. All parameters were kept constant and the duration of the activation was the only controlling parameter to obtain the different values for the apparent contact angles θ_{app}.

On the other hand, plasma polymerization forms high-molecular products from initially low-molecular substances, e.g., monomers [114]. This formation occurs in non-thermal plasma using a pressure of $\approx 10\ Pa$. The parameters of the process including generator power, pressure, mass flow of the monomer, temperature, and the process duration are fully controlled by a computer system. Perfluor-monomer was the initial low-molecular substance, which was distributed directly by the manufacturer of the plasma machines. This monomer forms a "Teflon®-like" coating which will not interfere with the optical setup. By using plasma polymerization the apparent contact angle can be increased in comparison to the untreated surfaces. The distributor affirms that well-polymerized smooth surfaces can achieve contact angles of $\approx 120°$ with water. Similar values were obtained in these experiments, then it can

be concluded that the surfaces were successfully treated.

3.2.5 Parameter Space

Table 3.3 summarizes the parameter space used in the study of single droplets impinging upon dry smooth or structured surfaces. Distilled water and isopropanol (2-propanol) were the working fluids, forming droplet diameters of $D_0 \approx 2.3 \pm 0.1\ mm$ and $D_0 \approx 1.9 \pm 0.1\ mm$, respectively. The thermophysical properties of these fluids at ambient temperature can be found in Tab. 3.2. As mentioned, two different surface materials were used, Lexan® (Polycarbonate, PC) and Plexiglas® (Poly(methyl methacrylate), PMMA). Different wetting behaviors are possible due to the plasma treatments and depending on the liquid. For distilled water, the natural apparent contact angle (untreated surface) is $\theta_{app} = 79.8°$ for PC and $\theta_{app} = 75.1°$ for PMMA. Therefore, the wettability of the surfaces can be increased by applying plasma activation. Two different increased wetting behaviors were obtained. First, the samples were fully activated, corresponding to an angle too flat to be measured, $\theta_{app} \approx 0°$. Then, performing a very short plasma activation resulted in a range of $\theta_{app} \in [25° - 40°]$, partially wettable. Contrarily, plasma polymerization is used to create an apparent contact angle larger than the natural one. The apparent contact angle of the hydrophobic surfaces ranged between $\theta_{app} \in [117° - 122°]$.

Isopropanol shows a superhygrophilic behavior for both untreated PC and PMMA surfaces, $\theta_{app} \approx 0°$. Thus, it is not possible to increase the wettability even more with plasma activation. Using plasma polymerization, the apparent contact angle increased to the range of $\theta_{app} \in [66° - 73°]$. In summary, four different wetting behaviors were obtained in the impacts with distilled water and two with isopropanol.

Continuing with the parameter space, for both liquids, four different droplet falling heights were used, resulting in four pairs of Reynolds and Weber numbers, calculated using eq. (2.1)

Table 3.3: Summary of the evaluated parameters. For each column, the indicated parameter range was investigated. The parameters which require a pre-treatment by plasma activation or polymerization are marked.

Liquid		distilled water				isopropanol (2-propanol)			
Material		PC		PMMA		PC		PMMA	
Contact angle		0° * 25° to 40° * 79.8° 117° to 122° ★		0° * 25° to 40° * 75.1° 117° to 122° ★		0° 66° to 73° ★		0° 66° to 73° ★	
Impact height		0.15	0.35	0.70	1.30	0.15	0.35	0.70	1.30
Impact conditions	Re:	4,130	6,860	9,360	12,240	1,135	1,745	**2,315**	2,955
	We:	80	205	385	665	165	400	715	1,165
Surface structure		smooth				smooth			
		surfaces: $S1 - S4$, see Tab. 3.1				surfaces: $S1 - S4$, see Tab. 3.1			
Plasma treatments		The used samples were treated by plasma activation (*) and plasma polymerization (★)							

and eq. (2.2). The surface samples are smooth or micro-structured. Four different micro-structured patterns were manufactured and are composed of grooves ($S1$) and pillars with a square cross-section ($S2 - S4$). The plasma treatments applied are also identified in Tab. 3.3. By changing all of these variables a wide range of impact parameters was obtained.

3.2.6 Experimental Procedure

The experimental procedure is similar for the smooth and structured surfaces. The major difference is the cleaning procedure of the structured samples since they cannot be trashed and have to be reused. The surfaces have to be prepared before impact. A unique pattern is cut in the outer edges of the smooth samples, whose dimensions are $2.5 \times 10^{-2} \times \ 3.0 \times 10^{-2}\ m^2$. This cut was made in order to keep always the same surface orientation since the plasma treatments were only reliably applied to one of the sides of the surface specimen. In this way, a flipped sample can be identified avoiding mistakes. The same pattern is cut on the structured samples since it helps to define the orientation for the micro-structured pattern composed of grooves $S1$. Then, the plasma treatment is applied to the surfaces if necessary. Note, that both the structured samples and the "partner" samples are treated together. After the plasma treatment, one of the samples is used to measure the apparent contact angle and define the surface wettability.

At this stage, the experiments begin. First, the surface samples are brushed to eliminate possible dust particles with *PFA Nitrogen Gun* by *Parker Hannifin Corporation* using high purity (99.999%) nitrogen. Nitrogen was chosen to avoid any influence of the gas on the polymer surface. Then, to allow the occurrence of total internal reflection for the bottom perspective, a thin film of isopropanol is deposited with a syringe onto the main glass prism, serving as a coupling medium. The isopropanol film also helps the surface sample to stay at a defined place due to the small adhesive forces of the thin liquid film. Nonetheless, it is fundamental to ensure that no air bubbles are formed between the polymer sample and the glass prism since this will affect the bottom images. Then, when the samples are placed and aligned, the cameras are set to await the trigger to start image acquisition. After that, the droplet stream is started generating a homogeneous droplet chain. When a uniform size of the droplets is achieved, a random droplet is allowed to pass the droplet barrier and falls onto the surface sample. When the droplet cuts the light barrier, a trigger signal is sent to the high-speed cameras and the recording of the droplet impact starts. For each set of experimental conditions, five experiments were made for the smooth surface samples and three for the micro-structured samples.

The structured surfaces have to be reused due to manufacturing constraints and an appropriate cleaning procedure was established. In this way, one structured sample was assigned to each wettability behavior for each fluid. Also, as mentioned, each structured sample has a smooth "partner" sample. The plasma treatments and cleaning procedure was done pairwise to preserve consistency. After droplet impact, the experimental setup is cleaned and set back to the initial state and the surface samples must also return to their original state. To do

that, the first step is to remove the impinging droplet from the micro-structured sample using the *PFA Nitrogen Gun*. Secondly, both the structured and the smooth "partner" samples are placed into a bath of liquid depending on the wetting behavior and used droplet fluid. If the droplet liquid is isopropanol, the samples were placed for about 10 minutes into an isopropanol bath. On the other hand, if the droplet liquid is distilled water and the wetting behavior is hydrophilic or superhydrophilic, the samples were flushed shortly with nitrogen and then placed into a bath of distilled water for approximately 10 minutes. This step of the cleaning procedure deactivates the surface samples before they are activated again for the following droplet impact. Finally, if the droplet liquid is distilled water and the wetting behavior is hydrophobic, the surface samples were directly placed into a bath of distilled water. To avoid interactions with the coating, isopropanol was not used since it could influence the next droplet impact experiments. It was not necessary to apply a new plasma polymerization as distilled water does not influence the coating or the non-wetting properties. Similarly to the smooth surfaces, after setting the experimental setup and surface samples to the initial state, a new droplet impact can be captured.

After finishing a set of experiments with a constant impact velocity U_0, the micro-structured samples have to be checked under the microscope to identify possible damages or irregularities. No damages were identified and the durability of the micro-structured samples was guaranteed. Regarding the plasma processes, it is very important to keep a short time between the application of the treatments and the droplet impact to avoid any influence of the environment on the wetting behavior. However, the influence of the environment on the degree of activation of the used PC and PMMA samples can be neglected for a range of several hours [115].

3.2.7 Image Processing and Evaluation

To evaluate the acquired images, a multi-step image processing routine was implemented. The images were processed in MATLAB considering three dimensions, the geometric coordinates x and y of the images and t, the coordinate representing the time. As explained in Section 3.2.1, due to the optical arrangement, the raw images of the phenomena are distorted and need to be corrected to be evaluated. Thus, this is the first step of the image processing. Each perspective is corrected separately by applying transformation matrices and bicubic interpolation, as can be seen in Fig. 3.7. The lateral and top views, which shared the same CMOS-chip, were separated before the correction procedure. The pixel size was determined for each perspective to be used in the following evaluations.

To continue the image processing, the background is subtracted and the images are binarized using the Otsu method [116]. Then, the images were filtered and cleaned. The determination of the impact frame is the first step to start the evaluation of the impact parameters by tracking the impinging droplets. The impact frame is considered the time reference point, $t = 0$. The droplet impact diameter D_0 is calculated by considering the area-equal diameter. The average droplet area A_{avg} of 10 frames before impact, corresponding to an average time

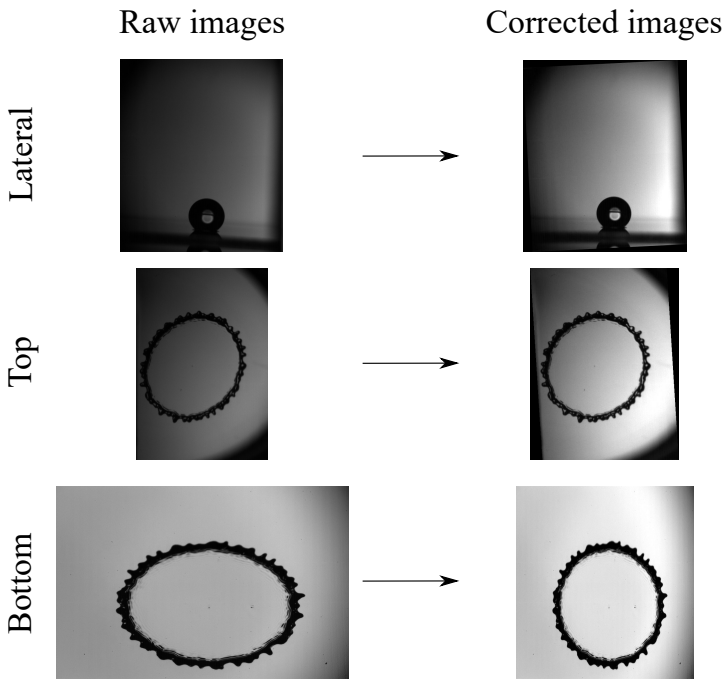

Figure 3.7: The raw images versus the corrected images for each perspective.

of $\Delta t_{avg} = 0.5\ ms$ is used to calculate the droplet diameter,

$$D_0 = \sqrt{(4A_{avg}/\pi)} \quad (3.9)$$

To calculate the droplet impact velocity U_0, the average of the same 10 images was used. By tracking the position of the droplet centroid coordinates X over time, the impact velocity U_0 can be calculated as follows,

$$U_0 = \sqrt{((X_i - X_{i-1})^2)}/(\Delta t) \quad (3.10)$$

The time Δt is the inverse of the camera frame rate ($20000\ fps$). During this study, other parameters, e.g. the spreading diameter D_{spread}, were measured from the processed images by counting the number of pixels and then multiplying them by the pixel size.

3.3 Droplet Impact onto Liquid Surfaces

In the second phase of this study, it is investigated the single droplet impact upon thin liquid films of the same liquid as the impinging droplet. Both the droplet and the liquid film are at room temperature. This study follows the findings of a previous work [70]. In this way, the application of this investigation is the implementation of biofuels in civil aviation to reduce fossil fuel consumption and pollutant emissions. Thus, mixtures of conventional jet fuel and alternative sustainable aviation fuels (SAF) were used as fluids.

In the next subsections, the experimental facility will be described and the fluids used will

be presented and their thermophysical properties defined. Then, the parameter space of this study will be characterized and the experimental procedure detailed. Finally, the image processing and evaluation to obtain the desired results will be explained.

3.3.1 Experimental Setup

To study the single droplet impact on thin liquid films of the same liquid an experimental facility was designed and built. Figure 3.8 shows a scheme of the experimental setup, which is composed of four main sections: image acquisition system, droplet dispensing system, liquid film container, and the illumination of the impact site.

The conventional angle for visualizing drop impact dynamics is from the side. The lateral perspective provides relevant information about the phenomena and enables the measurement and analysis of their features such as the crown height, diameter and angle, jet height, and the number and size of the secondary droplets. However, the lateral images do not allow a complete understanding of the phenomena, and other perspectives can also provide important knowledge. In these experiments, two viewpoints of the phenomena were captured, the common lateral perspective and also a bottom perspective. The images were acquired using a high-speed digital camera Photron FASTCAM mini UX50 and a macro lens Tokina AT-X M100 AF PRO D. The camera has 1.3 Megapixel resolution at frame rates up to $2000\ fps$ (frames per second) and up to $160000\ fps$ at reduced image resolution. The lens has a minimum focus distance of $0.3\ m$, a focal length of $100\ mm$, a macro ratio of 1:1, and a filter size of $55\ mm$. Regrettably, only one high-speed digital camera was available. Then, it is not possible to capture both perspectives simultaneously. Accordingly, the camera has to assume two different positions to acquire the lateral and the bottom perspectives, as can be seen in Fig. 3.8.

For the lateral images, the camera is placed parallel to the droplet falling plane and shadowgraphs are acquired by having backlighting. The recording of the bottom images is only possible due to the transparency of the liquid film, the liquid film container, and the glass that supports the liquid film container. Thus, the camera is placed underneath the glass that supports the liquid film container, parallel to the bottom of the container and centered with the droplet impact site, as can be also seen in Fig. 3.8. Again, shadowgraphs are acquired by using backlighting. The illumination of the impact site will be described onward. The frame rate, exposure time, and shutter time are not constant during all the experiments but they will be described ahead.

The impinging droplet is generated by a medical syringe pump NE-1000 that is connected through medical tubes to a straight-tip stainless steel needle. The pumping rate is set at $0.5\ ml/min$ to allow the droplet to fall when the gravity force exceeds the surface tension forces and to minimize oscillations on the droplet after its release. It is possible to vary the impact velocity U_0 by changing the droplet falling height. As for the droplet diameter D_0, several different needles with various inner diameters D_{in} were used, providing a fine range.

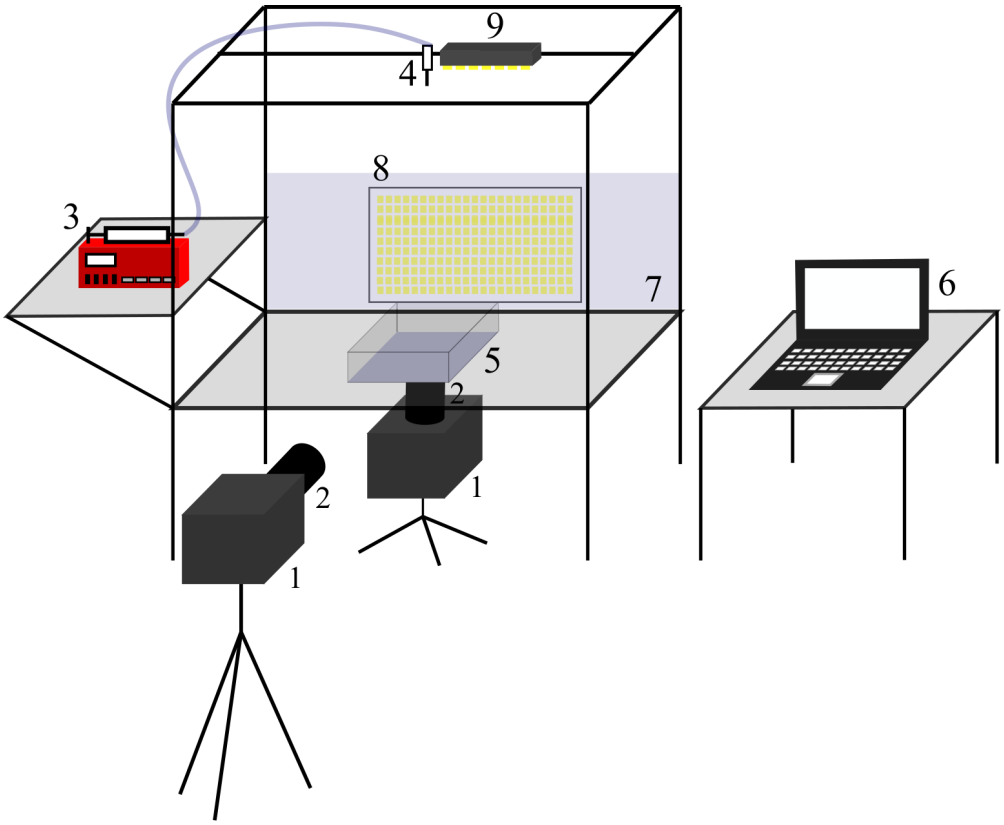

Figure 3.8: Experimental setup for single droplet impact upon thin liquid films: 1) high-speed digital camera; 2) macro lens; 3) syringe pump; 4) stainless steel dispensing needle; 5) liquid film container; 6) computer; 7) diffusion glass; 8 and 9) set of LED's.

To hold the liquid film a topless right-angled perspex container was used. The size of the container was calculated to ensure that its walls would not interfere with the phenomena. The edge length of the container is more than 50 times the maximum initial droplet diameter D_{0max}. The thickness of the liquid film h_f is defined according to the droplet initial diameter D_0. In this study, dimensionless film thicknesses $\delta_f = h_f/D_0$ between 0.1 and 1 were tested. A glass supports the liquid film container and due to the transparency of both the glass and the perspex of the container, it is possible to capture the bottom perspective.

Finally, the illumination of the impact site is vital to improve the quality of the images. Sets of LEDs connected to a power supply were the only light source in the room. Due to the two different perspectives, two different light sources were needed. For the lateral perspective, the light is parallel to the droplet falling plane and in front of the high-speed digital camera, providing backlighting. Additionally, a diffusion glass was put between the LEDs and the impact site to ensure the uniformization of the backlight source for visualization purposes. For the second perspective, due to the glass transparency, the Perspex, and the liquid film, the camera captured the shadowgraph images of the droplet impact from below using a light next to the dispensing needle, which works as a backlighting source. In this case, it is not possible to use a diffuse glass due to the experimental facility constraints.

3.3.2 Fluids

As mentioned before, this part of the study follows a previous work focused on the implementation of alternative fuels in civil aviation [70]. Therefore, mixtures with conventional jet fuel and alternative sustainable aviation fuels were used as working fluids. Nowadays, the legislation allows the use of fuel mixtures with at least 50% in volume of conventional jet fuel [117, 118]. Thus, Jet A-1 was selected as conventional jet fuel and NExBTL (Neste Renewable Diesel) as the alternative sustainable fuel. NExBTL is a type of HVO - Hydroprocessed vegetable oil. Considering this, the fluids used in the experiments are 100% Jet A-1, a mixture with 75% in volume of Jet A-1 and 25% of NExBTL, and a mixture with 50% in volume of Jet A-1 and 50% of NExBTL. Additionally, distilled water was also used as a reference fluid.

The physical properties of the fuels used were measured to increase the precision of the study (density ρ, surface tension σ, and dynamic viscosity μ) and their values can be seen in Tab. 3.4. The density ρ was measured using the pycnometer method, which is very precise and can be applied either to solids or liquids. The fluid density is calculated using:

$$\rho = \frac{(m_s - m_p)}{V_p} \quad (3.11)$$

where m_s is the mass of the pycnometer full with the substance, m_p is the mass of the empty pycnometer, and V_p is the volume of the pycnometer. The masses were measured with a Mettler Toledo PB303 DeltaRange precision balance with an error of $\pm 0.01\ g$. The surface tension σ was measured using the pendant droplet method using the Data Physics - OCAH200 with an accuracy of $0.6\ \%$. Finally, the dynamic viscosity μ was obtained using a Brookfield DV3TRVCP rheometer. More details about these measurements can be found in Ribeiro [70].

From Tab. 3.4, it is possible to conclude that both the density and the surface tension of the three fuels are similar. The major difference is related to the dynamic viscosity values. 100% jet fuel presents the lowest dynamic viscosity. However, in the mixtures, the dynamic viscosity increases while increasing the volume of HVO. The physical properties of distilled water were gathered from the literature and can also be found in Tab. 3.4.

Table 3.4: Physical properties of the fluids: density ρ, surface tension σ, and dynamic viscosity μ.

Substances	ρ [kg/m^3]	$\sigma \cdot 10^3$ [N/m]	$\mu \cdot 10^3$ [Pa·s]
H_2O (literature)	1000	72.0	1.00
100% Jet Fuel (JF)	798.3	25.4	1.12
75% JF - 25% HVO	794.9	25.5	1.44
50% JF - 50% HVO	792.3	24.6	1.79

3.3.3 Parameter Space

In this section, the parameter space defined for the experiments of a single droplet impinging upon thin liquid films will be defined. This part of the work is divided into two separate parts. First, the data acquired in a previous work [70] is used and the accuracy of spread/splash

thresholds presented in the literature is investigated. Secondly, a new experimental study is conducted to study in detail the phenomenon of bubble encapsulation.

The experimental conditions of the previous work will be presented here to simplify the understanding of the study. However, they are presented in detail in Ribeiro [70]. Four different fluids were used, the three fuels and distilled water. The initial diameter of the droplets D_0 was varied by using dispensing needles with five different inner diameters D_{in}. Table 3.5 shows the droplet initial diameter D_0 for each fluid depending on the inner diameter of the dispensing needle D_{in}.

The droplet initial diameters were measured to produce the liquid films since their thickness is based on it, $\delta_f = h_f/D_0$. For this study, the dimensionless liquid film thicknesses selected are $\delta_f = 0.1$, $\delta_f = 0.5$, and $\delta_f = 1.0$. Ahead, the process to produce the liquid films will be explained in detail. However, it is important to point out that it was not possible to produce the thinner liquid films for distilled water due to its high contact angle with the perspex surface. Therefore, in the impacts with distilled water, instead of having $\delta_f = 0.1$, the liquid film thickness is the smallest one that allows the production of a uniform liquid film. Therefore, Tab. 3.6 shows the thinner thickness that was possible to produce depending on the droplet initial diameter D_0 to study the impacts of distilled water.

To vary the impact energy of the droplets, the droplet impact velocity U_0 was changed by modifying the droplet falling height. Three different falling heights were tested ($z_1 = 0.175\,m$, $z_2 = 0.5\,m$, and $z_3 = 1.0\,m$). Table 3.7 shows the droplet impact velocity depending on the droplet falling height and initial droplet diameter D_0.

Using these experimental conditions resulted in the range of dimensionless numbers described in Tab. 3.8. The hydrodynamic phenomena obtained for this parameter space are

Table 3.5: Droplet diameters in the experiments of Ribeiro [70].

D_{in} [mm]	D_0 [mm]			
	H_2O	100%JF	75%JF/25%HVO	50%JF/50%HVO
1.50	4.03	3.04	3.05	3.06
0.84	3.61	2.76	2.77	2.78
0.51	3.23	2.44	2.47	2.47
0.25	2.80	2.07	2.12	2.18
0.10	2.27	1.73	1.74	1.78

Table 3.6: The dimensionless thickness of the thinner liquid films for distilled water.

D_0 [mm]	δ_f
4.03	0.22
3.61	0.24
3.23	0.27
2.80	0.31
2.27	0.39

Table 3.7: Droplet impact Velocities.

z [m]	**D_{in} [mm]**	**U_0 [m/s]**			
		H_2O	**100% JF**	**75% JF / 25% HVO**	**50% JF / 50% HVO**
$z_1 = 0.175$	1.50	1.83	1.80	1.80	1.81
	0.84	1.83	1.80	1.80	1.80
	0.51	1.82	1.79	1.79	1.80
	0.25	1.81	1.79	1.79	1.79
	0.10	1.81	1.79	1.78	1.79
$z_2 = 0.5$	1.50	3.07	2.97	2.99	3.00
	0.84	3.05	2.96	2.97	2.97
	0.51	3.04	2.93	2.94	2.95
	0.25	3.02	2.90	2.93	2.93
	0.10	2.96	2.88	2.90	2.91
$z_3 = 1$	1.50	4.21	4.05	4.06	4.06
	0.84	4.18	4.00	4.00	4.00
	0.51	4.15	3.95	3.96	3.96
	0.25	4.09	3.83	3.86	3.89
	0.10	3.98	3.68	3.68	3.78

detailed in Ribeiro [70]. In this study, the experimental conditions that resulted in spreading or splashing are compared to spreading/splashing thresholds presented in the literature to assess their universality.

The second part of the experimental study of single droplet impact upon thin liquid films is focused on a rather observed phenomenon called bubble encapsulation. The main goal of this section is to obtain experimental conditions that guarantee 100% occurrence of bubble encapsulation and study this phenomenon in more detail. To achieve this goal a range of experimental conditions were tested. The starting point was the condition where bubble encapsulation was found in the study of Ribeiro [70]. Then, the droplet impact diameter D_0, the impact velocity U_0 and the fluids were varied to observe where bubble encapsulation can be found.

The droplet's initial diameter D_0 varied by changing the inner diameter of the dispensing needle ($2.6 < D_0 < 3.1$ mm). Also, the impact velocity U_0 varied by changing the droplet falling height, providing impact velocities between 3.9 and 4.8 m/s. Only thin liquid films were considered in this study. Thus, the dimensionless thickness of the liquid film δ_f varied between $0.1 < \delta_f < 1.0$. Considering these thin thicknesses, bubble encapsulation was never observed on the droplet impact with distilled water. Therefore, only the three fuel-based fluids were considered. The usual dimensionless numbers that characterize the impact are the Weber number describing the ratio between the inertial and surface tension forces, $We_D = \rho U_0^2 D_0/\sigma$, and the Reynolds number as the ratio between the inertial and viscous forces, $Re_D = \rho U_0 D_0/\mu$. In this study, the Weber numbers varied between $1452 < We_D < 2180$ and the Reynolds numbers between $5659 < Re_D < 8358$, as shown in Tab. 3.8, where all impact conditions are detailed. Using this experimental facility and the impact conditions described above the phenomenon of bubble encapsulation was observed

Table 3.8: Summary of the evaluated parameters on the investigation of bubble encapsulation.

Liquid	**100% JF**	**75% JF - 25% HVO**	**50% JF - 50% HVO**
Material	Perspex		
Contact Angle	$\approx 0^{\circ}$		
δ_f	$0.1 - 1.0$		
$\mathbf{D_0}$ [mm]	$1.7 - 3.1$		
$\mathbf{U_0}$ [m/s]	$1.8 - 4.1$		
$\mathbf{Re_D}$	$5659 - 8358$		
$\mathbf{We_D}$	$1452 - 2180$		
La	$27987 - 288101$		
$\mathbf{Oh \cdot 10^3}$	$1.863 - 9.593$		

both from the side and from below and the perturbations imposed on the liquid film by the impact and crown collapse were analyzed, as well as the crown sheet angle before crown closure.

3.3.4 Experimental Procedure

In these experiments, a strict experimental procedure was followed. Taking into account that two separate perspectives were captured, there are also two different procedures regarding image acquisition. The first step of the experimental procedure concerns fluid preparation. Three different fluids were used and 100% Jet A-1 is ready to be tested. However, it is necessary to prepare the two fuel mixtures. The mixtures were prepared by volume and placed into a glass container to avoid possible interactions between the fluids and the container. A volumetric pipette was used to measure the volumes of fluid for the mixtures. The mixtures were prepared right before impact and were only kept for a few days to guarantee their quality.

The second step concerns the preparation of the droplet dispensing system. A glass syringe with $50\ mL$ is filled with the respective fluid as well as the medical tubes that connect to the dispensing needle, avoiding air bubbles. Before filling the dispensing system with fluid, the dispensing needle's inner diameter is selected and placed in its position. The pumping rate was varied and tested in order to discover which pumping rate would allow the creation of a uniform stream of droplets with a constant size but at the same time allow the droplet to detach when the gravity force exceeds the surface tension forces. After this study, the pumping rate was set to $0.5\ mL/min$.

The third step is to generate the liquid film. The dimensionless liquid film thickness δ_f is the ratio between the liquid film thickness h_f and the droplet initial diameter D_0, $\delta_f = h_f/D_0$. In these experiments, different dimensionless film thicknesses were considered, ranging between $\delta_f = 0.1$ and $\delta_f = 1.0$. These liquid films were produced by volume. The container has dimensions of $20 \times 20\ cm^2$ and right-angled edges. Thus, the volume of fluid necessary to have a specific thickness was calculated and inserted inside the container. Finally, the thick-

ness is confirmed by using the high-speed digital camera to acquire an image of the liquid film and measure its thickness through image processing, a process detailed in subsection 3.3.5. Producing such thin liquid films is difficult if the apparent contact angle (θ_{app}) between the fluid and the surface is considerably high. However, in this case, the jet fuel and the two mixtures show a superhygrophilic behavior with the perspex surface, $\theta_{app} \approx 0^{\circ}$ (see Tab. 3.8). This superhygrophilic behavior allows the production of very thin liquid films, $100\ \mu m$. In this study, at least 10 experiments were made for each set of experimental conditions. Thus, it was necessary to guarantee that these droplets would not affect the thickness of the liquid film. A study was developed and it was concluded that these 10 droplets will not change the thickness of the liquid film in more than 1%. Therefore, it was assumed that all 10 experiments were made using the same liquid film. The liquid film is exchanged after a set of experiments with the same experimental conditions.

When the droplet dispensing system and the liquid film are ready to be used, it is time to set the experimental conditions and start the experiments and the image acquisition. The droplet falling height is selected and the illumination is turned on. An important step of the experimental procedure is to record an image with a reference that enables the measurement of the pixel size. For the lateral images, a needle with a known diameter was placed at the droplet impact point. Through its diameter, the pixel size can be calculated. For the bottom images, a cylindrical tube with a known diameter was placed within the liquid film. Once more, its diameter was used to calculate the pixel size.

After recording this reference frame to establish the pixel size, the camera is set to record, awaiting the triggering signal. Then, the droplet dispensing system is activated and a chain of droplets is generated. A droplet is randomly selected to pass the barrier and impact the liquid film. The camera is manually triggered and the droplet impact is recorded by the high-speed digital camera. The majority of the experiments were recorded at $2000\ fps$, but there are also some cases recorded at $4000\ fps$. The images were saved on the computer and without changing anything in the setup, a new droplet impact is recorded following the procedure explained before. After the recording of 10 droplet impacts, the experiments for a set of impact conditions are concluded.

To start a new set of tests the setup has to be reset to its initial state. To do that, the liquid film is removed from the container, and the container is washed. After the wash, the container is dried and a new liquid film can be produced. Finally, the setup returns to its original state, and the experimental procedure can be followed again for a new set of experimental conditions.

3.3.5 Image Processing and Evaluation

From the raw images acquired by the high-speed digital camera, it is possible to identify the phenomena obtained and their main characteristics. However, these images have to be processed and evaluated to do a quantitative analysis of the phenomena. In this study, first,

the droplet's initial diameter D_0 and impact velocity U_0 have to be confirmed to calculate the dimensionless numbers that govern the impact, namely the Reynolds, Weber, and Ohnesorge numbers. An image processing routine was followed to measure these values and other important features of the phenomena like crown height, diameter, and angle.

As mentioned previously, a frame containing a reference was taken before each set of experiments. This frame is processed in Matlab to find the value of the pixel size. To do that, a needle with a defined outer diameter was used as a reference. Figure 3.9 (a) shows the raw image of the reference. The grayscale image is binarized using an algorithm written in the software Matlab. Figure 3.9 (b) shows the binarized image with only black and white pixels. At the top of the image, the outer diameter of the needle is well-defined. The treated image is then cut and 10 rows were selected to confirm that the needle is aligned with the vertical axis. Figure 3.9 (c) shows a $2x$ magnification of the cut image. Following, the difference between the two white pixels in the same row gives the outer diameter of the needle in pixels. The pixel size is determined by dividing the outer diameter value in mm by the number of pixels. Contrarily to the images from the single droplet impact upon dry smooth and micro-structured surfaces, no distortion is present in these images. The length scale resolution can vary between experiments, requiring proper calibration, but the average result is $34.6 \pm 0.2\ \mu m/pixel$.

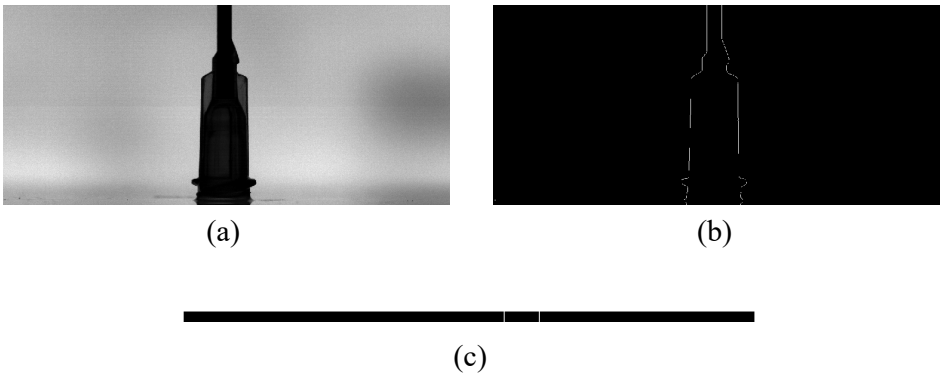

Figure 3.9: Image processing to determine the pixel size: (a) raw image; (b) binarized image; (c) measurement of the outer diameter of the needle ($2x$ magnification).

A similar image processing was applied to measure the features of droplet impact. To measure the droplet initial diameter D_0 and the droplet impact velocity U_0, the droplet shape that resulted from the binarized image was filled to create a white circular area. To measure the droplet initial diameter D_0, all images containing the falling droplet before impact were considered. Using the *regionprops* function of Matlab, the area, major axis, minor axis, and centroid of the droplet were calculated. The sphericity of the droplet was evaluated by using the major and minor axis values. Through the evaluation of these values, the droplet is considered spherical across all the experiments of single droplet impact upon thin liquid films. The droplet initial diameter D_0 is calculated considering the area-equal diameter, as explained in subsection 3.2.7. The average of all images before impact was considered to determine the droplet diameter D_0.

To calculate the droplet impact velocity U_0, the centroid position of two sequential images separated by 10 frames was considered. The vertical distance between the two centroid positions was measured and divided by the time between the two frames. The average of 10 impacts was considered to define the droplet impact velocity U_0.

To calculate the bubble height h_B and diameter D_B, the same image processing routine was used. The bubble was isolated from the image and the height and diameter were measured by counting the pixels and then multiplying them by the pixel size.

Finally, a different process was used to measure the crown sheet angle. It was complicated to develop an algorithm in Matlab to measure the crown sheet angle since due to the liquid film oscillation, the angle measurement keeps assuming the wrong line as the liquid film line. Therefore, due to the necessity of verifying every measurement made with the Matlab algorithm, it was decided to measure the crown sheet angle using the software ImageJ. In this software, the liquid film line can be defined manually by the user, and that simplifies the measurement.

3.4 Droplet Impact onto Heated Dry Surfaces

In the third and last part of this study, it is investigated the single droplet impact upon heated dry surfaces. The droplet is at room temperature but the surface is heated by a heating device. The application of this part of the study is also focused on the possible implementation of biofuels in civil aviation to reduce the consumption of fossil fuels and reduce pollutant emissions. In this thesis, the physical and chemical processes related to fuel injection in internal combustion engines were separated and this study starts with the physical processes: the atomization and the impact. However, it follows the evaporation component and finally the chemical reaction. This is the reason to include heat while studying the impact and atomization of single droplets. Thus, once again, mixtures of conventional jet fuel and alternative sustainable aviation fuels (SAF) were used as fluids.

In the following subsections, the experimental setup will be described. The fluids and their thermophysical properties will be presented. Then, the parameter space will be explained as well as the experimental procedure. Finally, the image processing and evaluation will be explained.

3.4.1 Experimental setup

The experimental study of single droplets impinging on heated surfaces demands an experimental setup with a powerful heating device. A scheme of the experimental facility is present in Fig. 3.10. It is composed of four main sections: the image acquisition system, the droplet dispensing unit, the heating system of the impact surface, and the illumination of the impact site.

To visualize the phenomena, a high-speed digital camera Photron FASTCAM mini UX50, and a macro lens Tokina AT-X M100 AF PRO D were used. The camera has a 1.3 Megapixel resolution at frame rates up to 2000 fps (frames per second) and at reduced image resolution for frame rates up to 160000 fps. The lens has a minimum focus distance of $0.3\ m$, a focal length of $100\ mm$, a macro ratio of $1:1$, and a filter size of $55\ mm$. To capture the phenomena two different perspectives were captured with the high-speed camera, a lateral perspective and another perspective with a camera inclination of $\approx 20°$. The images were acquired at $4000\ fps$ and a shutter time of $1/10000\ s$. The high-speed digital camera only captures the phenomena for a few seconds. However, that is not enough to capture the entire lifetime of the droplet. A different digital camera with a lower frame rate was also used in these experiments but only to capture the duration of the droplet lifetime.

The droplet dispensing system is composed of a medical syringe pump NE-1000 connected to a straight-tip stainless steel needle. The operational capacity of the syringe pump ranges between $1.49\ \mu l/h$ for a $1\ ml$ syringe and $127.2\ ml/min$ for a $60\ ml$ syringe. In this study, a glass syringe of $50\ ml$ was used to avoid any chemical interactions with the fluids. A medical tube connected the glass syringe to the stainless steel needle. A low pumping rate, of $0.5\ ml/min$, was set to guarantee the droplet leaves the needle when gravity exceeds the surface tension forces. The syringe pump can be controlled manually or can be connected and operated through a computer. In these experiments, the inner diameter of the dispensing needle was kept constant $D_{in} = 1.2\ mm$ for all fluids.

The focus of this experimental setup is the heating system of the impact surface. For this

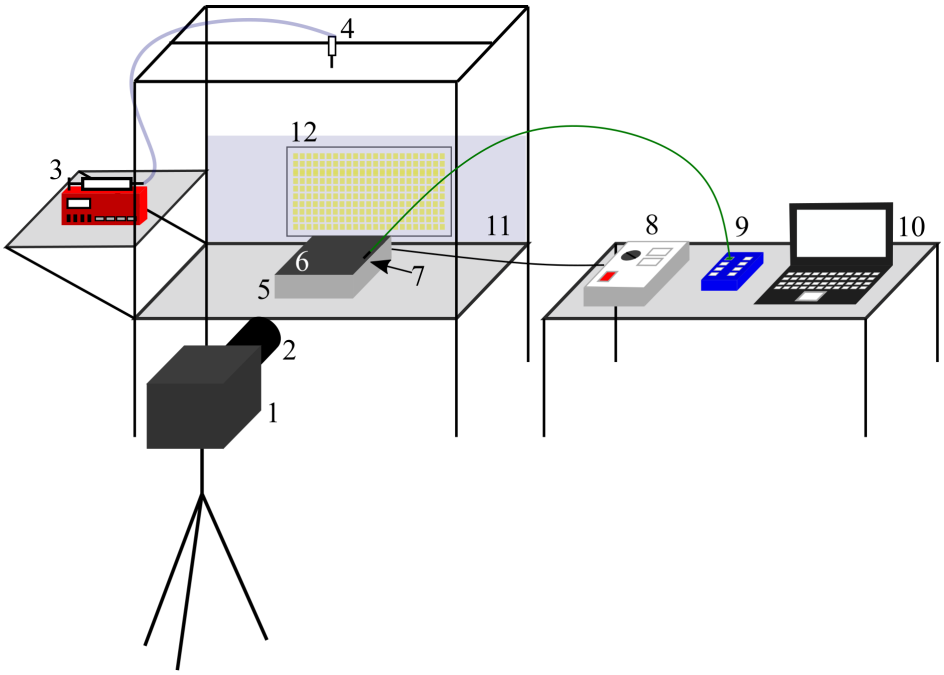

Figure 3.10: Experimental facility: 1) high-speed digital camera; 2) macro lens; 3) syringe pump; 4) straight tip needle; 5) heating device; 6) stainless-steel impact surface; 7) type-K thermocouple; 8) controller of the heating device; 9) data logger; 10) computer; 11) difussion glass; 12) set of LEDs.

purpose, an aluminum 5083 block was manufactured with 15x15x5 cm^3. Aluminum 5083 was chosen due to its high thermal conductivity. This aluminum block shown in Fig. 3.11 has four cartridge heaters of 250 W equally spaced to provide evenly distributed heat to the impact surface. This block also has an embedded type-K thermocouple which is connected to the heating device controller. On the controller, it is possible to define the aluminum block temperature in a range from $0 - 500°$ C.

The impact surface is a stainless-steel plate with the same size as the heating device 15x15 cm^2 and a thickness of 0.5 mm. This plate is placed above the aluminum block and fixed with screw clamps. The clamps are necessary since at high surface temperatures T_w the plate edges detach from the aluminum block. This detachment reduces the surface contact between the heating device and the surface, decreasing the heat conduction, and therefore, decreasing the stainless-steel plate temperature.

The heating device was tested before starting the experiments. Two type-K thermocouples, connected to the data logger, were placed on the stainless-steel plate. One is right in the middle since it is the place where the droplet will impinge, and the other is on the side, as represented in Fig. 3.11. Considering the room temperature as a starting point, $T_w = 20° C$, the temperature was increased at the controller in intervals of $20° C$ until $T_w = 300° C$. The procedure to test the heat transfer between the aluminum block and the stainless steel plate will be described in the following.

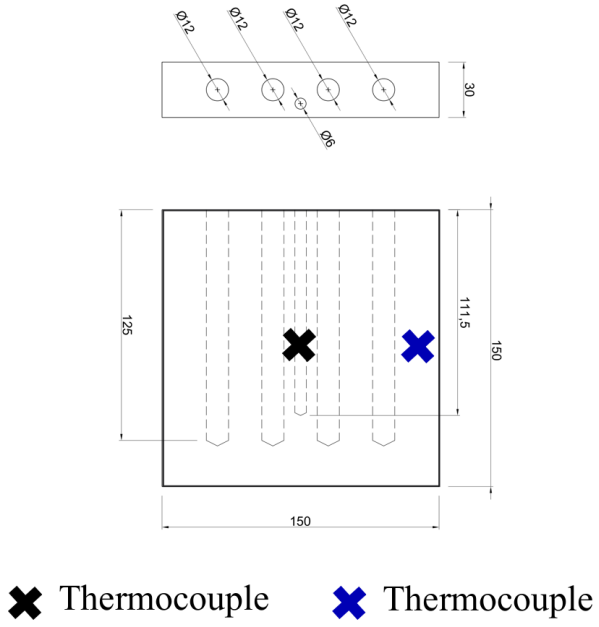

Figure 3.11: Heating device with four embedded cartridge heaters of 250 W equally spaced and a type-K thermocouple in the middle. The black and blue crosses represent the position of the type-K thermocouples used to measure the surface temperature at the stainless-steel plate.

First, the required temperature is set at the controller. Then, the temperature is acquired for 30 minutes which is more than enough to obtain a constant temperature at the stainless steel

plate. The surface temperature T_w measured in the center of the place corresponds to the same temperature measured by the type-K thermocouple embedded in the aluminum block. There are no significant thermal losses due to the high thermal conductivity of aluminum and stainless steel. On the other hand, the type-K thermocouple placed on the border of the plate measures a lower temperature than the thermocouple in the center. However, the maximum temperature deviation is $14°\ C$ for a surface temperature of $T_w = 300°\ C$ in the center of the plate. These results were evaluated and the thermocouple in the border of the plate was kept to supervise possible malfunctions in the heating device during the experiments since the thermocouple in the center has to be removed to enable the droplet impact. The position of this thermocouple can also be seen in Fig. 3.10.

Finally, the description of the illumination of the impact site. The room is kept dark and the only light source in the room is a set of LEDs connected to a power supply. As can be seen in Fig. 3.10, a diffusion glass was placed between the light source and the impact location.

3.4.2 Fluids

To study the differences in the heating regimes depending on the thermophysical properties of the fluids with the goal of implementing sustainable aviation fuels (SAF) in civil aviation, different fuel mixtures were used. The mixtures have to be composed of at least 50% in volume of conventional jet fuel, as demanded by the current legislation, and a biofuel to decrease the consumption of petroleum-based fuels and to reduce pollutant emissions [117, 118]. Four different fluids were used: 100% Jet A-1 (JF), 100% NExBTL (HVO), a mixture with 50% in volume of Jet A-1 and 50% of NExBTL, and distilled water, as a reference. Jet A-1 is a conventional jet fuel widely used in the civil aviation sector and NExBTL is Neste Renewable Diesel, a type of HVO (Hydroprocessed Vegetable Oil). Civil aviation only allows fuel blends with at least 50% in volume of conventional jet fuel [117, 118] and that is why the blend with 50% of each type of fuel was chosen.

The fluid thermophysical properties, density, surface tension, and viscosity at $20°\ C$ are presented in Tab. 3.9, as well, as the final boiling point. The values of these properties were given by previous studies and by the fuel suppliers [70, 119]. For the $50\%/50\%$ fuel blend, the final boiling point value is not available, and unfortunately, it was not possible to measure its value during the development of this study.

Table 3.9: Thermophysical properties of the fluids.

Substances	ρ [kg/m^3]	$\sigma \cdot 10^3$ [N/m]	$\mu \cdot 10^3$ [Pa·s]	Final Boiling Point [$°C$]
H_2O (literature)	1000	72.0	1.00	100
100% Jet Fuel (JF)	798.3	25.4	1.12	237
50% JF - 50% HVO	792.3	24.6	1.79	-
100% HVO	785.2	26.6	3.40	300

3.4.3 Parameter Space

A significant parameter space was experimentally tested to study single droplet impact upon heated dry surfaces. As described in subsection 3.4.2, four different fluids were used: 100% Jet A-1 (JF), 100% NExBTL (HVO), a mixture with 50% in volume of Jet A-1 and 50% of NExBTL, and distilled water. Stainless steel was the only surface material tested in these experiments. The aluminum block can achieve $500°\ C$, but for these experiments, the surface temperature was only varied between $20 - 300°\ C$. The inner diameter of the dispensing needle was kept constant at $D_{in} = 1.2\ mm$ during the entire experimental campaign, which originated droplet initial diameters of $D_0 = 2.8 - 3.8\ mm$. The impact velocity U_0 was altered by changing the droplet falling height. Two different droplet falling heights were tested, which resulted in impact velocities of $U_0 = 1.7 - 3.2\ m/s$. The Weber We and Reynolds Re numbers are important influencing parameters. Considering all parameters mentioned, the dimensionless numbers obtained are $174 < We < 955$ and $1099 < Re < 12365$. The entire parameter space is described in Tab. 3.10.

Table 3.10: Summary of the parameters used in this study: wall temperature T_w, droplet initial diameter D_0, impact velocity U_0, Weber number We, and Reynolds number Re.

Liquid	100% JF	50% JF - 50% HVO	100% HVO	Water
Material	Stainless steel			
T_w [$°\ C$]	$20 - 300$			
D_0 [mm]	$2.8 - 3.8$			
U_0 [m/s]	$1.7 - 3.2$			
We	$174 - 955$			
Re	$1099 - 12365$			

3.4.4 Experimental Procedure

A strict experimental procedure was defined to perform the experiments of single droplet impact upon heated dry surfaces. To start the tests, the experimental rig has to be prepared. The first step is to clean the stainless steel plate, ensuring that no dust particles remain on the surface since they can affect the impact dynamics. As mentioned in subsection 3.4.1, the thin stainless steel plate is attached to the aluminum block using four clamps, one in each vertex. In the meanwhile, a $50\ ml$ glass syringe is filled with the fluid to be tested and placed in the syringe pump. Then, it is connected to the medical tubes that will take the liquid to the dispensing needle. The dispensing needle is placed at the droplet falling height selected for the experiment. The fluid will be pumped through the dispensing system at a high frame rate to fill the tubes avoiding possible air bubbles. After the liquid film reaches the dispensing needle, the pumping rate will be set at $0.5\ ml/min$ and the dispensing system is now ready to perform the experiments.

Before starting the image acquisition is necessary to take an image of a reference to measure the pixel size. Therefore, the illumination system is turned on and the lights of the room are turned off. The reference needle is placed at the droplet impact point and an image is

taken by the high-speed digital camera, which is parallel to the droplet falling plane. All measurements are made from the lateral images and not from the images captured with an angle. In such a manner, any distortion is avoided in the image evaluation. The reference is removed from the stainless steel plate and the surface must be cleaned again to assure that no dirt or dust remains on the surface. After that step, the setup is ready to start the experiments.

To study single droplet impact upon heated dry surfaces, the surface temperature T_w has to be constant and well-defined. The first step of each experiment is to set the temperature of the aluminum block at the heating device controller and wait 30 minutes to ensure that the stainless steel plate has a constant surface temperature. The time interval of 30 minutes was established during the evaluation of heat transfer between the heating device and the impact surface described in subsection 3.4.1.

After this time, the temperature of the impact surface is considered constant and the experiments can start. The high-speed camera is set to record awaiting the signal from the trigger. The second digital camera with a low frame rate is also set to record, to measure the droplet lifetime. The droplet dispensing system is started and the droplet is chosen to pass the barrier and impact the heated dry surface. The trigger is activated and the images are acquired and saved on the computer. This process is repeated 10 times for each set of experimental conditions. After 10 impacts, it is time to tilt the camera with an angle and record 10 more impacts. After that, the experiments for a set of experimental conditions are finished. The experimental procedure can now be followed again to perform new experiments.

3.4.5 Image Processing and Evaluation

The images acquired in the study of single droplet impact upon heated dry surfaces are fundamental to identify the phenomena obtained and doing a qualitative analysis. However, similar to the other studies reported in this thesis, these raw images have to be processed to perform a quantitative analysis of the phenomena obtained. The image processing and evaluation followed with these raw images are the same as explained in subsection 3.3.5.

First, the droplet initial diameter D_0 and impact velocity U_0 have to be measured to allow the calculation of the dimensionless numbers that govern the impact dynamics, namely the Weber We and Reynolds Re numbers. Due to the similarities between the raw images acquired during single droplet impact upon thin liquid films and single droplet impact upon heated dry surfaces, the same Matlab algorithms were used to do the quantitative analysis. The details regarding the image processing routine can be seen in subsection 3.3.4.

Chapter 4

Results and Discussion

4.1 Introduction

In this chapter, the results of the experimental studies developed under the scope of this thesis will be presented, evaluated, and discussed. Similar to the previous chapter, where the experimental methodology is described, chapter 3, this chapter will also be divided into three main sections. First, the results of the experiments of single droplet impact upon smooth and micro-structured dry surfaces with variable wettability. Secondly, the results of the experiments of single droplet impact upon liquid films. Finally, the results of single droplet impact upon smooth heated dry surfaces.

4.2 Droplet Impact onto Dry Surfaces

Droplet impact upon dry surfaces has been widely studied and reported in the literature. This type of study has multiple applications in several areas, as described in subsection 2.2.1. In this thesis, single droplet impact upon smooth and micro-structured dry surfaces with variable wettability was studied to be used for aeronautical applications. First, there is an increasing demand for applications in need of self-cleaning mechanisms, which extends the search for water-repellent hydrophobic surfaces with induced roughness. Understanding the small-scale interface phenomena on the wetting behavior is essential to designing efficient hydrophobic materials with defined topography. On the other hand, the spreading behavior concerning the formation of thin films on a surface is required to ensure the quality of spray cooling and coatings.

In this study, the wettability behavior of the samples was changed by applying plasma treatments, and the roughness of the surfaces was varied by using smooth and micro-structured samples. In this way, this section is divided into the results of droplet impact onto smooth surfaces and droplet impact onto micro-structured surfaces.

4.2.1 Droplet impact onto smooth Surfaces

The first results to be described and analyzed will be the ones from single droplet impact upon dry smooth surfaces. As described in subsection 3.2.5, a wide parameter space was tested. Within this parameter space, several outcomes were identified. In this subsection, these results will be detailed. First, the obtained outcomes will be compared with deposition/splashing boundaries available in the literature. Then, the spreading behavior will be

evaluated, and finally, the impact morphologies will be described in detail.

4.2.1.1 Deposition/splashing boundary

In this experimental study, droplet impact upon dry smooth surfaces was tested for four different impact energies to assess the influence of impact energy on the morphology of the phenomena obtained. Additionally, the wettability of the surface samples was varied, providing four different wettability behaviors for distilled water and two for isopropanol. This wide range of impact conditions provides the possibility to establish a comparison between the different cases.

Considering the entire parameter space three main phenomena were identified: deposition, splashing, and rebound. In Fig. 4.1 a regime map shows the occurrence of each phenomenon depending on the Reynolds number Re, the Weber number We, and the apparent contact angle θ_{app}. Deposition is represented by the blue circles, rebound by the orange triangles, and splash by the yellow squares. The left part of the graphic shows the impacts of isopropanol droplets, and the right part shows the impacts of distilled water droplets. It is important to mention that the splashing regime includes both the prompt and crown splash phenomena and rebound comprises both the partial and complete rebound. These results were compared with empirical correlations presented in the literature to analyze their agreement with them. Therefore, different deposition/splashing limits were considered.

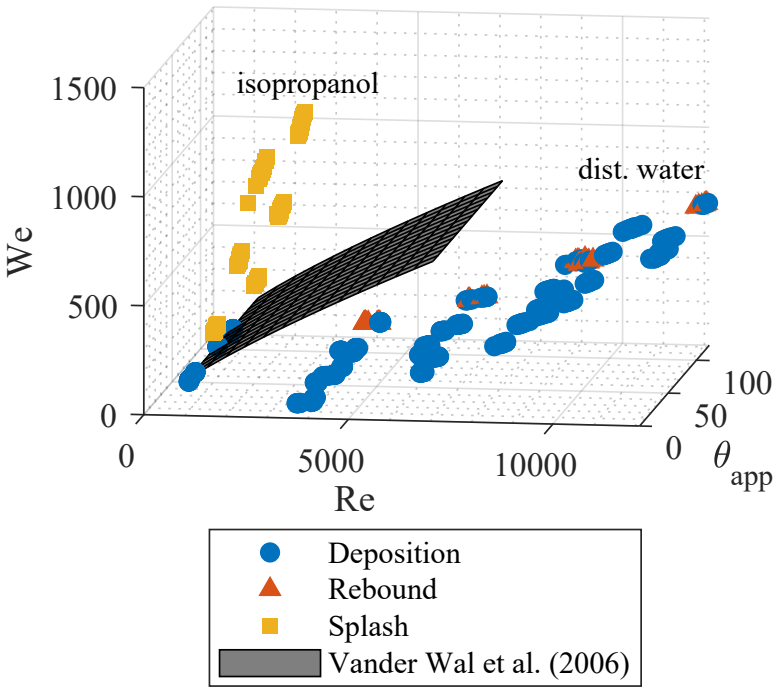

Figure 4.1: Regime map including all experiments onto dry smooth surfaces and the morphology of their outcomes, deposition, splashing, and rebound, depending on the Weber number We, the Reynolds number Re, and the apparent contact angle θ_{app}. Additionally, it presents the deposition/splashing limit defined by Vander Wal et al. [40] for droplet impact onto dry smooth surfaces.

Subsection 2.3.1 describes several deposition/splashing boundaries proposed in the literature for single droplet impact upon dry surfaces. Therefore, a selection of the criteria that may fit these experiments was made and compared to the present data. Two of the most well-known criteria presented in the literature, the criterion developed by Bai and Gosman [80] and the criterion developed by Mundo et al. [120] could not be applied since the parameter space of the present study is out of their validity range. On the other hand, the empirical correlation proposed by Vander Wal et al. [40] for single droplet impact onto dry surfaces with a mean surface roughness of $R_a = 10\ nm$ has a validity range of $0 < Re < 7500$, which fits the majority of the present study results. Their deposition/splashing boundary is defined in the following equation:

$$K_c = OhRe^{0.609} = 0.85 \quad (4.1)$$

Vander Wal et al. [40] did a very detailed study with a wide range of fluid physical properties. Several fluids were used, alkanes, alcohols, deionized water, and glycerol-water solutions. In addition, the impact surface was a dry aluminum plate with a full wettable behavior for the hydrocarbon fluids. However, water forms an apparent contact angle of $\theta_{app} = 30°$. Due to their validity range and also due to the quite similar impact conditions, this correlation was chosen to be compared with the results. Thus, the grey plane in Fig. 4.1 shows the Vander Wal et al. [40] deposition/splashing boundary, which is independent of the apparent contact angle θ_{app}. It is possible to conclude that this correlation fits the experimental results. Some exceptions include the isopropanol impacts at the lowest impact velocity, where only the deposition regime is observed. However, these events are very close to the boundary which distinguishes both regimes, consequently, the experimental parameters shall be near to the splashing regime.

In summary, the Vander Wal et al. [40] deposition/splashing threshold is adequate for the parameter space of this study and predicts accurately the onsets of deposition and splashing. The splashing limit is not influenced by the wettability behavior since the onset of splash formation takes place during a fast spreading rate. Therefore, the dynamic contact angle can be considered $\approx 180°$ by virtue of the high spreading velocity [49, 48]. Contrarily, the wettability behavior has a strong influence on the receding phase, which will be explained ahead in the morphology description of the outcomes.

4.2.1.2 Spreading evaluation

Surface wettability is a relevant parameter in single droplet impact upon dry surfaces. However, as mentioned in the last subsection, it does not play a significant role in determining the outcome regimes, as already declared in the literature [56, 113]. Yet, it plays a major role during the spreading and receding phases, which will then influence the droplet morphology, leading to a certain impact regime [54]. Considering this, the effect of surface wettability both in the spreading and in the receding behavior is evaluated. The spreading diameter D_{spread} was measured and it was normalized by the maximum spreading diameter D_{max}. Figure 4.2

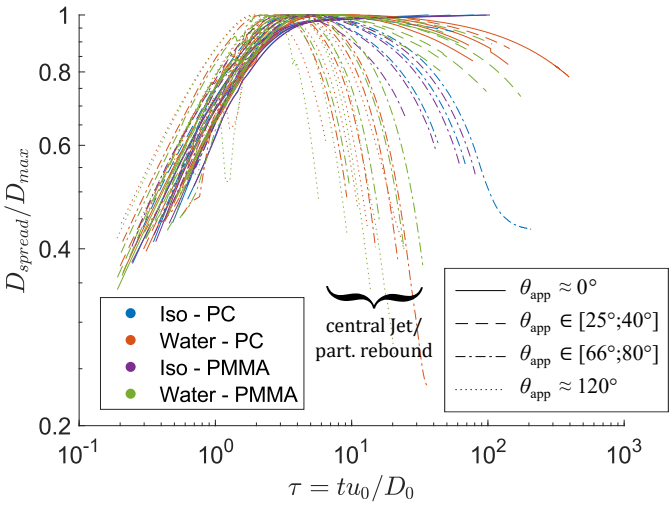

(a)

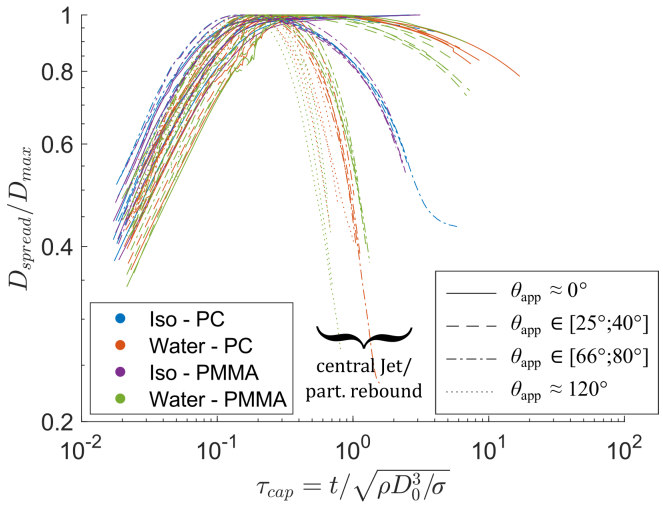

(b)

Figure 4.2: Spreading diameter D_{spread} normalized with the maximum spreading diameter D_{max} vs. (a) the dimensionless (inertial) time τ and (b) the dimensionless (capillary) time τ_{cap}.

(a) shows the normalized spreading diameter D_{spread}/D_{max} as a function of the dimensionless (inertial) time $\tau = tU_0/D_0$ for the entire parameter space. Additionally, Fig. 4.2 (b) also shows the normalized spreading diameter D_{spread}/D_{max} but as a function of the time normalized by the capillary time [121], $\tau_{\text{cap}} = t/\sqrt{\rho D_0^3/\sigma}$. In Fig. 4.2, each line represents the averaged values of at least 10 repetitions with the same impact parameters which define one experimental set. All cases show a similar behavior during the spreading phase, when the inertial forces are dominant, and the spreading diameter quickly increases. As mentioned before, this fact can be explained by a large dynamic contact angle of $\approx 180°$ [48]. This is supported especially in Fig. 4.2 (a), by using the dimensionless inertial times, where the lines are well agglomerated during the spreading phase.

Considering the dimensionless capillary time τ_{cap}, the lines in Fig. 4.2 (b) group up to a single line for each fluid and wettability behavior. This behavior supports the fact that the receding phase is significantly influenced by the wettability of the solid-liquid system and the capillary forces. Therefore, an analysis based on the dimensionless inertial time τ is inadequate for this objective. Analyzing the graphic, it is possible to observe that the impacts of isopropanol with full wetting surfaces keep on slowly spreading after the dissipation of the kinetic energy. On the other hand, a faint receding movement is detected for the experiments of distilled water and an apparent contact angle of $\theta_{app} \approx 0°$. Thus, it is assumed that the apparent contact angle is very close to $0°$, but not exactly this value. Then, while decreasing the wettability of the surface, the receding movement becomes more significant, which leads to the formation of a central jet. The formation of this jet can even promote the occurrence of partial rebound. Nonetheless, the receding rate is also influenced by the fluid surface tension σ and viscosity μ. Consequently, with similar wettability behavior, the receding rate of isopropanol is significantly lower than for water due to the combination of higher viscosity and lower surface tension. Due to that, while for isopropanol no central jet is formed, for distilled water, central jet formation and partial rebound were observed.

Subsequently to the temporal evolution of the droplet spreading and receding, the maximum spreading diameter should also be evaluated. On the other hand, the receding diameter should be considered in future works. In this analysis, the maximum spreading diameter D_{max} is related to the droplet initial diameter D_0. Figure 4.3 (a) shows the spreading diameter related to D_0 versus the dimensionless inertial time at which this diameter is reached $\tau((D_{spread}/D_0)_{max})$ for the four different impact heights, the four wettability behaviors and two fluids, distilled water, and isopropanol. The spreading diameter increases with increasing the impact energy, independently of the surface material. The increase in impact energy is given by increasing the impact height or the surface wettability (by decreasing the apparent contact angle θ_{app}). Figure 4.3 (a) does not show the full wetting cases of isopropanol due to the continuous spreading mentioned previously. However, as described by Rioboo et al. [51], the maximum spreading diameter increases with increasing viscosity, which is the case of isopropanol in comparison with distilled water.

Additionally, the dimensionless spreading diameter $(D_{spread}/D_0)_{max}$ and the dimensionless inertial time at which this diameter is reached $\tau((D_{spread}/D_0)_{max})$ were normalized with the spreading diameters of the full wetting cases $(D_{spread}/D_0)_{max}(\theta_{app} \approx 0°)$ and the dimensionless inertial time at which this diameter is reached $\tau((D_{spread}/D_0)_{max}(\theta_{app} \approx 0°))$, respectively:

$$\tilde{D}_{\text{max}} = \frac{(D_{\text{spread}}/D_0)_{max}}{(D_{\text{spread}}/D_0)_{\text{max}}(\theta_{\text{app}} \approx 0°)} \tag{4.2}$$

$$\tilde{\tau}_{\text{max}} = \frac{\tau((D_{\text{spread}}/D_0)_{max})}{\tau((D_{\text{spread}}/D_0)_{\text{max}}(\theta_{\text{app}} \approx 0°))} \tag{4.3}$$

This normalization is independent of the selection of dimensional inertial and capillary time.

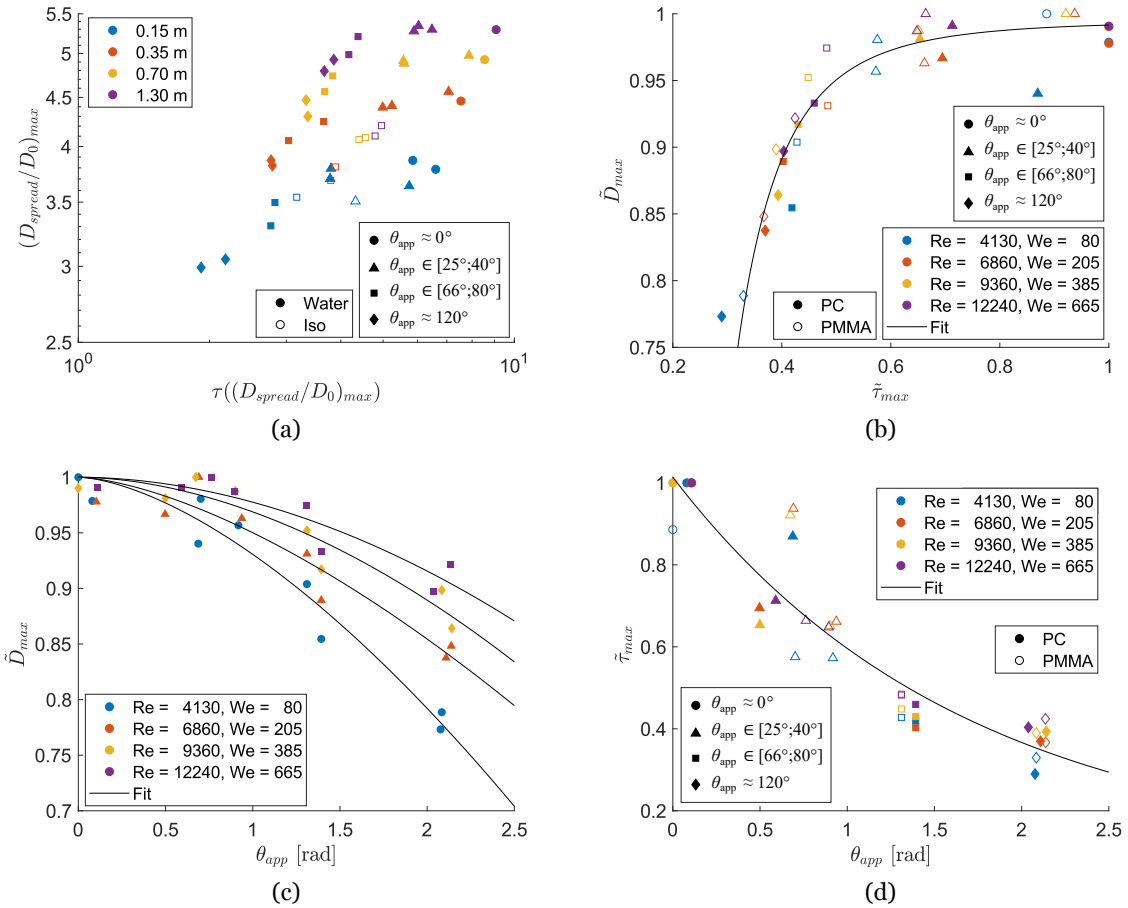

Figure 4.3: (a) Dimensionless spreading diameter ($(D_{spread}/D_0)_{max}$) over the dimensionless inertial time at which the maximum spreading is reached $\tau((D_{spread}/D_0)_{max})$ depending on the wetting behavior and impact energy (represented by the falling height); (b) Maximum normalized dimensionless spreading diameter $\tilde{D}_{max}$ versus the corresponding time at which this diameter is reached $\tilde{\tau}_{max}$ for the distilled water events; (c) $\tilde{D}_{max}$ in dependency of the wetting behavior (θ_{app}) and the impact energy for the distilled water events; and (d) $\tilde{D}_{max}$ over the apparent contact angle θ_{app} showing the influence of the impact energy and the wetting behavior for the distilled water events.

Furthermore, it shows how less the droplet is spreading and how much shorter the spreading process is in comparison to the full wetting cases. Figure 4.3 (b) shows the maximum normalized dimensionless spreading diameter $\tilde{D}_{max}$ versus the corresponding time τ_{max} at which this diameter is reached $\tilde{\tau}_{max}$ just for the distilled water cases. As shown in the plot, all measurements can be agglomerated in one fitted line. It is possible to conclude that, with decreasing wettability (high apparent contact angles θ_{app}) the spreading magnitude becomes smaller in diameter and shorter in time. Additionally, Fig. 4.3 (c) shows the maximum normalized dimensionless spreading diameter $\tilde{D}_{max}$ depending on the wettability behavior just for distilled water. With increasing impact energy, the decrease in the spreading diameter becomes less significant. This trend agrees with the studies of Pasandideh-Fard et al. [53] in which they report that at a certain impact energy, the influence of wettability disappears. Finally, Fig. 4.3 (d) shows the normalized time at which the maximum normalized dimensionless spreading diameter is reached $\tilde{\tau}_{max}$ depending on the wettability behavior just for the distilled water events. According to this plot, the time when the maximum spreading diameter is reached is almost independent of the wetting behavior since the scatter points are agglomerating into the respective clusters for the impact energies which can be fitted again.

4.2.1.3 Impact morphologies

The study of a single droplet impinging upon a dry smooth surface with variable wettability originated several phenomena that will be now described in detail. In this subsection, for each droplet falling height, the phenomena obtained and their characteristics will be described and discussed.

Starting at the lower impact energies tested, $We = 80$ for distilled water and $We = 165$ for isopropanol, Fig. 4.4 shows a scheme of the most relevant results depending on the surface material and wettability. According to Pasandideh-Fard et al. [53], wettability plays a negligible role for high-impact energies, however, it may be important for lower-impact energies. In Fig. 4.4 there is a table for each fluid, distilled water, and isopropanol, with the corresponding Reynolds and Weber numbers. The different wettabilities, defined by the apparent contact angles θ_{app} are indicated at the top of the tables and the two different surface materials are divided, Lexan® (PC) at the upper part and Plexiglas® (PMMA) at the bottom part.

The lower impact height $h_1 = 0.15\ m$ results in Weber numbers below the critical Weber number We_{crit} which defines the boundary between spreading and splashing, since splashing is never observed for these impact conditions. The single droplet impact upon fully wettable surfaces resulted in a wide-spreading with practically no receding movement, as shown previously in Fig. 4.2 and 4.3. By slightly decreasing the wettability for $\theta_{app} \in [25° - 40°]$, the wide spreading continues but there is a slow receding. Figure 4.5 (a) shows the spreading of a distilled water droplet on a fully wettable Lexan® surface from three different perspectives (lateral, top, and bottom views). In the four image sequences presented in Fig. 4.5, the dimensionless inertial time τ is identified for each frame. As mentioned, Fig. 4.5 (a) shows

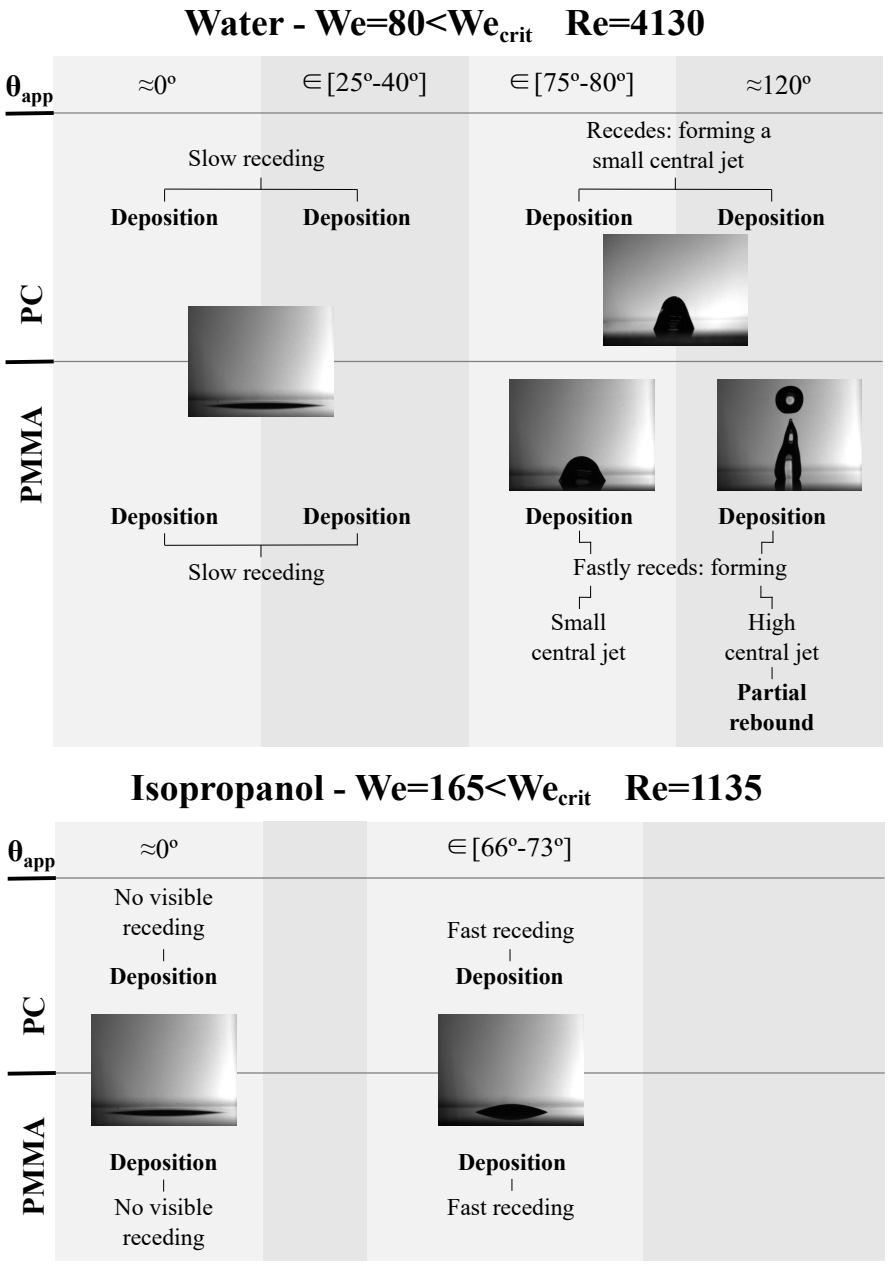

Figure 4.4: Description of the droplet morphology evolution depending on the surface wettability and material for the lowest impact energy.

spreading, and a characteristic barely noticeable by the top and bottom views due to its size is a small air bubble produced at the droplet impact point. The formation of bubbles may happen due to different mechanisms. The droplet impact is upon a surface at ambient temperature, therefore, below the liquid boiling point. Thus, air entrapment at the liquid-solid interface during droplet impact is a possible mechanism for bubble formation [38]. In a vertical droplet impact, the gas between the impinging droplet and the solid surface forms a dimple and softens the impact. Therefore, some air is entrapped in the droplet by the dimple and a tiny air bubble is formed since this air cannot escape [36]. This is the only air bubble formed within the liquid lamella. Inertia directs the liquid lamella to spread radially on the smooth surface. On the other hand, the surface tension (interfacial energy) and viscosity (dissipation of energy) are counteracting, which will limit the maximum spreading diameter

[36]. Due to the full wetting behavior, after reaching the maximum spreading diameter, the liquid film remains on the surface and apparently does not recede inwards or it recedes at a very low velocity.

As mentioned, by using plasma treatments it was possible to obtain four different wettabilities on the droplet impacts with distilled water. Therefore, for higher contact angles (partial wetting and non-wetting systems), the receding of the liquid lamella is quick enough to enable the formation of a small central jet. Additionally, for the higher apparent contact angle ($\theta_{app} \approx 120°$) on the impact with the Plexiglas® (PMMA) surfaces, this central jet grows further, and in some cases, breaks up ejecting a secondary droplet. This phenomenon is called partial rebound as described in Fig. 4.4. An image sequence showing the development of this phenomenon is displayed in Fig. 4.5 (b). The liquid droplet spreads radially on the surface forming a thick rim and reaching its maximum spreading diameter, $\tau = 1.36$. Then, the liquid lamella recedes inwards forming a central jet ($\tau = 6.48$) that keeps increasing in height ($\tau = 8.19$) and breaks ejecting one or two secondary droplets ($\tau = 12.97$). These large secondary droplets will ascend upwards until reaching a velocity of $0\ m/s$, and then, they start a descendant movement towards the impact surface while their impact velocity increases by gravity. After detaching the secondary droplets, the central jet decreases and the liquid film balances on the surface until reaching an equilibrium position ($\tau = 23.89$).

Also, for the Lexan® (PC) surfaces with the same non-wetting behavior as the Plexiglas® (PMMA) surfaces ($\theta_{app} \approx 120°$), as shown in Fig. 4.2, the receding velocity seems to be slower. Therefore, the central jet is smaller and does not break and eject secondary droplets. This shows that even keeping all other parameters constant, including wettability, the change in the surface material influences the morphology of the outcome. As described in subsection 3.2.4, the surface wettability was altered by using plasma treatments, plasma activation, and plasma polymerization. Therefore, plasma polymerization was used to treat the samples and achieve a hydrophobic system. Both materials have the same wettability. However, the surface free energy and polarity of the surfaces are different, which possibly plays a role in the observed morphology [105]. Therefore, the role of these parameters should be investigated in detail in future studies. Finally, it can be concluded from the distilled water droplet impacts upon smooth dry surfaces at low impact energies that increasing the apparent contact angle θ_{app} increases the receding velocity. For fully wettable surfaces, the liquid lamella eventually stops spreading on the surface and does not or barely recede. On the other hand, for non-wettable surfaces, the liquid lamella quickly recedes forming a central jet that may break producing partial rebound or not.

Now, moving on to the isopropanol results, for the full wetting condition, the morphology behavior is similar to the distilled water. However, for the partially wettable condition of $\theta_{app} \in [66° - 73°]$, contrarily to water for a similar wettability, the small central jet does not form. This is probably due to the smaller surface tension. For isopropanol, the liquid film recedes inwards but stops when reaches equilibrium. Also, comparing the maximum spreading diameter of both fluids, isopropanol produces a smaller maximum spreading diameter

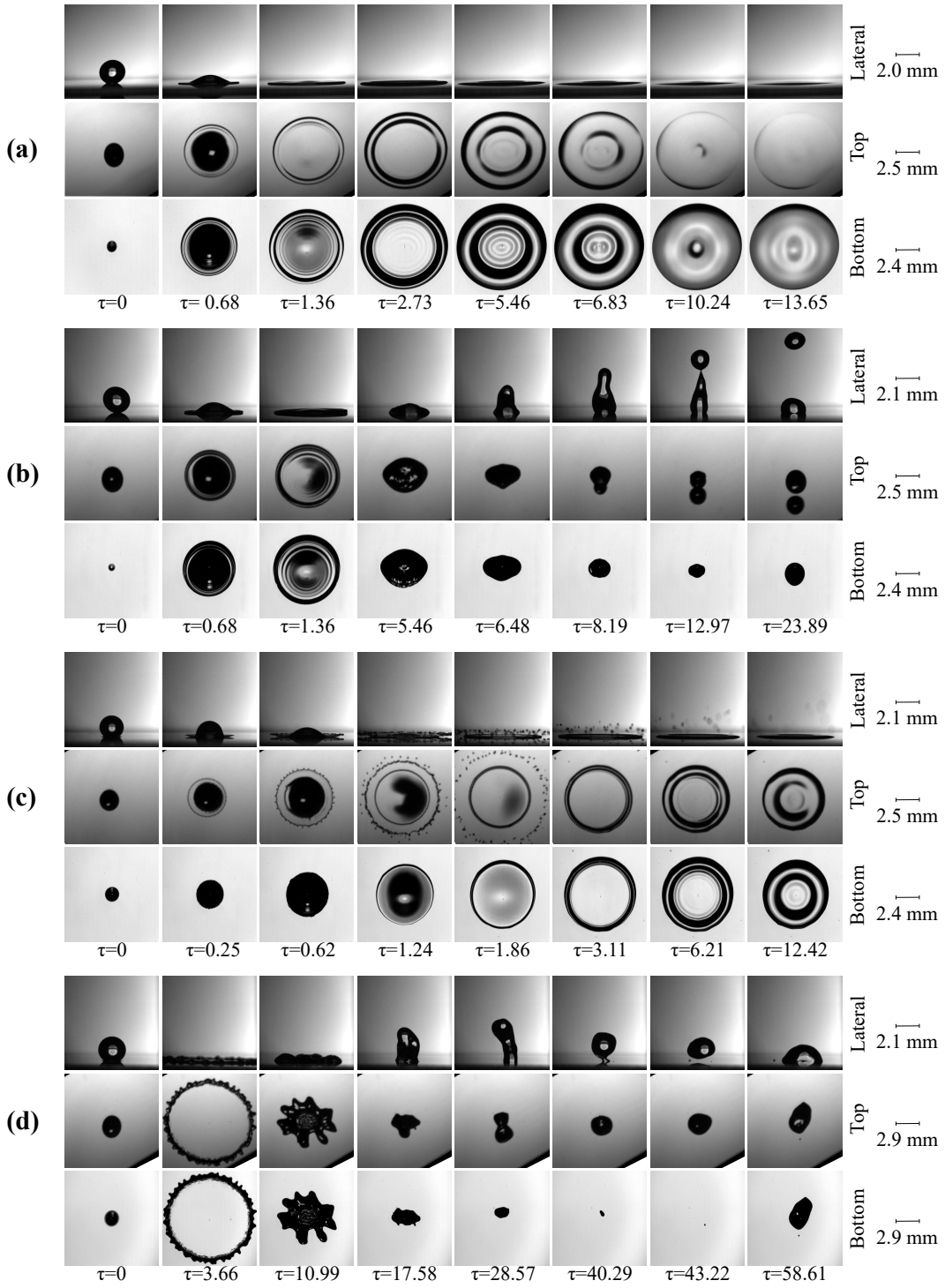

Figure 4.5: Sequence of images showing the phenomena obtained by the lateral, top, and bottom views: (a) spreading of a water droplet impinging onto a fully wettable Lexan® surface ($\theta_{app} \approx 0°$) for $We = 80$ and $Re = 4130$; (b) partial rebound of a water droplet impinging onto a non-wettable Plexiglas® surface ($\theta_{app} \approx 120°$) for $We = 80$ and $Re = 4130$; (c) splashing of an isopropanol droplet impinging onto a partially wettable Plexiglas® surface ($\theta_{app} \approx 70°$) for $We = 400$ and $Re = 1745$; (d) complete rebound of a water droplet impinging onto a non-wettable Plexiglas® surface ($\theta_{app} \approx 120°$) for $We = 385$ and $Re = 9360$.

than distilled water. Mao et al. [50] reported that both viscosity and the equilibrium contact angle have a significant influence on the formation of rebound. Isopropanol has a higher viscosity than distilled water, which will result in a smaller maximum spreading diameter. Therefore, it will have less available energy to recede inwards, and consequently, it will decrease the possibility of originating partial or total rebound. Furthermore, isopropanol also has a lower surface tension, which can be considered as the restoring force. The tendency of rebound is inhibited by both high viscosity and low surface tension. As seen in Fig. 4.2, the receding for distilled water seems to be faster than for isopropanol for similar impact conditions. Nonetheless, it should be noted that the Reynolds number of the isopropanol droplets is significantly lower than the distilled water cases. Although, while increasing the apparent contact angle θ_{app} an increase in the receding velocity is noticeable. To conclude the analysis of this impact height outcomes, the tiny air bubble created at the impact point is observed for all experimental cases.

Now, the analysis of the second impact height $h_2 = 0.35\ m$ starts. For water, $We = 205$ which continues to be below the splashing limit (We_{crit}), and for isopropanol $We = 400$ and splashing is observed, thus, it is above the splashing limit. Figure 4.6 shows a scheme of the phenomena observed and their main characteristics. For water, splashing was not observed, only deposition, except for the impact on non-wettable surfaces where partial rebound was observed. In fact, the impact morphology is very similar to the first impact height, and the receding velocity keeps increasing while decreasing surface wettability. For the partial wetting cases $\theta_{app} \in [75° - 80°]$, for both materials, a small jet forms but does not break, while for the non-wetting cases $\theta_{app} \approx 120°$, for both surface materials, some events of partial rebound are observed. Therefore, considering the surface wettability influence in the receding behavior, the impact energy is high enough to allow the breakup of the central jet, ejecting one or two secondary droplets on the single droplet impact upon a non-wettable Lexan® (PC) surface and not only on Plexiglas® (PMMA), as for the lower impact height.

As already mentioned, for the isopropanol droplet impact, splashing was observed for both wettabilities and surface materials. However, for full-wetting surfaces, there is no visible receding and for partial-wettable surfaces $\theta_{app} \in [66° - 73°]$, the receding is rather fast. Again this confirms that increasing the apparent contact angle increases the receding velocity. The evolution of the splashing event on an isopropanol droplet impact onto a partially-wettable Plexiglas® (PMMA) surface is shown in Fig. 4.5 (c). Once again, a tiny air bubble is formed at the moment of impact and entrapped in the liquid lamella. When the droplet touches the surface, it immediately produces prompt splash from the breakup of tiny jets, $\tau = 0.25$. These jets evolve and create a liquid crown sheet ($\tau = 0.62$) that keeps growing in diameter and height producing even more secondary atomization. The crown eventually breaks ($\tau = 1.24$) and the liquid lamella remains on the surface, receding towards the impact point until finding an equilibrium position, $\tau = 12.42$.

Moving on to the third impact height $h_3 = 0.7\ m$, their outcomes and correspondent characteristics are described in Fig. 4.7. The impact energy of the distilled water impacts, $We = 385$,

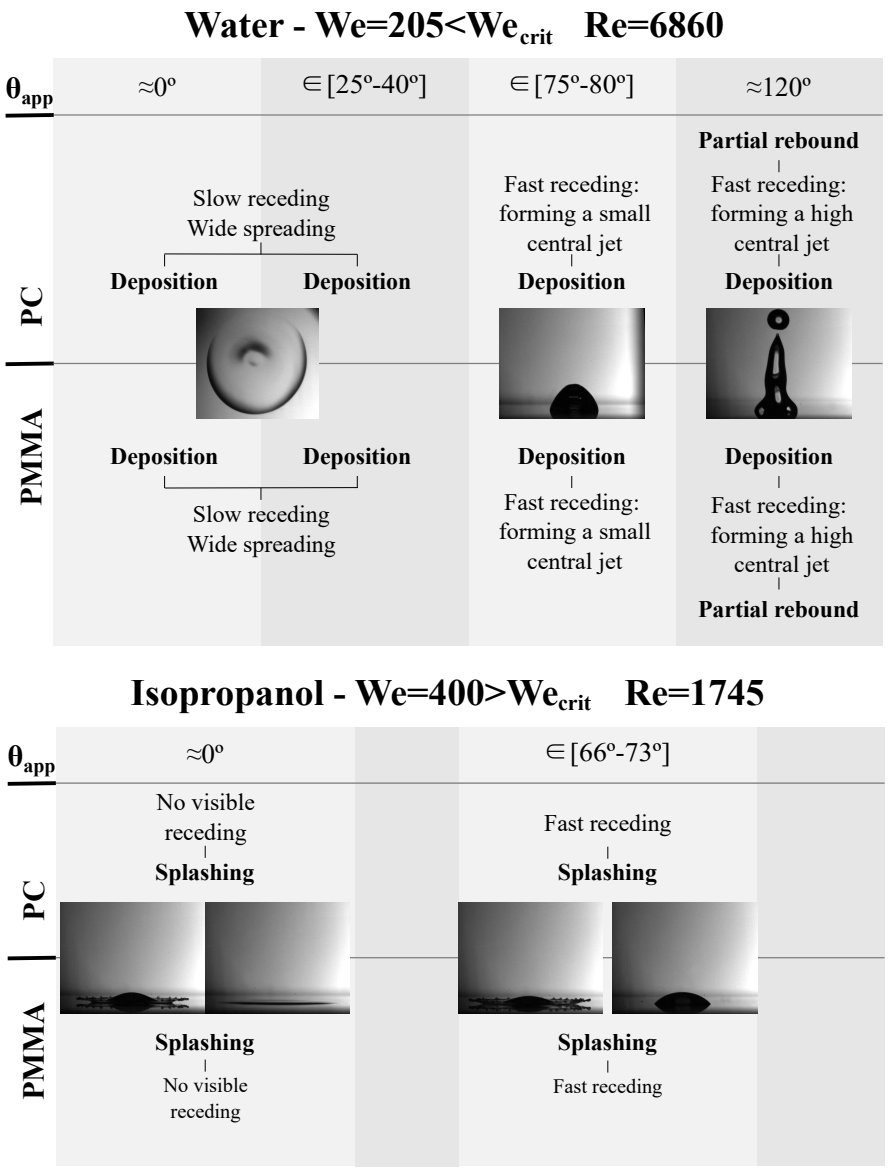

Figure 4.6: Morphology evolution depending on surface wettability for the second impact energy tested, $h_2 = 0.35\ m$.

continues to be below the splashing limit since no splashing is observed. However, for the higher contact angles $\theta_{app} \approx 120°$ partial and complete rebound is observed. A novelty includes the generation of fingering caused by instabilities on the advancing liquid rim. Also, at this impact energy a new phenomenon was observed, complete rebound, shown in Fig. 4.5 (d) for a water droplet impact upon a non-wettable Plexiglas® (PMMA) surface. The liquid film spreads showing a fingering pattern until reaching its maximum spreading diameter ($\tau = 3.66$), then it quickly recedes ($\tau = 10.99$) and forms a high central jet ($\tau = 17.58$). This jet can keep growing upwards, becoming thicker at the top and thinner at the bottom ($\tau = 28.57$). With time, for some cases (two of ten experiments), the jet starts to acquire a droplet-like shape at $\tau = 40.29$. Eventually, the liquid jet detaches totally from the surface and originates a complete rebound, $\tau = 43.22$. After a very short time, the rebound droplet impinges again on the surface with a low-impact energy.

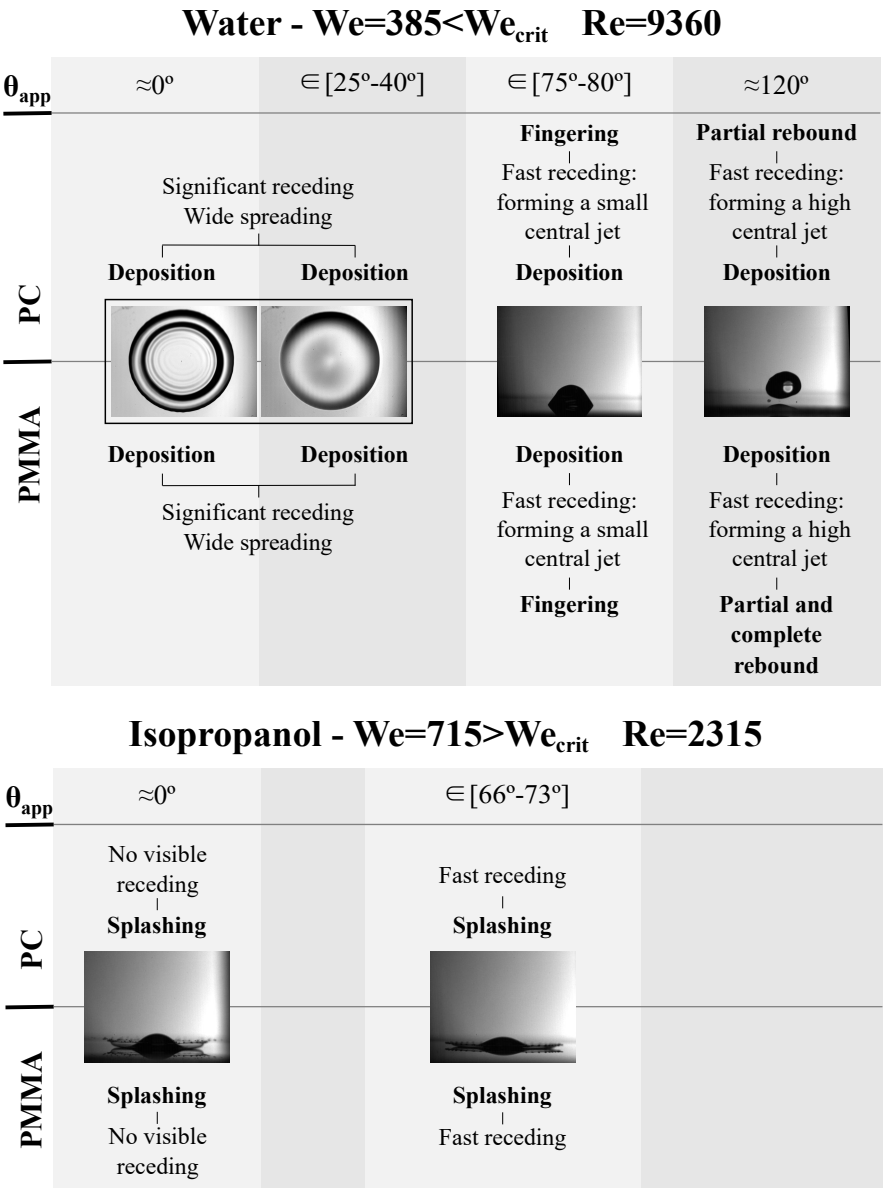

Figure 4.7: Morphology evolution depending on surface wettability for the third impact energy tested, $h_3 = 0.7\ m$.

For isopropanol, at an impact energy of $We = 715$, splashing was observed for all impact conditions and both prompt and crown splash were observed. The major difference in comparison to the lower impact height, $h_2 = 0.35\ m$, is related to the magnitude of the splash. At this impact energy, it produces more secondary atomization.

To conclude this analysis, a really high-impact energy was also considered to evaluate its influence on the observed morphologies. As already concluded by this analysis, surface wettability plays an important role in the spreading, receding, and consequently, rebound dynamics. Nonetheless, according to Moghtadernejad et al. [122] this influence can be decreased or suppressed by the impact conditions. The droplet impact velocity U_0 strongly affects the spreading and splashing regimes due to the kinetic energy after impact. Figure 4.8 shows the phenomena obtained and their characteristics for the highest impact energy, $h_4 = 1.0\ m$.

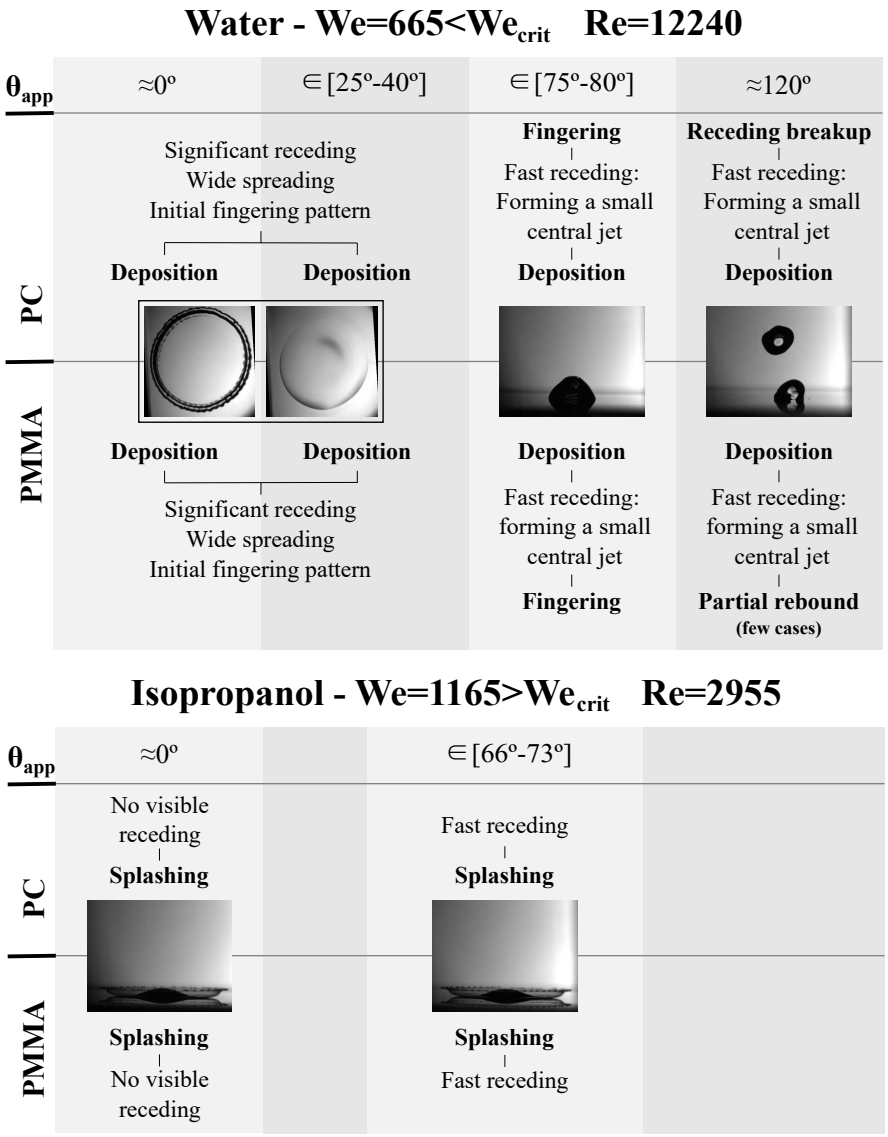

Figure 4.8: Morphology evolution depending on surface wettability for the highest impact energy, $h_4 = 1.0\ m$.

Distilled water droplets impinging on the surfaces with the lowest apparent contact angles θ_{app} at $We = 665$ resulted in deposition. Therefore, due to the higher kinetic energy, the spreading was wider and with a significant receding, and the rim had an initial fingering-like pattern. Increasing the apparent contact angle for droplet impacts upon partially-wettable surfaces $\theta_{app} \in [75° - 80°]$, the only phenomenon observed is deposition with a significant fingering pattern in the initial stages of spreading. After reaching its maximum spreading diameter, the liquid lamella quickly recedes inwards forming a small central jet, similar to the lower impact energies. It is assumed that a significant part of the droplet kinetic energy is spent on the spreading phase since the spreading is wider. Finally, looking at droplet impact onto non-wettable surfaces $\theta_{app} \approx 120°$, a fast and wide receding is observed followed by a rather fast receding as well which originates receding breakup. This receding breakup reduces the events of partial rebound since part of the fluid remains on the surface, and therefore, there is not enough fluid to form a high central jet that will break and eject secondary droplets. Although, on the impact with the Plexiglas® surfaces, there are still some events of

partial rebound.

To finish this analysis, for isopropanol droplet impacts at high-impact energy $We = 1165$, splashing is always observed. Here, with higher magnitude than for lower impact energies, resulting in more secondary droplets. Once again, the receding velocity is higher for surfaces with $\theta_{app} \in [66° - 73°]$ than for fully wettable surfaces.

To summarize this study, three different regimes were observed: deposition, splashing, and rebound. The lowest impact energy tested is below the splashing limit for both fluids since only deposition was observed for all sets of impact conditions. The receding rate increases while decreasing surface wettability. On the water droplet impact upon hydrophobic surfaces, the liquid lamella quickly recedes and forms a central jet that may break originating partial rebound. Despite having the same initial impact conditions different outcomes can occur depending on the surface material. This can be justified by the differences in the polarity and free surface energy of the surface samples due to the plasma treatments. Isopropanol, with a higher viscosity than water, shows a smaller spreading diameter and produces splashing for $We = 400$. Increasing the impact energy, increased the probability to observe partial rebound on the droplet impact onto hydrophobic surfaces. However, increasing the impact energy even further will create a wide spread that will break up during receding. Therefore, less fluid is left to form the central jet, and consequently, partial rebound is inhibited.

Finally, it is important to note that a tiny air bubble was entrapped at the liquid lamella at the moment of impact for all impact conditions tested. As already mentioned, the top perspective shows this bubble but also a shadow of the bubble. As a parallel work, it was demonstrated that a new method was capable of measuring the liquid film thickness considering the distance between this air bubble and its shadow [10]. In previous studies developed by Foltyn et al. [123], a Laser Pattern Shift Method (LPSM) was developed to measure the liquid film thickness. In this study, the pattern was replaced with the natural existing pattern, the two shadows of an air bubble that sticks to the solid surface. More details about this parallel study can be found in Foltyn et al. [10].

4.2.2 Droplet impact onto micro-structured Surfaces

After evaluating the results of single droplet impact upon dry smooth surfaces with variable wettability, it is now time to move on to the description and analysis of the single droplet impact upon dry micro-structured surfaces with variable wettability. A wide parameter space, as described in 3.2.5, was also tested with micro-structured surfaces with four different patterns. From these impacts several outcomes were observed.

In this subsection, the results of these experiments will be described in detail. First, similarly to the previous subsection, the outcomes of droplet impact will be compared with deposition/splashing thresholds presented in the literature. The spreading behavior will be analyzed and the impact morphologies and their characteristics will be described in detail.

4.2.2.1 Deposition/splashing boundary

The study of distilled water and isopropanol droplets impinging upon micro-structured surfaces with variable wettability resulted in the observation of three different impact regimes: deposition, splashing, and rebound. Inside these regimes, it was identified deposition with and without fingering, prompt and crown splash, and partial rebound. One of the goals of this study is to assess how the surface topography and wettability affect the splashing threshold. Therefore, as explained in subsection 3.2.2, the surface topography of the surface samples was altered, and consequently, their roughness. Additionally, the surface wettability was modified independently of the micro-structured pattern using plasma treatments, see subsection 3.2.4.

To investigate how these two parameters affect the splashing limit, correlations and approaches available in the literature were compared with the results and eventually modified to describe the splashing limit. The first correlation considered was developed by Vander Wal et al. [40] for the droplet impact onto dry solid surfaces. This was the first correlation investigated since it was the one that better fitted the results for droplet impact upon dry smooth surfaces with variable wettability as shown in subsection 4.2.1.1. The Vander Wal et al. [40] transition boundary described in eq. (4.4) depends on the Ohnesorge and Reynolds numbers. In an attempt to adapt the splashing limit correlation to include the influence of the surface topography, a modified K factor was investigated including the influence of the Wenzel factor r. Therefore, the existing equation was empirically modified to assess the influence of the surface roughness and liquid properties on the splashing limit. Additionally, the influence of the apparent contact angle θ_{app} on the deposition/splashing boundary could not be found. Thus, the splashing limit seems independent of the surface wettability, at least on the considered parameter space. The only difference between the modified K factor (K_{mod}) and the original one is the exponent of the Ohnesorge number Oh which includes the Wenzel factor r, as shown in eq. (4.5)

$$K_{crit} = OhRe^{0.609} \qquad \text{(Vander Wal et al. [40])} \quad (4.4)$$

$$K_{mod} = Oh^{1/(1.3\sqrt{r})}Re^{0.609} \qquad \text{(This study)} \quad (4.5)$$

Figure 4.9 shows the modified K-factor and how it increases with an increase of the Wenzel factor r. The value of the critical K factor from the original correlation (eq. (4.4)) for smooth surfaces is given in eq. (4.6). Oh the other hand, the value of the proposed empirically found K_{mod} for the impact onto rough surfaces using the modified correlation (eq. (4.5)) is reported in eq. (4.7).

$$K_{crit} = 0.85 \qquad \text{(Vander Wal et al. [40])} \quad (4.6)$$

$$K_{mod} = 3.5(r-1)^2 + 2(r-1) + 2.6 \qquad \text{(This study)} \quad (4.7)$$

This equation was developed to properly describe the splashing limit considering the influence of the Wenzel factor r. Furthermore, the few cases of rebound do not allow a clear

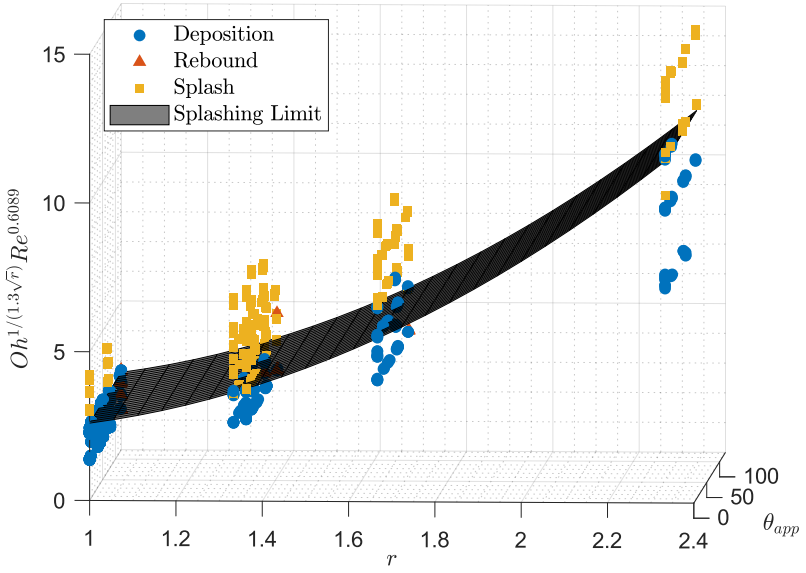

Figure 4.9: Regime map including all experiments onto micro-structured surfaces considering the modified K-factor based on the original K-factor of Vander Wal et al. [40] over the roughness factor r introduced by Wenzel [92] and the apparent contact angle θ_{app}. The modified critical K-factor can be calculated from equation (4.7). A roughness factor of $r = 1$ corresponds to the results for the impact on smooth surfaces.

definition of an individual limit to predict the rebound occurrence. Therefore, to develop a correlation that includes this regime, it is necessary to explore a wider parameter space in future works.

Roisman et al. [94] proposed a correlation for the deposition/splashing limit for droplet impact with rough surfaces. In their studies, they determined that the parameters that influence the most this type of impact are the Weber number We and the characteristic slope of the substrate morphology. The latter is defined as the ratio between the average height of the protruding peaks above the roughness profile and the mean width of a profile element, R_{pk}/R_{sm}. Therefore, their transition boundary is defined as:

$$We_{crit} = 10.2(R_{pk}/R_{sm})^{-0.83} \quad (4.8)$$

However, in their study, they only considered target surfaces with irregular roughness, while in this study only surfaces with regular micro-structures were investigated. Thus, R_{pk} is difficult to define for regular micro-structures since there are no protruding peaks on structures with well-defined heights. Considering this fact, it was not possible to use the Roisman et al. [94] deposition/splashing boundary to compare with the obtained results.

A geometrical approach was also chosen to describe the splashing limit on rough surfaces. Tsai et al. [93] reported that the arrangement of pillars strongly influences the splashing outcomes. They introduced the parameter $\alpha = b/w$ which defines the largest length scale of the cavity that can be passed by air (b is the diagonal between two elements) related to the roughness element width in one micro-pattern unit w. However, they described the surface

topography in a two-dimensional way, which may not be the best approach for this case. Thus, a splashing limit was proposed considering the Weber number We, following Roisman et al. [94] approach, and the modified parameter α_{mod}, describing the surface topography in a three-dimensional way. The modified parameter α_{mod} is the ratio between b and the height of the pillars h, $\alpha_{mod} = b/h$. In Fig. 4.10 the observed phenomena were plotted depending on the Weber number We, the modified parameter α_{mod}, and the apparent contact angle θ_{app}. The Weber number and α_{mod} are significant influencing parameters, while θ_{app} does not influence the splashing limit. Therefore, the critical Weber number We_{crit} for splashing only depends on α_{mod}, as defined in eq. (4.9).

$$We_{crit} = 30\left(\frac{b}{h}\right)^2 - 260\left(\frac{b}{h}\right) + 730 \quad (4.9)$$

Considering this equation, the critical Weber number We_{crit} decreases with increasing α_{mod}. This assumption is true if only the surface patterns composed of pillars with a square cross-section with spacing equal to the pillars' width ($S2-S4$) are considered. The different spacing of the $S1$ surfaces, the micro-structured surfaces with grooves, slightly enhances the formation of prompt splash, mostly because of the $15\ \mu m$ gaps.

Finally, a third approach was also considered to attempt to explain why the surface sample $S1$ promotes the formation of secondary atomization. This is also a geometrical approach but uses different influencing parameters than the last one. According to Xu [97] the pillars' height can promote or suppress splashing. Nonetheless, in this experimental study, all micro-structured patterns considered have the same height $h = 20\ \mu m$, as can be seen in

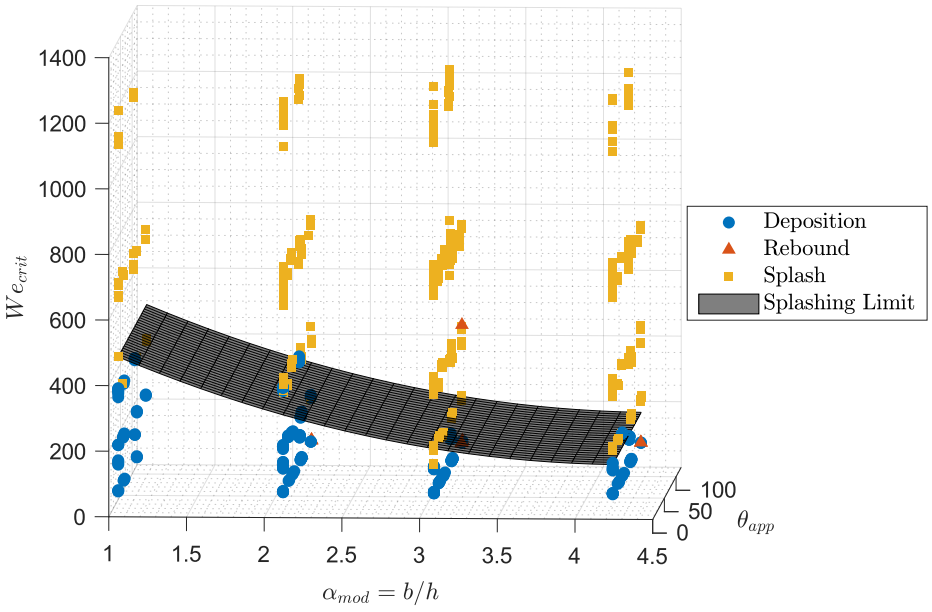

Figure 4.10: Regime map including all experiments onto micro-structured surfaces using a modified parameter of Tsai et al. [93] extended by the apparent contact angle θ_{app}. α_{mod} was chosen as the relation of the width of the junctions b and the height of the pillars, which can be both extracted from Tab. 3.1 for the respective surface types. The plane for the splashing limit (We_{crit}) can be described by the eq. (4.9).

Tab. 3.1. However, the results show that the relative height of the pillars is significant to promote splashing. Further, including the droplet's initial diameter D_0 is important since the outcome also depends on the ratio between the initial diameter of the droplet D_0 and the size of the structures. To include all these influencing factors in the splashing threshold, a new dimensionless parameter was studied $hD_0/(w_1w_2)$, where the pillar height h, droplet diameter D_0 and structure top area w_1w_2 were combined. By using empirically fitting of the data points inside the deposition/splashing transition zone and this newly introduced dimensionless parameter, the splashing limit can be defined as:

$$We_{crit} = 0.008\left(\frac{hD_0}{w_1w_2}\right)^2 - 0.11\left(\frac{hD_0}{w_1w_2}\right) + 180 \quad (4.10)$$

In Fig. 4.11 the outcomes obtained from this parameter space are plotted depending on the Weber number We, the dimensionless parameter $hD_0/(w_1w_2)$, and the apparent contact angle θ_{app}. The critical Weber We_{crit} increases when $hD_0/(w_1w_2)$ increases. The surface topography $S1$ is the structure pattern that promotes splashing the most and it is also the one that has the smallest $hD_0/(w_1w_2)$. If a constant D_0 is considered, $S1$ surfaces have the surface pattern with the smallest relative height in comparison to the top area of the micro-structures. However, as already mentioned, splashing is promoted by a small pillar height [97], and if a relative height is considered it explains why $S1$ is the surface topography that promotes the occurrence of splashing the most, followed by $S2$.

In summary, all three empirical correlations proposed can predict accurately the splashing limit. As mentioned in subsection 4.2.1.1, the correlation proposed by Vander Wal et al. [40]

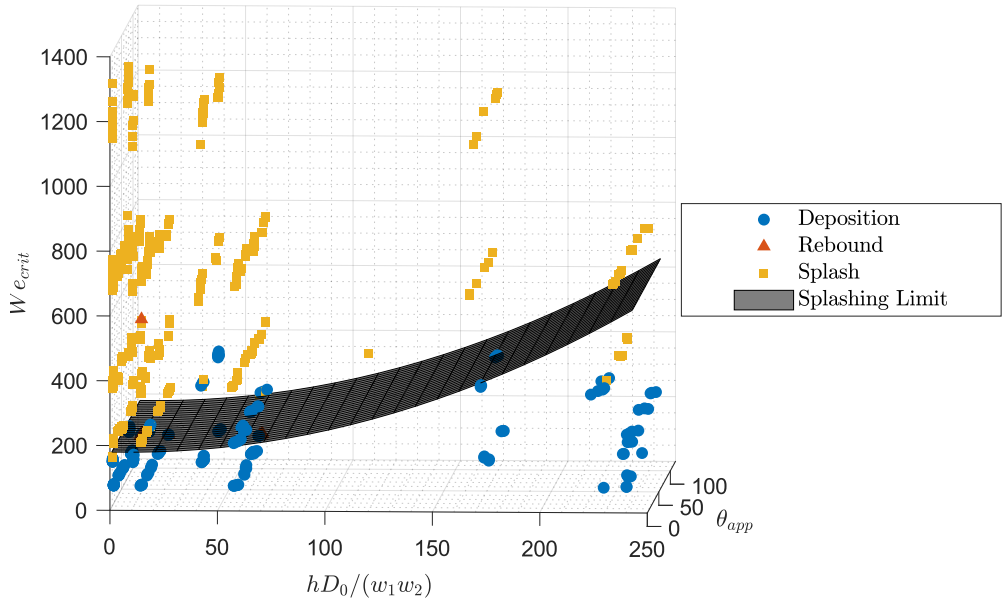

Figure 4.11: Regime map including all experiments onto micro-structured surfaces using the dimensionless parameter $hD_0/(w_1w_2)$ extended by the apparent contact angle θ_{app}. This parameter relates the pillar height h, the droplet Diameter D_0, and the structure top area w_1w_2. h, w_1, and w_2 can be extracted from Tab. 3.1 for the respective surface types. The plane for the splashing limit (We_{crit}) can be described by the equation (4.10).

is in great agreement with the outcomes obtained for the droplet impacts upon smooth surfaces. However, the proposed modified correlation defined in eq. (4.5) is able to predict correctly both the smooth and micro-structured surfaces. The second approach is based on the Tsai et al. [93] studies and it is focused on the spacing between the micro-structures in regular patterns. However, for the same mean roughness values and the same α-parameter, it is shown that different morphological outcomes can be obtained. Considering that, to assess the geometric conditions in more detail, the three-dimensional α_{mod} parameter was introduced. Using α_{mod}, a new correlation to define the spreading/splashing limit was proposed. Finally, the last approach introduces the dimensionless parameter $hD_0/(w_1w_2)$ that relates three important influencing factors: pillar height h, droplet initial diameter D_0, and top surface area of the micro-structures w_1w_2. In these experiments, all surface patterns tested have the same pillar height $h = 20\ \mu m$. However, the relative height of the micro-structures in comparison to their top area is smaller for $S1$, which is the surface topography that promotes splashing the most. This assumption is supported by the findings of Xu [97] reporting that surface height plays a significant role in the splashing occurrence.

4.2.2.2 Spreading evaluation

Similarly to the study of droplet impact upon dry smooth surfaces, the study of droplet impact upon dry micro-structured surfaces was performed under a wide parameter space including different fluids, micro-structured patterns, surface materials, wettabilities, and impact energies. The droplet spreading phase is characterized by an increasing spreading diameter D_{spread}. On the other hand, the receding phase implies a decrease in the spreading diameter D_{spread}. As already mentioned in subsection 4.2.1.2 and known from the literature [51], the receding phase is significantly dependent on the surface wettability. As for the spreading phase, different wettability behaviors only have an effect in the time range during which the inertial forces are dominant [53, 9]. Nevertheless, these findings are related to droplet impact upon smooth surfaces. The study of regularly micro-structured surfaces presented here is more complex.

For smooth and structured surfaces, a continuous spreading can be observed even though the inertial forces have been completely dissipated. Additionally, for $\theta_{app} \leq 40°$ the continuous spreading can also be observed, but less significantly than for $\theta_{app} \approx 0°$. For similar wettability behaviors, for droplet impact onto smooth surfaces, a significant receding movement of the liquid front was already observed. A reason for this is probably the capillary forces inside the surface structures. For this reason, the definition of a maximum spreading diameter for continuous spreading is not possible. Therefore, it is only possible to define the maximum spreading diameter for $\theta_{app} > 40°$. Figure 4.12 shows the maximum spreading diameter normalized by the droplet initial diameter $(D_{spread}/D_0)_{max}$ versus the dimensionless inertial time at which the maximum spreading diameter is reached $\tau((D_{spread}/D_0)_{max})$. On the other hand, the graphic on the right plots the maximum spreading diameter normalized by the droplet initial diameter $(D_{spread}/D_0)_{max}$ versus the Wenzel factor r. The spreading diameter was averaged over the complete azimuthal angle range of $360°$.

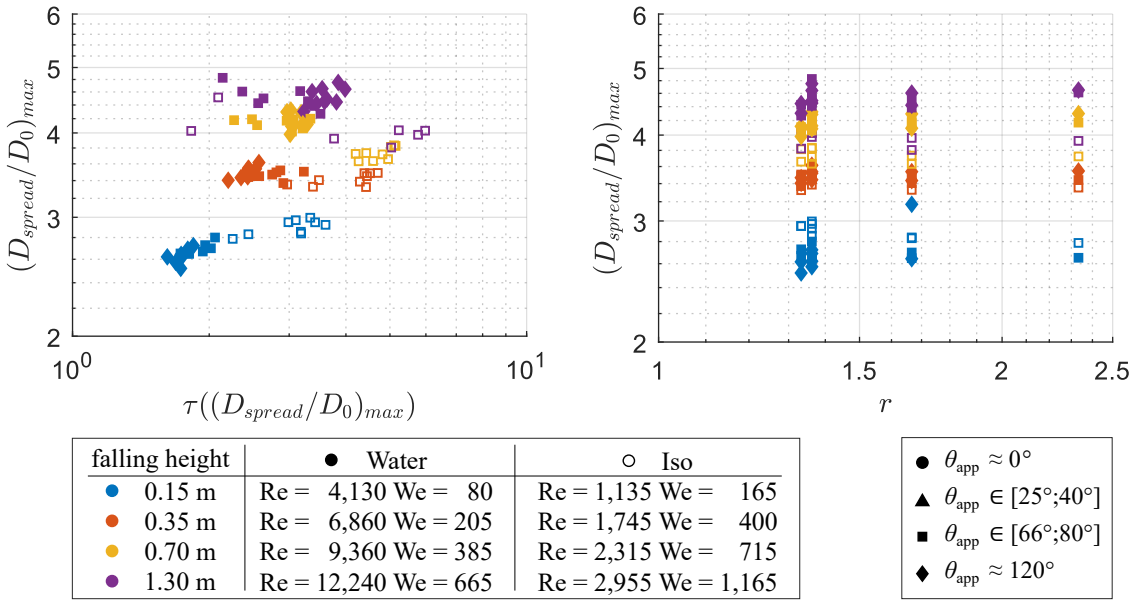

Figure 4.12: Normalized droplet spreading diameter over the dimensionless time τ and the Wenzel factor r characterizing the surface topography type.

The scatter points in Fig. 4.12 represent the arithmetic mean value of a complete experimental data set which is defined by a certain surface material, a micro-structured pattern, a wettability behavior, an impact energy, and a droplet fluid. As already reported for the study of droplet impact upon smooth surfaces, the spreading diameter increases while increasing the impact energy. Additionally, it is shown in Fig. 4.12 that the duration of the spreading phase is also increasing with the impact energy. Nevertheless, it is noteworthy that some experiments for the two highest impact energies reach the maximum spreading diameter faster. These experiments correspond to the surface patterns with larger micro-structures, i.e., grooves $S1$ and large pillars $S2$. This is justified by the formation of crown splashing. Then, the spreading liquid sheet does not interact with the micro-structure surface for most of the time, and therefore, it can spread faster in comparison to the other cases. Noteworthy that the corresponding cases are only experiments with an apparent contact angle of $\theta_{app} \in [66°; 80°]$. At higher contact angles, the crown collapsed earlier causing a slower spreading.

Comparing these results with the events on smooth surfaces, the influence of the wettability behavior is lower, except for the crown splashing events. Regarding the fluid's viscosity, it shows the same tendency as seen for the smooth surfaces. High viscosity usually decreases the absolute spreading diameter while increasing the duration of the spreading process. The only exception is for the lowest impact height $h = 0.15\ m$ where the fluid with higher viscosity (isopropanol) originated larger spreading diameters. This might be caused by the low inertial forces and changes while increasing impact energy. This contradicts the findings of Rioboo et al. [51] but was also observed for droplet impact with smooth surfaces. However, the range and viscosity increment of their study is larger than in this one. Analyzing how a fine increment in fluid viscosity behaves could be an interesting subject for future stud-

ies, mainly to find a possible turning point in the relation between liquid viscosity and the spreading diameter.

Analyzing the influence of surface topography by using the Wenzel factor r shows that its influence in maximum spreading diameter is essentially negligible, see the graphic on the right in Fig. 4.12. Looking closer, a slight increase in the spreading diameter can be observed for the thinner pillars, $S3$ and $S4$. Similarly, the grooves $S1$ also show a slightly higher maximum spreading diameter than $S2$, which presents the lowest values.

4.2.2.3 Impact morphologies

Similarly to the analysis for the droplet impact upon dry smooth surfaces (subsection 4.2.1.3), it will be shown a detailed description of the impact morphologies obtained in the droplet impact onto micro-structured surfaces depending on the structure type, the roughness length scales, the impact energy, the fluid properties, and the surface wettability. Considering the parameter space experimentally tested, different phenomena are observed including deposition, fingering, prompt splash, crown splash, receding breakup, and partial rebound. Thanks to the three different perspectives enabled by the experimental setup, the influence of certain parameters can be determined.

Starting with the first impact energy, $We = 80$ for distilled water impacts and $We = 165$ for isopropanol impacts, three different regimes were obtained: deposition, splashing, and rebound. However, deposition dominates, being the outcome for 93% of the events for this impact height $h = 0.15\ m$. Within the rebound regime, only partial rebound was observed. Figure 4.13 shows a scheme with a summary of the outcomes obtained and their main characteristics depending on the surface structure and the wettability behavior for water impacting onto Lexan® (PC) and Plexiglas® (PMMA) micro-structured surfaces at the lowest impact energy tested. The wettability behavior is identified by the apparent contact angle θ_{app} at the upper part of the scheme. Additionally, the surface micro-structured pattern is identified by $S1 - S4$, as defined in Tab. 3.1. All micro-structured patterns were used in the experiments upon Lexan®-surfaces (PC). On the other hand, on the impacts onto Plexiglas® (PMMA) only three patterns were considered, $S1$, $S2$, and $S3$. The micro-structured pattern with the smallest pillars with a squared cross-section $S4$ was damaged in the fabrication process and cannot be used in the experiments.

The impact of a single water droplet onto fully wettable surfaces $\theta_{app} \approx 0°$ only resulted in deposition with no receding for all micro-structured patterns.

Increasing the apparent contact angle to $\theta_{app} \in [25° - 40°]$, deposition is also the only phenomenon observed and once again with no receding phase. From the bottom perspective, it is noticeable air entrapment within the gaps between the micro-structures for all surface patterns and both surface materials. Figure 4.14 shows the bottom perspective resultant from a water droplet impact onto a fully wettable $S1$ Lexan® surface. The dimensionless time

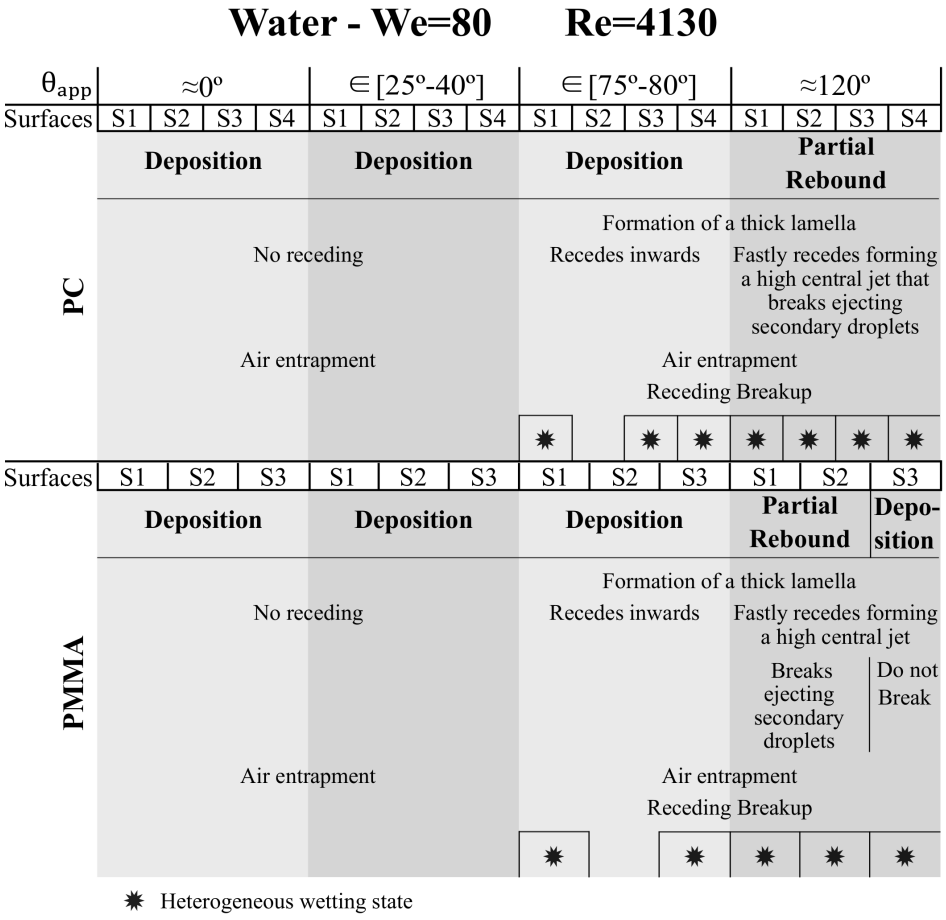

Figure 4.13: Description of the outcomes and their morphology depending on surface wettability and surface micro-structure pattern for PC and PMMA on the water droplet impact at the lowest impact energy, $We = 80$.

$\tau = tU_0/D_0$ is defined for each frame and the scale is also included. In this figure, several tiny air bubbles are entrapped inside the liquid lamella, $\tau = 11.03$. In the impact with smooth surfaces only a tiny air bubble was entrapped inside the liquid lamella at the impact point [38, 124, 125]. Accordingly, in the impact onto micro-structured surfaces, several bubbles are entrapped at the liquid lamella due to multiple discontinuities in the liquid-solid interface. These bubbles are able to escape from the liquid-air interface at the top of the liquid film as shown in Fig. 4.14 at $\tau = 11.78$, where the bursting of an air bubble can be observed, as pointed by the arrow.

Moving on to the water droplet impact upon partial wetting surfaces $\theta_{app} \in [75° - 80°]$, again only the deposition regime is observed for all surface patterns and materials. Nonetheless, in this wettability behavior, a thick lamella forms and spreads until its maximum spreading diameter, after that, it recedes inwards reaching an equilibrium position. However, during the receding phase, a part of the fluid breaks due to the micro-structures producing receding breakup. Air is also entrapped at the moment of impact, similar to the aforementioned impact conditions. At this wettability behavior, an important phenomenon arises concerning how the liquid film spreads and wets the surface. For the surface patterns $S1$, $S3$, and $S4$ there are places where the fluid cannot enter the gaps within the micro-structures. Figure 4.15 shows the bottom and top perspectives of an event where the liquid cannot completely

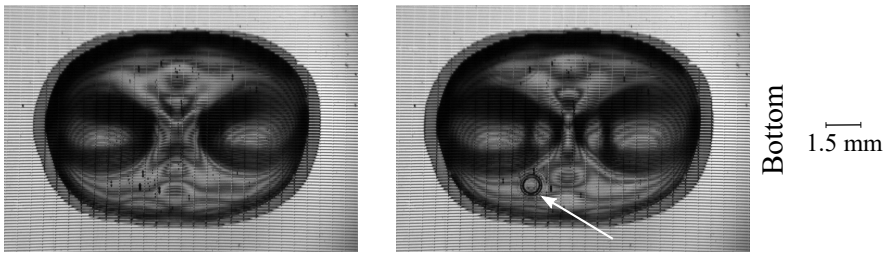

Figure 4.14: Air entrapment observed from the bottom perspective on the water droplet impact at $We = 80$ onto a fully wettable $S1$ Lexan® surface. Capillary waves emerging due to a bursting bubble at the liquid surface are indicated by the arrow.

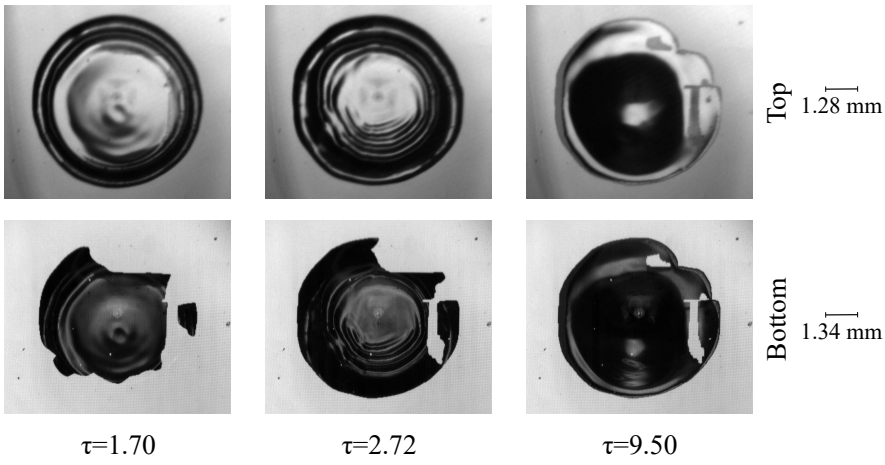

Figure 4.15: Top and bottom views of non-wetted areas caused by heterogeneous wetting on a water droplet impact on a partially wettable $S4$ Lexan® surface, $\theta_{app} \in [75° - 80°]$, $We = 80$.

penetrate between all micro-structures and only wets the top of the pillars in these areas. At $\tau = 1.70$ the fluid seems to completely wet the surface from the top perspective, but from the bottom perspective, it is noticeable that the fluid does not enter all the gaps between the micro-structures. Later, at $\tau = 2.72$ the fluid penetrates some of the gaps and encircles part of the areas to complete the lamella perimeter. Finally, at $\tau = 9.50$, the perimeter of the lamella is well defined. However, there are areas within the lamella where the liquid is only above the pillars without entering the spaces between them which are filled with air. Interestingly, the surface pattern $S2$ is the only one that does not present this behavior.

It is called omniphobic surfaces to the surfaces that can maintain a heterogeneous wetting state even for low surface tension fluids [126]. The heterogeneous wetting state occurs when the asperities in the topography of rough surfaces can sustain air entrapped inside the grooves underneath the liquid film. The well-known Young contact angle θ_Y, also called "intrinsic contact angle" by Hensel et al. [126] is one of the parameters that define the heterogeneous wetting state. A thermodynamically stable heterogeneous wetting state for water can be achieved at a high enough Young contact angle θ_Y, usually for $\theta_Y > 90°$, and a certain roughness. Considering fluids with lower surface tension in comparison to water, the heterogeneous wetting state can be reached at $\theta_Y < 90°$ even on low-energy surface materials.

The heterogeneous wetting stated is energetically metastable and can shift into a homogeneous wetting state by pressure fluctuations as acoustical or mechanical vibrations that would result in insufficient resistance to wetting. Typically, for low Young contact angles $\theta_Y < 20°$, the liquid immediately penetrates the cavities due to the continuously downward-directed capillary net force.

In this study, the heterogeneous wetting state was found for both partially wettable surfaces $\theta_{app} \in [75° - 80°]$ and non-wettable $\theta_{app} \approx 120°$ surfaces for both surface materials. For the lower wettability $\theta_{app} \approx 120°$, all micro-structured patterns reached the heterogeneous wetting state for both fluids used. Contrarily, for $\theta_{app} \in [75° - 80°]$, with a smaller θ_Y than the non-wettable surfaces, the surface pattern $S2$ reaches a homogeneous wetting state on the entire extension of the liquid lamella.

Due to the continuous increase of the hydrostatic pressure inside the cavity, the liquid-air interface can fall into the cavity. To reach this breakthrough scenario a critical pressure difference needs to be achieved, and two phenomena are possible. First, the canthotaxis effect where the critical pressure difference corresponds to the geometrical boundary condition and is defined as:

$$\Delta p_{break} = p_h - p_0 = \frac{2\sigma \ \sin(\theta_Y + \Psi)}{X} \quad (4.11)$$

where p_h and p_0 are the hydrostatic and air pressure, respectively, σ is the liquid surface tension, Ψ is the geometrical edge angle, and X is the distance between the three-phase contact line and the symmetry center of the cavity. Secondly, the Laplace breakthrough phenomenon, where the liquid-air interface assumes a semicircular shape before filling the cavity. In this case, the critical pressure difference is defined as:

$$\Delta p_{break} = p_h - p_0 = \frac{2\sigma}{X} \quad (4.12)$$

The critical pressure difference calculation, for both phenomena, has X as the denominator, which, in this study, is assumed to be the parameter b defined by Tsai et al. [93]. Therefore, a larger X value requires a smaller pressure difference to reach a homogeneous wetting state. The micro-structured pattern $S2$ has the highest b value, therefore, it is the one that requires the lowest pressure difference to reach the breakthrough pressure.

Returning to the analysis, considering the behavior of a distilled water droplet impinging upon the micro-structured hydrophobic Lexan® surfaces, $\theta_{app} \approx 120°$, partial rebound was the outcome for all surface patterns. Figure 4.16 shows an image sequence of partial rebound from three different perspectives on the water droplet impact onto a hydrophobic Lexan® $S4$ micro-structured surface.

On the frame of droplet impact $\tau = 0$, a non-wetted zone is observed around the impact point from the bottom perspective. This corresponds to an area where the fluid was not able to

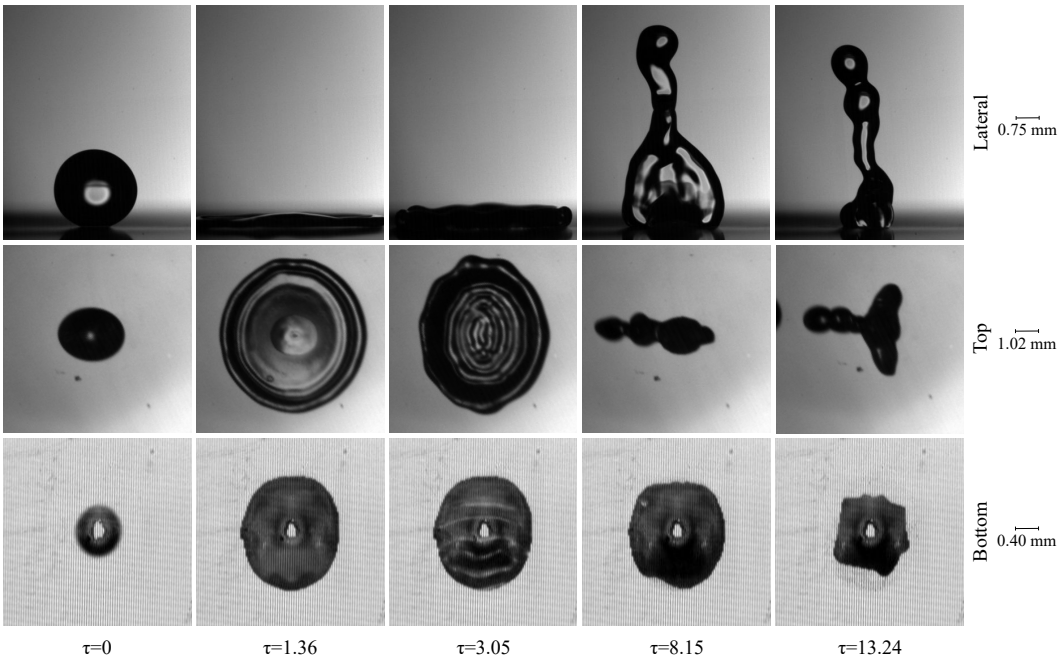

Figure 4.16: Partial rebound of a water droplet onto a hydrophobic $S4$ Lexan® micro-structured surface for $We = 80$ from three different perspectives: lateral, top and bottom.

penetrate the gaps within the micro-structures due to a heterogeneous wetting state, similar to Fig. 4.15. As mentioned before and reported in the literature by Chandra and Avedisian [38], Mehdi-Nejad et al. [124], and van Dam and Le Clerc [125], a droplet starts to flatten in the bottom when approaching the target surface. At the moment of impact, an air cushion can even be formed between the droplet and the target surface. The formation of an air cushion led to a heterogeneous wetting state at the impact site, creating a non-wetted area that was observed for the micro-structured patterns $S3$ and $S4$. On the other hand, for the micro-structured patterns $S1$ and $S2$, only a bright small spot is observed at the impact point, implying just the formation of a tiny air bubble. After impact, at $\tau = 1.36$, a thick lamella forms and spreads radially until reaching the maximum spreading diameter. For all surface patterns, there are spaces where the fluid cannot enter, at the center for $S3$ and $S4$ and at the periphery for $S1$ and $S2$. After reaching the maximum spreading diameter, the lamella quickly recedes inwards $\tau = 3.05$, forming a high central jet $\tau = 8.15$, that eventually breaks and ejects large secondary droplets producing partial rebound $\tau = 13.24$. These secondary droplets will ascend and then fall onto the target surface again. Noteworthy that during the receding phase, receding breakup occurs but with a smaller magnitude than on partial wettable surfaces $\theta_{app} \in [75° - 80°]$. This can be attributed to the higher receding velocity due to the lower tendency of liquid to stick to the surface, not allowing the breakup of the liquid lamella. Therefore, the formation of a high central jet is enhanced since less liquid is "lost" on the receding breakup.

Keeping the same droplet falling height using isopropanol droplets led to a higher Weber number $We = 165$ and a smaller Reynolds number $Re = 1135$. For isopropanol only two wettability behaviors were used: full wetting $\theta_{app} \approx 0°$, and partial wetting $\theta_{app} \in [66° - 73°]$.

Similarly to water, Fig. 4.17 shows a scheme with a summary of the outcomes obtained and their main characteristics. At low-impact energy, isopropanol impacts only generate deposition and prompt splash. The formation of prompt splash was only observed for the impact onto the micro-structured pattern $S1$. It is considered a directional prompt splash and an example is shown in Fig. 4.18 from both the lateral and top perspectives. Immediately after impact, two tiny droplets were formed and are pointed out by the arrows in Fig. 4.18. These two droplets were ejected in the direction in which the air flows through the surface micropattern. According to Tsai et al. [93], the formation of splashing is significantly affected by the pillar arrangement and is promoted by the small inter-spaces. The micro-structured pattern $S1$ has a $15\ \mu m$ spacing between pillars and that should be the motive for why splashing is promoted by this pillar arrangement in that direction. However, it is important to highlight that the magnitude of this prompt splash is very small.

On isopropanol droplet impact onto fully wettable surfaces $\theta_{app} \approx 0°$, no receding phase is observed. Contrarily, on the impact with partially wettable surfaces $\theta_{app} \in [66° - 73°]$, the liquid lamella slowly recedes inwards. Air entrapment and non-wetted areas at the bottom were similar to the ones for water droplet impacts with similar impact conditions. Also, similarly to water, the heterogeneous wetting state was not observed for the surface pattern $S2$.

The analysis of the lowest droplet falling height tested shows that wettability influences the occurrence of heterogeneous wetting states and the receding phase. For hydrophobic systems, a central jet forms and breaks producing partial rebound. Finally, small inter-spaces between pillars trigger prompt splash.

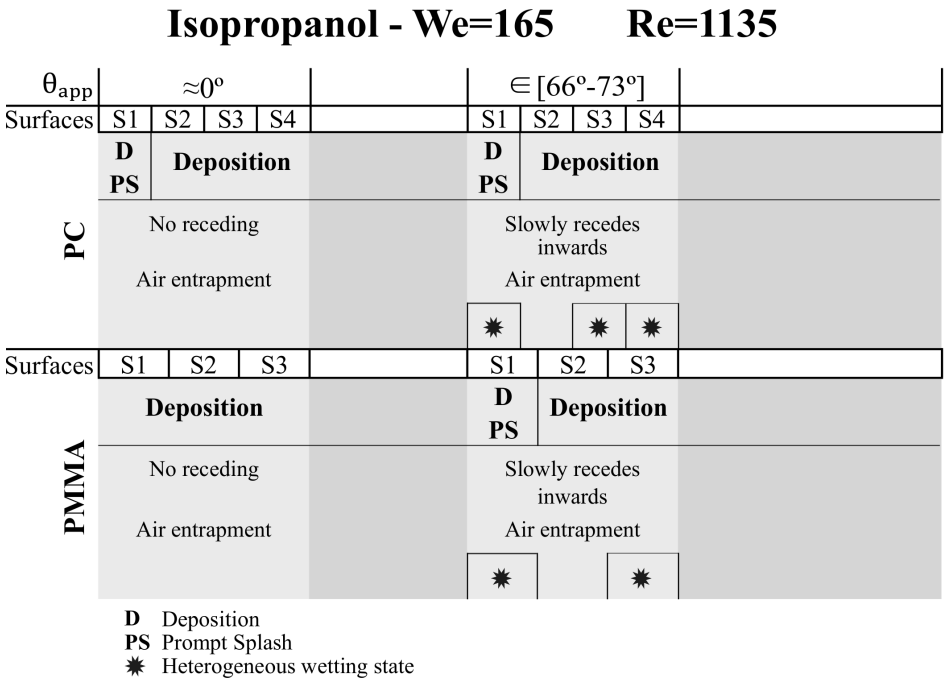

Figure 4.17: Description of the outcomes and their morphology depending on surface wettability and surface micro-structured pattern for PC and PMMA on the isopropanol droplet impact at the lowest impact energy, $We = 165$.

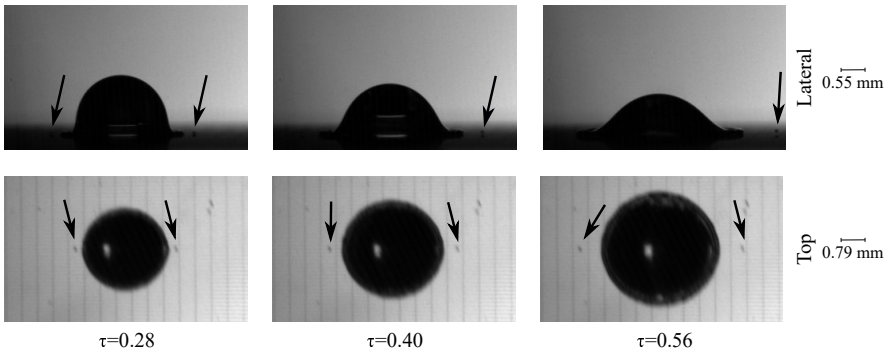

Figure 4.18: Directional prompt splash from an isopropanol droplet impinging at $We = 165$ onto a partially wettable $S1$ Plexiglas® surface, $\theta_{app} \in [66^\circ - 73^\circ]$.

The impact energy was increased to assess their influence on the outcomes and their characteristics. Figure 4.19 shows a scheme with the outcomes obtained on the impact of water droplets at the second of four droplet falling heights tested, $We = 205$ and $Re = 6860$. Contrary to the lower impact height, prompt splash was observed several times.

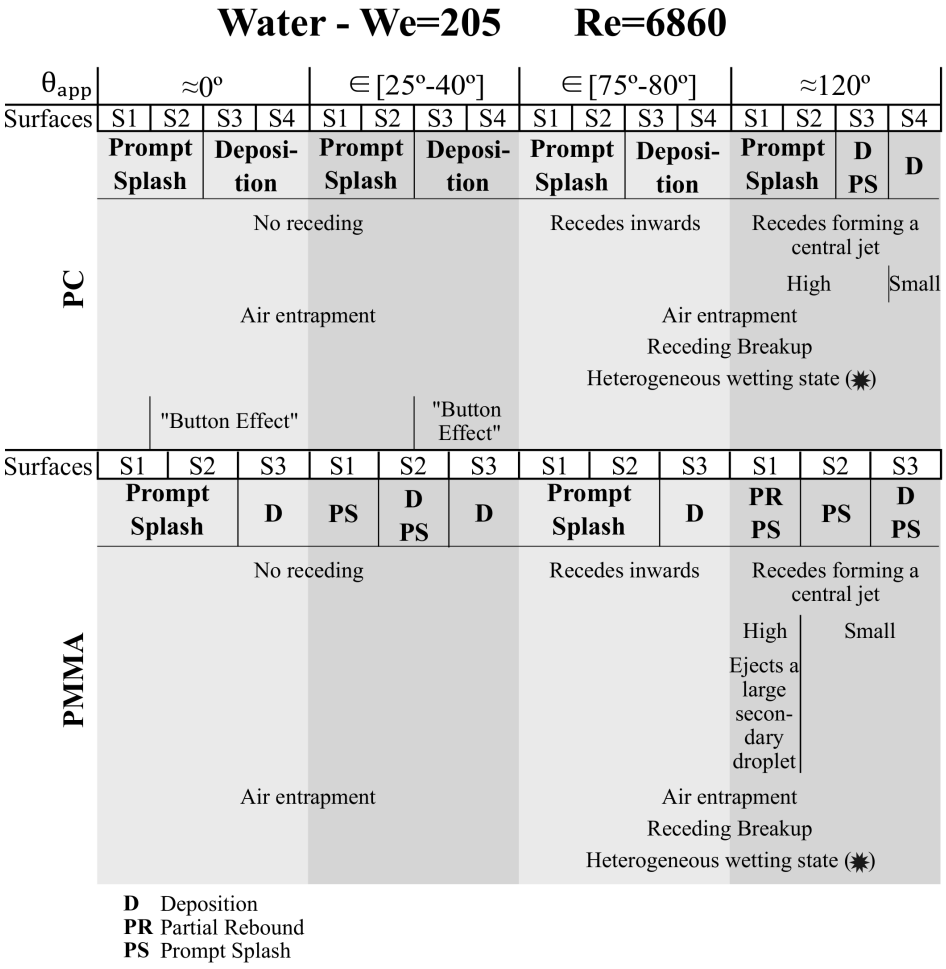

Figure 4.19: Description of the outcomes and their morphologies depending on surface wettability and surface micro-structured pattern for PC and PMMA on the water droplet impact at the second impact energy tested, $We = 205$.

The phenomenon obtained clearly depends on the micro-structured pattern for the impact with fully wettable surfaces $\theta_{app} \approx 0°$. For both surface materials, prompt splash was promoted by the $S1$ and $S2$ patterns. However, for $S3$ and $S4$, the droplet spreads on the target surface without releasing any secondary droplet. Noteworthy that, as mentioned, the micro-structured pattern $S4$ was not used in the Plexiglas® experiments due to manufacturing constraints. For this wetting behavior, the liquid lamella keeps spreading with time, there is no receding movement. Also, on the water droplet impact with the micro-structured pattern $S3$, a pattern forms at the center region of the liquid lamella. Figure 4.20 shows the pattern called the ”button effect”.

The ”button effect” pattern has four round areas centered at the impact point. These areas are formed by a higher concentration of very small air bubbles within the liquid lamella. This pattern is also observed for $S2$ and $S4$, but $S3$ is the micro-structured pattern that better shows this phenomenon. These three micro-structured arrangements are composed of pillars with a square cross-section and that might be the reason for the four round areas arrangement. In 1991, Chandra and Avedisian [38] reported similar structures and called them ”cellular structures” but from a different origin since their studies were on impacts onto heated smooth stainless steel surfaces, and the structures were formed due to the interaction of heptane with the heated wall. Therefore, these two different observations originated from different mechanisms. This pattern should be studied in more detail in future studies to understand the physics behind it. Directional prompt splash and finger formation were observed for the micro-structured surfaces with smaller roughness factors r, $S1$, and $S2$.

Increasing the apparent contact angle to $\theta_{app} \in [25° - 40°]$, the outcomes are similar to the full wetting case. The major difference is the simultaneous occurrence of prompt splash and deposition in the impact with $S2$ Plexiglas® surfaces. No receding is observed but air entrapment is always present. The ”button effect” is observed for the micro-structured patterns $S3$ and $S4$. A new characteristic is the formation of a few fingers normal to the groove orientation

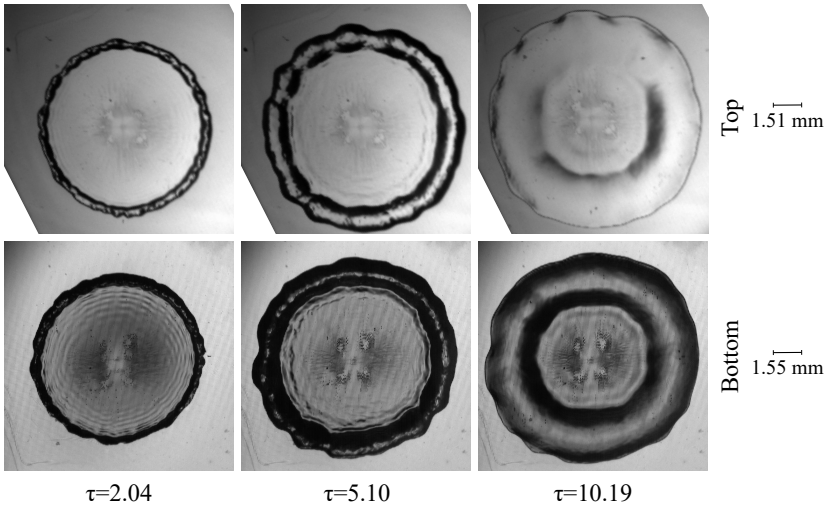

Figure 4.20: The ”button effect” from the top and bottom perspectives for a water droplet impact onto a fully wettable $S3$ Lexan® surface for $We = 205$.

and its consequent breakup, producing secondary droplets. This particular phenomenon is shown in Fig. 4.21 from the lateral and top perspectives. This event happens in a short period of time where fingers are formed normally to the ejection direction of the prompt splashed droplets at $\tau = 0.56$. One of these fingers grows and eventually breaks at $\tau = 0.76$ producing a large secondary droplet.

For the impacts on partially wettable conditions $\theta_{app} \in [75° - 80°]$, the phenomena obtained are similar to the ones for the impact with fully wettable surfaces $\theta_{app} \approx 0°$. Prompt splash is the outcome of water droplet impact upon the micro-structured patterns $S1$ and $S2$, and deposition for the other surfaces. The liquid lamella recedes inwards, due to the lower wettability, and breaks over the gaps between the micro-structures generating receding breakup. Finger formation is observed for all micro-structured patterns and both surface materials, and prompt splash is always directional following the pillars/grooves orientation. The breakup of fingers normal to the orientation of the grooves is observed for the droplet impact of water droplets onto the $S1$ Lexan® surfaces, similar to Fig. 4.21. Converging to a scenario where the wettability behavior is typical of a partially wettable surface, the Young contact angle increases, and mixed with the proper roughness, results in a heterogeneous wetting state. The bottom perspective enables the observation of non-wetted areas for all micro-structured patterns.

Decreasing the wettability behavior for $\theta_{app} \approx 120°$ enhances prompt splash. Impacts onto the $S4$ Lexan® surfaces are the only exception where only deposition is observed. Several finger-like structures were formed at the rim of the liquid lamella and air entrapment is also observed for this wettability behavior. In addition, in the majority of the cases, the lamella spreads over the structures without entering the gaps between them in some regions, which is noticeable from the bottom perspective. This is due to the high apparent contact angle θ_{app} which increases the Young contact angle and favors the presence of the heterogeneous wetting state.

Figure 4.22 shows an example of the heterogeneous wetting state seen from the top (upper images) and the bottom (bottom images). The lamella is uniformly spreading along the surface from the top perspective ($\tau = 1.53$). However, observing the bottom perspective, it is

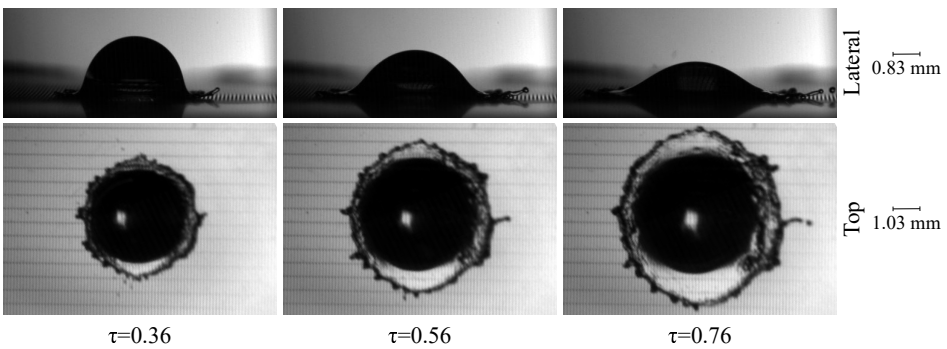

Figure 4.21: Finger formation normal to the orientation of the grooves and its consequent breakup for a water droplet impact onto a wettable $S1$ Lexan® surface, $\theta_{app} \in [25° - 40°]$, $We = 205$.

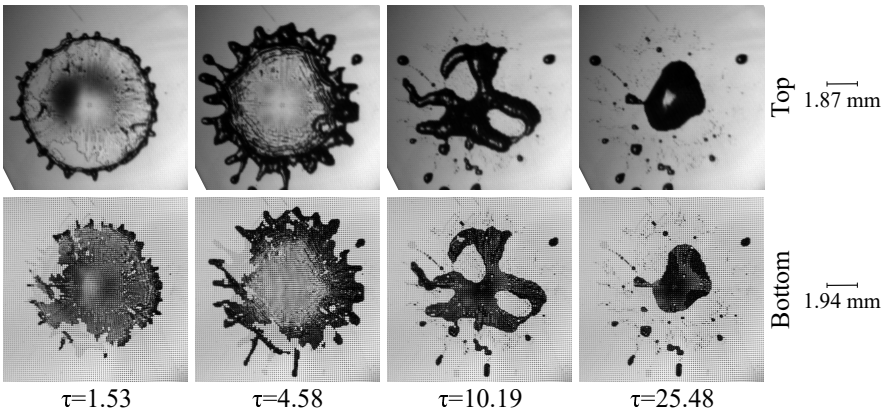

Figure 4.22: Heterogeneous wetting state seen by the top and bottom perspectives for a water droplet impact onto a hydrophobic $S2$ Lexan® surface, $We = 205$.

seen that part of the micro-structures are not wetted. At $\tau = 4.58$, it is noticeable, from both perspectives, zones where the fluid circumvents small areas. With time, the hydrostatic pressure increases, and the breakthrough pressure is achieved during the receding phase for a significant part of the liquid, as seen in $\tau = 10.19$. At $\tau = 25.48$ the magnitude of the receding breakup is evidenced. Additionally, an air cushion is formed at the impact point for the water droplet impact onto $S4$ Lexan® surfaces. This is the micro-structure surface that does not present splashing despite being the one that has the smallest interspace between pillars. This fact contradicts the Tsai et al. [93] conclusions which say that small interspaces promote splashing. In opposition, $S4$ surfaces have smaller X and b values due to the smaller interspaces which results in a higher pressure difference for the breakthrough of the liquid. This might be the reason for being the only micro-structured surface that shows an air cushion for this impact energy.

Lastly, for this wettability behavior, $\theta_{app} \approx 120°$, a central jet is formed due to the receding phase. For the surfaces made of Lexan®, the central jet is high for $S1$, $S2$, and $S3$, but it is small for $S4$. Differently, the impact with Plexiglas® surfaces resulted in low central jets for $S2$ and $S3$, although for $S1$ the jet is high and breaks ejecting a large secondary droplet, as shown from three different perspectives in Fig. 4.23. At $\tau = 1.53$ the liquid lamella reaches its maximum spreading diameter. Considering the top and bottom views, it is noticeable that the liquid spreads on the top of the pillars while does not enter the gaps between them. Later, at $\tau = 6.12$, it quickly recedes inwards thickening the lamella. A central jet forms at $\tau = 10.19$ and a large droplet is ejected from this jet, $\tau = 24.46$. A small portion of the jet stays attached to the surface, as can be confirmed by the lateral and bottom views. It seems that in the events where partial rebound was observed, the fluid left on the surface due to the receding breakup is less. Therefore, it remains fluid enough to form a high central jet.

The second impact height was also tested for the impacts with isopropanol droplets, providing $We = 400$ and $Re = 1745$ as impact conditions. As a result of the increase in impact energy, splashing was observed for more sets of impact conditions, as seen in Fig. 4.24. Crown splash, prompt splash, and deposition were observed on the impact of isopropanol droplets

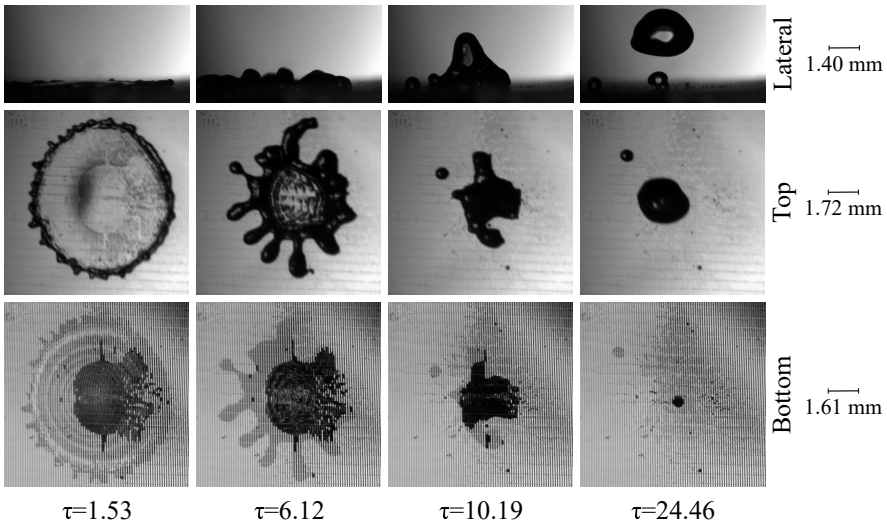

Figure 4.23: Partial rebound for a water droplet impinging onto a hydrophobic $S1$ Plexiglas® surface at $We = 205$ from three different perspectives: lateral, top, and bottom.

with fully wettable Lexan® surfaces $\theta_{app} \approx 0°$. For all conditions, no receding movement is identified and air is entrapped in the liquid lamella. Crown splash is observed for the first time on the isopropanol droplet impact with $S1$ surfaces. An incomplete crown liquid sheet is formed parallel to the length of the grooves, as shown in Fig. 4.25. At $\tau = 0.30$, directional prompt splash forms parallel to the length of the grooves, and at $\tau = 0.48$ a small crown sheet develops sideways. The tiny liquid sheet grows and quickly breaks producing secondary atomization, at $\tau = 0.73$.

Continuing looking for the isopropanol impact onto fully wettable Lexan® surfaces $\theta_{app} \approx 0°$, prompt splash is the outcome observed in the impact with $S2$ showing also finger breakup, similar to the previously shown in Fig. 4.21. On the other hand, in the impact onto the surface pattern $S3$ the prompt splash and deposition regimes coexist, therefore, this is a transition zone. Finally, only deposition was observed in the impact with $S4$ surfaces. For the same initial impact conditions ($We = 400$ and $Re = 1745$), but on the impact with fully wettable Plexiglas® surfaces (PMMA), prompt splash is observed for $S1$ and $S2$, and a mixture of prompt splash and deposition for $S3$.

Decreasing the surface wettability to $\theta_{app} \in [66° - 73°]$ and considering both materials, prompt splash was the phenomena obtained for the $S1$ and $S2$ surfaces, and deposition for the $S3$ and $S4$ surfaces. At these impact conditions, a particular effect was distinguished from the impacts onto $S3$ and $S4$, the patterns with higher roughness factors r. This phenomenon was called the "cookie effect" and it is shown in Fig. 4.26. Due to the heterogeneous wetting state, empty round areas were formed in the liquid lamella, as can be seen at $\tau = 12.09$. These empty areas were created since the fluid cannot enter the gaps within the structures and then the fluid on top of the pillars circumvents these zones. The several "holes" in the liquid lamella remind a cookie and that is why it was termed the "cookie effect". One or two empty areas are also observed in the impacts with the surface patterns $S1$ and $S2$. Finally, in Fig. 4.26 two unilateral fingers were formed on one side of the lamella. The formation

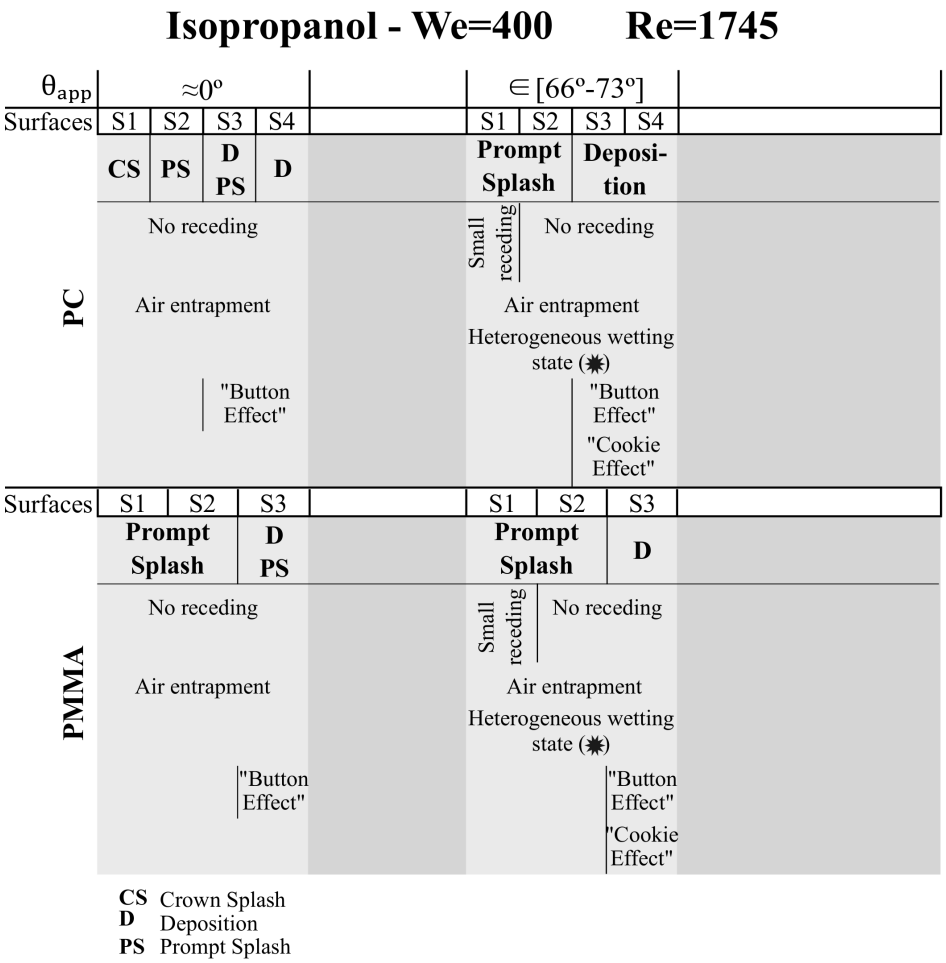

Figure 4.24: Description of the outcomes and their morphology depending on the surface wettability and the surface micro-structured pattern for PC and PMMA for the isopropanol droplet impact, $We = 400$.

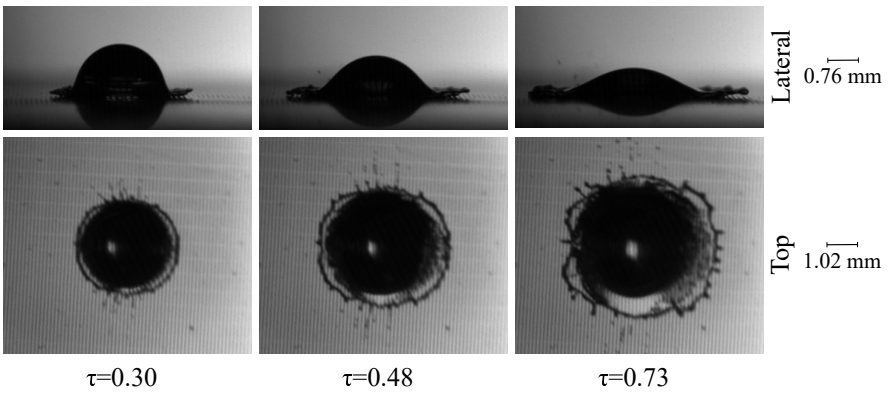

Figure 4.25: Directional prompt splash and crown splash with an incomplete crown for the isopropanol droplet impact onto a fully wettable ($\theta_{app} \approx 0°$) $S1$ Lexan® surface, $We = 400$.

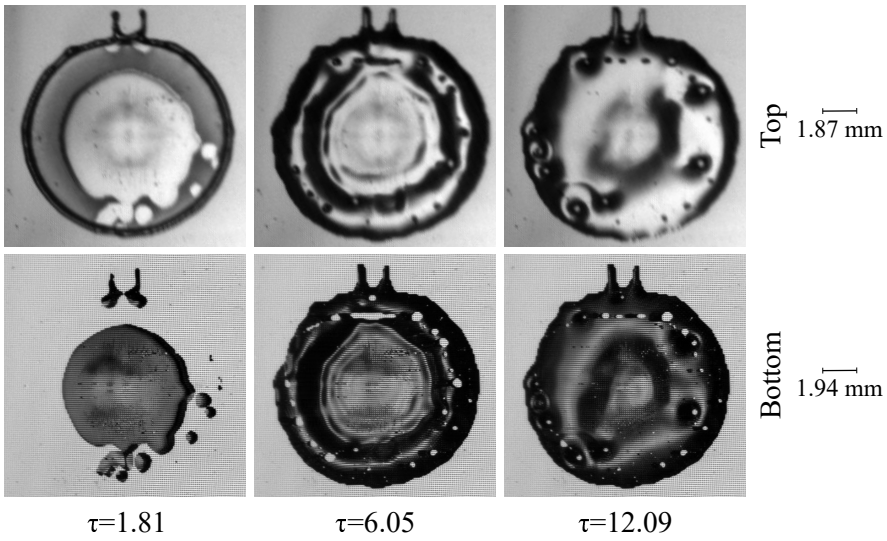

Figure 4.26: The "cookie effect" seen from the top and bottom perspectives for the isopropanol droplet impact onto a $S3$ Plexiglas® surfaces with $\theta_{app} \in [66° - 73°]$, $We = 400$.

mechanisms of these fingers should be investigated in future works.

Concluding, here are some remarks related to the second impact height tested, providing $We = 205$ and $Re = 6860$ for distilled water, and $We = 400$ and $Re = 1745$ for isopropanol. Large micro-structures can promote prompt splash while small micro-structures can inhibit it, possibly due to energy dissipation. Yet, the impact energy seems to be the most significant parameter to trigger splashing. The wettability of the surface has a major role in the receding phase. Increasing the apparent contact angle θ_{app} enhances the receding movement resulting in a partial rebound and also in the formation and breakup of finger-like structures during the receding phase. The micro-structured patterns influence the formation and orientation of the finger-like structures and also the crown and partial-crown liquid sheets. Additionally, the small interspaces favor the formation of heterogeneous wetting states.

Once more, the droplet falling height was increased creating a third set of impact conditions. The outcomes and their characteristics for the water droplet impacts are shown in Fig. 4.27 for $We = 385$ and $Re = 9360$. The occurrence of deposition decreased significantly and splashing is the dominant outcome, which can also be seen from the regime maps defining the deposition/splashing thresholds in Figs. 4.9, 4.10, and 4.11. For the fully wettable Lexan® surfaces $\theta_{app} \approx 0°$, three different outcomes were observed depending on the micro-structured pattern: deposition for $S4$, prompt splash for $S2$ and $S3$, and both prompt and crown splash for $S1$. Following the conclusions for the previous impact height h_2, splashing seems to be suppressed by the small interspaces in the $S4$ micro-structured pattern or by its higher roughness factor r, as can be seen in Fig. 4.9. An explanation might be that energy is dissipated inside the gaps within the micro-structures and not enough energy is left to promote splashing. On the other hand, for the micro-structured pattern $S1$ an incomplete crown is formed and the "button effect" is observed for both the $S3$ and $S4$ surfaces. Differently, the same outcome, prompt splash, is observed on the impact with fully wettable Plexiglas®

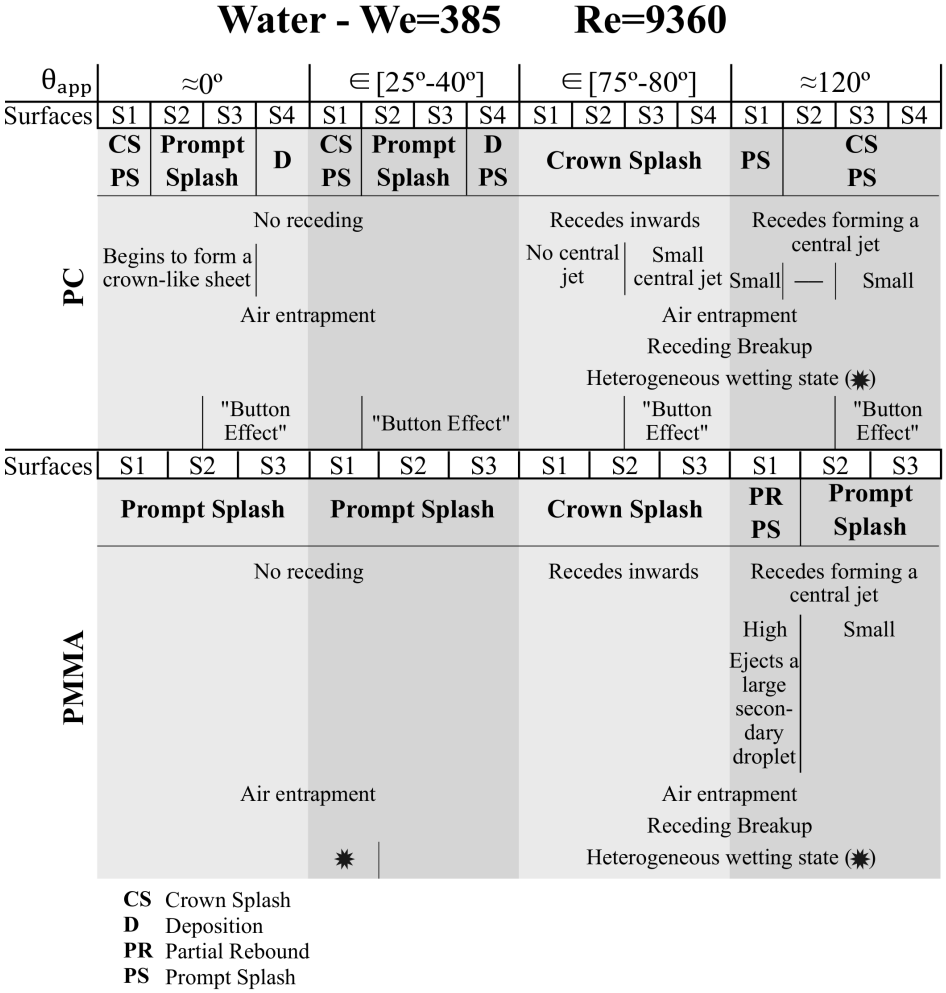

Figure 4.27: Description of the outcomes and their morphology depending on the surface wettability and the surface micro-structured pattern for PC and PMMA for the water droplet impact at the third impact energy tested, $We = 385$.

surfaces independent of the surface pattern. Finally, there is no receding movement, air is entrapped inside the liquid lamella, and heterogeneous wetting states are observed independent of the micro-structured pattern and material.

Slightly increasing the contact angle to $\theta_{app} \in [25° - 40°]$, the outcomes are the same except for the impact with $S4$ Lexan® surfaces where some events of prompt splash are also observed. Nonetheless, the characteristics of these outcomes are different than the previous wettability behavior. There is no receding movement, air is entrapped in the lamella, and a heterogeneous wetting state is observed for all cases.

For partially wettable surfaces $\theta_{app} \in [75° - 80°]$ crown splash is observed for all patterns and both materials. Many secondary droplets are ejected due to the burst of the incomplete crown sheets. For this wettability behavior, the receding phase is present and produces a receding breakup. Considering the impacts onto the Lexan® surfaces, the liquid lamella quickly recedes inwards, forming a small central jet for the micro-structured patterns $S3$ and $S4$. On the other hand, onto Plexiglas®, despite the quick receding, a central jet is not formed for

any micro-structured pattern. Another difference between these two materials is the wetting condition. The heterogeneous wetting state is observed in both materials but for Plexiglas® surfaces only small non-wetted points are observed from the bottom perspective as can be seen in Fig. 4.28. In the first stages at $\tau = 1.41$, the surface is non-uniformly wetted. With time ($\tau = 12.02$), the surface is practically fully wetted despite a few small points probably at the bottom of the gaps between the micro-pillars. Finally, at $\tau = 61.50$ large areas with no fluid are formed within the liquid lamella.

In the impact with hydrophobic surfaces $\theta_{app} \approx 120°$, splashing was observed for all cases. On the impact with Lexan®, all micro-structured patterns developed both prompt and crown splash except $S1$ where only prompt splash was observed. For surfaces made of Plexiglas® prompt splash was the obtained phenomena for all micro-structured patterns with only one exception which is $S1$ where also partial rebound was observed. The occurrence of crown splash is inhibited for this wettability behavior. Several finger-like structures were created but crown-like liquid sheets have not been formed. The spreading and receding velocities are very high due to the elevated impact velocity, which produces more receding breakup. During the receding phase, the liquid lamella becomes really thick, and a central jet is formed. Its size depends on the micro-structured pattern and the surface material. The only exception is the $S2$ Lexan® surface where no central jet is formed. Also, due to the high apparent contact angle θ_{app}, the heterogeneous wetting state is present for all cases. Regarding the fact that crown splash on Lexan® surfaces is only inhibited on the micro-structured pattern $S1$, a possible reason could be the greater magnitude of prompt splash that could weaken the crown sheet formation. The energy needed for the crown sheet formation might have been splashed away during the prompt splash. Finally, the analysis of why the $S1$ Plexiglas® surface is the only one that produces partial rebound, which could be related to the height of the central jet. In this case, the central jet is higher than in the other cases, which seems to be promoted by this specific micro-structured pattern, and that causes its breakup.

Moving on to the experiments with the same droplet falling height $h_3 = 0.70\,m$ but using isopropanol as droplet fluid, which resulted in impacts with $We = 715$ and $Re = 2315$. It is noticeable in Fig. 4.29 that splashing is enhanced by the increase in the impact energy. For fully wettable Lexan® surfaces, crown splash was observed for $S1$ and $S2$, and prompt splash for $S3$ and $S4$. Therefore, as shown previously in Fig. 4.9, surfaces with higher roughness factor

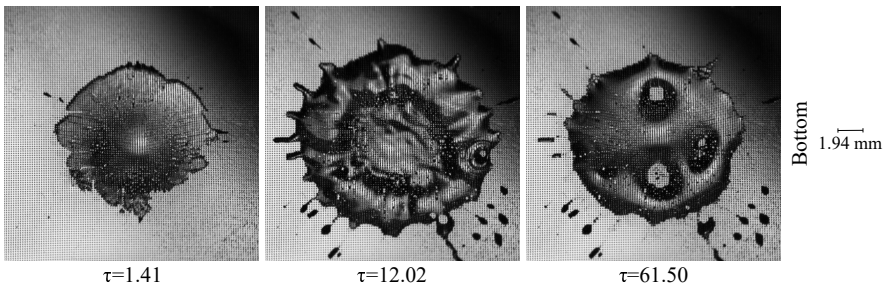

Figure 4.28: Heterogeneous wetting state with small non-wetted points seen by the bottom perspective for a water droplet impact onto a $S2$ Plexiglas® partially wettable surface, $\theta app \in [75° - 80°]$, $We = 385$.

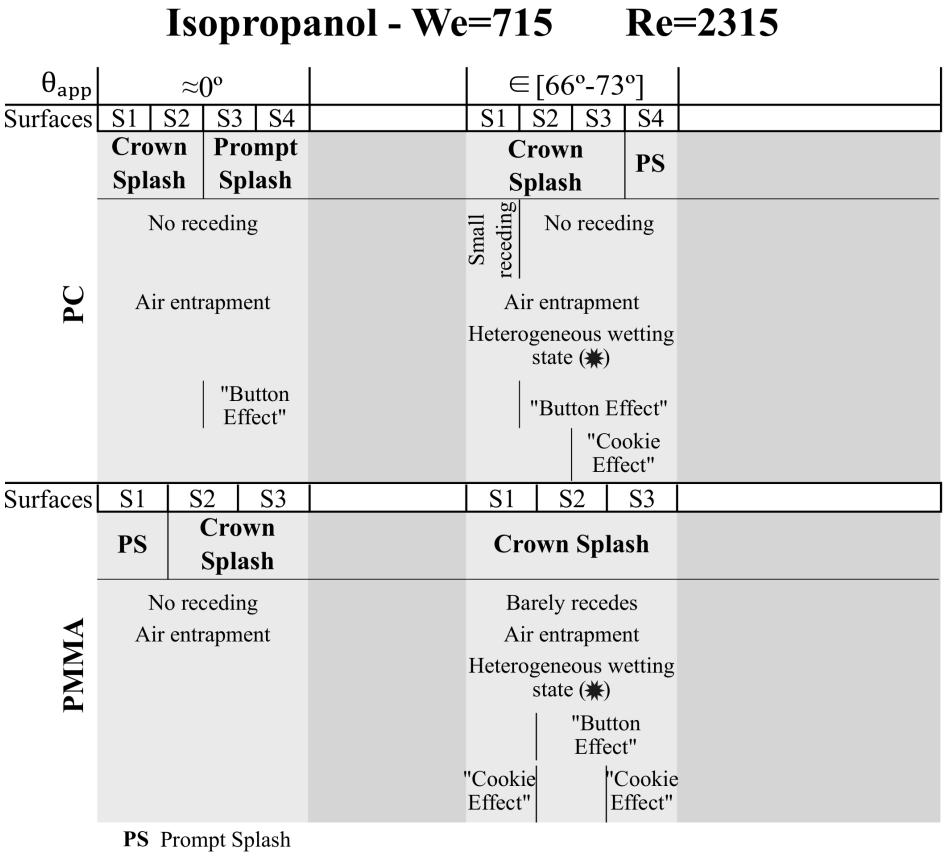

Figure 4.29: Description of the outcomes and their morphology depending on the surface wettability and the surface micro-structured pattern for PC and PMMA for the isopropanol droplet impact, $We = 715$.

r need more impact energy to produce splashing, thus a higher K_{mod}. The micro-structured patterns $S3$ and $S4$ have smaller interspaces, i.e. b, and energy might be dissipated in these spaces not allowing the crown sheet formation. At this impact energy and as can be seen in Fig. 4.30, the crown extent and duration are larger. On the contrary to prompt splash, which is formed normally to the length of the grooves, the crown liquid sheet is formed sideways, $\tau = 0.35$. The crown sheet keeps evolving sideways, $\tau = 0.79$, and the crown angle is larger than for lower impact energies. Later at $\tau = 1.15$, the crown liquid sheet breaks ejecting more secondary droplets. Finally, for this condition, the ”button effect” is well-defined for the micro-structured patterns $S3$ and $S4$.

For fully wettable Plexiglas® surfaces, crown splash was observed for all micro-structured patterns except $S1$. In this case, crown splash is inhibited for the micro-structured pattern composed of grooves, similar to the impact of water droplets onto hydrophobic Lexan® surfaces. Once again, the strongest magnitude of the prompt splash can suppress the formation of the thin crown liquid sheet. This impact energy might be a transition zone between prompt and crown splash since the formation of crown splash depends on specific conditions like the impact point. The heterogeneous wetting state is observed for both surface materials. As always, air is entrapped within the liquid lamella and the ”button effect” is observed for the micro-structured patterns $S3$ and $S4$ on Lexan® surfaces.

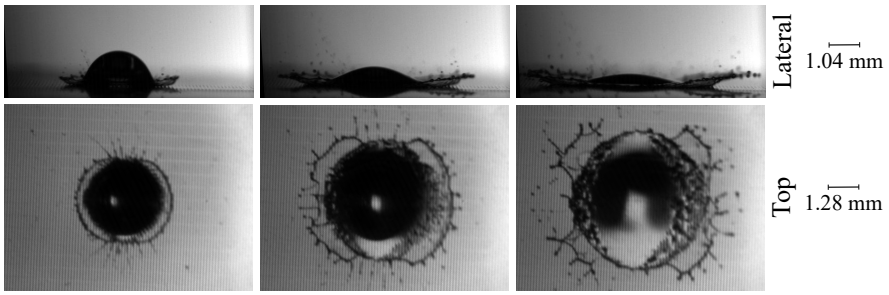

Figure 4.30: Prompt and crown splash seen from the lateral and top perspectives of an isopropanol droplet impinging onto a fully wettable $S1$ Lexan® surface at $We = 715$.

Increasing the apparent contact angle to $\theta_{app} \in [66° - 73°]$, crown splash is observed for all cases except in the impact with $S4$ Lexan® surfaces. A small receding movement is only noticeable for the micro-structured pattern $S1$ on Lexan®. The heterogeneous wetting state is observed for all cases and the "button effect" is observed for all micro-structured patterns except $S1$. On the other hand, the "cookie effect" is observed for all cases except $S2$.

Concluding, here are some remarks related to the third impact height tested $h_3 = 0.70\ m$, providing $We = 385$ and $Re = 9360$ for water, and $We = 715$ and $Re = 2315$ for isopropanol. The increase in impact energy resulted in splashing with a higher magnitude. However, for larger micro-structures, crown splash can be observed at lower impact energies. Nonetheless, they can also be able to suppress crown splashing if the magnitude of the prompt splash is too high and no fluid is left to form the crown liquid sheet.

The fourth and highest droplet falling height tested in this study is $h_4 = 1.30\ m$, which provided water droplet impacts at $We = 665$ and $Re = 12240$. Looking at Fig. 4.31, it is noticeable that crown splash is the dominant outcome. The droplet impacts with fully wettable surfaces $\theta_{app} \approx 0°$ resulted in crown splash for all the Lexan® (PC) surfaces and prompt splash for all the Plexiglas® (PMMA) surfaces. Once again, air is entrapped in the liquid lamella, there is no receding phase and the heterogeneous wetting state is present. The "button effect" is observed in the impact with $S3$ and $S4$ Lexan® surfaces.

Increasing the apparent contact angle to $\theta_{app} \in [25° - 40°]$, crown splash was observed for the patterns with larger micro-structures and prompt splash for the smaller ones, as shown in Fig. 4.31. The impact morphology is very similar to the fully wettable case.

In the experiments with the lower wettability behaviors, $\theta_{app} \in [75° - 80°]$ and $\theta_{app} \approx 120°$, crown splash is observed for all cases. Due to the elevated impact energy, the crown liquid sheet is complete. After the liquid lamella reaches its maximum spreading diameter, a receding phase follows generating a central jet for some micro-structured patterns. However, the partial rebound was never observed. An important finding of this study about the impact on micro-structured surfaces with different wettability behaviors and impact energies is that while increasing the impact energy, the tendency to produce partial rebound does not

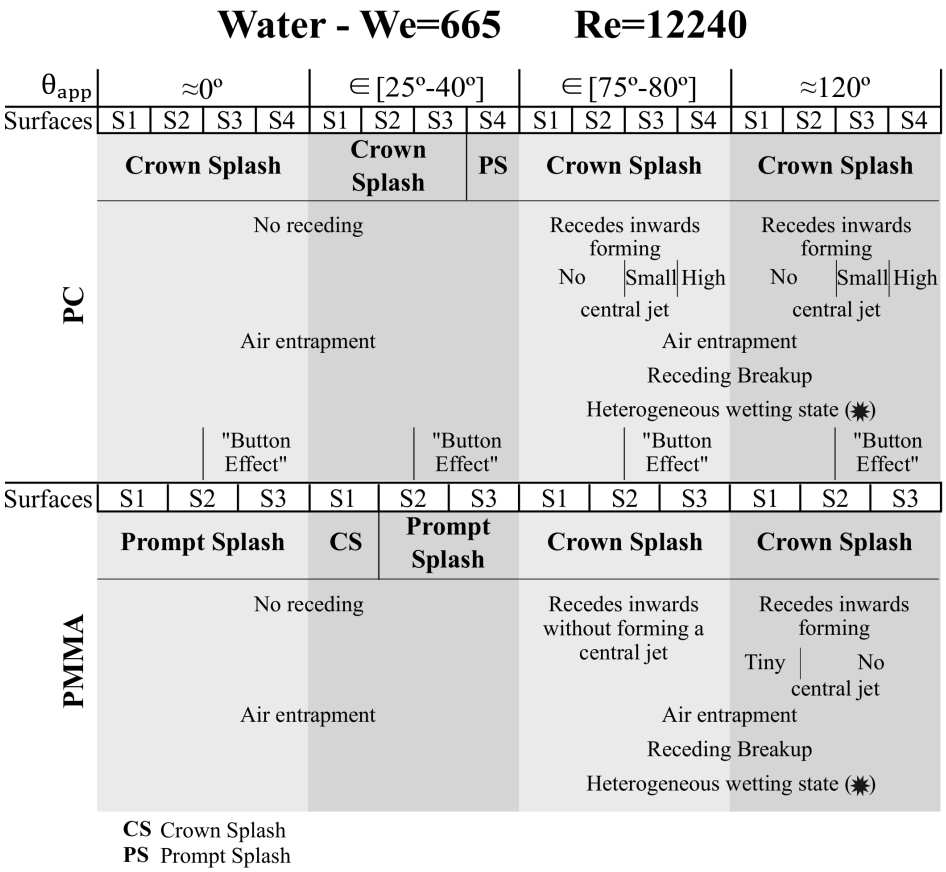

Figure 4.31: Description of the outcomes and their morphology depending on the surface wettability and the surface micro-structured pattern for PC and PMMA for the water droplet impact at the higher impact energy tested, $We = 665$.

increase. Contrary to what was observed in the literature for the impact with smooth surfaces. Moreira et al. [66] report that the tendency to observe partial rebound increases while increasing the impact velocity U_0. On smooth surfaces, the increase in the impact energy will increase the receding velocity, consequently increasing the height of the central jet and promoting its breakup and ejection of secondary droplets. However, the increase in the receding velocity on rough surfaces also results in the enhancement of the receding breakup. Therefore, not enough fluid is left to form a high central jet and this is what causes the suppression of partial rebound for droplet impacts on rough surfaces at high impact energies. Actually, for some droplet impacts with hydrophobic surfaces, the liquid lamella breaks into five or six smaller droplets during the receding phase. Therefore, it does not even form a central jet like observed in the lower impact energies.

To finish this analysis, a higher impact energy was also experimentally tested for the impact of isopropanol. This fourth droplet's falling height resulted in $We = 1165$ and $Re = 2955$ and the observed outcomes and correspondent morphology are described in Fig. 4.32. At this impact energy, the effect of the micro-structured patterns is not distinguishable anymore, originating the same outcomes with similar characteristics independent of the size and spacing of the micro-pillars. All experimental conditions resulted in crown splash and no receding phase is observed. Also, for $\theta_{app} \in [66° - 73°]$ the heterogeneous wetting state is

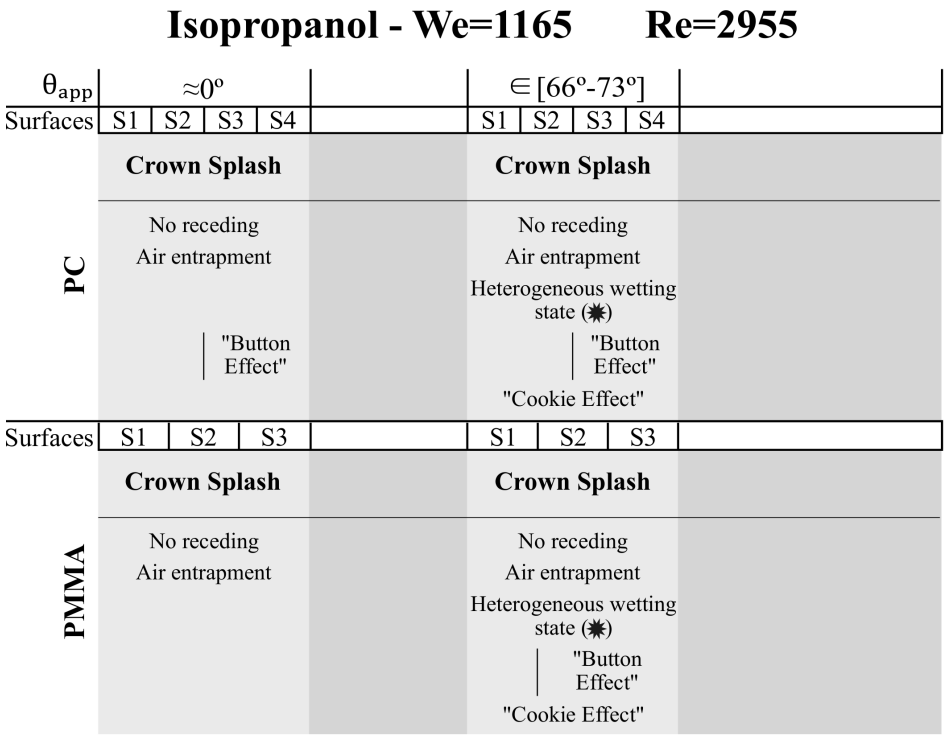

Figure 4.32: Description of the outcomes and their morphology depending on the surface wettability and the surface micro-structured pattern for PC and PMMA on the isopropanol droplet impact, $We = 1,165$.

achieved.

Concluding, here are some remarks related to the fourth impact height tested $h_4 = 1.30\ m$, providing $We = 665$ and $Re = 12240$ for water, and $We = 1165$ and $Re = 2955$ for isopropanol. The tendency to obtain rebound cannot be increased by increasing the impact energy, since at a certain point, the magnitude of the receding breakup does not even allow the formation of a central jet. On the other hand, the occurrence of crown splash is increased by increasing the impact energy. However, only for the cases where the magnitude of prompt splash leaves enough energy to allow the crown sheet formation. At considerably high impact energies, the effect of surface roughness seems to be neglected since all outcomes were similar independent of the micro-structured pattern.

4.3 Droplet Impact onto Liquid Surfaces

The second part of this thesis concerns the single droplet impact on liquid films. This is important for several applications, as mentioned in subsection 2.2.1. The work developed here follows the study performed in Ribeiro [70]. In this previous study, single droplet impact upon liquid films was experimentally tested to implement biofuels in civil aviation. Therefore, fuel mixtures were used as working fluids, and a wide range of impact parameters was tested. From these results, the accuracy of the transition criteria presented in the literature was evaluated. The results of this study will be presented and discussed in the first subsection.

Secondly, in the previous study of Ribeiro [70] a seldom known phenomenon was found, called bubble encapsulation. This phenomenon aroused attention and it was decided to study it in detail. Thus, more experiments were performed using the same fluids to increase the knowledge about bubble encapsulation. In the following, the occurrence and repeatability of bubble encapsulation will be assessed. Then, its phenomenologies will be described in detail, followed by a study related to the propagation of the first perturbation imposed on the liquid film. Additionally, the bubble geometry will be evaluated, and a threshold will be proposed to predict the onset of bubble encapsulation. Finally, the crown sheet angle seems to be an important parameter in determining the occurrence of bubble encapsulation and its evolution will be studied depending on the thickness of the liquid film.

4.3.1 How accurate are transition criteria?

The splashing mechanism is the most investigated throughout the years in the literature. The droplet is initially spherical on a typical vertical impact on a steady liquid film, and it does not suffer any deformation during the fall. Using precisely the same fluids, the effect of droplet initial deformation on the splashing dynamics was investigated and is described in Ferrão et al. [7]. However, due to the interaction between the droplet and the airflow before impact, the droplet is deformed and assumes different shapes before impact that will affect its outcome. From this study, it is concluded that spherical droplets promote splashing while deformed droplets promote spreading.

The physical processes involved in fuel combustion include fuel atomization and impact, followed by evaporation. The mixture preparation, which includes the impact on dry and wet surfaces, is recognized as of major importance. The fuel combustion efficiency is optimized by the secondary atomization produced by splashing.

There are many correlations proposed in the literature to predict the transition boundary between spreading and splashing for single droplet impact upon dry and wetted surfaces, as explained in subsection 2.3.1 and in subsection 2.4.2. In an attempt to assure the universality of some of these empirical correlations establishing a spread/splash transition boundary for single droplet impact onto a wetted liquid film, the phenomena obtained in a previous experimental work [70] were compared with the phenomena predicted by these transition criteria. All models considered were designed for the impact of spherical droplets upon a liquid film, establishing a limit between the spreading and splashing regimes. The morphology of splashing includes the formation of a crown, a rim in its upper bound and due to instabilities in this rim, a cusp can emerge that eventually disintegrates into secondary droplets.

The empirical correlations that categorize the outcomes of droplet impact depend on dimensionless parameters such as the Weber (We), Reynolds (Re), Ohnesorge (Oh), and Laplace (La) numbers. Most empirical correlations follow a relation between Weber and Reynolds

numbers expressed as

$$Re^{\alpha}We^{0.8} = K_c \quad (4.13)$$

where K_c is the criterion between a droplet spreading and splashing.

In this study, the transition criteria developed by Bai and Gosman [80], Cossali et al. [39], Tropea and Roisman [59], and Vander Wal et al. [40] were considered. Table 4.1 shows the different transition criteria and the correspondent validation ranges in terms of the Reynolds number Re and the dimensionless thickness of the liquid film δ_f.

The criterion of Bai and Gosman [80] was the first threshold selected from the literature and considers droplet impact onto a wetted surface equivalent to its impact on a very rough surface ($r_s > 12$ μm). The data used to develop this spread/splash boundary can be traced back to the original contribution of Stow and Stainer [81] with experiments within the range of $8000 < Re < 33600$.

The second criterion considered was developed by Cossali et al. [39], which considers the influence of the liquid film thickness in the impact outcome. To enlarge their experimental data, they used not only pure water but also mixtures of glycerol and water, thus, increasing the range of thermophysical properties of the fluids. Additionally, they used different dimensionless film thicknesses ($\delta_f = h_f/D_0$) in their experiments. The validation range of this criterion includes $428 < Re < 1828$ and $0.1 < \delta_f < 1.0$.

Tropea and Roisman [59] developed the third correlation considered in this study. Their criterion includes a random element through the mass ratio η. This mass ratio can be above 1 in the sense that part of the liquid film may contribute to the mass of secondary droplets emerging from the splash. Actually, Bai and Gosman [80] consider a similar random element in the numerical model of spray impingement as $\eta = 0.2 + 0.9\, rnd(0,1)$. A value of $K_c = 2800$ is suggested by Roisman and Tropea [127], corresponding to $\eta \approx 0.58$. However, no proper explanation is given for using this value.

Finally, the last deposition/splashing threshold considered was developed by Vander Wal

Table 4.1: Transition criteria for single droplet impact upon liquid films.

Reference	**Exponent** α	**Criterion,** K_c	Re **Validation Range**	δ_f **Validation Range**
Bai and Gosman [80]	0.3584	1136.7	$8000 - 33600$	†
Cossali et al. [39]	0.4	$2100 + 5880 \cdot \delta_f^{1.44}$	$428 - 1828$	$0.1 - 1$
Tropea and Roisman [59]	0.4	$2823.6 + 357.7 \ln\left(\frac{\eta}{1.2-\eta}\right)$ ‡	$150 - 3184$	–
Vander Wal et al. [40]	0.272	756.7	$988 - 13900$	0.1

† Bai and Gosman [80] consider a wetted condition equivalent to the impact on a very rough surface.
‡ with $\eta = m_s/m_0$ as the mass ratio between the mass of secondary droplets produced by splash and the mass on the initial impinging droplet.

et al. [63]. They used their own data to fit the correlation using different fluids, providing a wide range of impact conditions. However, they only tested impacts with thin liquid films ($\delta_f = 0.1$).

Figure 4.33 plots the criteria synthesized in Tab. 4.1 showing the measurement region of this study, the region for the Cossali et al. [39] correlations depending on the dimensionless liquid film (δ_f or δ) and the region for the Tropea and Roisman [59] correlation depending on η. The correlations have a similar logarithmic slope, except the one proposed by Vander Wal et al. [63]. In scale, the correlation of Vander Wal et al. [63] is close to the dimensionless film thickness condition of $\delta = 0.1$. Nonetheless, their experiments covered a wider range of Reynolds, eventually, leading to a lower influence of Re, as the corresponding exponent points with its lower value.

Figure 4.34 shows info-graphics identifying the accuracy of the different transition criteria in comparison to the experimental results of this study. In these experiments, despite the fuel mixtures, distilled water is also tested as a reference fluid. In these graphics, the impact conditions are identified, being the fuel mixtures described by their concentration of jet fuel in volume. The increase in the droplet initial diameter (D_0) and droplet impact velocity (U_0) are established through arrows. The agreement between the experimental results and the criteria is described by a color scheme. Black represents the cases where the phenomena obtained experimentally agree with the criteria, white displays the cases where the phenomena

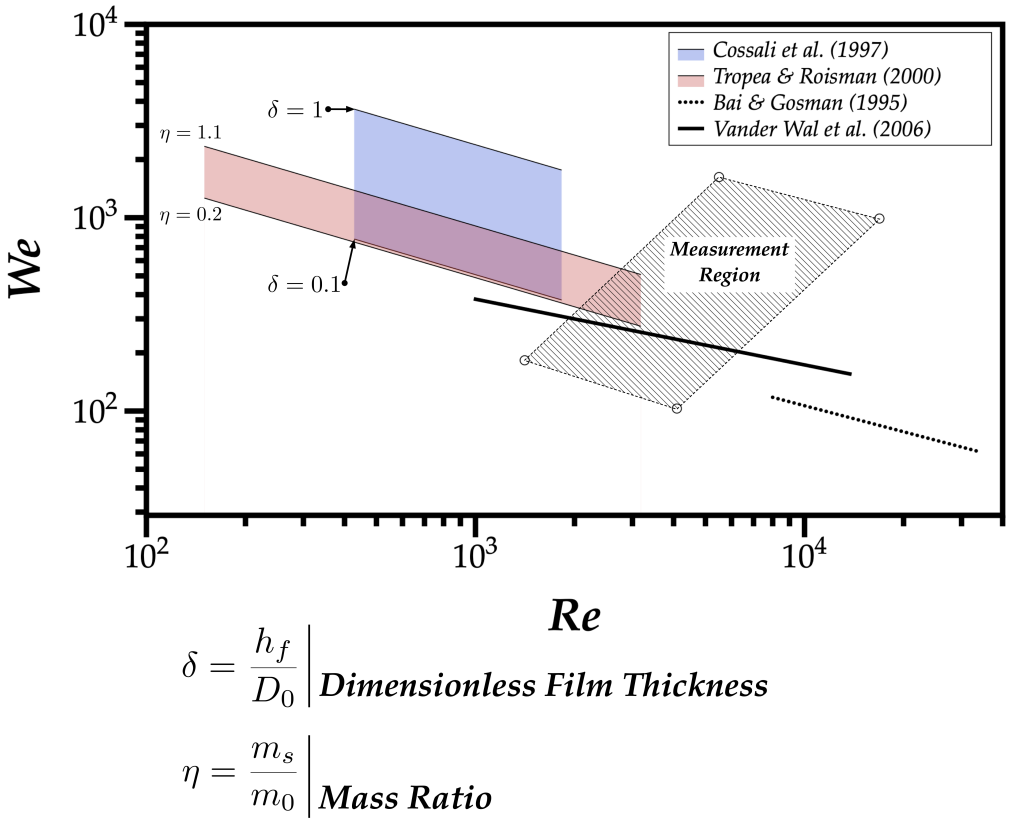

Figure 4.33: Transition criteria between spread and splash after drop impact onto a liquid film.

obtained experimentally do not agree with the predicted outcome, and grey defines the cases outside the validation range of empirical correlations.

The validation range of the Bai and Gosman [80] empirical correlation only fits a small part of the experimental data. Namely, its validation range only predicts some events of pure water and 100% Jet A-1. However, it agrees 100% with these results, correctly predicting the outcome.

The transition boundary proposed by Cossali et al. [39] is the only one considered that includes the influence of the liquid film thickness, δ_f. Another important detail is the fact that the experimental data used to define this correlation includes a wide range of liquid film thicknesses. Similarly to the previous criterion, it only fits part of the data. Only the impact conditions of the two fuel mixtures fit the validation range of this correlation. Therefore, considering only the cases within the validation range, 78% are correctly predicted by the Cossali et al. [39] spread/splash transition boundary. This criterion fails mostly for higher liquid film thicknesses and higher impact velocities.

On the other hand, the empirical correlation of Tropea and Roisman [59] includes a random element in the determination of the mass ratio. This value was assumed as $\eta = 1$ and the outcome of these experiments was compared with the correlation predictions within its validation range. The only fluid that can not be predicted by this correlation is water. Looking at Fig. 4.34, it can be observed that this transition boundary correctly predicts 80% of the cases. For the lowest impact velocity, it fits all data except four events with the lowest droplet initial diameters for the mixture with 75% Jet fuel and 25% HVO. Additionally, for the intermediate impact velocity, it only fits the second-highest droplet initial diameter for the mixture with 50% of each type of fuel. Besides, for the higher impact velocity, all cases within the validation range are correctly predicted by the empirical correlation developed by Tropea and Roisman [59].

The empirical correlation of Vander Wal et al. [40] is the final transition criterion that will be evaluated and is the most recent. It was developed by considering only experiments of single droplets impinging on thin liquid films. Therefore, its validation range only fits the experiments for the thinner liquid film thickness, $\delta_f = 0.1$. This transition boundary correctly predicts 95% of the experiments and only fails for the smaller diameters and lower impact velocities on the impact with the fuel mixtures.

If we restrict the use of these correlations to their validation ranges, the transition criterion that better predicts the outcomes of this experimental study about single droplet impact onto liquid films using conventional and alternative fuels is the one developed by Bai and Gosman [80] since it fitted 100% of the experiments within its validation range. Nevertheless, the criteria of Cossali et al. [39] and Tropea and Roisman [59] have a similar prediction accuracy $\approx 80\%$. The criterion developed by Cossali et al. [39] is the only one that considers the influence of the liquid film thickness δ_f, yet, its prediction capability decreases for high

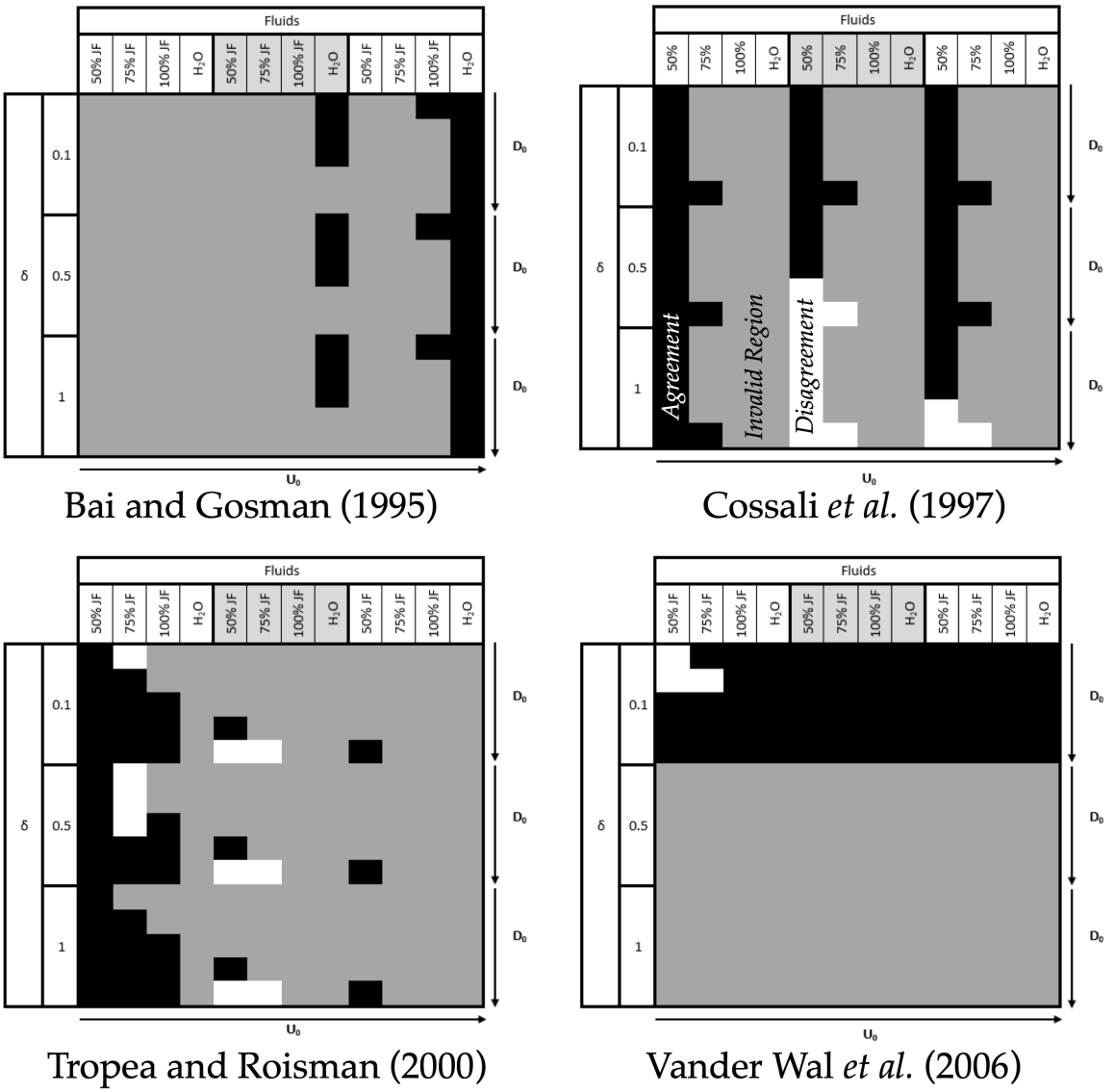

Figure 4.34: Comparison of the experimental results with the proposed transition criteria established by Bai and Gosman [80], Cossali et al. [39], Tropea and Roisman [59], and Vander Wal et al. [40] within their validation ranges. Color scheme: Black - the phenomena obtained experimentally agree with the criteria; White - the phenomena obtained experimentally do not agree with the predicted outcome; Grey - do not belong within the validation range of that criterion.

Reynolds numbers Re and dimensionless film thicknesses δ_f. Finally, the Vander Wal et al. [40] boundary is focused on thin liquid films. Its accuracy is very high and only fails for the smaller droplet diameters for both fuel mixtures. In summary, the assumption of Bai and Gosman [80], that a liquid film behaves as a very rough surface is, in fact, valid. Additionally, it is considered that the Vander Wal et al. [40] spread/splash threshold should include a range of dimensionless film thicknesses in order to universalize the criterion.

However, a question arises: How far can we extrapolate these transition criteria to assess their universality? The use of dimensionless numbers in the criteria allows their use for impact conditions completely different from their validation range. Considering this, Fig. 4.35 shows an info-graphic where the results were compared with the different transition criteria in regions outside their validation domain. Similarly to Fig. 4.34 the impact conditions are identified, as well as, the increase of droplet initial diameter (D_0) and droplet impact velocity (U_0), established by the arrows.

Now, the agreement between the experimental results and the criteria is described by a new color scheme. Black represents the cases where the phenomena obtained experimentally agree with the criteria within the validation range, white displays the cases where the phenomena obtained do not agree with the predicted outcome within the validation range, grey defines the cases where the phenomena obtained agree with the criteria outside the validation range, and beige represents the cases where the phenomena obtained do not agree with the predicted outcome outside the validation range. There are also two cases identified with an "R", which means rebound. Since rebound is not included in the phenomena predicted by these correlations, it was decided to identify them differently.

The fitting of the different criteria changed significantly by considering all the experimental data. The criterion proposed by Bai and Gosman [80] predicts correctly 83% of the data. This shows that the efficiency of the correlation decreases significantly when compared with data outside its validation range. On the other hand, Cossali et al. [39] predict correctly 74% of the results. Therefore, its prediction capability decreased but not substantially. This empirical correlation predicts better the impact on the thinner liquid films ($\delta_f = 0.1$). However, this is the only criterion that considers the influence of the dimensionless liquid film thickness, therefore, it should fit the different dimensionless thicknesses.

The empirical correlation of Tropea and Roisman [59] fits correctly 89% of the cases and shows the best agreement for high Weber numbers We. For this criterion, the prediction capability increased when considering events outside its validation range. Finally, the criterion of Vander Wal et al. [40] fits 93% of the cases, being the one that better predicts the outcomes of these experiments. This threshold only failed for the lowest impact velocities U_0 and the lowest droplet initial diameters D_0.

Looking at Fig. 4.35, it is concluded that the threshold developed by Vander Wal et al. [40] is the one that shows the best universality, being capable of correctly predicting the events out-

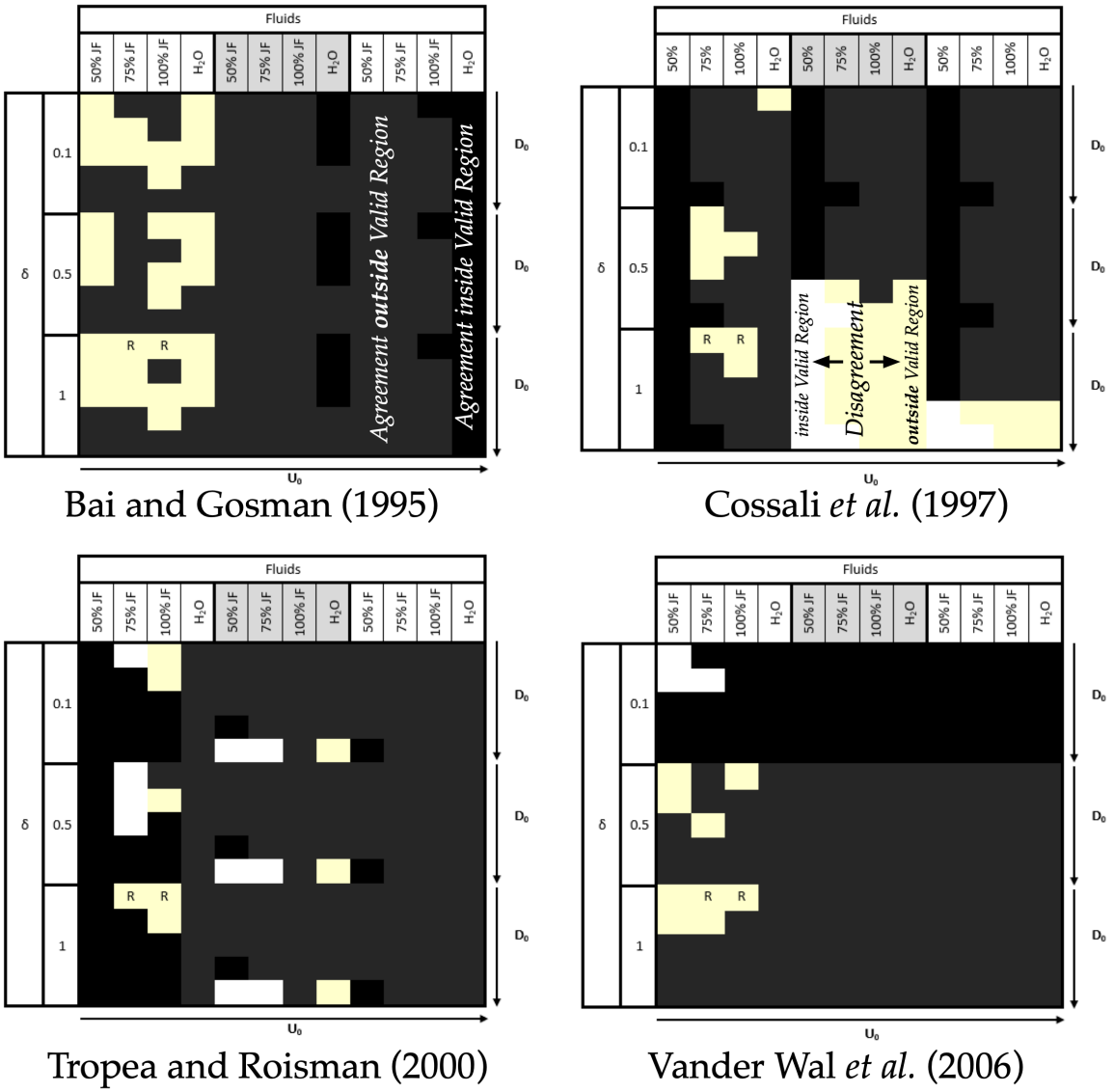

Figure 4.35: Comparison of the experimental results with the proposed transition criteria established by Bai and Gosman [80], Cossali et al. [39], Tropea and Roisman [59], and Vander Wal et al. [40]. Color scheme: Black - the phenomena obtained experimentally agree with the criteria within the validation range; White - the phenomena obtained experimentally do not agree with the predicted outcome within the validation range; Grey - the phenomena obtained experimentally agree with the criteria out of the validation range; Beige - the phenomena obtained experimentally do not agree with the predicted outcome out of the validation range.

side its validation range. Therefore, a question arises: What is so special about Vander Wal et al. [40] criterion? This threshold proved to be a universal criterion, but it does not even account for the influence of the dimensionless liquid film thickness δ_f. Remembering the insight from Fig. 4.33, the correlation of Cossali et al. [39] which includes the influence of the dimensionless liquid film thickness δ_f, shows that thicker liquid films lead to a shift into higher Weber numbers We. This happens since the energy required to generate splashing is higher. Assuming the same principle in the experiments performed by Vander Wal et al. [40], it is expected that more experiments with thicker liquid films lead to similar results. Figure 4.36 plots the experimental results obtained for each dimensionless liquid film thickness tested and the empirical correlation of Vander Wal et al. [40]. The white symbols represent

the spreading cases and the black symbols the splashing ones. The Vander Wal et al. [40] correlation is identified by the solid black line. If we consider $K_c = f(\delta_f)$, and proportional to it, even in a nonlinear form, an increase of K_c while keeping the logarithm slope constant, should improve the prediction capability of this splashing threshold. Therefore, for $\delta_f = 1$, a test with a 15% increase of K_c, identified by the dashed black line, validates this hypothesis. However, to refine this criterion, much more experimental research is needed.

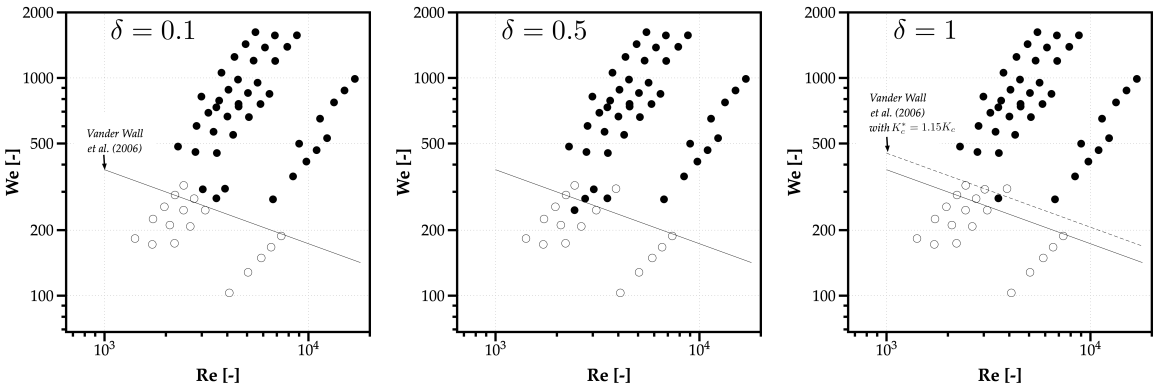

Figure 4.36: Experimental results in the present work and the Vander Wal et al. [40] empirical correlation. In the case of $\delta_f = 1$, we plotted a qualitative curve representing an increase of 15% in the splashing criterion value K_c.

4.3.2 Bubble encapsulation

This subsection is focused on the complex phenomenon of bubble encapsulation. As mentioned in subsection 2.4.1, it is seldom reported in the literature. Therefore, it seemed important to enhance the knowledge about this hydrodynamic phenomenon and investigate its occurrence and characteristics. Using high-speed imaging, this phenomenon is observed from two different perspectives. The common lateral perspective and a bottom perspective, which provided more insight into this scarcely studied phenomenon.

First, the occurrence and repeatability of bubble encapsulation are investigated. Then, it focuses on the features related to the bubble formation after a single droplet impact upon a thin liquid film. These features include phenomenology, crown sheet angle, bubble geometry, the thickness of the hemispherical thin sheet, and the cavity underneath the bubble. The influence of dimensionless film thickness on the first perturbation imposed on the steady liquid film and on bubble geometry is also studied. Finally, an empirical correlation was adapted attempting to predict the onset of bubble encapsulation.

4.3.2.1 Occurrence and Repeatability of Bubble Encapsulation

In previous studies [70], bubble encapsulation was observed for the dimensionless film thickness of $\delta_f = 0.5$ and the droplet impact velocity of $U_0 = 4.2\ m/s$ using a mixture with 75% Jet A-1 and 25% NExBTL. The first goal was to understand if this event was random or if 100% repeatability could be obtained. Therefore, 10 experiments were performed to investigate this matter. In these 10 events, 100% repeatability was guaranteed for this set of impact

conditions. Figure 4.37 shows an image sequence with bubble encapsulation captured from a lateral perspective. Here, it is possible to observe the main hydrodynamic structures for different dimensionless time instants after impact with $\tau = tU_0/D_0$, where t is time after the moment the droplet touched the liquid film defined as $t = 0\ s$. These images were acquired with an angle of $\approx 10^{\circ}$ with the horizontal plane. The camera was only inclined for visualization imaging. In the remaining experiments, the camera was parallel to the horizontal liquid film.

Right after impact on a steady liquid film, the droplet prompt splashes ($\tau = 0$), followed by the formation of an uprising crown liquid sheet producing secondary droplets from instabilities in its bounding rim ($\tau = 14$). In the first stages, the uprising sheet propagates almost normally to the liquid film, but the radius of the crown base continues to expand. This will eventually lead to the inward gradual closing of the crown-bounding upper rim. Several secondary droplets are ejected by the fingering breakup at the top of the crown. Their size is proportional to the transient accumulation of mass in the rim as the splashing mechanism unfolds. The crown sheet walls bend inwards leading to its inward collapse at $\tau = 42$. It is also possible to identify the shapes of capillary waves propagating on the crown liquid sheet. The closure of the crown at the top entraps air and starts forming a bubble-like shape ($\tau = 56$), and in this case, two jets ($\tau = 70$). One jet moves upwards and the other in a downward direction. While the upward jet eventually stops and recedes due to gravitational forces, the downward jet reaches the horizontal liquid film ($\tau = 98$), attaches to it, stretches, and detaches from the top at the hemispheric thin-sheet ($\tau = 126$ and $\tau = 140$). After this detachment, a fully formed bubble remains on the liquid film, $\tau = 210$.

Meanwhile, many secondary droplets strike the bubble dome ($\tau = 252$) and one of them will eventually break the dome, which generates even more secondary droplets ($\tau = 291.2$). These secondary droplets will impinge immediately on the liquid film inducing more perturbations ($\tau = 294$). As time evolves, the perturbations cease and the liquid film returns to the initial steady condition.

Motzkus et al. [74] stated that the bubble hemispherical thin-sheet progressively becomes thinner and more susceptible to break due to the impact of secondary droplets previously created by the crown splash. The wavy pattern observed at $\tau = 210$ in Fig. 4.37 evidences the draining of liquid from the bubble thin-wall to the liquid film.

Figure 4.38 shows the evolution of the crown liquid sheet until closure. A phenomenological feature worth mentioning is the constant height of the crown liquid sheet that propagated first in the direction normal to the liquid film ($\tau \leq 4.2$). The uprising sheet walls reach the maximum height in a relatively short timescale ($\tau = tU_0/D_0 < 5$), but the crown base still has enough radial momentum to grow into a diameter larger than its upper bounding rim. However, the hydrodynamic reason for keeping the upper rim in a fixed position can only be the supply of liquid through the vertical crown liquid sheet. During the radial expansion for $4.2 < \tau < 25.9$, this height remains unaltered, as shown in Fig. 4.38, but also the crown

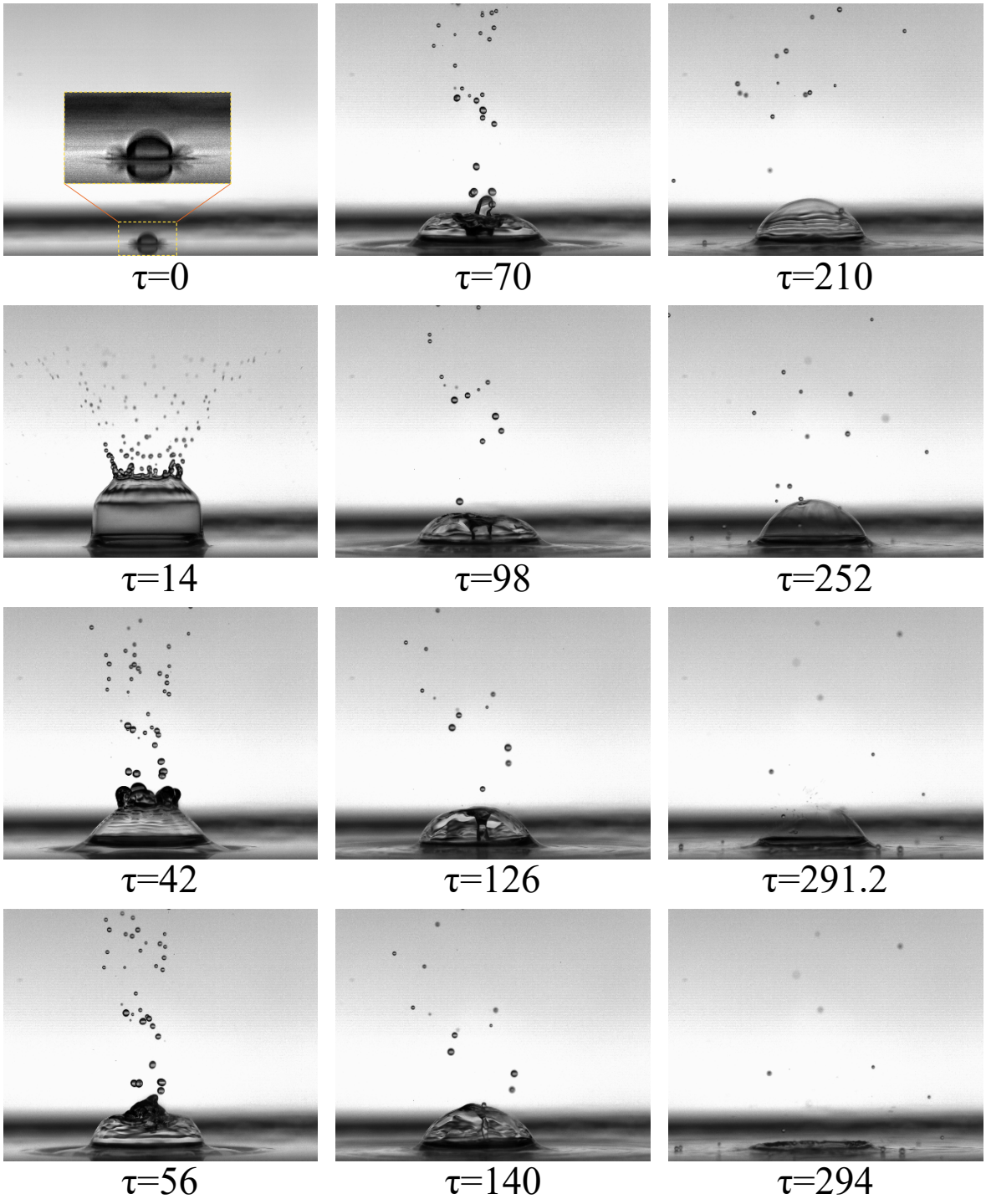

Figure 4.37: A sequence of images showing bubble encapsulation for the following impact conditions: 75% JF/25% HVO, D_0=3.0 mm, $U_0 = 4.2\ m/s$, and $\delta_f = 0.5$.

angle at $90°$. Considering the constant height, Wang and Chen [64] also observed a perpendicular uprising of the crown wall relative to the horizontal liquid film for the dimensionless film thickness of 0.5. They considered a higher Weber number ($We_D = 2010$), but a six times significantly lower Reynolds number ($Re_D = 1168$), implying a role played by viscous forces allowing a radial expansion of the crown base. Additionally, Fedorchenko and Wang [61] reported that the crown sheet angle depends entirely on the liquid film thickness, regardless of the impact velocity and liquid physical properties. Nonetheless, they stated that for $\delta_f \geqslant 0.25$ the angle is constant and equal to $90°$. Furthermore, recently Lamanna et al. [128] showed that the viscous losses are negligible during the spreading phase but only in the early stage of crown propagation. However, while decreasing the liquid film thickness they become increasingly significant.

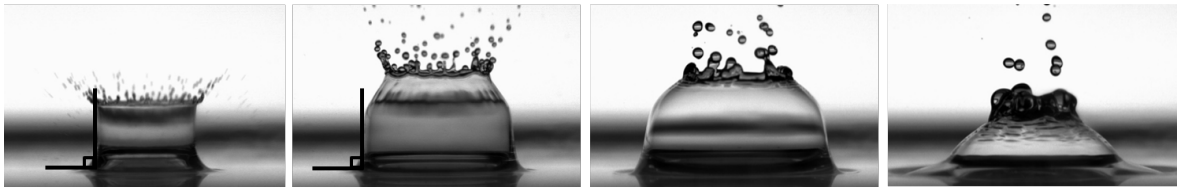

Figure 4.38: Evolution of the crown sheet angle during the formation of bubble encapsulation.

The morphological structures associated with the crown dynamics leading to bubble encapsulation seem related to the expansion of the annular crown base and the mass transfer in the crown liquid sheet. Therefore, the phenomenon was observed from a bottom perspective to investigate its dynamics. Accordingly, the high-speed digital camera was mounted below the glass supporting the Perspex container, proving the sequence of images presented in Fig. 4.39. It is important to remember that only one high-speed digital camera was available and the images in Fig. 4.37 and Fig. 4.39 do not correspond to the same droplet impact, but two separate droplet impacts with the same initial impact conditions.

The droplet impinges upon the steady liquid film ($\tau = 0$), and shortly after, the crown sheet rises and starts bending inwards ($\tau = 14$), as visualized by the bounding rim of the crown sheet pointed by the arrow. Figure 4.40 shows in detail the first stages of the impact from a bottom perspective, including illustrations of the lateral perspective. It shows a different experiment than the one in Fig. 4.39 to emphasize the fact that due to the manual triggering of the imaging system, the first frame of impact has a slight variation from experiment to experiment. The white in the image implies the light is transmitted through a stagnated liquid film. Once the droplet approaches the liquid film, and after its impact, the curvature reflects light and produces a shadow [129]. After impact, the fingering structures typical of a prompt splash are visible, and the thin white circular line sets the beginning of the kinematic discontinuity forming the uprising crown. The white spot in the middle of the first image results from the convergence of light at the top hemisphere of the impinging droplet, which works as a focal lens. This small spot enlarges as the droplet mixes with the liquid film,

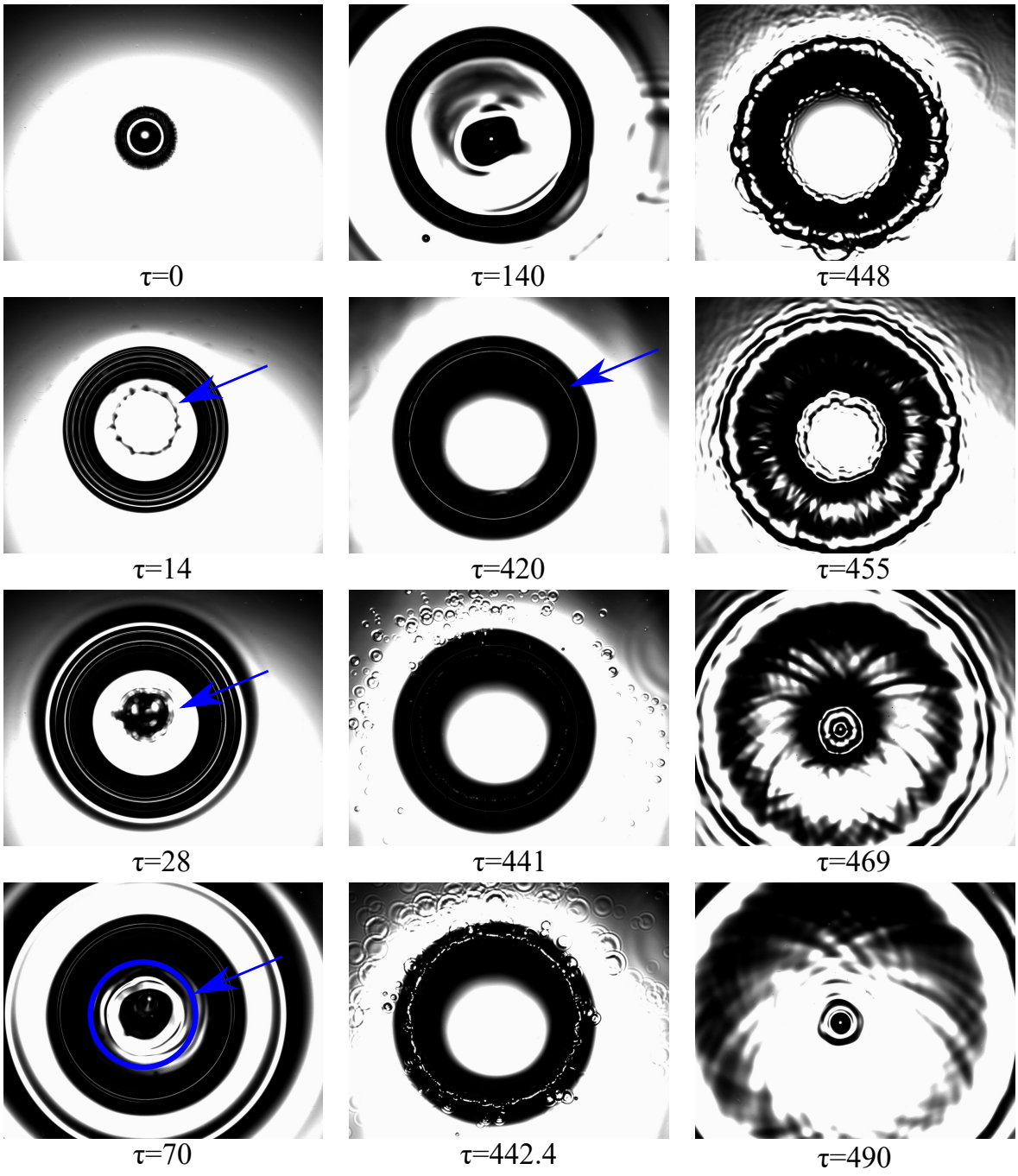

Figure 4.39: Sequence of images showing bubble encapsulation from below for the following impact conditions: 75%JF/25% HVO, $D_0 = 3.0\,mm$, $U_0 = 4.2\,m/s$, and $\delta_f = 0.5$.

but the thin line thickens due to the inner curvature of the splashing uprising crown. The third image illustrates the complete immersion of the impinging droplet into the liquid film forming a disc-shaped crater. The shadow is proportional to the size of the perturbed liquid film forming the base that sustains crown development.

Returning to Fig. 4.39, the crown sheet height keeps increasing and capillary waves begin forming from the crown liquid sheet at its bottom [85]. For high-impact velocities and a combination of fluid thermophysical properties and dimensionless film thickness, the crown walls continue to expand at the base after the crown has reached its maximum height. This implies that the timescale of crown formation is shorter than the timescale of its base expansion. Then, the crown sheet closes by the increase of mass of the crown rim fed by the liquid sheet, plus surface tension forces at $\tau = 28$, as pointed by the arrow. At $\tau = 70$, in the center (delimited by a circle), the dark area corresponds to the downward jet connecting to the bottom of the crater (see frames $\tau = 70$ and $\tau = 98$ of Fig. 4.37 showing this morphology from the side). From this perspective, nothing can be concluded about the existence of the upward jet. There are also waves developing from the impact site to the undisturbed liquid film identified by the difference between black, grey, and white areas since the light transverses differently depending on whether the curvature of the liquid film is concave or convex. The downward jet continues its motion to the liquid film ($\tau = 140$). In this frame, it is easily observed the bubble-thin liquid sheet by the large white circle, and the jet by the darker circle in the middle. Later, the downward jet detaches from the thin-liquid dome, forming an empty bubble, identified by the thin white circumference within the dark circle, pointed by the arrow at $\tau = 420$. The frame $\tau = 210$ in Fig. 4.37 shows the same morphology from a lateral point of view. At this time, the liquid film is almost steady, and the dark portion of the circle identifies the curvature of the bubble dome attached to the liquid film.

Bubble lifetime further depends on small local instabilities, but also on the impingement of tiny secondary droplets on the dome. In this case, the bubble breaks at $\tau = 441$ by reaching the critical thickness of the hemispherical liquid sheet or by the impingement of a tiny secondary droplet (frame $\tau = 252$ in Fig. 4.37). It is not possible to identify the cause of the bubble bursting from this point of view. The following frames show the perturbations imposed on the liquid film by the bubble bursting. The capillary waves generated by the impact of tiny secondary droplets propagate and interact with each other creating complex patterns. The evolution of the pattern created at the liquid film by the breakup of the bubble is shown in frames $\tau = 448$ to $\tau = 490$. From the bottom perspective, it is possible to observe the capillary waves' behavior and understand their evolution within and outside the area delimited by the pre-existing bubble dome. In the study of Yu et al. [130], it is also possible to observe these capillary waves but from a top perspective.

By virtue of the bottom images, it is possible to accurately measure the bubble diameter and also the diameter and velocity of the first perturbation imposed on the liquid film by the droplet impact. Comparing both sequences of images (Fig. 4.37 and Fig. 4.39) is easy to infer that the phenomena or timescales are different. However, the bubble's lifetime strongly

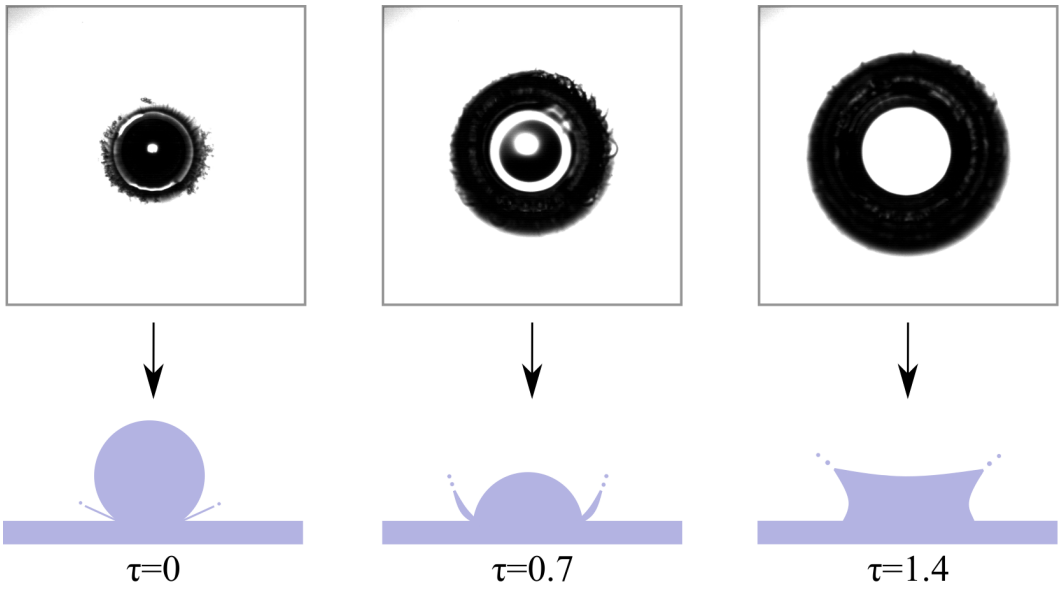

Figure 4.40: First stages of impact seen from the bottom perspective with schematics of the correspondent images from the lateral perspective. Length scale resolution of $31.5\ \mu m/pixel$.

depends on the number of secondary droplets that can puncture the bubble's dome when its thickness is thin enough.

4.3.2.2 Phenomenologies of Bubble Encapsulation

During the experiments, different impact conditions led to different phenomenologies in the bubble formation. These differences are related to the jet formation and evolution from the crown closure point. In summary, there are three different paths to obtain the same outcome - bubble encapsulation. Figure 4.41 shows the evolution of the phenomena morphology depending on the three different phenomenologies identified:

- Phenomenology 1 - formation of a downward jet after the crown closure, Fig. 4.41 (a);
- Phenomenology 2 - formation of a downward and an upward jet on the crown closure point, Fig. 4.41 (b);
- Phenomenology 3 - formation of a downward and an upward jet on the crown closure point, combined with the ejection of large droplets due to the upward jet breakup, Fig. 4.41 (c).

Figure 4.37 is an example of the phenomenology 2. The initial stages of phenomenology 1, shown in Fig. 4.41 (a) are similar to phenomenology 2. However, in this phenomenology at $\tau = 56$ only a downward jet forms, instead of two in opposite directions. As time evolves, the liquid is drained by the jet ($\tau = 112$) to the liquid film until its detachment from the hemispherical sheet's top ($\tau = 133$), forming an empty bubble at $\tau = 175$.

On the other hand, phenomenology 3, Fig. 4.41 (c), has exactly the same formation as phe-

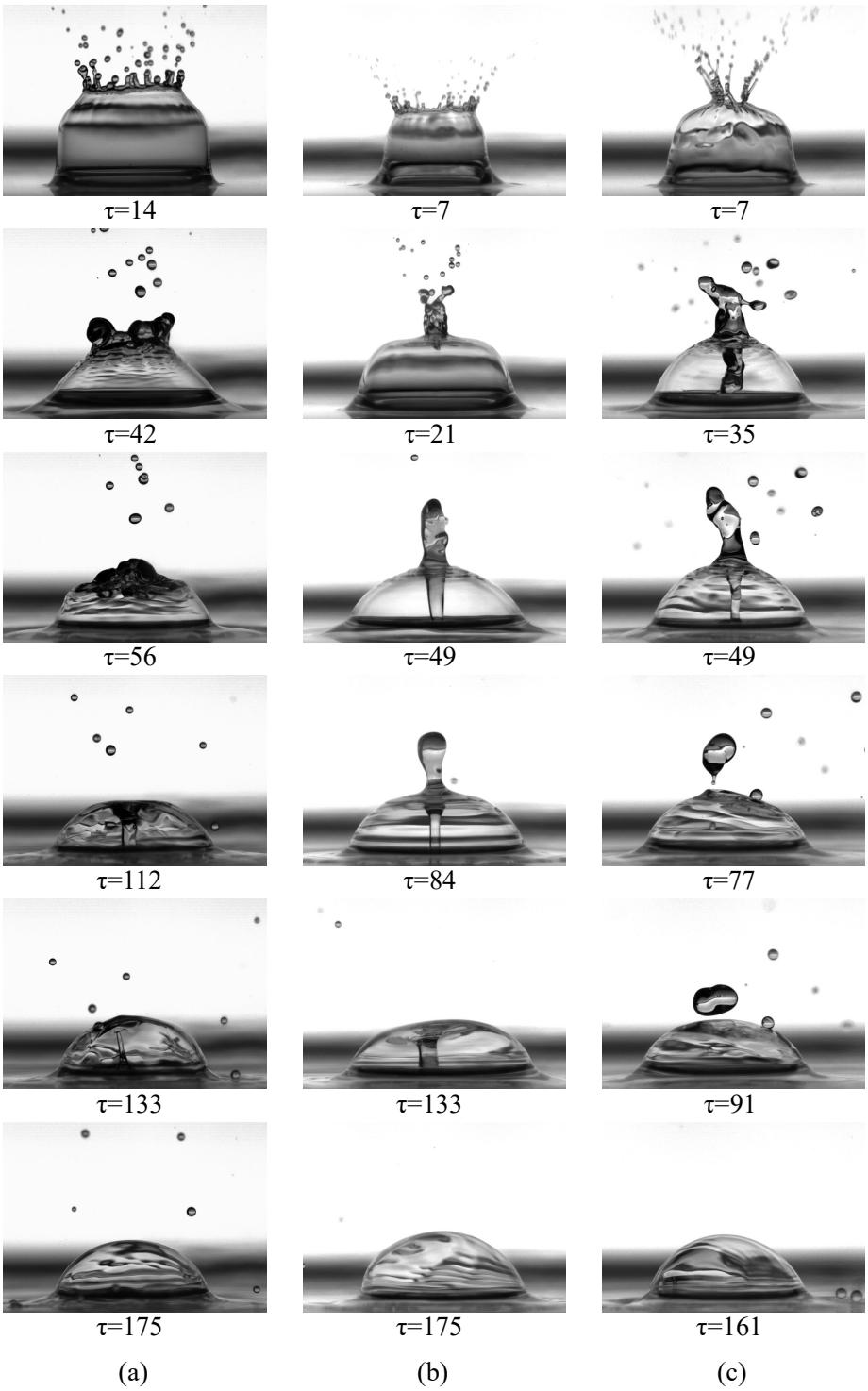

Figure 4.41: Different phenomenologies during bubble formation for a $3.0\ mm$ droplet of 75% jet fuel/25% HVO mixture at $U_0 = 4.2\ m/s$ and $We_D = 1650$: (a) Phenomenology 1 - only a downward jet is formed by the crown closure for $\delta_f = 0.5$; (b) Phenomenology 2 - both a downward and an upward jet are formed on the crown closure point for $\delta_f = 0.6$; (c) Phenomenology 3 - both a downward and an upward jet are formed on the crown closure point, combined with the ejection of large droplet due to the breakup of the upward jet $\delta_f = 0.4$.

nomenology 2, but due to the excess of kinetic energy, the upward jet is larger ($\tau = 49$). Consequently, it breaks into a large secondary droplet ($\tau = 77$), which heavily falls on the hemispherical dome. In some cases, it merges with the liquid sheet or slips from the hemispherical walls towards the liquid film, or in a few cases, the large secondary droplet immediately breaks the bubble.

After validating the 100% occurrence of bubble encapsulation for the impact conditions of $We_D = 1650$, $Re_D = 6956$, and $\delta_f = 0.5$, more experiments were made keeping the same impact conditions except for the dimensionless thickness of the liquid film δ_f to assess its influence. This dimensionless film thickness was varied between $0.1 \leq \delta_f \leq 1.0$ with intervals of 0.1. From this study, 100% repeatability of bubble encapsulation was guaranteed for $0.4 \leq \delta_f \leq 1.0$. On the other hand, for the thinner liquid film thickness $\delta_f = 0.1$ no event of bubble encapsulation was observed, only prompt and crown splash. The phenomenon was too quick to allow crown closure. Finally, for $\delta_f = 0.2$ and $\delta_f = 0.3$ less than 50% of the experiments originated bubble encapsulation.

Table 4.2 shows the different phenomenologies observed depending on the dimensionless thickness of the liquid film for $0.4 \leq \delta_f \leq 1.0$, which correspond to the 100% occurrence of bubble encapsulation. For $0.6 \leq \delta_f \leq 1.0$ only phenomenology 2 was detected on the 10 experiments performed. On the other hand, for $\delta_f = 0.4$ all three different phenomenologies were observed, and for $\delta_f = 0.5$ phenomenologies 1 and 2 coexist. Additionally, the dimensionless bubble formation time $\tau_{bubble} = t_{bubble}U_0/D_0$, with t_{bubble} being the formation time of the bubble, was measured and included in Tab. 4.2. For the events where only phenomenology 2 was observed the dimensionless bubble time seems to decrease while increasing the dimensionless film thickness δ_f, which may be caused by the increased liquid volume of the crown. Regarding, $\delta_f = 0.4$ and $\delta_f = 0.5$ since different phenomenologies coexist, it is difficult to conclude about the dimensionless bubble formation time.

For $0.4 \leq \delta_f \leq 1.0$ the crown sheet angle seems almost perpendicular to the horizontal liquid film for all the cases, as shown in Fig. 4.38. Therefore, the crown sheet angles obtained agree with Fedorchenko and Wang [61] conclusions. On the other hand, it is verified that a crown sheet angle normal to the horizontal liquid film is not restricted to $\delta_f = 0.5$ as Wang and

Table 4.2: Phenomenologies observed depending on the dimensionless film thickness δ_f and the correspondent dimensionless bubble formation time τ_{bubble}. The uncertainty values are absolute and obtained with a confidence interval of 95%.

δ_f	phenomenology	τ_{bubble}
0.4	1, 2, 3	80.8 ± 9.4
0.5	1, 2	134.2 ± 5.7
0.6	2	155.0 ± 9.7
0.7	2	107.8 ± 11.7
0.8	2	101.6 ± 11.4
0.9	2	90.7 ± 4.8
1.0	2	90.7 ± 3.9

Chen [64] reported. The crown sheet angle will be studied in detail in subsection 4.3.2.6. According to Pan et al. [73], the closure of the crown depends on the balance between the upward motion of the liquid sheet and the downward pull of gravity. Therefore, it could be expected that reducing the thickness of the liquid film can reduce the enclosing of the crown sheet since the inertia of the uprising liquid sheet weakens. These experiments validate this assumption since bubble encapsulation never occurred for $\delta_f = 0.1$ and only some events were observed for $\delta_f = 0.2$ and $\delta_f = 0.3$. Moreover, increasing the dimensionless film thickness apparently leads to thickening the hemispherical liquid sheet, as visualized in Fig. 4.42 and it extends the time until the bubble bursts, Geppert et al. [76] also detected this.

Regarding a possible boundary for the bubble encapsulation occurrence, many more experiments are necessary including more fluids, impact velocities, and initial droplet diameters. Proposing a correlation to predict the onset of bubble encapsulation is one of the goals of this study. Therefore, more experiments were performed and will be presented ahead. Nevertheless, for this fluid, 75% Jet A-1 - 25% NExBTL, bubble encapsulation forms at a minimum Weber number of $We_D = 1650$ for $\delta_f \geq 0.2$, and with 100% occurrence for $\delta_f \geq 0.4$. Returning to the results described in the literature, Pan et al. [73] observed bubble encapsulation for $We_D \geq 2570$ and $\delta_f > 1$, and for $We_D \geq 4000$ for thinner liquid films. Additionally, Geppert et al. [76] saw this phenomenon for $We_D > 1100$ and $\delta_f \geq 0.2$. Considering all the studies reviewed, none of them considered other dimensionless numbers than the Reynolds and Weber numbers. Therefore, the only comparative element present in all studies is the minimum Weber number for the bubble encapsulation occurrence combined with the dimensionless film thickness used. This justifies the search for a boundary that predicts bubble formation since the Weber number excludes the effect of viscous forces that may play a relevant role in the radial expansion of the crown base. Thus, as a starting point, the Ohnesorge number is proposed as a better dimensionless number for developing a criterion for bubble encapsulation since it correlates inertia, surface tension, and viscous effects on the phenomenon's morphology. Figure 4.43 compiles a preliminary map with the points setting the onset of bubble encapsulation for the available data.

The cavity formed underneath the bubble and the physical parameters that govern bubble encapsulation are worthy of attention. Several research studies presented in the literature are focused on the cavity shape and evolution [71, 72, 73, 131, 132]. However, in this work,

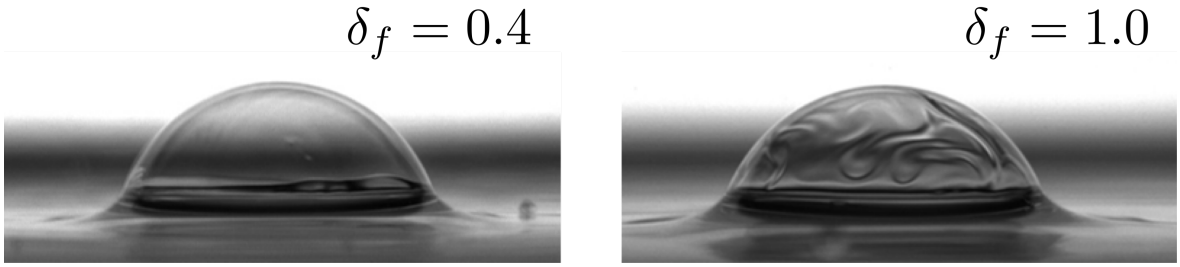

Figure 4.42: Bubble hemispherical sheet becomes thicker by increasing the dimensionless film thickness.

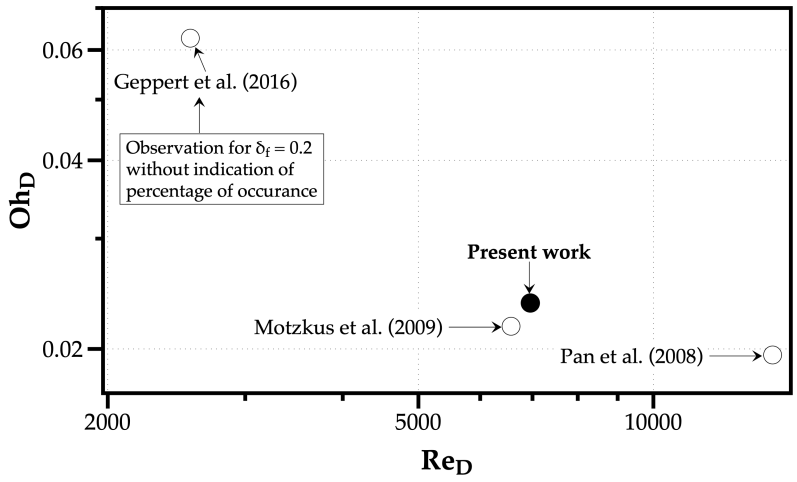

Figure 4.43: Reynolds-Ohnesorge map synthesizing the points analyzed in this work, and by other authors, where bubble encapsulation was observed.

visualization results confirm that bubble encapsulation is independent of the formation of a hemispherical crater. Instead, the cavity morphological development seems determined by the thickness of the liquid film with its hydrodynamics. For deep pools, the cavity formed is usually hemispherical [131]. However, If the liquid film is thin ($\delta_f < 1$), the impact crater collides with the solid surface at the bottom, as shown in Fig. 4.44.

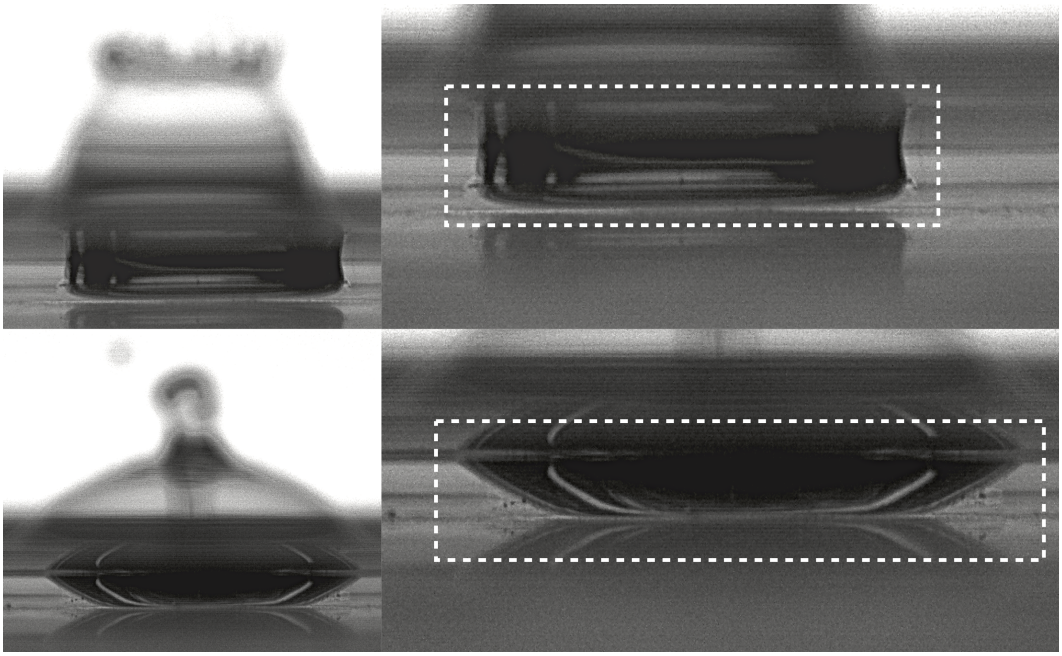

Figure 4.44: Cavity shape during crown sheet development (top) and during bubble encapsulation (bottom), evidencing its collision with the solid surface.

After droplet impact on a thin liquid film, the cavity immediately touches the bottom of the container, eventually inducing capillary instabilities on the morphological structures leading to bubble encapsulation. Roisman et al. [133] mentioned that capillary waves arrive on the surface of the cavity and a similar event seems present. At first, while the crown sheet ascents, the cavity assumes a cylindrical shape and touches the bottom of the container. As

the crown sheet wall bends and closes the cavity becomes round at the sides, but still touches the bottom. This shows that it is not necessary to have a fully developed cavity or a specific cavity shape to allow the formation of bubble encapsulation.

4.3.2.3 Propagation of the First Perturbation Imposed on the Liquid Film

When a single droplet impinges upon a steady liquid film, it creates a wave perturbation that spreads radially along the liquid film. In this study, the first perturbation imposed on the steady liquid film by the droplet impact is considered the first wave propagating on its free surface. The propagation of the first perturbation corresponds to a significant part of the encapsulated bubble size formed in a short time interval in comparison to the total interval that takes to form the bubble. Additionally, the prediction of the first perturbation propagation velocity and diameter is of great interest for numerical modeling applications. The bottom images were used to accurately measure the diameter and velocity of the first perturbation on the liquid film.

The dynamics of bubble encapsulation found in a previous work [70, 134] were numerically simulated by Vasconcelos et al. [135]. In their 2D axisymmetric simulations, the crown liquid sheet bends inwards but it never closes. Evidence on how the dynamic behavior of the first perturbation generated by droplet impact evolves with time can help improve the numerical simulations in order to reproduce this phenomenon. The first $12\ ms$ after impact were considered to measure the propagation diameter and velocity for each dimensionless liquid film thickness between 0.4 and 1.0. Figure 4.45 shows the evolution of the first perturbation, which is identified at $\tau = 0$ by the red circle.

Several authors [39, 136, 137] scale the crown radius growth by $D_c^* = D_c/D_0 \sim \tau^{1/2}$, being D_c the crown diameter. However, in their cases, the crown angle with the plane of the liquid film (α_c) is smaller than $\pi/2$. Having a crown angle superior to $\pi/2$ is a required step toward the morphology of bubble encapsulation. Considering $D_p(t)$ as the diameter of the first perturbation, Fig. 4.46 (a) shows the growth of the first perturbation diameter, normalized by the droplet impact diameter ($D_p^* = D_p/D_0$), and Fig. 4.46 (b) shows the growth of the first perturbation velocity, normalized by the droplet impact velocity ($U_p^* = U_p/U_0$). A preliminary analysis of the evolution of the propagation velocity of the first perturbation pointed

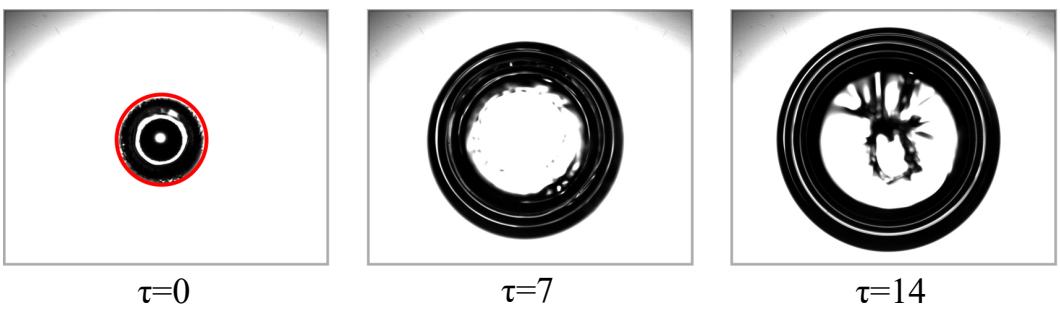

Figure 4.45: Sequence of images illustrating the propagation velocity of the first perturbation on the liquid film delimited by the red circle in the first frame.

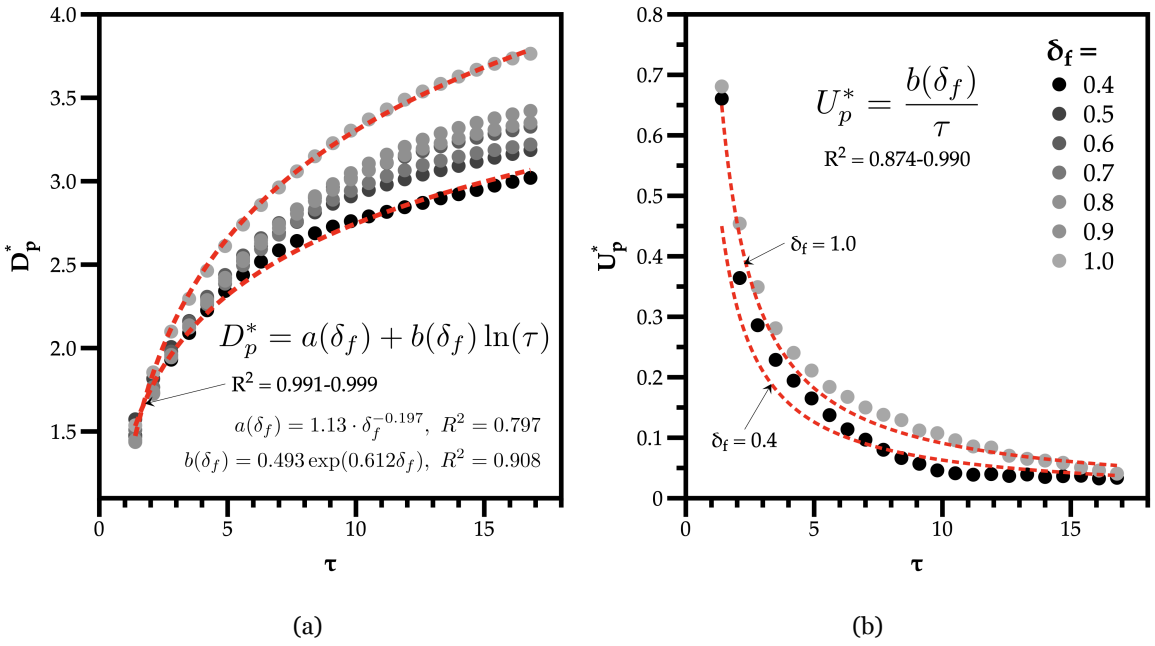

Figure 4.46: Evolution of the normalized (a) diameter of first perturbation (D_p^*) and (b) velocity (U_p^*). The curves fitting D_p^*, which depend on the logarithm of time and dimensionless film thickness, are used for modeling U_p^*.

to $U_p^* = U_p/U_0 \sim \tau^{-1}$, since $dD_p^*/d\tau = U_p^*$, it suggested an evolution for the first perturbation diameter scaled by $D_p^* \sim \ln(\tau)$. Additionally, without physical boundaries, this first perturbation has no upper limit in its growth. Although, it is physically expected its damping in time while propagating, which is the physical meaning mathematically expressed by the natural logarithm.

The empirical modeling outcome of the perturbation diameter evolution considers a growth depending on the logarithm of dimensionless time τ and dimensionless film thickness δ_f as

$$D_p^*(\delta_f, \tau) = a(\delta_f) + b(\delta_f)\ln(\tau) \qquad (4.14)$$
$$a(\delta_f) = 1.13\delta_f^{-0.197}$$
$$b(\delta_f) = 0.493\ e^{0.612\delta_f}$$
$$\text{valid for } 0.4 \leq \delta_f \leq 1.0$$

The normalized velocity of the first perturbation results in

$$U_p^* = \frac{dD_p^*}{d\tau} = \frac{b(\delta_f)}{\tau} \qquad (4.15)$$

The results show the validity of this approach.

Figure 4.47 shows a comparison between the experimental D_p^* and U_p^* with the values obtained from Eqs. (4.14) and (4.15), evidencing the accuracy of the empirical approaches explored. These results are useful for future modeling of drop impact conditions leading to bubble encapsulation.

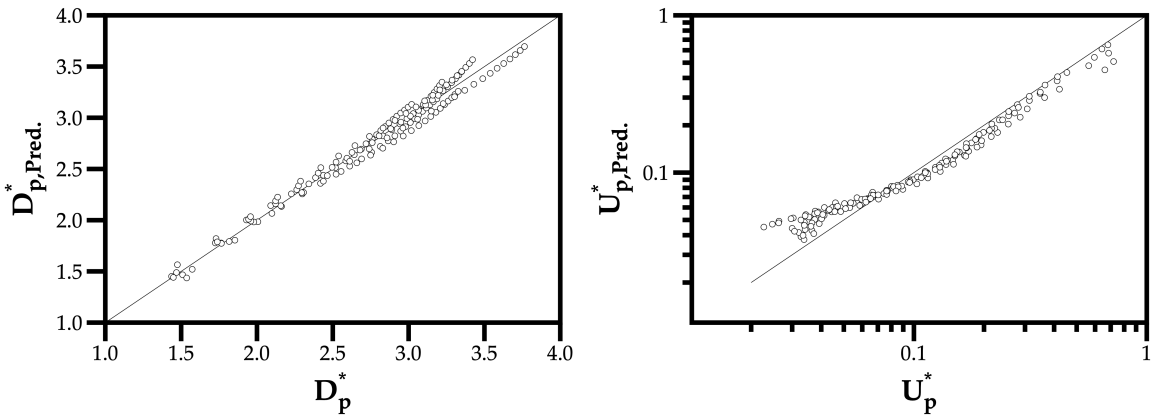

(a) (b)

Figure 4.47: Comparing the experimental results for (a) D_p^* and (b) U_p^* with the predictions based on the logarithm of time growth of the first perturbation diameter.

4.3.2.4 Bubble Geometry

The next step of this study includes the analysis of the bubble geometry. The two most evident geometry features of an encapsulated bubble are the bubble height (h_B) and diameter (D_B). To measure the bubble height, the images taken from the side were used, and for the bubble diameter the images from below, as illustrated in Fig. 4.48.

Considering the experimental parameter space, it allows the investigation of the influence of the dimensionless film thickness δ_f on these two features of bubble encapsulation. Since the initial droplet diameter D_0 and impact velocity U_0 are constant during all the experiments, they can be used as scaling parameters. Table 4.3 shows the measured bubble height h_B and diameter D_B, as well as, the dimensionless bubble height h_B^* and diameter D_B^*, depending on the dimensionless thickness of the liquid film δ_f. Additionally, the values of the bubble height and diameter are plotted in Fig. 4.49 depending on the dimensionless film thickness δ_f.

Table 4.3: Bubble height h_B, dimensionless bubble height h_B^*, bubble diameter D_B and dimensionless bubble diameter D_B^* for the different dimensionless film thickness δ_f. The uncertainty values are absolute and obtained with a confidence interval of 95%.

δ_f	$h_B[mm]$	h_B^*	$D_B[mm]$	D_B^*
0.4	7.2 ± 0.009	2.4	17.0 ± 0.008	5.7
0.5	7.1 ± 0.024	2.4	18.5 ± 0.016	6.1
0.6	7.2 ± 0.010	2.4	19.0 ± 0.018	6.3
0.7	6.9 ± 0.005	2.3	16.9 ± 0.021	5.6
0.8	7.2 ± 0.007	2.4	16.7 ± 0.010	5.5
0.9	6.9 ± 0.006	2.3	17.0 ± 0.016	5.6
1.0	7.2 ± 0.002	2.4	17.7 ± 0.018	5.9

The propagation velocity of the first perturbation imposed on the steady liquid film depends

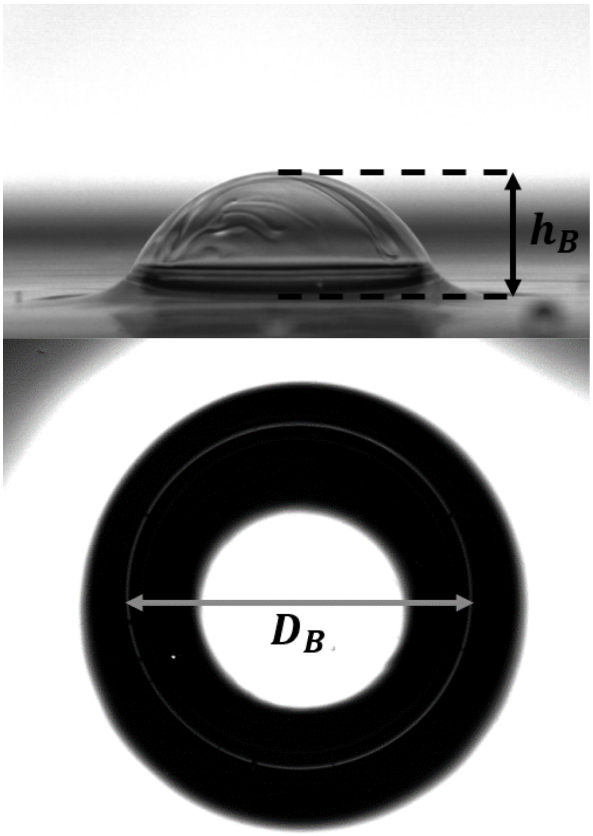

Figure 4.48: Measurements of bubble height (h_B) and diameter (D_B).

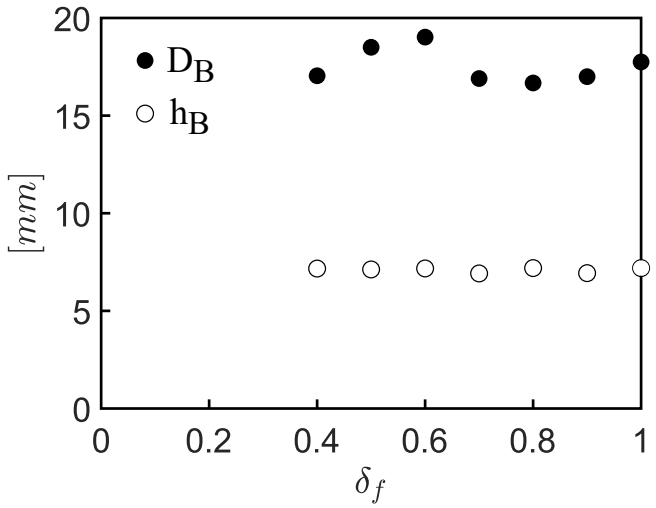

Figure 4.49: Bubble height h_B and diameter D_B depending on the dimensionless thickness of the liquid film δ_f.

on the dimensionless film thickness δ_f. However, the results for the bubble height h_B and diameter D_B did not show the same behavior. Both values are similar for all cases, independently of the dimensionless film thickness for $0.4 \leq \delta_f \leq 1$. The bubble diameter D_B shows a slight variation since it increases until $\delta_f = 0.6$ then decreases until $\delta_f = 0.8$, and finally slightly increases again until $\delta_f = 1.0$. However, the values are close to each other and it is not possible to distinguish any trend. As for the bubble height h_B, it is nearly constant. When normalized by the droplet initial diameter D_0, the normalized bubble height results in $h_B^* = h_B/D_0 = 2.4 \pm 0.03$, and the normalized bubble diameter in $D_B^* = D_B/D_0 = 5.8 \pm 0.07$. This suggests that the initial impact energy could play a major role in the characteristic size of the bubble. Therefore, different impact energies should be tested in future works to assess which dominant features influence the bubble size.

4.3.2.5 Onset of bubble encapsulation

As explained in the last subsections, the phenomenon of bubble encapsulations always occurs for certain impact conditions. This means that its probability of occurrence is equal to the unity $p = 1$. However, as mentioned before in subsection 4.3.2.2, there are cases where $p < 1$. To calculate its probability of occurrence 10 experiments were performed for each set of impact conditions. With the goal of finding a correlation that can predict the onset of bubble encapsulation, a wide range of impact conditions was experimentally tested to investigate its probability of occurrence. This study aims to answer the following questions: What promotes this phenomenon? Can we relate this phenomenon with any existent correlations found in the literature?

The answer to these questions is relevant since the creation of bubble encapsulation needs to be avoided in applications involving spray painting. However, in applications involving spray cooling and fuel injection, the enlargement of the atomization process due to bubble bursting can be beneficial. Therefore, a wider parameter space was experimentally tested, Tab. 4.4. Figure 4.50 shows a regime map on the bubble encapsulation occurrence depending on the Reynolds number Re_D and the Ohnesorge number $Oh_D = \sqrt{We_D}/Re_D$, since it relates the viscous to the inertial and surface tension forces. In Fig. 4.50 by varying the impact energy (Re_D), a band associated with the emergence of bubble encapsulation appears. This implies that there are two transition boundaries: 1) a transition from splash to bubble encapsulation; 2) another transition returning to the splash phenomenon. Additionally, there is no evident effect of the liquid film thickness on the onset of bubble encapsulation.

Bubble encapsulation happens after prompt and crown splashing and it is triggered by the kinematic discontinuity at the boundary of the impinging droplet and the liquid film. This means that depends on a combination of viscous, inertial, and surface tension forces. These results were compared with correlations available in the literature for the splash threshold. The reason for this is the fact that splashing always happens before bubble encapsulation. Therefore, the condition to obtain splashing has to be fulfilled to reach the phenomenon of bubble encapsulation. In the previous subsection 4.3.1, some of the most used spread/splash

Table 4.4: Wider parameter space tested in the study of bubble encapsulation.

Substance	Weber number We_D	Reynolds number Re_D	Dimensionless film thickness δ_f
100% Jet A-1	1565	8283	0.6, 1.0
	1593	8358	0.6, 1.0
75% Jet A-1 - 25% NExBTL	1502	6747	0.6, 1.0
	1503	6526	0.4, 0.6, 1.0
	1534	6817	0.6, 1.0
	1543	6263	0.4, 0.6
	1554	6637	0.4, 0.6, 0.8, 1.0
	1575	6327	0.6, 0.8
	1584	6345	0.8
	1587	6352	1.0
	1626	6429	1.0
	1650	6956	0.2, 0.3, 0.4, 0.5, 0.6, 0.7, 0.8, 0.9, 1.0
	1700	6943	0.8, 1.0
	1711	6594	0.4, 0.6, 0.8, 1.0
	1805	7395	0.4, 0.6, 0.8, 1.0
	1930	7396	0.4, 0.6, 0.8, 1.0
	2180	8127	0.6, 1.0

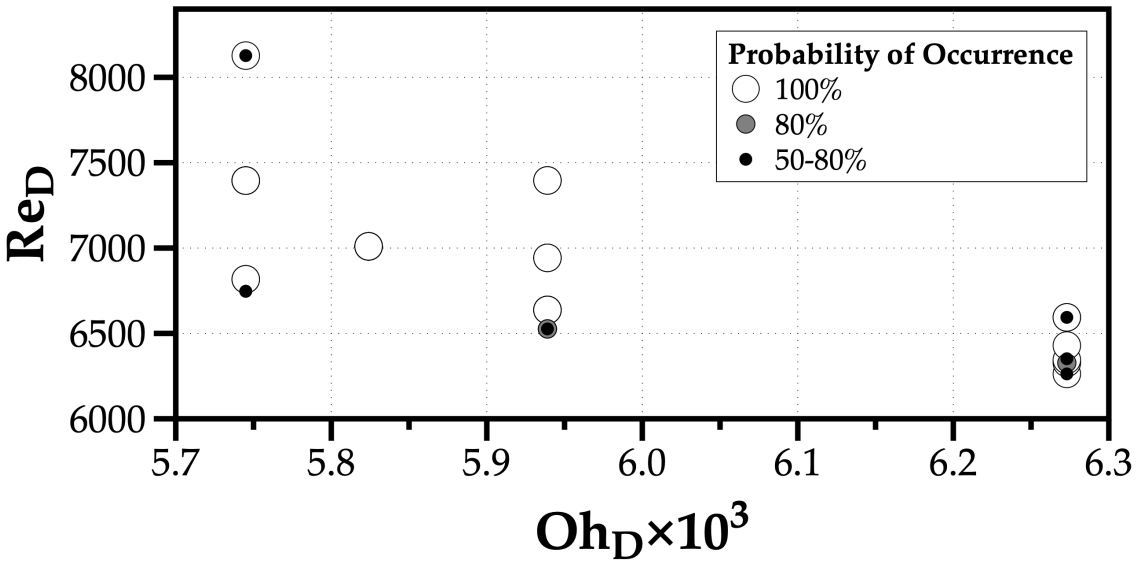

Figure 4.50: Ohnesorge *vs.* Reynolds number map based on the initial droplet size as length scale, with the conditions resulting in 100%, 80%, and $50 - 80\%$ occurrence of bubble encapsulation.

correlations were investigated in order to assess whether each one is the most universal. During this analysis, it is noted that the majority of the empirical correlations for this transition involving a constant coefficient K_c are in the form of:

$$Re_D^a We_D^{0.8} = K_c \quad (4.16)$$

As explained in subsection 4.3.1, the predictive value of some empirical correlations proposed in the literature was investigated. The criterion proposed by Vander Wal et al. [40] provided the best agreement with the experimental data both within and without its validation domain. The Vander Wal et al. [40] correlation is defined as:

$$Re_D^{0.272} We_D^{0.8} = 756.7 \quad (4.17)$$

Therefore, considering that the Ohnesorge number Oh_D relates all three forces involved in the morphology of bubble encapsulation, the correlation form was rearranged to include this dimensionless number. Thus, the general form of eq. 4.16 becomes:

$$Re_D Oh_D^a = K_c \quad (4.18)$$

Accordingly, the Vander Wal et al. [40] transition boundary becomes:

$$Re_D Oh_D^{0.8547} = 34.5 \quad (4.19)$$

Figure 4.51 shows the correlation proposed by Vander Wal et al. [40] for the spread/splash transition limit with the data acquired considering the phenomenon of bubble encapsulation with different probabilities of occurrence. The black line represents the Vander Wal et al. [40] criterion for the transition between spreading and splashing after droplet impact onto a liquid film, which does not depend on the dimensionless thickness of the liquid film. Different symbols were used depending on the probability of occurrence. The white symbols describe the conditions where bubble encapsulation occurred for $p = 1$, the red middle-size ones for $p = 0.8$, and the blue smaller-size ones for $0.5 \leq p < 0.8$. The events of bubble encapsulation obtained in this experimental study are within a region defined by a bottom (red line) and a top (blue line) boundary with the corresponding a and K_c values. The bottom boundary is parallel to the Vander Wal et al. [40] correlation for splashing on a logarithmic scale, it only changes the value of the exponent a. Regarding the top boundary, the transition was identified but does not follow the same trend, changing the values of a and K_c as $\mathrm{Re}_D\mathrm{Oh}_D^{2.2} = 0.1$. However, the aforementioned analysis based on the Vander Wal et al. [40] correlation does not consider the influence of the liquid film thickness.

According to several studies presented in the literature [138, 139, 140], the material of the crown liquid sheet formed after the droplet impact onto liquid films is mainly composed of liquid from the liquid film and not from the main droplet. This fact is highly relevant in this study. Therefore, a modification to the Vander Wal et al. [40] transition boundary is proposed. Instead of considering the droplet initial diameter D_0 as the characteristic length

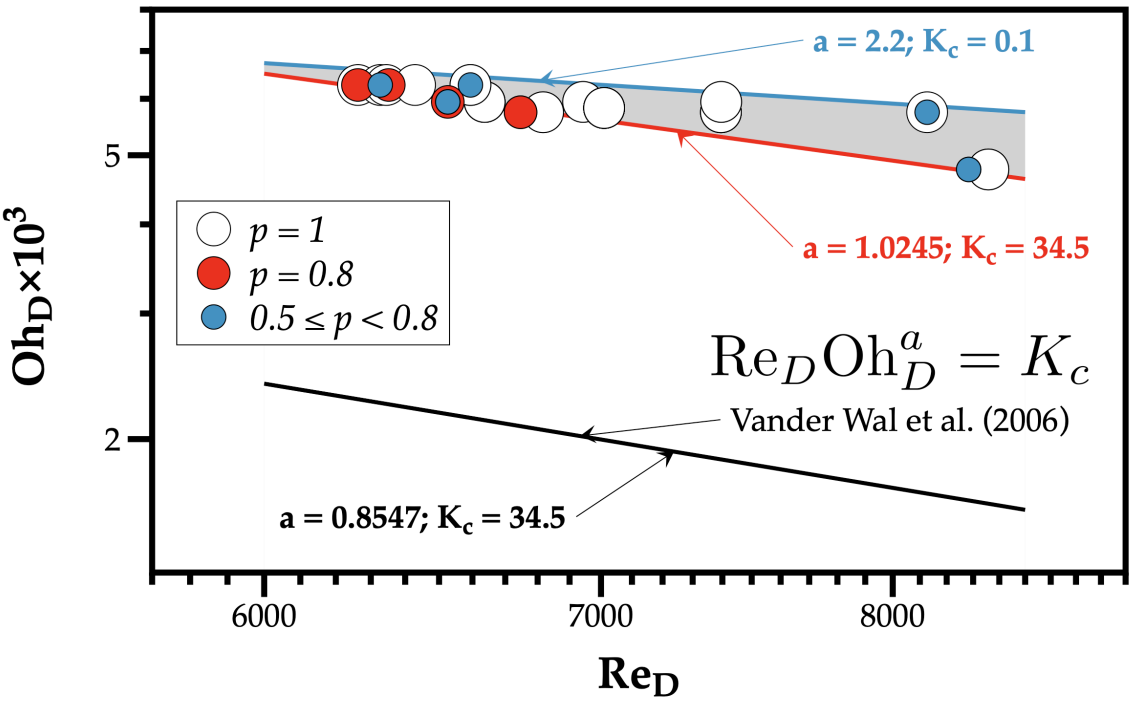

Figure 4.51: Bubble encapsulation events compared with the spreading/splashing transition boundary of Vander Wal et al. [40].

scale to calculate the Ohnesorge number Oh_D, the characteristic length scale was modified to the thickness of the liquid film h_f, obtaining Oh_f.

Figure 4.52 shows a clearer region where bubble encapsulation can be expected, defined by two limiting boundaries based on the Vander Wal et al. [40] threshold. This graphic seems to have more data points than Fig. 4.51 due to considering the influence of the thickness of the liquid film. The two boundaries on Fig. 4.52 set the beginning of impact conditions that lead to bubble encapsulation (red line) and when this phenomenon ceases to occur (blue line), meaning bubble encapsulation occurs for $1.022 < a < 1.142$. With this approach, the K_c value is constant for all equations, $K_c = 34.5$, and a criterion can be developed for the onset of bubble encapsulation as

$$k_{be} = \ln(34.5/\mathrm{Re}_D)/\ln(\mathrm{Oh}_f),\ \forall k_{be} \in [1.022, 1.142] \quad (4.20)$$

valid for $\mathrm{Re}_D \in [6263; 8358]$ and $\mathrm{Oh}_f \times 10^3 \in [4.776; 9.918]$. Other authors, including Pan et al. [73], Motzkus et al. [74], and Geppert et al. [76], observed bubble encapsulation for experimental conditions outside the dimensionless film thickness validation range, where the experiments performed in this work had a probability of occurrence lower than 50% ($p < 0.5$). The validation domain of eq. (4.20) and the values obtained outside this domain are plotted in Fig. 4.53. These authors did not specify which was the occurrence probability of obtaining bubble encapsulation with their conditions. Furthermore, the differences between this study values with $p < 0.5$ and the values of Geppert et al. [76] and Motzkus et al. [74] are lower than 2%. However, the extension of the validation domain of the correlation would

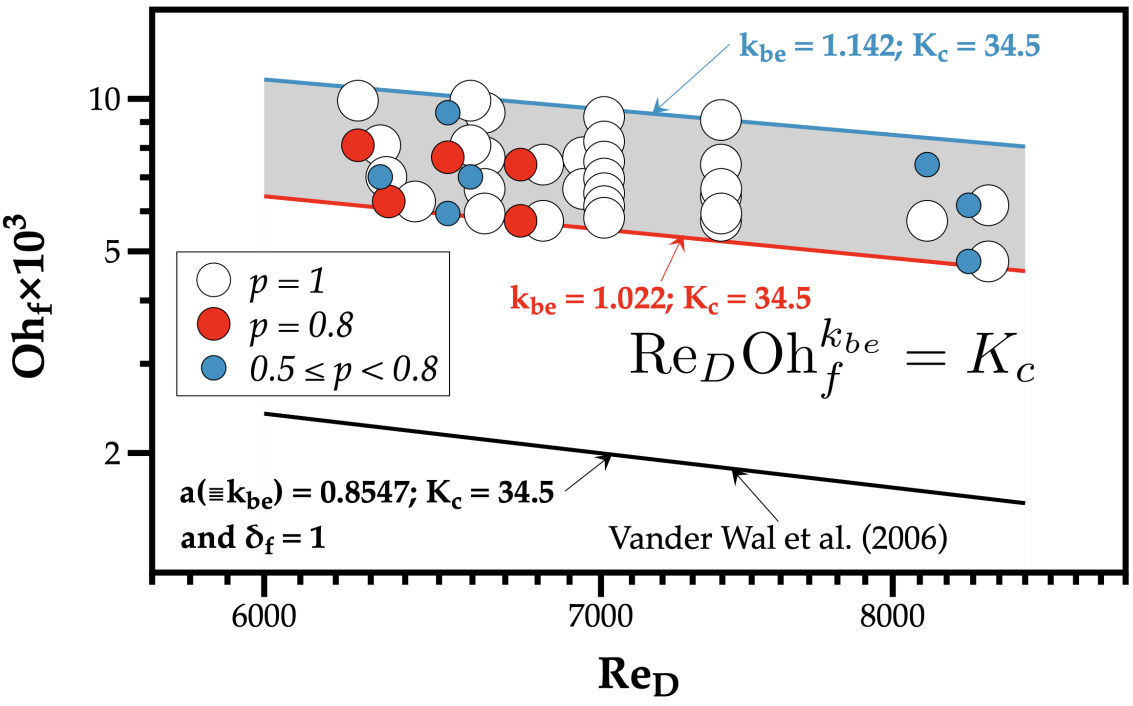

Figure 4.52: Bubble encapsulation events compared with the spreading/splashing transition boundary of Vander Wal *et al.* [40] using the thickness of the liquid film h_f as the characteristic length scale in the calculation of the Ohnesorge number, Oh_f.

demand more experiments.

Within our research center, AEROG - Aeronautics and Astronautics Research Center, several studies related to droplet impact are being developed [7, 83, 135, 141]. One of them includes the single droplet impact upon heated liquid films [141]. Curiously, it was noticed that by increasing the temperature of the liquid film, the crown sheet walls seemed to start bending inwards. That finding arouses a question: What if bubble encapsulation can be promoted by varying the properties of the liquid film and not only its thickness?

Heating the liquid film changes the thermophysical properties of the fluid. The threshold proposed to predict the onset of bubble encapsulation considers the thickness of the liquid film as the characteristic length scale to calculate the Ohnesorge number included in the threshold. Therefore, it is reasonable to search for possible impact conditions that can originate bubble encapsulation by heating the liquid film.

The fluids used in this study are n-heptane and n-decane since their properties are described in the literature, e.g. the boiling point. It was found that increasing the temperature of the liquid film increases the probability of observing bubble encapsulation [141]. Figure 4.54 shows the events of bubble encapsulation observed in comparison with the correlation proposed for the onset of bubble encapsulation. The majority of the conditions where bubble encapsulation was observed are outside of the regime delimited by the threshold (grey area). However, this threshold was developed for isothermal conditions and did not account for the

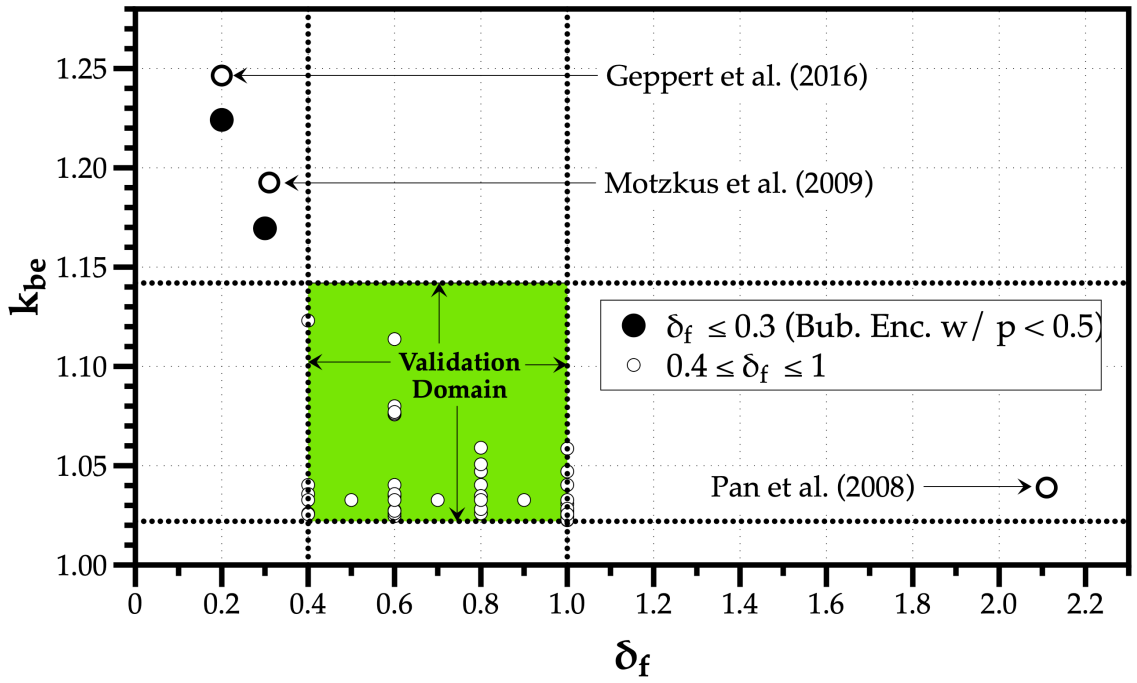

Figure 4.53: Comparison between the events of bubble encapsulation obtained by other authors and by the present study when $p < 0.5$.

change in the liquid film temperature.

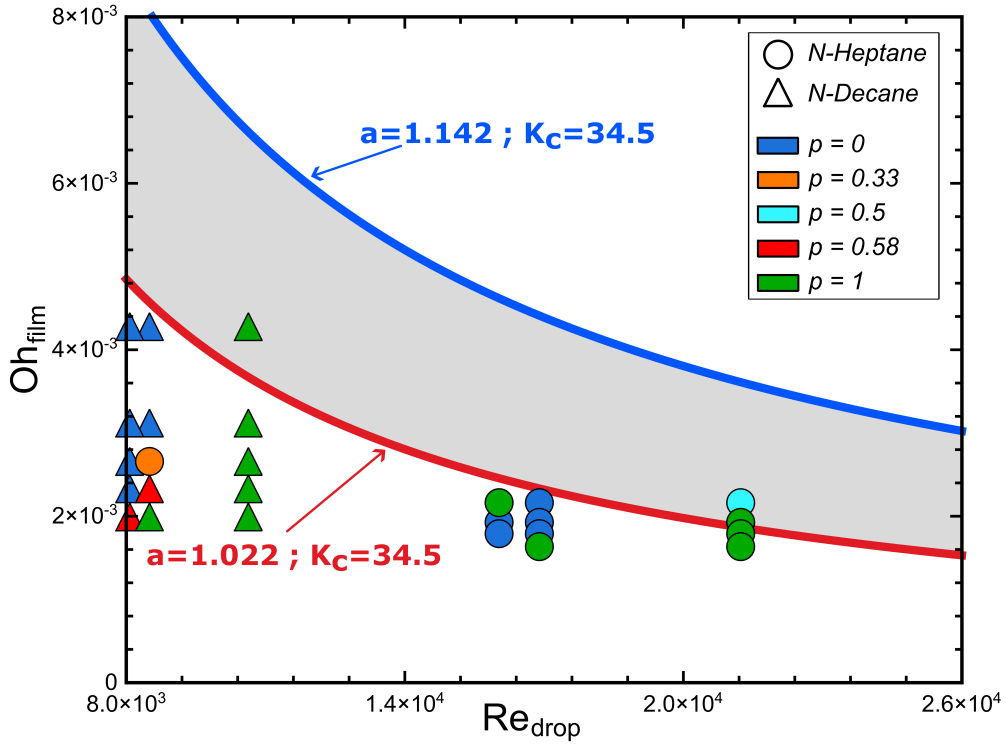

Figure 4.54: Bubble encapsulation events compared with the threshold proposed [141].

The results from single droplet impact upon heated liquid films show that the temperature of the liquid film has a significant role in the development of bubble encapsulation. Accordingly,

it was decided to adapt the calculation of the Reynolds number presented in the threshold. Instead of using the properties of the droplet, the adapted Reynolds number used a combination of the liquid film and droplet properties, $Re_{film,\,drop}$, as described in eq. (4.21).

$$Re_{film,\,drop} = \frac{\rho_f \, U_0 \, D_0}{\sigma_f} \quad (4.21)$$

In this study, the volume of the droplet is lower than the liquid film by several orders of magnitude. Besides, bubble encapsulation is the event with a higher timescale in comparison to other outcomes. Therefore, a very short timescale is expected for the heating of the droplet liquid. That fact justifies the calculation of the Reynolds number using the properties of the droplet combined with the properties of the liquid film. Considering this adaptation the parameter a becomes:

$$a = \frac{ln(34.5/Re_{film,\,drop})}{ln(Oh_f)} \;,\; \forall\, a \in [1.022, 1.142] \quad (4.22)$$

Figure 4.55 shows the events of bubble encapsulation considering the adaptation made to the criterion. All events with a probability of occurrence higher than 50%, $p \geq 0.5$ are within the bubble encapsulation region (grey area). All events with a probability of occurrence lower than 50%, $p < 0.5$ are outside the bubble encapsulation region or at the lower boundary. In summary, the new adaptation fits well with the results obtained and validates the assumptions made to perform the changes.

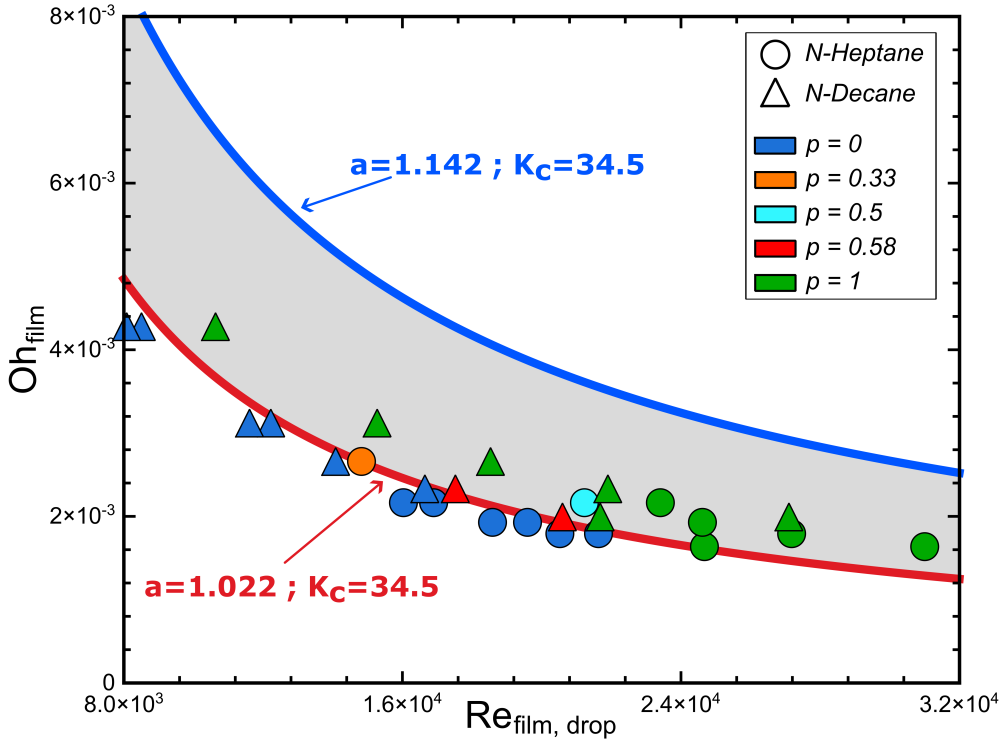

Figure 4.55: Bubble encapsulation events compared with the adaptation of the threshold proposed [141].

4.3.2.6 Evolution of the Crown sheet Angle

To finalize the study about single droplet impact upon thin liquid films, another aspect related to the formation of bubble encapsulation was investigated. The formation mechanism of this phenomenon is not completely understood, but the crown sheet angle α certainly plays a significant role in its formation, as can be seen in Fig. 4.56. In this way, crown development was investigated for a range of different impact parameters to understand how the crown sheet angle evolves after impact and until the crown collapses.

Figure 4.57 represents the impact event and its main features, including droplet, fluid, and liquid film characteristics, and the crown sheet angle. Describing the sequence of images presented in Fig. 4.56, the initial crown sheet angle α seems to be close to $90°$ for all thicknesses studied. As time evolves the crown starts bending inwards, increasing the crown sheet angle α. This angle keeps increasing and the fingers at the top of the crown start merging. The initially cylindrical crown sheet ends up closing forming a perfect bubble, as displayed in Fig. 4.56.

The crown sheet angle was then measured from the moment after impact until crown closure to form bubble encapsulation or until crown collapse when no bubble is formed. Starting with the smallest liquid film thickness tested $\delta_f = 0.2$, Fig. 4.58 (a) shows the crown sheet angle evolution depending on the dimensionless time $\tau = tU_0/D_0$, where t is the time after impact. This data corresponds to experiments of a 75% JF-25% HVO droplet impact onto a film of the same fluid.

The blue symbols correspond to the events where the crown collapsed without forming the bubble and the black symbols correspond to the only event where bubble encapsulation was observed for these specific impact conditions. Moments after impact, the crown sheet angle is $\alpha \approx 85°$ and slightly decreases until $\tau \approx 10$. After that moment increases again. However, during the crown collapse, the crown liquid sheet changes its angle but also its diameter and that is why there are some oscillations in the crown angle α. Considering the bubble encapsulation case (black symbols), the crown sheet angle is slightly higher than the other experiments near the crown closure moment. Maybe this small difference is the reason for the crown closure. Additionally, the crown sheet angle is related to the crown lifetime. So, the dimensionless time τ was divided by the crown lifetime $\tau_{lifetime}$, $\tau/\tau_{lifetime}$. From Fig. 4.58 (b) it is possible to see that the crown sheet angle tends to a limit of $\alpha_{lim} < 150°$ before

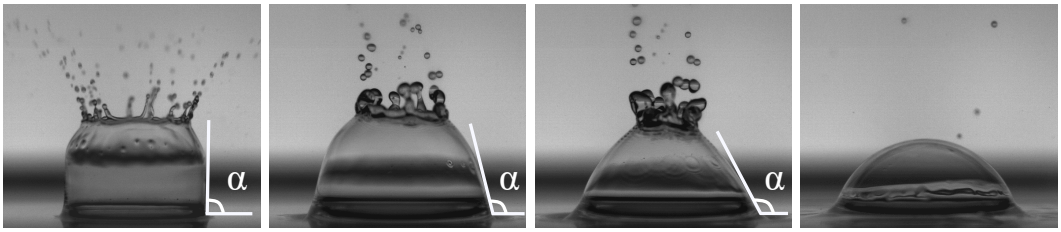

Figure 4.56: Crown sheet angle evolution resulting in bubble encapsulation.

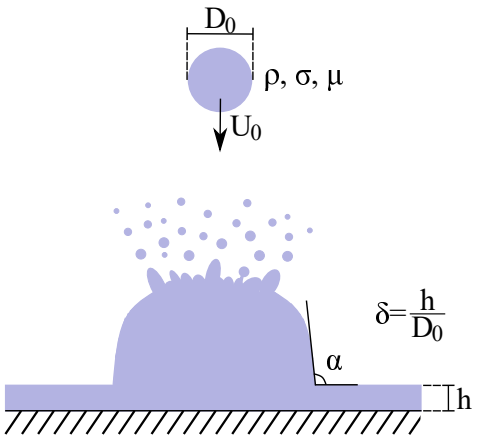

Figure 4.57: Representation of single droplet impact upon a liquid film of the same fluid. Definition of the crown sheet angle α, droplet characteristics (diameter D_0, impact velocity U_0), fluid characteristics (density ρ, surface tension σ, and viscosity μ) and liquid film characteristics (thickness h and dimensionless thickness $\delta = h/D_0$).

.

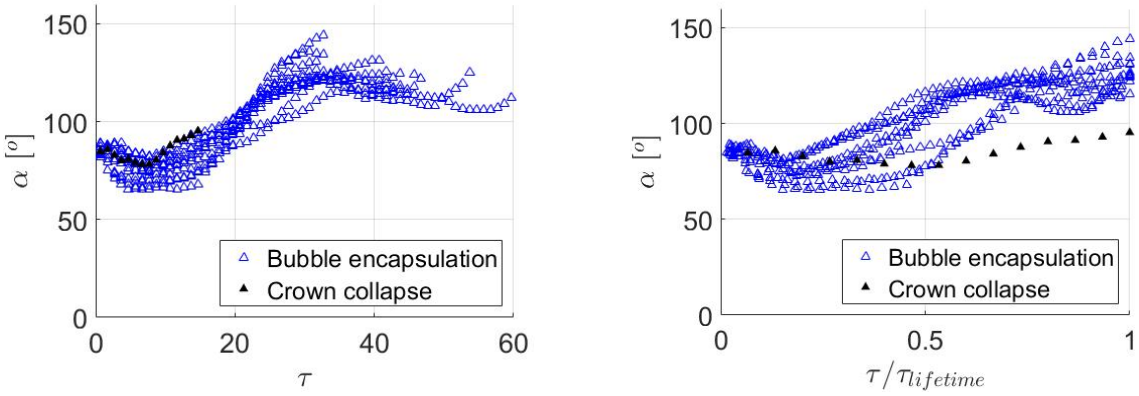

(a) (b)

Figure 4.58: Crown sheet angle evolution on the impact of a 75% JF-25% HVO droplet onto a liquid film of the same fluid with $\delta = 0.2$: (a) depending on the dimensionless time τ; (b) depending on the dimensionless time divided by the crown lifetime $\tau/\tau_{lifetime}$. The blue symbols correspond to cases where no bubble is formed and the red case to the only event where bubble encapsulation was observed.

collapsing on the liquid film. On the other hand, for the bubble encapsulation case, the crown sheet angle decreases slightly and then slightly increases until crown closure and formation of bubble encapsulation. While the cases with no bubble formation show several oscillations in their crown sheet angle evolution, the bubble encapsulation case (red symbols) is almost constant.

Considering the same set of impact conditions used in Fig. 4.58, the crown sheet angle was measured for other dimensionless film thicknesses δ_f. Figure 4.59 shows the crown angle evolution α depending on the dimensionless inertial time τ for (a) $\delta_f = 0.4$, (b) $\delta_f = 0.6$, (c) $\delta_f = 0.8$, and (d) $\delta_f = 1.0$. The length of the axis was kept the same to compare their behavior for the different dimensionless thicknesses. For all these thicknesses, it was observed 100% occurrence of bubble encapsulation. The crown closure time decreases while increasing the

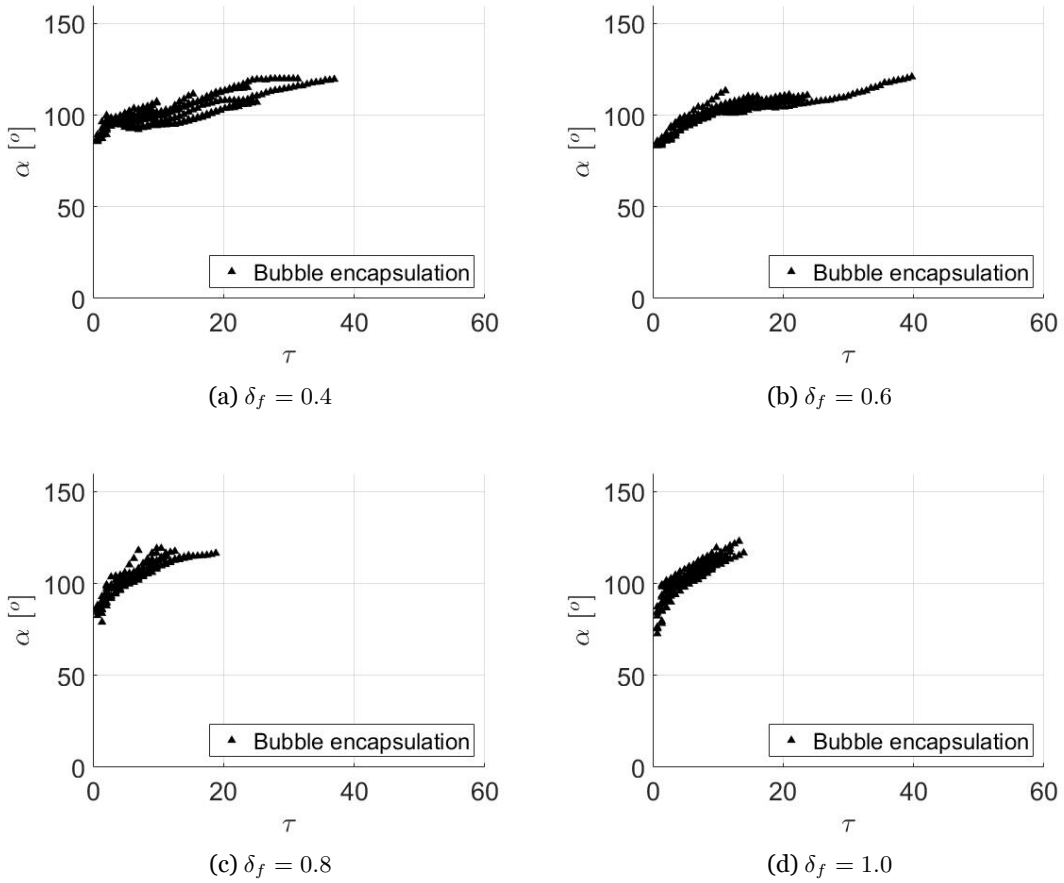

(a) $\delta_f = 0.4$ (b) $\delta_f = 0.6$

(c) $\delta_f = 0.8$ (d) $\delta_f = 1.0$

Figure 4.59: Crown sheet angle evolution on the impact of a 75% JF-25% HVO droplet onto a liquid film of the same fluid for different dimensionless film thicknesses depending on the dimensionless time: (a) $\delta_f = 0.4$; (b) $\delta_f = 0.6$; (c) $\delta_f = 0.8$; $\delta_f = 1.0$.

dimensionless thickness of the liquid film. Additionally, the initial crown angle is similar independent of the dimensionless film thickness. In the first stages of impact, the crown shows an angle around $80 - 90°$, similar to the case of $\delta_f = 0.2$.

Several authors tried to predict the crown sheet angle α. Wang and Chen [64] reported that for $\delta_f = 0.5$ the crown sheet angle is perpendicular to the horizontal liquid film, $\alpha = 90°$. Later, Roisman and Tropea [142] proposed a theoretical model for the crown sheet angle. However, it includes properties that are difficult to measure. A few years later, Fedorchenko and Wang [61] observed that crown angle only depends on the thickness of the liquid film. They found that $\alpha = 90°$ for $\delta_f \geq 0.25$, but they proposed an expression to determine the crown sheet angle for thinner liquid films $\delta_f < 0.25$: $cos\alpha = 1 - 4\delta_f$.

The findings of this experimental study disagree with Wang and Chen [64] since crown sheet angles close to $90°$ were observed for very thin liquid films $\delta_f = 0.2$. As mentioned several times, in this study, only thin films were considered $0.2 < \delta_f < 1.0$. As reported in the subsection 4.3.2.2, only one event of bubble encapsulation was found for $\delta_f = 0.2$. For this liquid film thickness, the crown sheet angle is almost perpendicular to the liquid film but does not evolve to bubble encapsulation, except for that one event. In this way, this analysis

focuses on the crown sheet angle not only after impact but also during crown expansion and collapse.

The crown sheet angle was measured for a wide range of impact conditions, but it was not possible to find an empirical correlation that properly describes the crown sheet angle depending on the impact energy and dimensionless film thickness. In future works, more results should be included in this study, mainly considering cases where bubble encapsulation was not observed.

4.4 Droplet Impact onto Heated Surfaces

The study of single droplet impact upon heated dry surfaces is of vital importance to understand the possible phenomena that happen inside the combustion chamber of an internal combustion engine. In the following subsections, the results of this study will be presented and discussed.

First, a description of the heat transfer regimes depending on the Weber number We, the Reynolds number Re, and surface temperature T_w. Then, some considerations about the hydrodynamic impact regimes and their differences between fluids. Finally, the evaporation time measurements will be presented and discussed.

4.4.1 Heat Transfer Regimes

Within the entire parameter space tested, all four heat transfer regimes were observed: film evaporation, nucleate boiling, transition boiling, and film boiling. Figure 4.60 shows an image sequence example of each heat transfer regime. Every frame is identified with its dimensionless inertial time $\tau = tU_0/D_0$, where t is time after impact.

Film evaporation regime usually occurs when the surface temperature is lower than the saturation temperature $T_w < T_{sat}$. The film evaporation sequence in Fig. 4.60 corresponds to the droplet impact of 100% NExBTL with $We = 244$ and $Re = 1099$ at $T_w = 220° \ C$. This is the fluid with the highest final boiling point, as can be seen in Tab. 3.9. In this impact regime, the droplet spreads on the surface forming a thin liquid lamella and quickly recedes inwards. In this specific case, it forms a small central jet. The jet descends and the liquid droplet stays on the surface evaporating due to the surface temperature T_w.

Increasing the temperature of the impact surface T_w, the nucleate boiling regime begins. This regime is characterized by a surface temperature of the same order as the saturation temperature $T_w = T_{sat}$. In Fig. 4.60, a 50% Jet A-1 - 50% NExBTL droplet with $We = 305$ and $Re = 2311$ impinges on the surface stainless steel surface with $T_w = 300° \ C$. In this impact regime, the droplet spreads on the surface in thick liquid lamella and with some oscillations on the bounding rim. It barely recedes and the liquid lamella breaks forming some puddles. These puddles start to boil. The evaporation is easily seen in the images. This regime is well

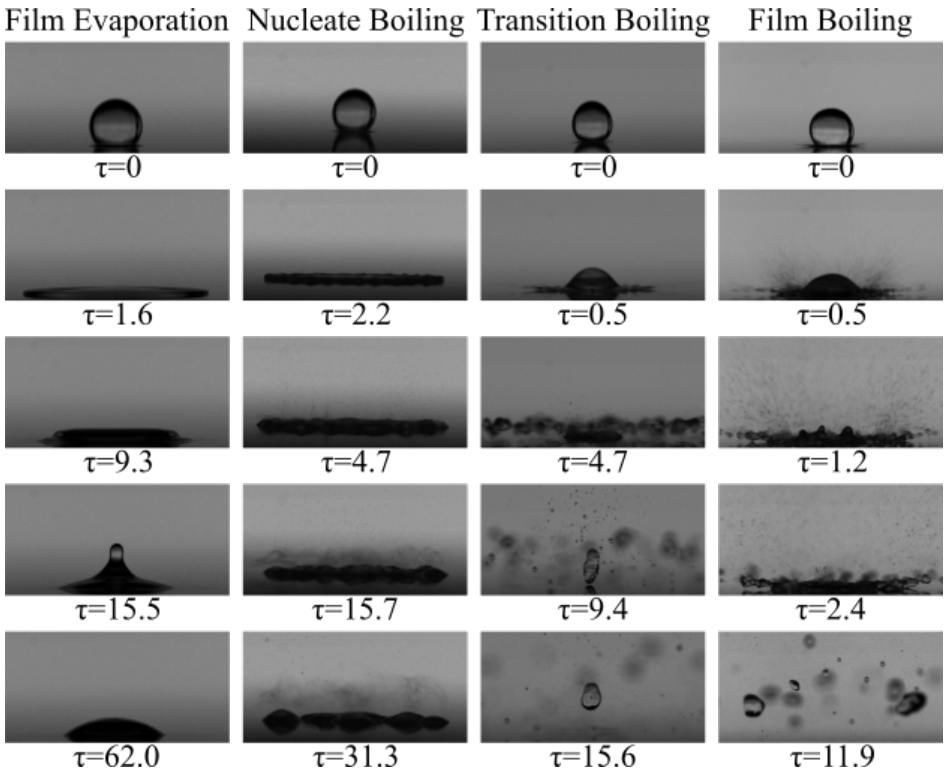

Figure 4.60: Heat Transfer Regimes: Film evaporation for 100% NExBTL at $We = 244$ and $Re = 1099$ at $T_w = 220^\circ\ C$; Nucleate Boiling for 50% Jet A-1 - 50% NExBTL for $We = 305$ and $Re = 2311$ at $T_w = 300^\circ\ C$; Transition Boiling for 100% Jet A-1 for $We = 299$ and $Re = 3746$ at $T_w = 300^\circ\ C$; and Film Boiling for distilled water for $We = 174$ and $Re = 6930$ at $T_w = 300^\circ\ C$.

known for the formation of pagoda-like bubbles, which also occur in these experiments but not in the sequence of images displayed in Fig. 4.60.

The third sequence of images in Fig. 4.60 represents the transition boiling regime, where the temperature of the surface is between the critical heat flux temperature and the Leidenfrost temperature, $T_{CHF} < T_w < T_{Leid}$. In this regime, the contact between the droplet and the surface is intermittent. The droplet is able to ”levitate” due to the tiny unstable vapor layer beneath it. The sequence shows a 100% Jet A-1 droplet impinging on the stainless-steel surface at $T_w = 300^\circ\ C$, $We = 299$, and $Re = 3746$. Right after impact, secondary atomization is generated and splashed away. The droplet is completely shattered and only a small volume of fluid remains ”levitating” above the surface in the so-called droplet dancing phenomenon.

Finally, the film boiling regime typically occurs for surface temperatures higher than the Leidenfrost temperature, $T_w > T_{Leid}$. The sequence of images fro the film boiling regime displayed in Fig. 4.60 shows the impact of a distilled water droplet impact with $We = 174$, $Re = 6930$, and $T_w = 300^\circ\ C$. In this regime, there is no contact between the liquid and the solid surface. After impact, the droplet shatters completely and none of the liquid volume remains on the surface.

One of the goals of this study is to observe the differences in the heat transfer regimes de-

pending on the fluids and their thermophysical properties. Figure 4.61 shows a heat transfer regime map depending on the wall temperature T_w and on the Weber number We for all fluids tested. The different fluids are identified by different colors: black for distilled water, blue for 100% Jet A-1, green for 50%JF-50%HVO, and red for 100% NExBTL. The heat transfer regimes are identified by different symbols.

Looking at Fig. 4.61, it is noticeable that 100% NExBTL originated the same heat transfer regimes independently of the impact energy. For the other three fluids, at the highest impact energies, the transition for the following heat transfer regime happens for lower wall temperatures than at the lowest impact energies. For example, for 100% Jet A-1 it reaches the nucleate boiling regime at $T_w = 180° C$ for the lowest impact energy and at $T_w = 160° C$ for the highest impact energy. Distilled water is the only fluid that reached the film boiling regime for the range of wall temperatures tested, which is justified by its low boiling point. Despite having similar Weber number values to the 50%/50% mixture, the 100% Jet A-1 reaches nucleate boiling and transition boiling at significantly lower surface temperatures.

Additionally, to evaluate the influence of the Reynolds number Re in the heat transfer regimes, Fig. 4.62 shows a heat transfer regime map depending on the wall temperature T_w and on the Reynolds number Re for all fluids. The same symbols and color scheme were kept. From this plot, it is easier to understand the differences between the fluids regarding reaching the same heat transfer regime at different wall temperatures. Due to its high viscosity, 100% NExBTL shows the lowest Reynolds number values and it is also the fluid with the higher final boiling point. In this way, it only transitions to nucleate boiling at $T_w = 280° C$. In general, increasing the Reynolds number will help to reach the same heat transfer regime at lower wall temperatures.

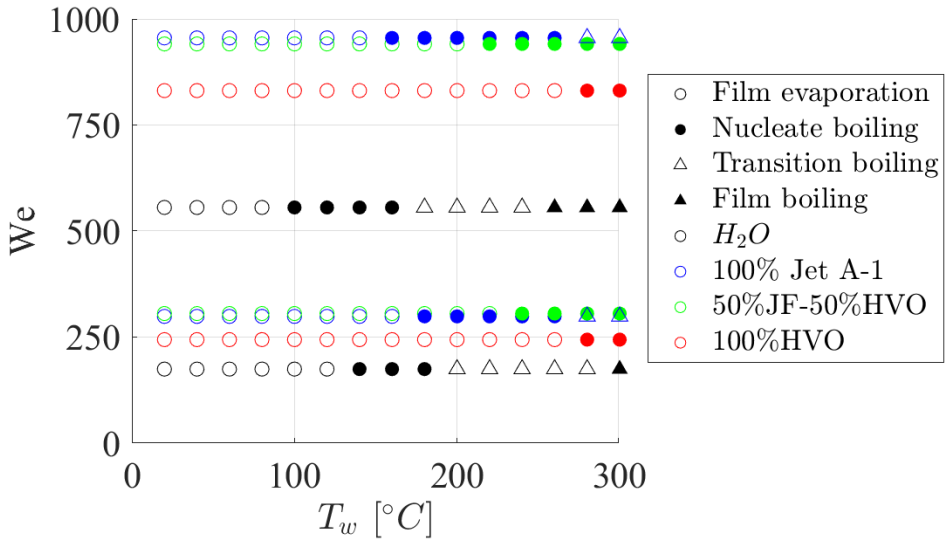

Figure 4.61: Heat transfer regimes map depending on the wall temperature T_w and on the Weber number We for all fluids. The heat transfer regimes are identified by the different symbols, empty and filled, and the fluids are identified by different colors. Black for distilled water, blue for 100% Jet A-1, green for 50%JF-50%HVO, and red for 100% NExBTL.

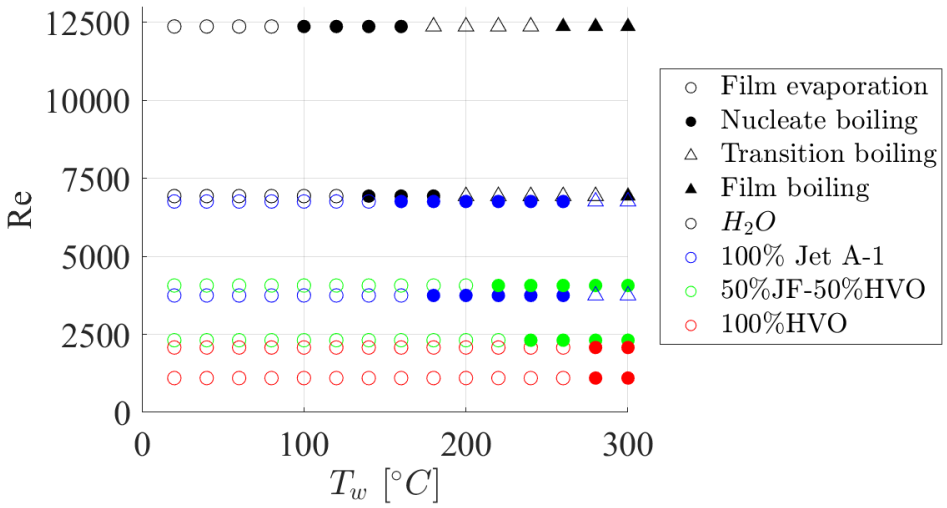

Figure 4.62: Heat transfer regimes map depending on the wall temperature T_w and on the Reynolds number Re for all fluids. The heat transfer regimes are identified by the different symbols, empty and filled, and the fluids are identified by different colors. Black for distilled water, blue for 100% Jet A-1, green for 50%JF-50%HVO, and red for 100% NExBTL.

4.4.2 Evaporation Time

As explained before, a third perspective of the phenomena was captured by a digital camera at a lower frame rate. This perspective has the purpose of capturing the droplet evaporation time. Using these images, the impact frame and the last frame where there is still a part of the droplet on the stainless steel plate were identified.

Figure 4.63 shows the evaporation time for a distilled water droplet for the two impact energies studied. The horizontal axis is the wall temperature T_w and the vertical axis is the time after impact t. The evaporation time was measured for $T_w \geq 80° \ C$. For the lower impact energy $We = 174$, at $T_w = 80° \ C$ the evaporation time is $\approx 120 \ s$. Increasing the wall temperature, the evaporation time drastically decreases until $T_w = 140° \ C$, within the nucleate boiling regime. Then, slightly oscillates until reaching the lowest evaporation time for $T_w = 300° \ C$.

For the higher impact energy $We = 556$, at $T_w = 80° \ C$ the evaporation time is higher $\approx 150 \ s$. Increasing the wall temperature the evaporation time also drastically decreases until $T_w = 160° \ C$, which marks the boundary between the nucleate boiling and transition boiling regimes. After that, the evaporation time also slightly oscillates until reaching the lowest evaporation time for $T_w = 300° \ C$.

The evaporation time was also measured for the fuels but even after 30 minutes there is still fluid on the stainless-steel surface. All fuels used are multi-component substances and that could be the reason for the delayed evaporation.

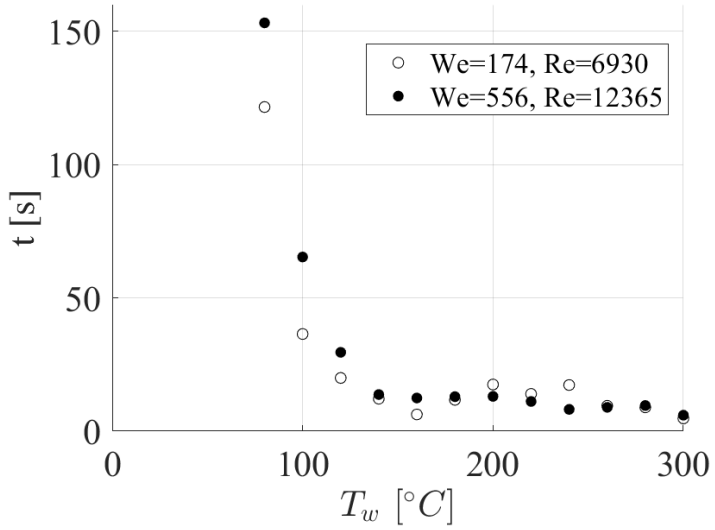

Figure 4.63: Evaporation time for a distilled water droplet depending on wall temperature for two different impact energies.

Chapter 5

Conclusions

In the final chapter of this thesis, the conclusions of this study will be summarized. Additionally, some suggestions for future works will be proposed considering the work developed in this study.

5.1 Conclusions

The study of droplet-surface collisions is relevant for a variety of areas. In this study, they were studied with the goal of being implemented in aeronautical applications. The study was divided into three main parts: single droplet impact upon dry smooth or micro-structured surfaces with variable wettability, single droplet impact upon liquid films, and single droplet impact upon dry heated smooth surfaces. Therefore, the main conclusions of each part will be summarized in the following.

Single droplet impact upon dry smooth or micro-structured surfaces with variable wettability constitutes the first part of this thesis. Wettability is an important parameter in the study of droplet impingement. The goal of this part of the study was to assess the influence of wettability on the impact of single droplets onto a dry smooth surface and to identify the originated phenomena and their characteristics. Two different fluids, distilled water and isopropanol, were used as droplet liquid and impinged onto two different surface materials, Lexan ® and Plexiglas®. The wettability of the surface materials was altered by applying plasma treatments which change the apparent contact angle between the liquid and the solid surface. Four different wettability behaviors were obtained for the impacts with distilled water and two for isopropanol. Additionally, four different impact energies were experimentally tested to study their influence on the outcomes. Due to a complex experimental facility, the phenomena were observed from three different perspectives: lateral, top, and bottom view. The perspective captured from below is less reported in the literature and it is captured in an internal total reflection configuration.

On the single droplet impact with smooth surfaces three different regimes were observed: deposition, splashing, and rebound. Comparing the results with the deposition/splashing threshold correlation proposed by Vander Wal et al. [40] provides a good agreement.

The first impact energy tested is below the splashing limit for both fluids since only deposition was observed. Decreasing wettability increases the receding rate. Also, the maximum spreading diameter decreases as well as the spreading duration. On impact with non-

wettable surfaces, the liquid lamella quickly recedes and forms a central jet that may break producing partial rebound. A curious finding relates to the water droplet impact on hydrophobic surfaces. Despite having the same initial impact conditions, originates a different outcome depending on the surface material. This can be caused by the differences in the polarity and free surface energy of the samples due to the plasma treatments applied.

Isopropanol has a higher viscosity than distilled water, which results in a smaller maximum spreading diameter. Furthermore, it produces splashing for the second impact energy tested, which shows that the critical deposition/splashing limit is located within $165 < We < 400$.

From this study, it was also concluded that increasing the impact energy increases the probability of observing partial rebound in the water droplet impacts upon hydrophobic surfaces. A few cases of complete rebound were observed for the impacts upon non-wettable Plexiglas® surfaces. However, increasing the impact energy even further will form a wide spreading. Consequently, the liquid lamella will be very thin and will break up during the receding phase. Due to the receding breakup, not enough fluid will be available to form the central jet and partial rebound will be inhibited.

The second part of the study about single droplet impact upon dry surfaces considers micro-structured surfaces in replacement of smooth surfaces. Therefore, four micro-structured patterns were considered to understand their influence on the obtained phenomena. All experimental conditions considered in the impacts upon smooth surfaces were also applied to these surfaces, including the plasma treatments to vary the wettability behavior.

Similarly to the impacts upon smooth surfaces, three different regimes were observed: deposition, splashing, and rebound. Therefore, the obtained outcomes were also compared with deposition/splashing thresholds available in the literature. First, similarly to the impacts upon smooth surfaces, the results were compared with the deposition/splashing threshold proposed by Vander Wal et al. [40] since it showed a good agreement for the smooth surfaces. However, based on this threshold, a modified correlation including the influence of the Wenzel roughness factor r was proposed, as defined in eq. (4.5). This modified correlation was able to measure correctly both the smooth and micro-structured surfaces. Nonetheless, a second approach was considered based on the Tsai et al. [93] studies and focused on the spacing between the micro-structures in regular patterns. Unfortunately, for the same mean roughness values and the same α-parameter, different outcomes were obtained. Thus, a three-dimensional α_{mod} parameter was introduced. By using this new parameter, a new spreading/splashing limit that fits these results was proposed. Finally, a third approach was considered introducing the dimensionless parameter $hD_0/(w_1w_2)$ that relates the pillar height h, droplet diameter D_0, and top surface area of the micro-structures w_1w_2. All surface patterns have the same pillar height $h = 20\ \mu m$, but the relative height of the micro-structures in comparison to their top area is smaller for $S1$, which is the surface topography that promotes splashing the most. Therefore, another deposition/splashing threshold that fits the results of this study was proposed.

The single droplet impact upon micro-structured surfaces shows that wettability influences the occurrence of heterogeneous wetting states and the receding phase. Similarly to the smooth surfaces, a central jet forms and breaks producing partial rebound on the impact with hydrophobic surfaces for low-impact energies. Additionally, the small inter-spaces between pillars trigger prompt splash, while small micro-structures can inhibit it, possibly due to energy dissipation. Yet, the impact energy seems to be the most significant parameter to trigger splashing. Increasing the impact energy on the impact with hydrophobic surfaces still results in partial rebound, but also in the formation and breakup of finger-like structures during the receding phase. The micro-structured patterns influence the formation and orientation of the finger-like structures and the crown-like liquid sheets. Additionally, the small interspaces favor the formation of heterogeneous wetting states.

Increasing the impact energy for the third droplet falling height resulted in splashing with a higher magnitude. For larger micro-structures, crown splash was already observed for lower impact energies. However, these structures can also suppress crown splashing if the magnitude of the prompt splash is too high and not enough fluid is available to form the crown liquid sheet.

For the higher impact energy, it was found that the tendency to obtain rebound cannot be increased by increasing the impact energy. At a certain point, the magnitude of the receding breakup does not even allow the formation of a central jet. On the other hand, the occurrence of crown splash is increased by increasing the impact energy. However, only for the cases where the magnitude of prompt splash leaves enough energy to allow the crown sheet formation. Finally, at considerably high impact energies, the effect of surface roughness seems to be neglected since all outcomes were similar independent of the micro-structured pattern of the impact surface.

The second part of this thesis concerns the study of single droplet impact upon thin liquid films. First, the results obtained previously in Ribeiro [70] were compared with deposition/splashing boundaries presented in the literature to assess their universality. It was concluded that the deposition/splashing threshold developed by Vander Wal et al. [63] is the one that shows the best universality. This threshold is able to correctly predict the events both inside and outside its validation range, which is curious since this correlation does not even account for the influence of the dimensionless thickness of the liquid film. Furthermore, it was developed considering only experiments with very thin liquid films. However, the deposition/splashing correlation of Cossali et al. [39] which includes the influence of the dimensionless film thickness shows that thicker films lead to a shift into higher Weber numbers since the energy required to obtain splashing is higher. Therefore, if the correlation of Vander Wal et al. [63] is considered as a function of the dimensionless film thickness and proportional to it, even in a nonlinear form an increase of K_c while keeping the logarithm slope constant, should improve the prediction capability of the threshold. However, to refine this criterion, much more experimental research is needed.

Bubble encapsulation is a phenomenon seldom reported in the literature that results from a single droplet impact upon liquid films for specific impact conditions. After a single droplet impacted upon a liquid film, prompt and crown splash were generated and the crown sheet walls started to bend inwards and eventually close forming an empty bubble. This phenomenon was studied in detail to understand better its formation mechanisms and main features. First, its occurrence and repeatability were evaluated since it was only observed once in a previous study [70]. It was observed that bubble encapsulation can be found with 100% of occurrence for a certain pair of Weber and Reynolds numbers and for dimensionless film thicknesses between 0.4 and 1.0 for the single droplet impact of 75% Jet A-1 and 25% NExBTL.

The parameter space was enlarged and three different phenomenologies of bubble encapsulation were observed. In phenomenology 1 only a downward jet is formed after the crown closure, in phenomenology 2 both a downward and an upward jet are formed at the crown closure point, and finally, in phenomenology 3 a downward and an upward jet are formed at the crown closure point and large droplets are ejected due to the upward jet breakup. The cavity underneath the bubble was also observed and it was concluded that due to the thin liquid film it always touches the bottom of the liquid container. Therefore, the formation of bubbly encapsulation is independent of the cavity shape.

The bubble encapsulation phenomenon was captured both from a lateral and a bottom perspective. Through the bottom perspective, it was possible to measure the propagation of the first perturbation imposed on the liquid film. Therefore, an empirical correlation was proposed to predict the diameter of the first perturbation imposed on the liquid film in the first stages of impact depending on the dimensionless thickness of the liquid film. Additionally, another empirical correlation was proposed to predict the velocity of this perturbation depending on the dimensionless thickness of the liquid film.

To increase the knowledge about the phenomena, the bubble geometry was studied. Both bubble height and diameter were measured and the influence of the dimensionless liquid film thickness on them was evaluated. As mentioned, the propagation velocity of the first perturbation imposed on the steady liquid film depends on the dimensionless liquid film thickness. However, the results for the bubble height and diameter does not show the same behavior. Both values seem independent of the dimensionless film thickness for $0.4 \leq \delta_f \leq 1$. The bubble diameter shows a slight variation but the values are very close to each other and it is not possible to distinguish any trend. In this evaluation, it was considered a constant impact energy and this study suggests that this parameter might have a significant role in the characteristic size of the bubble.

There are several criteria for the spread/splashing threshold presented in the literature, but there is no criterion for the onset of bubble encapsulation. Therefore, this work aims to provide a detailed morphology of the bubble encapsulation event from a bottom-view perspective and develop a criterion for its onset. Results evidence a region above the transition to

splash threshold with 100% occurrence. However, there is no clear boundary considering that, in some cases, the phenomenon is observed with a lower probability of occurrence. The occurrence of bubble encapsulation corresponds to a region above the spreading/splashing transition. Therefore, based on the criterion proposed by Vander Wal et al. [40], a correlation was proposed based on the Ohnesorge number calculated using the thickness of the liquid film as the characteristic length scale and the Reynolds number based on the initial drop diameter as its characteristic scale, $k_{be} = \ln(34.5/\mathrm{Re}_D)/\ln(\mathrm{Oh}_f)$ with $k_{be} \in [1.022, 1.142]$, valid for $\mathrm{Re}_D \in [6263; 8358]$ and $\mathrm{Oh}_f \times 10^3 \in [4.776; 9.918]$.

Changing the temperature of the liquid film changes the thermophysical properties of the fluid. Therefore, after realizing that the crown liquid sheet starts to bend inward while increasing the temperature of the liquid film, a search for impact conditions that may originate bubble encapsulation on the impact with heated liquid films was initiated. The event was observed for several sets of impact conditions and compared with the correlation proposed. Nonetheless, this threshold was developed for isothermal conditions and did not account for the changes in the liquid film thermophysical properties. Yet, the results show that liquid film temperature has a significant role in the development of bubble encapsulation. Therefore, the Reynolds number calculation was adapted and used in the proposed correlation. Instead of using the properties of the droplet, the adapted Reynolds number used a combination of the liquid film and droplet properties. With this adaptation, the threshold was able to predict the onset of bubble encapsulation on the impact with heated liquid films with good agreement.

The crown sheet angle until crown closure or collapse was measured for a wide range of impact conditions. However, not enough data is available to develop an empirical correlation that can describe the crown sheet angle evolution depending on the impact energy and dimensionless liquid film thickness.

Finally, the last part of this study includes the single droplet impact upon heated dry smooth surfaces. Within the parameter space experimentally tested all four heat transfer regimes were observed: film evaporation, nucleate boiling, transition boiling, and film boiling. One of the goals of this study is to observe the differences in the heat transfer regimes depending on the fluids and their thermophysical properties. Therefore, a regime map depending on the surface temperature T_w and on the Weber number We was developed considering all fluids experimentally tested.

From this regime map, it is observed that 100% NExBTL originated the same heat transfer regimes independently of the impact energy. For the other three fluids tested, an increase in impact energy results in the transition for the following heat transfer regime at lower surface temperatures. For the impact conditions tested, distilled water is the only fluid that reached the film boiling regime for the range of wall temperatures defined, which is justified by its low boiling point. Despite having similar Weber number values to the $50\%/50\%$ mixture, 100% Jet A-1 reaches nucleate boiling and transition boiling at significantly lower surface

temperatures.

A regime map depending on the surface temperature T_w and on the Reynolds number Re was also developed. With that, differences between the fluids were identified. 100% NExBTL is the fluid with the highest viscosity, shows the lowest Reynolds number, and has the highest boiling point. Therefore, it only transitions to nucleate boiling at $T_w = 280° \ C$. In general, it can be concluded that increasing the Reynolds number helps reach the same heat transfer regime at a lower wall temperature.

Using a third camera with a lower frame rate allowed the measurement of the droplet evaporation time. In fact, it was only possible to measure the evaporation time for the impacts with distilled water since for the fuels even after 30 minutes there still remains some substance on the surface. The fuels were multi-component mixtures and the substance that remains on the surface must be part of these components.

For the lowest impact energy, the evaporation time for distilled water was measured for $T_w \geq 80° \ C$. For $T_w = 80° \ C$ the evaporation time is $120 \ s$. The evaporation time drastically decreased until $T_w = 140° \ C$, within the nucleate boiling regime. Then, slightly oscillates until it reaches the lowest evaporation time for $T_w = 300° \ C$.

For the highest impact energy, the evaporation time for $T_w = 80° \ C$ is higher, approximately $150 \ s$. Again, by increasing the wall temperature, the evaporation time drastically decreased until $T_w = 160° \ C$, which marks the boundary between the nucleate boiling and transition boiling regimes. After that, the evaporation time also slightly oscillates until it reaches the lowest evaporation time for $T_w = 300° \ C$.

5.2 Future Work

In this study, droplet-surface collisions were studied for aeronautical applications. Three different parameter spaces were tested depending if the impact was on a dry solid surface, a liquid film, or a heated dry solid surface. From these studies, many conclusions were drawn. However, many questions arise. Therefore, in this section, some suggestions for future work will be proposed.

First, some suggestions will be made concerning the study of droplet impact upon dry smooth or micro-structured surfaces with different wettability. It was found that there are cases where despite having the same initial impact conditions, a different outcome is obtained depending on the surface material. This can be related to the differences in the polarity and free surface energy of the samples due to the plasma treatment applied. The influence of the polarity and free surface energy variations caused by the plasma treatments applied should be further investigated. Additionally, in this study, the spreading diameter was investigated in detail. However, the receding phase was not properly investigated and should be studied in more detail in future works. Also, evaluating how a slight increment in fluid viscosity

behaves could be an interesting subject for future studies, mainly to find a possible turning point in the relation between liquid viscosity and the spreading diameter.

The outcomes obtained both on droplet impact upon smooth and micro-structured surfaces were compared with deposition/splashing thresholds available in the literature and some adapted thresholds were proposed. The universality of these thresholds should be assessed by comparing them with more experimental results. Furthermore, the few cases of rebound do not allow a clear definition of an individual limit to predict its occurrence. Therefore, to develop a correlation that includes this regime, it is necessary to explore a wider parameter space in future works.

Finally, regarding droplet impact upon micro-structured surfaces, more patterns should be experimentally tested. Perhaps with different geometries such as cylinders or pyramids.

Regarding single droplet impact upon thin liquid films, the bubble encapsulation phenomena deserve further research. First, evaluate the universality and extend the validation domain of the proposed threshold that predicts the onset of bubble encapsulation. Also, investigate further how this threshold can be applied to heated liquid films.

More measurements of the crown sheet angle should be made in order to develop an empirical correlation that can describe the crown sheet angle evaluation depending on the impact energy and the dimensionless thickness of the liquid film. More cases where bubble encapsulation was not observed should also be included.

Finally, for the single droplet impact upon heated dry smooth surfaces, different target materials should be used with different thermal conductivities. Additionally, more fluids should also be tested, and possibly extend the range of surface temperatures to observe more heat transfer regimes on the impacts of the fuels. Developing empirical correlations to predict the different heat transfer regimes will also be of great value to the scientific community.

Bibliography

[1] I. E. Agency, *Key world energy statistics 2019*, 2019.

[2] S. Blakey, L. Rye, and C. W. Wilson, "Aviation gas turbine alternative fuels: A review," *Proceedings of the combustion institute*, vol. 33, no. 2, pp. 2863–2885, 2011.

[3] M. Bomgardner, "Solar energy: Solar airplane resumes world tour," *Chemical and Engineering News*, vol. 94, 05 2016.

[4] E. Adler and J. Martins, "Hydrogen-powered aircraft: Fundamental concepts, key technologies, and environmental impacts," *Progress in Aerospace Sciences*, vol. 141, p. 100922, 08 2023.

[5] M. Kousoulidou and L. Lonza, "Biofuels in aviation: Fuel demand and co2 emissions evolution in europe toward 2030," *Transportation Research Part D: Transport and Environment*, vol. 46, pp. 166–181, 2016. [Online]. Available: https://www.sciencedirect.com/science/article/pii/S1361920915300092

[6] G. Liang and I. Mudawar, "Review of drop impact on heated walls," *International Journal of Heat and Mass Transfer*, vol. 106, pp. 103–126, 2017.

[7] I. Ferrão, D. Vasconcelos, D. Ribeiro, A. Silva, and J. Barata, "A study of droplet deformation: The effect of crossflow velocity on jet fuel and biofuel droplets impinging onto a dry smooth surface," *Fuel*, vol. 279, 2020.

[8] D. F. Ribeiro, A. R. Silva, and M. R. Panão, "Insights into single droplet impact models upon liquid films using alternative fuels for aero-engines," *Applied Sciences*, vol. 10, no. 19, p. 6698, 2020.

[9] P. Foltyn, D. Ribeiro, A. Silva, G. Lamanna, and B. Weigand, "Influence of wetting behavior on the morphology of droplet impacts onto dry smooth surfaces," *Physics of Fluids*, vol. 33, no. 6, p. 063305, jun 2021.

[10] P. Foltyn, L. K. Rihm, D. Ribeiro, A. Silva, and B. Weigand, "Measurement of the lamella thickness during droplet impact onto differently wettable smooth surfaces using an extension of the laser pattern shift method with naturally occurring patterns," *Review of Scientific Instruments*, vol. 92, no. 10, p. 105111.

[11] P. Foltyn, D. Ribeiro, A. Silva, G. Lamanna, and B. Weigand, "Influence of wetting behavior on the morphology of droplet impacts onto dry-patterned micro-structured surfaces," *Physics of Fluids*, vol. 34, no. 12, p. 123322, 12 2022. [Online]. Available: https://doi.org/10.1063/5.0124692

[12] D. Ribeiro, A. R. R. Silva, and M. R. O. Panão, "Criterion for bubble encapsulation on drop impact onto a liquid film," *Physics of Fluids*, vol. 35, no. 3, p. 033305, 03 2023. [Online]. Available: https://doi.org/10.1063/5.0138901

[13] D. F. Ribeiro, M. R. Panão, J. M. Barata, and A. R. Silva, "Insights on bubble encapsulation after drop impact on thin liquid films," *International Journal of Multiphase Flow*, vol. 164, p. 104450, 2023. [Online]. Available: https://www.sciencedirect.com/science/article/pii/S030193222300071X

[14] D. Ribeiro, M. Panão, J. Barata, and A. Silva, "Insights on bubbling formation after drop impact on thin liquid films," in *LASS 2019: 29th European Conference Liquid Atomization Spray Systems*, Paris, France, 2019.

[15] I. Ferrão, D. Ribeiro, J. Barata, and A. Silva, "Comparative study of droplet impact onto sloped surface versus a droplet impact onto a surface with a crossflow," in *2019 AIAA SciTech: AIAA Science and Technology Forum and Exposition*, California, USA, 2019.

[16] G. Carrolo, D. Ribeiro, J. Barata, and A. Silva, "Aerodynamic breakup of a single droplet due to a crossflowed airstream," in *2019 AIAA SciTech: AIAA Science and Technology Forum and Exposition*, California, USA, 2019.

[17] I. Ferrão, D. Ribeiro, J. Barata, and A. Silva, "Experimental study of droplet impact on oblique dry surface," in *9th European Combustion Meeting*, Lisbon, Portugal, 2019.

[18] D. Vasconcelos, D. Ribeiro, J. Barata, and A. Silva, "Vof method: Numerical analysis of single droplets impinging upon liquid film," in *9th European Combustion Meeting*, Lisbon, Portugal, 2019.

[19] ——, "Experimental and numerical study of single droplets impinging upon liquid films," in *4th Thermal and Fluid Engineering Conference*, Las Vegas, USA, 2019.

[20] ——, "Modelling of single droplets impinging upon liquid films using the vof method," in *Congress on Numerical Methods in Engineering*, Guimarães, Portugal, 2019.

[21] D. Ribeiro, M. O. Panão, J. M. Barata, and A. R. Silva, "Morphology of bubble formation on droplet impact upon thin liquid layers," in *AIAA Scitech 2020 Forum*. Orlando, FL: American Institute of Aeronautics and Astronautics, January 2020.

[22] D. Vasconcelos, D. Ribeiro, J. Barata, and A. Silva, "3d simulations of droplets impacting liquid films: Crown parameters measurements," in *2020 AIAA SciTech: AIAA Science and Technology Forum and Exposition*, Orlando, USA, 2020.

[23] P. Pinto, D. Vasconcelos, D. Ribeiro, J. Barata, and A. Silva, "Collision dynamics of a single droplet onto a heated dry surface: Jet fuel and hvo mixtures," in *CLASS 2021, 15th Triennial International Conference on Liquid Atomization and Spray Systems*, Edinburgh, Scotland, 2021.

[24] J. Cardoso, D. Vasconcelos, D. Ribeiro, J. Barata, and A. Silva, "Design and fabrication of a low cost, push-mode piezoelectric stream droplet generator with interchangeable nozzle"," in *CLASS 2021, 15th Triennial International Conference on Liquid Atomization and Spray Systems*, Edinburgh, Scotland, 2021.

[25] D. Ribeiro, P. Foltyn, A. Silva, G. Lamanna, and B. Weigand, "The influence of wettability on the droplet impact onto micro-structured surfaces," in *CLASS 2021, 15th Triennial International Conference on Liquid Atomization and Spray Systems*, Edinburgh, Scotland, 2021.

[26] P. Foltyn, D. Ribeiro, A. Silva, G. Lamanna, and B. Weigand, "Effect of surface wettability on the droplet impact morphologies on dry smooth polycarbonate surfaces," in *CLASS 2021, 15th Triennial International Conference on Liquid Atomization and Spray Systems*, Edinburgh, Scotland, 2021.

[27] D. Ribeiro, J. Barata, and A. Silva, "The role of crown sheet angle evolution on the single droplet impact upon a thin liquid film," in *V LAETA Young Researchers Meeting*, Lisbon, Portugal, 2022.

[28] D. Ribeiro, P. Foltyn, A. Silva, G. Lamanna, and B. Weigand, "Comparison between droplet impact onto dry smooth and micro-structured surfaces with variable wettability," in *V LAETA Young Researchers Meeting*, Lisbon, Portugal, 2022.

[29] D. Ribeiro and J. B. A. Silva, "The influence of liquid film thickness on crown development: Crown sheet angle," in *7th Thermal and Fluids Engineering Conference (TFEC)*, Las Vegas, USA, 2022.

[30] D. Ribeiro, M. Panão, and J. B. A. Silva, "Analysis and visualization of the perturbations imposed on the liquid film by crown sheet collapse or closure," in *20th International Symposium on Application of Laser and Imaging Techniques to Fluid Mechanics*, Lisbon, Portugal, 2022.

[31] D. Ribeiro and J. B. A. Silva, "Experimental study of a single droplet impinging upon a heated dry surface using jet fuel and biofuel mixture," in *31st Conference on Liquid Atomization and Spray Systems*, Virtual, 2022.

[32] A. Mendes, D. Vasconcelos, D. Ribeiro, M. Panão, and A. Silva, "Does liquid film temperature affect single drop impact dynamics?" in *8th Thermal and Fluids Engineering*

Conference (TFEC), May, Partially Online Virtual, University of Maryland, 2023.

[33] W. C. Macklin and G. J. Metaxas, "Splashing of drops on liquid layers," *Journal of Applied Physics*, vol. 47, no. 9, pp. 3963–3970, 08 1976. [Online]. Available: https://doi.org/10.1063/1.323218

[34] G. Cossali, G. Brunello, A. Coghe, and M. Marengo, "Impact of a single drop on a liquid film: Experimental analysis and comparison with empirical models," 01 1999.

[35] M. Panão and A. Moreira, "Flow characteristics of spray impingement in pfi injection systems," *Experiments in Fluids*, vol. 39, pp. 364–374, 08 2005.

[36] C. W. Visser, P. E. Frommhold, S. Wildeman, R. Mettin, D. Lohse, and C. Sun, "Dynamics of high-speed micro-drop impact: numerical simulations and experiments at frame-to-frame times below 100ns," *Soft Matter*, pp. 1708–1722, 2015.

[37] G. Liang and I. Mudawar, "Review of mass and momentum interactions during drop impact on a liquid film," *International Journal of Heat and Mass Transfer*, vol. 101, pp. 577–599, 2016.

[38] S. Chandra and C. Avedisian, "On the collision of a droplet with a solid surface," *Proceedings of the Royal Society of London. Series A: Mathematical and Physical Sciences*, vol. 432, no. 1884, pp. 13–41, 1991.

[39] G. Cossali, A. Coghe, and M. Marengo, "The impact of a single drop on a wetted solid surface," *Experiments in Fluids*, vol. 22, no. 6, pp. 463–472, 1997.

[40] R. L. Vander Wal, G. M. Berger, and S. D. Mozes, "The splash/non-splash boundary upon a dry surface and thin fluid film," *Experiments in fluids*, vol. 40, no. 1, pp. 53–59, 2006.

[41] A. L. Yarin, I. V. Roisman, and C. Tropea, *Collision Phenomena in Liquids and Solids*. Cambridge University Press, 2017.

[42] N. Ashgriz, *Handbook of atomization and sprays: theory and applications*. Springer Science & Business Media, 2011.

[43] R. Rioboo, C. Tropea, and M. Marengo, "Outcomes from a drop impact on solid surfaces," *Atomization and Sprays*, vol. 11, no. 2, 2001.

[44] R. Blossey, "Self-cleaning surfaces — virtual realities," *Nature Materials*, vol. 2, no. 5, pp. 301–306, 2003.

[45] B. S. Yilbas, A. Al-Sharafi, and H. Ali, "Chapter 7 - application of water droplet for self-

cleaning of surfaces," in *Self-Cleaning of Surfaces and Water Droplet Mobility*, B. S. Yilbas, A. Al-Sharafi, and H. Ali, Eds. Elsevier, 2019, pp. 375–421. [Online]. Available: https://www.sciencedirect.com/science/article/pii/B9780128147764000070

[46] M. Zhang, S. Feng, L. Wang, and Y. Zheng, "Lotus effect in wetting and self-cleaning," *Biotribology*, vol. 5, p. 31–43, 2016.

[47] T. Young, "Iii. an essay on the cohesion of fluids," *Philosophical Transactions of the Royal Society of London*, vol. 95, pp. 65–87, 1805. [Online]. Available: https://royalsocietypublishing.org/doi/abs/10.1098/rstl.1805.0005

[48] V. E. B. Dussan, "The moving contact line: the slip boundary condition," *Journal of Fluid Mechanics*, vol. 77, pp. 665–684, 1976.

[49] G. Elliott and A. Riddiford, "Dynamic contact angles: I. the effect of impressed motion," *Journal of Colloid and Interface Science*, vol. 23, no. 3, pp. 389–398, 1967. [Online]. Available: https://www.sciencedirect.com/science/article/pii/002197976790183X

[50] T. Mao, D. C. S. Kuhn, and H. Tran, "Spread and rebound of liquid droplets upon impact on flat surfaces," *AIChE Journal*, vol. 43, no. 9, pp. 2169–2179, 1997.

[51] R. Rioboo, M. Marengo, and C. Tropea, "Time evolution of liquid drop impact onto solid, dry surfaces," *Experiments in Fluids*, vol. 33, pp. 112–124, 2002.

[52] A. S. Moita and A. L. N. Moreira, "Influence of surface properties on the dynamic behavior of impacting droplets," in *Proceedings in 9th ICLASS - Europe*. Sorrento,Italy: Institute for Liquid Atomization and Spray Systems, July 2003.

[53] M. Pasandideh-Fard, Y. M. Qiao, S. Chandra, and J. Mostaghimi, "Capillary effects during droplet impact on a solid surface," *Physics of Fluids*, vol. 8, no. 3, pp. 650–659, 1996. [Online]. Available: https://doi.org/10.1063/1.868850

[54] C. Antonini, A. Amirfazli, and M. Marengo, "Drop impact and wettability: From hydrophilic to superhydrophobic surfaces," *Physics of Fluids*, vol. 24, no. 10, p. 102104, 2012. [Online]. Available: https://doi.org/10.1063/1.4757122

[55] M. A. Quetzeri-Santiago, K. Yokoi, A. A. Castrejón-Pita, and J. R. Castrejón-Pita, "Role of the dynamic contact angle on splashing," *Physical review letters*, vol. 122, no. 22, p. 228001, 2019.

[56] A. Latka, A. M. P. Boelens, S. R. Nagel, and J. J. de Pablo, "Drop splashing is independent of substrate wetting," *Physics of Fluids*, vol. 30, no. 2, p. 022105, 2018.

[Online]. Available: https://doi.org/10.1063/1.5012529

[57] A. Karl, W. J., and F. A., "Interaction of droplet groups with hot walls above the leidenfrost-temperature," in *Proc. 13th Int. Conf. on Liquid Atomization and Spray Systems*, vol. 13, 1997, pp. 458–464.

[58] N. Roth, A. Karl, and A. Frohn, "Observation of liquid-wall contact during droplet impact," in *Proc. 14th Int. Conf. on Liquid Atomization and Spray Systems*, vol. 14, 1998, pp. 103–107.

[59] C. Tropea and I. V. Roisman, "Modeling of spray impact on solid surfaces," *Atomization and Sprays*, vol. 10, no. 3-5, 2000.

[60] G. Cossali, M. Marengo, A. Coghe, and S. Zhdanov, "The role of time in single drop splash on thin film," *Experiments in Fluids*, vol. 36, no. 6, pp. 888–900, 2004.

[61] A. I. Fedorchenko and A.-B. Wang, "On some common features of drop impact on liquid surfaces," *Physics of Fluids*, vol. 16, no. 5, pp. 1349–1365, 2004.

[62] K. Range and F. Feuillebois, "Influence of surface roughness on liquid drop impact," *Journal of Colloid and Interface Science*, vol. 203, no. 1, pp. 16–30, 1998.

[63] R. L. Vander Wal, G. M. Berger, and S. D. Mozes, "Droplets splashing upon films of the same fluid of various depths," *Experiments in Fluids*, vol. 40, pp. 33–52, 2006.

[64] A.-B. Wang and C.-C. Chen, "Splashing impact of a single drop onto very thin liquid films," *Physics of fluids*, vol. 12, no. 9, pp. 2155–2158, 2000.

[65] R. L. Vander Wal, G. M. Berger, and S. D. Mozes, "The combined influence of a rough surface and thin fluid film upon the splashing threshold and splash dynamics of a droplet impacting onto them," *Experiments in Fluids*, vol. 40, no. 1, pp. 23–32, 2006.

[66] A. Moreira, A. Moita, and M. Panão, "Advances and challenges in explaining fuel spray impingement: How much of single droplet impact research is useful?" *Progress in Energy and Combustion Science*, vol. 36, no. 5, pp. 554–580, 2010. [Online]. Available: https://www.sciencedirect.com/science/article/pii/S0360128510000031

[67] Y. Zhang, P. Liu, Q. Qu, F. Liu, and R. K. Agarwal, "Numerical simulation of a droplet impacting upon films with varied liquid properties," in *55th AIAA Aerospace Sciences Meeting*, 2017, p. 1468.

[68] Z. Che and O. K. Matar, "Impact of droplets on immiscible liquid films," *Soft Matter*, vol. 14, no. 9, pp. 1540–1551, 2018.

[69] D. A. Burzynski and S. E. Bansmer, "Droplet splashing on thin moving films at high weber numbers," *Energy*, vol. 101, pp. 202–211, 2018.

[70] D. F. S. Ribeiro, "Experimental study of a single droplet impinging upon liquid films: jet fuel and biofuel mixtures," Master's thesis, University of Beira Interior, 2018.

[71] A. M. Worthington, *A study of splashes*. Longmans, Green, and Company, 1908.

[72] O. G. Engel, "Crater depth in fluid impacts," *Journal of Applied Physics*, vol. 37, no. 4, pp. 1798–1808, 1966.

[73] K.-L. Pan, K.-R. Cheng, P.-C. Chou, and C.-H. Wang, "Collision dynamics of high-speed droplets upon layers of variable thickness," *Experiments in Fluids*, vol. 45, no. 3, pp. 435–446, 2008.

[74] C. Motzkus, F. Gensdarmes, and E. Géhin, "Parameter study of microdroplet formation by impact of millimetre-size droplets onto a liquid film," *Journal of aerosol science*, vol. 40, no. 8, pp. 680–692, 2009.

[75] K.-L. Pan and C.-Y. Hung, "Droplet impact upon a wet surface with varied fluid and surface properties," *Journal of colloid and interface science*, vol. 352, no. 1, pp. 186–193, 2010.

[76] A. Geppert, D. Chatzianagnostou, C. Meister, H. Gomaa, G. Lamanna, and B. Weigand, "Classification of impact morphology and splashing/deposition limit for n-hexadecane," *Atomization and Sprays*, vol. 26, no. 10, 2016.

[77] N. Ninomiya and K. Iwamoto, "Piv measurement of a droplet impact on a thin fluid layer," in *AIP Conference Proceedings*, vol. 1428, 2012, pp. 11–17.

[78] J.-H. Guo, S.-Q. Dai, and D. Qin, "Experimental research on the droplet impacting on the liquid film," *Acta Physica Sinica*, vol. 59, no. 4, pp. 2601–2609, 2010.

[79] R. Rioboo, M. Marengo, G. Cossali, and C. Tropea, "Comparison of drop impact: dry and wetted cases," in *Proceedings of the 16th International conf. On Liquid Atomisation and Spray Systems (ILASS). Darmstadt, Germany*, 2000.

[80] C. Bai and A. Gosman, "Development of methodology for spray impingement simulation," *SAE transactions*, pp. 550–568, 1995.

[81] C. D. Stow and R. D. Stainer, "The physical products of a splashing water drop," *Journal of the Meteorological Society of Japan. Ser. II*, vol. 55, no. 5, pp. 518–532, 1977.

[82] Q. Huang and H. Zhang, "A study of different fluid droplets impacting on a liquid film,"

Petroleum Science, vol. 5, no. 1, pp. 62–66, 2008.

[83] I. Abrantes, A. F. Ferreira, A. Silva, and M. Costa, "Sustainable aviation fuels and imminent technologies - co2 emissions evolution towards 2050," *Journal of Cleaner Production*, vol. 313, p. 127937, 2021. [Online]. Available: https://www.sciencedirect.com/science/article/pii/S0959652621021557

[84] Y. Katto, "Critical heat flux," *International Journal of Multiphase Flow*, vol. 20, pp. 53–90, 1994. [Online]. Available: https://www.sciencedirect.com/science/article/pii/0301932294900701

[85] Y. D. Chashechkin, "Visualization of the fine perturbation structure of a liquid surface by flows induced by a drop impact," *Fluid Dynamics*, vol. 54, no. 7, p. 919–926, 2019.

[86] E. Hecht, Ed., *Optik*, 3rd ed. Bonn [u.a.]: Addison-Wesley, 1994.

[87] SCHOTT AG, "Optisches glas - datenblätter," Tech. Rep., 2010. [Online]. Available: https://www.schott.com/d/advanced_optics/47d79895-2965-472d-83ed-af9e48ac72c0/1.11/schott-optisches-glas-datenblatt-sammlung-german-17012017.pdf

[88] P. E. Ciddor, "Refractive index of air: new equations for the visible and near infrared," *Appl. Opt.*, vol. 35, no. 9, pp. 1566–1573, Mar 1996. [Online]. Available: http://ao.osa.org/abstract.cfm?URI=ao-35-9-1566

[89] Photron, *Fastcam SA-X2 - Dataseheet*, rev# 17.03.03 ed., 2017.

[90] P. Foltyn, M. Guttmann, M. Schneider, S. Fest-Santini, D. Wildenschild, and B. Weigand, "Fabrication and evaluation methods of micro-structured surfaces for droplet impact experiments," in *Droplet Interactions and Spray Processes*, G. Lamanna, S. Tonini, G. E. Cossali, and B. Weigand, Eds. Cham: Springer International Publishing, 2020, pp. 71–86.

[91] P. Foltyn, F. Restle, M. Wissmann, S. Hengsbach, and B. Weigand, "The effect of patterned micro-structure on the apparent contact angle and three-dimensional contact line," *Fluids*, vol. 6, no. 2, 2021. [Online]. Available: https://www.mdpi.com/2311-5521/6/2/92

[92] R. W. Wenzel, "Resistance of solid surfaces to wetting by water," *Industrial and Engineering Chemistry*, vol. 28, pp. 988–994, 1936.

[93] P. Tsai, R. C. A. van der Veen, M. van de Raa, and D. Lohse, "How micropatterns and air pressure affect splashing on surfaces," *Langmuir*, vol. 26, no. 20, pp.

16 090–16 095, Oct. 2010. [Online]. Available: https://doi.org/10.1021/la102330e

[94] I. V. Roisman, A. Lembach, and C. Tropea, "Drop splashing induced by target roughness and porosity: The size plays no role," *Advances in Colloid and Interface Science*, vol. 222, pp. 615–621, 2015.

[95] A. S. Moita and A. L. N. Moreira, "Influence of surface properties on the dynamic behavior of impacting droplets," in *Proceedings in 9th ICLASS - Europe*. Sorrento,Italy: Institute for Liquid Atomization and Spray Systems, July 2003.

[96] Q. Wang, X. Lin, Y. Lin, J. Ma, J. Xiao, Y. Wu, and J. Wang, "Effects of surface roughness on splashing characteristics of large droplets with digital inline holographic imaging," *Cold Regions Science and Technology*, vol. 191, p. 103373, 2021. [Online]. Available: https://www.sciencedirect.com/science/article/pii/S0165232X21001543

[97] L. Xu, "Liquid drop splashing on smooth, rough, and textured surfaces," *Phys. Rev. E*, vol. 75, p. 056316, May 2007. [Online]. Available: https://link.aps.org/doi/10.1103/PhysRevE.75.056316

[98] L. Courbin, J. C. Bird, and H. A. Stone, "Splash and anti-splash: Observation and design," *Chaos: An Interdisciplinary Journal of Nonlinear Science*, vol. 16, no. 4, p. 041102, 2006.

[99] A. Marmur, C. Della Volpe, S. Siboni, A. Amirfazli, and J. W. Drelich, "Contact angles and wettability: towards common and accurate terminology," *Surface Innovations*, vol. 5, no. 1, pp. 3–8, 2017. [Online]. Available: https://doi.org/10.1680/jsuin.17.00002

[100] D. K. Owens and R. C. Wendt, "Estimation of the surface free energy of polymers," *Journal of Applied Polymer Science*, vol. 13, no. 8, pp. 1741–1747, 1969. [Online]. Available: http://dx.doi.org/10.1002/app.1969.070130815

[101] W. Rabel, "Einige Aspekte der Benetzungstheorie und ihre Anwendung auf die Untersuchung und Veränderung der Oberflächeneigenschaften von Polymeren," *Farbe und Lacke*, vol. 77, no. 10, pp. 997–1005, 1971.

[102] D. H. Kaelble, "Dispersion-polar surface tension properties of organic solids," *The Journal of Adhesion*, vol. 2, no. 2, pp. 66–81, 1970. [Online]. Available: https://doi.org/10.1080/0021846708544582

[103] F. M. Fowkes, "Attractive forces at interfaces," *Ind. Eng. Chem.*, vol. 56, no. 12, pp. 40–52, Dec. 1964. [Online]. Available: https://doi.org/10.1021/ie50660a008

[104] G. Ström, M. Fredriksson, and P. Stenius, "Contact angles, work of adhesion, and interfacial tensions at a dissolving hydrocarbon surface," *Journal of Colloid and Interface Science*, vol. 119, no. 2, pp. 352 – 361, 1987. [Online]. Available: http://www.sciencedirect.com/science/article/pii/0021979787902803

[105] DataPhysics Instruments GmbH, "Surface tensions/energies," https://www.dataphysics-instruments.com/Downloads/Surface-Tensions-Energies.pdf, 2018. [Online]. Available: https://www.dataphysics-instruments.com/Downloads/Surface-Tensions-Energies.pdf

[106] M. Greiveldinger and M. E. Shanahan, "A critique of the mathematical coherence of acid/base interfacial free energy theory," *Journal of Colloid and Interface Science*, vol. 215, no. 1, pp. 170 – 178, 1999. [Online]. Available: http://www.sciencedirect.com/science/article/pii/S0021979799962598

[107] W. Wagner and A. Pruß, "The iapws formulation 1995 for the thermodynamic properties of ordinary water substance for general and scientific use," *Journal of Physical and Chemical Reference Data*, vol. 31, no. 2, pp. 387–535, 2002. [Online]. Available: https://doi.org/10.1063/1.1461829

[108] J. R. Rumble, "Density rho at the temperature in °c indicated by superscript," *CRC Handbook of Chemistry and Physics*, 2019.

[109] IAPWS, "Revised release on surface tension of ordinary water substance," International Association for the Properties of Water and Steam, Tech. Rep. R1-76, 2014.

[110] J. R. Rumble, "Viscosity of liquids as a function of temperature," *CRC Handbook of Chemistry and Physics*, 2019.

[111] M. L. Huber, R. A. Perkins, A. Laesecke, D. G. Friend, J. V. Sengers, M. J. Assael, I. N. Metaxa, E. Vogel, R. Mareš, and K. Miyagawa, "New international formulation for the viscosity of h2o," *Journal of Physical and Chemical Reference Data*, vol. 38, no. 2, pp. 101–125, jun 2009. [Online]. Available: https://doi.org/10.1063/1.3088050

[112] J. R. Rumble, "Surface tension at various temperatures," *CRC Handbook of Chemistry and Physics*, 2019.

[113] H. Zhang, X. Zhang, X. Yi, F. He, F. Niu, and P. Hao, "Effect of wettability on droplet impact: Spreading and splashing," *Experimental Thermal and Fluid Science*, vol. 124, p. 110369, 2021. [Online]. Available: https://www.sciencedirect.com/science/article/pii/S0894177721000224

[114] A. Fridman, *Plasma Chemistry*. Cambridge University Press, 2008. [On-

line]. Available: https://www.ebook.de/de/product/7253167/alexander_fridman_plasma_chemistry.html

[115] P. Foltyn, A. Schlottke, and B. Weigand, "Effect of plasma activation on the contact angle of smooth polymer surfaces and its long-term durability in ambient air," in *10th International Colloids Conference, 7-9 December 2020 (Online) Palma de Mallorca, Spain*, vol. 10, 12 2020.

[116] N. Otsu, "A threshold selection method from gray-level histograms," *IEEE Transactions on Systems, Man, and Cybernetics*, vol. 9, no. 1, pp. 62–66, 1979.

[117] A. D1655-19a, "Astm d1655-19a, standard specification for aviation turbine fuels," ASTM International, Tech. Rep., 2019.

[118] A. D7566-19b, "Astm d7566-19b, standard specification for aviation turbine fuel containing synthesized hydrocarbons," ASTM International, Tech. Rep., 2019.

[119] G. Pacheco, A. Silva, and M. Costa, "Single-droplet combustion of jet a-1, hydroprocessed vegetable oil, and their blends in a drop-tube furnace," *Energy & Fuels*, vol. 35, no. 9, pp. 7232–7241, 2021. [Online]. Available: https://doi.org/10.1021/acs.energyfuels.0c03476

[120] C. Mundo, M. Sommerfeld, and C. Tropea, "Droplet-wall collisions: Experimental studies of the deformation and breakup process," *International Journal of Multiphase Flow*, vol. 21, no. 2, pp. 151–173, 1995.

[121] Y. Zhu, H.-R. Liu, K. Mu, P. Gao, H. Ding, and X.-Y. Lu, "Dynamics of drop impact onto a solid sphere: spreading and retraction," *Journal of Fluid Mechanics*, vol. 824, p. R3, 2017.

[122] S. Moghtadernejad, C. Lee, and M. Jadidi, "An introduction of droplet impact dynamics to engineering students," *Fluids*, vol. 5(3), p. 107, 2020.

[123] P. Foltyn, N. Roth, and B. Weigand, "Development and calibration of the laser pattern shift method for measuring the lamella topology during drop impact on walls," in *29th European Conference on Liquid Atomization and Spray Systems*, 2019. [Online]. Available: https://ilass19.sciencesconf.org/241623

[124] V. Mehdi-Nejad, J. Mostaghimi, and S. Chandra, "Air bubble entrapment under an impacting droplet," *Physics of Fluids*, vol. 15, no. 1, pp. 173–183, jan 2003.

[125] D. B. van Dam and C. Le Clerc, "Experimental study of the impact of an ink-jet printed droplet on a solid substrate," *Physics of Fluids*, vol. 16, no. 9, pp. 3403–3414, aug

2004.

[126] R. Hensel, R. Helbig, S. Aland, H. Braun, A. Voigt, C. Neinhuis, and C. Werner, "Wetting resistance at its topographical limit: The benefit of mushroom and serif t structures," *Langmuir*, vol. 29, pp. 1100–1112, 2013.

[127] I. Roisman and C. Tropea, "Fluctuating flow in a liquid layer and secondary spray created by an impacting spray," *International Journal of Multiphase Flow*, vol. 31, no. 2, pp. 179–200, 2005.

[128] G. Lamanna, A. Geppert, R. Bernard, and B. Weigand, "Drop impact onto wetted walls: an unsteady analytical solution for modelling crown spreading," *Journal of Fluid Mechanics*, vol. 938, p. A34, 2022.

[129] M. Selmke, "Bubble optics," *Applied Optics*, vol. 59, no. 1, pp. 45–58, 2020.

[130] X. □. Yu, Y. □. Shao, K.-Y. Teh, and D. L. S. Hung, "Force of droplet impact on thin liquid films," *Physics of Fluids*, vol. 34, no. 4, p. 042111, 2022. [Online]. Available: https://doi.org/10.1063/5.0083437

[131] A. Singh and P. Kumar, "Droplet impact dynamics onto a deep liquid pool of wavy free surface," *Physics of Fluids*, vol. 34, no. 2, p. 022107, 2022. [Online]. Available: https://doi.org/10.1063/5.0084530

[132] T. Sun, H. Wang, Z. Zong, G. Zhang, A. Wang, and C. Xu, "Splash formation and cavity dynamics of sphere entry through a viscous liquid resting on the water," *AIP Advances*, vol. 9, no. 7, p. 075211, 2019. [Online]. Available: https://doi.org/10.1063/1.5109252

[133] I. V. Roisman, N. P. van Hinsberg, and C. Tropea, "Propagation of a kinematic instability in a liquid layer: capillary and gravity effects," *Physical Review E*, vol. 77, no. 4, p. 046305, 2008.

[134] D. Ribeiro, N. Cunha, J. Barata, and A. Silva, "Dynamic behaviour of single droplets impinging upon liquid films with variable thickness: Jet a-1 and hvo mixtures," in *14th International Conference on Liquid Atomization & Spray Systems, July 22-26*, 2018, p. 8pp.

[135] D. Vasconcelos, D. Ribeiro, J. M. Barata, and A. R. Silva, "Experimental and numerical study of single droplets impinging upon liquid films," in *4th Thermal and Fluid Engineering Conference, April 14-17*, 2019, p. 4pp.

[136] A. L. Yarin and D. A. Weiss, "Impact of drops on solid surfaces: self-similar capillary waves, and splashing as a new type of kinematic discontinuity," *Journal of fluid me-*

chanics, vol. 283, pp. 141–173, 1995.

[137] D. A. Weiss and A. L. Yarin, "Single drop impact onto liquid films: neck distortion, jetting, tiny bubble entrainment, and crown formation," *Journal of Fluid Mechanics*, vol. 385, pp. 229–254, 1999.

[138] C. Josserand, P. Ray, and S. Zaleski, "Droplet impact on a thin liquid film: anatomy of the splash," *Journal of Fluid Mechanics*, vol. 802, pp. 775–805, 2016.

[139] A. B. Aljedaani, C. Wang, A. Jetly, and S. T. Thoroddsen, "Experiments on the breakup of drop-impact crowns by marangoni holes," *Journal of Fluid Mechanics*, vol. 844, pp. 162–186, 2018.

[140] L. Lu, Y. Pei, J. Qin, Z. Peng, Y. Wang, and Q. Zhu, "Impingement behaviour of single ethanol droplet on a liquid film of glycerol solution," *Fuel*, vol. 276, p. 117820, 2020.

[141] A. F. S. F. Mendes, "The influence of temperature in regime transition boundaries for single droplet impact upon heated liquid films," Master's thesis, University of Beira Interior, 2023.

[142] I. V. Roisman and C. Tropea, "Impact of a drop onto a wetted wall: description of crown formation and propagation," *Journal of Fluid Mechanics*, vol. 472, p. 373–397, 2002.